Nanoscopic atomic lattices with light-mediated interactions

Thesis by

Juan Andres Muniz Silva

In Partial Fulfillment of the Requirements for the
degree of
Doctor of Philosophy

CALIFORNIA INSTITUTE OF TECHNOLOGY
Pasadena, California

2017
Defended May 12, 2017

Juan Andres Muniz Silva
ORCID: [0000-0001-6756-6218]

ACKNOWLEDGEMENTS

There are few occasions in the life of a normal person where one can publicly acknowledge the support received. First, I would like to thank Jeff for his support and encouragement during the past 6 years. The experiment was complex from the beginning, and Jeff's long term insight and effort have been crucial in the progress we have made in Lab 2 and the group. He has challenged me since my first term here, and although I am sure I have a negative record in bet beers and one dollar bills, I have always, and will, learned and valued his example as physicist.

I have also been fortunate to interact with Oskar Painter and Darrick Chang, as both have helped develope the set of tools needed for this experiment. I appreciate their time, as well as the time and effort of all the members of the committee.

I have been extremely lucky to make friends during my time here. More than once, Andrew and I have been back-to-back trying to make things work, thinking how to split the work or what is wrong, sharing a beer, or just listening to terrible music in the lab. I am always happy to received his advice and learn what he has been doing. Andrew is very creative, from trivia to physics, and he is usually the one who asks and answers the hard questions. Thanks you Andrew, and Hannah, for being since the beginning such a nice friends. Aki has been another great running-racquetball-beer friend. I have always enjoyed talking with Aki, most of the times until late in room 4. I always look at him when I need to work harder and be more humble. I'm excited to have him around soon. Outside the Lab, I found a great friend in Christos. He was always there when I needed to talk with someone. I appreciate your constant effort to be great company, to buy me cake for my birthday, or to just help me clean the house.

I had the chance to work with great and talented people in Lab 2. Lucas and Alex, the warriors, are doing an excellent job, and I only hope things get better in the future. I wish we could capitalize on the momentum with the new fringe sensitive signal and have that progress happen faster with a new setup. I have learned a lot from both of you and I am thankful for the help received on numberless occasions. Mike and Jae never hesitated to get their hands dirty doing small, big, or impossible things. I appreciate everything I learned from both of you, your immense patience, and your support to help me be a better researcher. I hope Lab 2 will pour another whiskey glass for the win soon. Although Ana is our star theorist, not surprisingly she asks

the right questions about the experiment. I always enjoy thinking about what she asks, but foremost I prize her friendship and laughs about my Uruguayan-Spanish, Charlotte, the Chocolate song, or the cow in my passport. And Héctor, thanks for the frittata!

Many other coworkers had helped me during the past years, including and specially Su-Peng, Ding, Chen-Lung, Alejandro, Jon, Xingsheng, Daniel, Tao, Kevin, Marco, James, Jenny, Sean, and Justin. Everyone had the patience to teach me something; I am in debt with you guys. Scott helped me so many times, things always seem easier after talking with him. Also, my thanks to other members of the Caltech community, Elvira, Maria, and Martha, who kept my Spanish fresh and made me feel closer to home, and Laura, who always offers a smile every time I had questions about "Being in the US-101".

A mis amigos en Uruguay, que en estos 6 años han estado siempre pendiente de mi. Cada vez que los visito me recargan las baterías y refuerza la amistad que nos une. A la extendida y creciente familia del Requengan, por ser parte de una de las mejores memorias que conservo, por muchos años más de amistad. No se pierdan! En especial a los Reques que se las patean. Viva Vesco! A Pablo y familia, muy especialmente por ser un gran amigo, preocuparse por mi y dejarme ser parte de la familia aunque sea un fin de semana cada tanto. A Miguel que me pasó el gusto por la Física en el Liceo y se preocupó siempre de saber en qué andaba y cómo iba todo. A Maxi, Fer y el Luispe, tres grandes de la Física rioplatense que la van a romper donde sea. A Rodolfo por su infinita paciencia. También a Mauri, Lourdes y Ale, el príncipe de Ramallo, que grandes amigos! Gracias a todos!

Qué decir de mis viejos y hermana. SIEMPRE ayudando, dándome su cariño y queriendo verme bien. Si hay algo que aprendí de mi papá y mamá es a nunca bajar los brazos, a no rendirse y no aceptar un "no se puede" caprichoso (gracias por comprarme aquella enciclopedia celeste!). Y de mi hermana, la inteligente de la familia, a cuidar y preocuparse más por los seres queridos (me debes chivitos aún!). A todos mis primos, tíos, mis suegros y muy especialmente a mi abuelita Yaya que es la mejor abuela del mundo. Gracias por siempre estar ahí. Gracias.

Finally, this can be written either in English or Spanish. I want to thank Carmen. She is the woman I looked for all my life, the one that was hard to find until one day, by chance or by destiny, we found each other. Life is better with you. Thanks for being there always and giving me another home with you.

This thesis is dedicated to my brother Felipe, who always takes care of his siblings.

ABSTRACT

Integrating ultracold atoms with nanophotonics enables the exploration of new paradigms in quantum optics and many body physics. Advanced fabrication capabilities for low-loss dielectric materials provide powerful tools to engineer light-matter coupling of photons and atoms. For example, dispersion-engineered photonic crystal waveguides (PCWs) permit not only stable trapping and probing of atoms via interactions with guided mode (GM) light, but also the possibility to study the physics of strong photon-mediated interactions between atoms. This thesis describes the design of a quasi-one-dimensional structure, the alligator photonic crystal waveguide (APCW), which has already allowed for the observation of some of those features.

Furthermore, external illumination schemes allow for the trapping and transport of atoms near the dielectric device. Here, atoms loaded into a one-dimensional optical lattice are transported through the APCW. As the atoms trapped in the lattice approach the APCW, the combination of lattice and GM potential can smoothly guide atoms into the gap between the two dielectric nanobeams. Therefore, the transmission of a weak guided mode probe is modulated at the rate determined by the lattice moving through the APCW. In the near future, single atoms can then be transferred from the moving lattice into optical traps formed in each unit cell by GMs of the APCW. Moreover, a characterization of a simple 2D photonic crystal slabs design is presented.

TABLE OF CONTENTS

LIST OF ILLUSTRATIONS

LIST OF TABLES

Chapter 1

INTRODUCTION

Atoms and light are one of the oldest subjects of study in the history of human knowledge. In the modern physics era, the invention of masers and lasers paved the way for the study of light-matter interactions in ways that were not previously possible. Numerous applications have dealt with neutral atoms, ions, solid state systems, and even biological samples. In quantum optics, the quantum properties of light pushed the limits of precision measurements beyond the standard quantum limit, the observation of non-classical effects, and the generation of entangled states of photons, atoms and photons, or even atoms [1].

The integration of several quantum systems in a network configuration, where the nodes and channels have quantum properties, is still an ongoing effort [2]. High degrees of control and isolation can be achieved using neutral atoms, and interfacing them with different light fields, making them a natural candidate for the quantum nodes and quantum channel, respectively. These networks can have a big impact on the way quantum information protocols are performed, as the connectivity properties of the network can help to overcome scaling and error-correction problems. On the other hand, connecting single quantum systems to form a quantum many-body system, by means of coherent and incoherent interactions, can emulate similar systems that in principle could be harder to analyze. For example, interacting spin systems can be represented by atoms whose interactions are mediated by photons that can propagate among the network.

As quantum optics has nurtured many other research fields, quantum optics has also been changing as other fields advance. Two major fields have had a significant impact in recent years. Solid-state systems have been integrated with electromagnetic fields in very different environments. Superconducting quantum circuits and the possibility to create well controlled qubits have pushed the efforts towards developing quantum computing architectures [3]. Superconducting systems have been coupled to microwave resonators and waveguides and have been used to perform numerous error-correcting protocols relevant to develop quantum computing [4, 5]. In the semiconductor community, quantum dos, rare-earth ions, and vacancy centers in diamond have been observed to have a vast range of coherence times, and have been

interfaced with nanostructures that enhance spectroscopic measurements [6, 7, 8, 9, 10, 11].

Naturally, advances in the optical community have high impact on different areas across quantum optics. Progress in micro and nanophotonics has made possible the creation of new platforms to engineer light-matter interactions, and test different architectures in order to explore many-body physics to quantum information protocols [1]. A paradigmatic example in quantum optics is cavity quantum electrodynamics (cavity QED) [12], which traditionally investigated the interaction of single atoms and photons inside an almost perfect cavity, but it has expanded over many other fields like ion trapping and solid-state systems.

New physical regimes in quantum optics and atomic physics have been available due to the increasingly high level of experimental control over atomic and optical systems. The appearance of quantum many-body phenomena, originally confined to the condensed-matter physics community, and the experimental opportunity to access sufficient information to characterize different phases in these systems are now common in the AMO community [13, 14]. Atomic ensembles trapped inside optical resonators have shown impressive levels of spin squeezing, showing its potential for applications in quantum metrology [15, 16]. In cavity QED, quantum many-body systems can be formed by creating arrays of interacting cavities coupled to atomic systems [14]. These arrays can work as quantum simulators with high degree of addressability. A main challenge is to find the appropriate architecture to perform these procedures.

An auspicious platform is the integration of atomic systems with nanophotonics, where serious advances have already been made in the last two decades [17, 18, 19]. Beyond the cavity QED and waveguide QED [20, 21, 22, 23, 24] framework, photonic crystals offer a way to tailor strong light-matter coupling for single atoms and photons in a complex and scalable fashion. For instance, by designing and fabricating the dielectric structure of photonic crystal waveguides, the dispersion relation and mode structure permit the trapping and probing of ultracold neutral atoms with commensurate spatial periodicity for both, while slow light effects near the band-edge enhance the coupling [25, 26]. Such systems can lead to atom-atom interactions mediated by photons within the waveguide [27, 28, 29, 30].

The work described in this thesis is part of a larger collaboration between different members of the Quantum Optics Group at Caltech. Our objective is to trap atoms along a photonic crystal waveguide with high filling fraction, in order to study light-

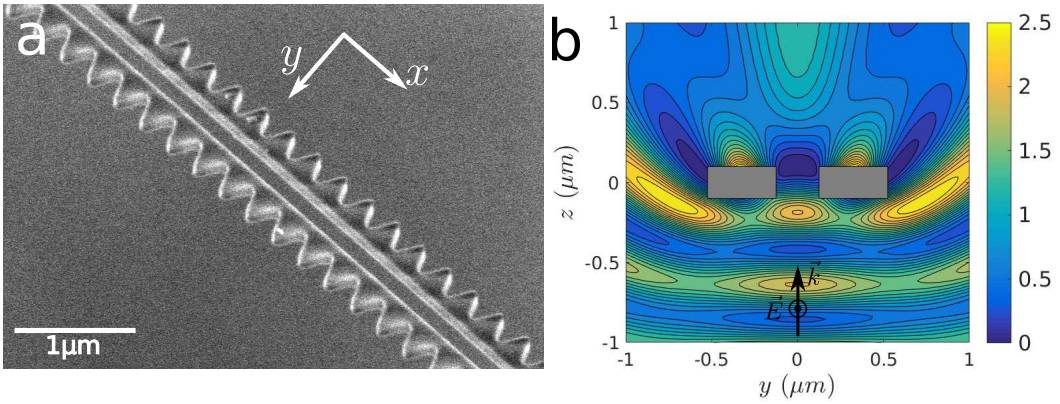

Figure 1.1: The alligator photonic crystal waveguide (APCW) and the side illumination trap. In (a) an SEM image of the APCW is shown, taken by Andrew McClung. External illumination can be used to create intricate light potentials near the device, as seen in the intensity pattern $|\mathbf{E}(\mathbf{r})|^2$ seen in (b). Details on these pictures will appear later in the text.

matter interactions in tailored photonic environments [25, 30], many-body physics [31, 32, 33], atom-atom photon-mediated interactions [28, 30], dispersive, spin-dependent and collective forces on atoms [34, 35, 36], and non-linear physics at the single photon level [37, 38], just to name a few. Although modest results were obtained at the time this thesis was finished, a diverse set of tools was developed.

The main actor of this work is the alligator photonic crystal waveguide (APCW), a standing structure fabricated in a SiN substrate that is integrated into the vacuum system, and where light can be coupled in an out. A SEM image of a section of the APCW is shown in Fig. 1.1(a). The structure follows the ideas mentioned before, such that it is possible to create localized traps along the structure where a strong probe mode can interrogate the trapped atoms. However, loading these traps with atoms is challenging [39]. In order to overcome this difficulty, external illumination schemes are used to trap atoms along the device using the device's high reflection [40] as seen in Fig. 1.1(b).

Trapped atoms along the device behave differently than in free-space [30, 28, 31, 33]. Remarkably, the photonic properties of the APCW have effects on the light-matter interaction. The APCW has bands $\omega_n(k)$ and frequency ranges where light cannot propagate through the structure because of the presence of bandgaps. If the atomic transition frequency is in the bandgap, as in Fig. 1.2(b), the atom cannot decay into that photonic mode, and it is said that the atom is in the dispersive regime. The incoherent interaction between the field and the array of atoms is partially or totally

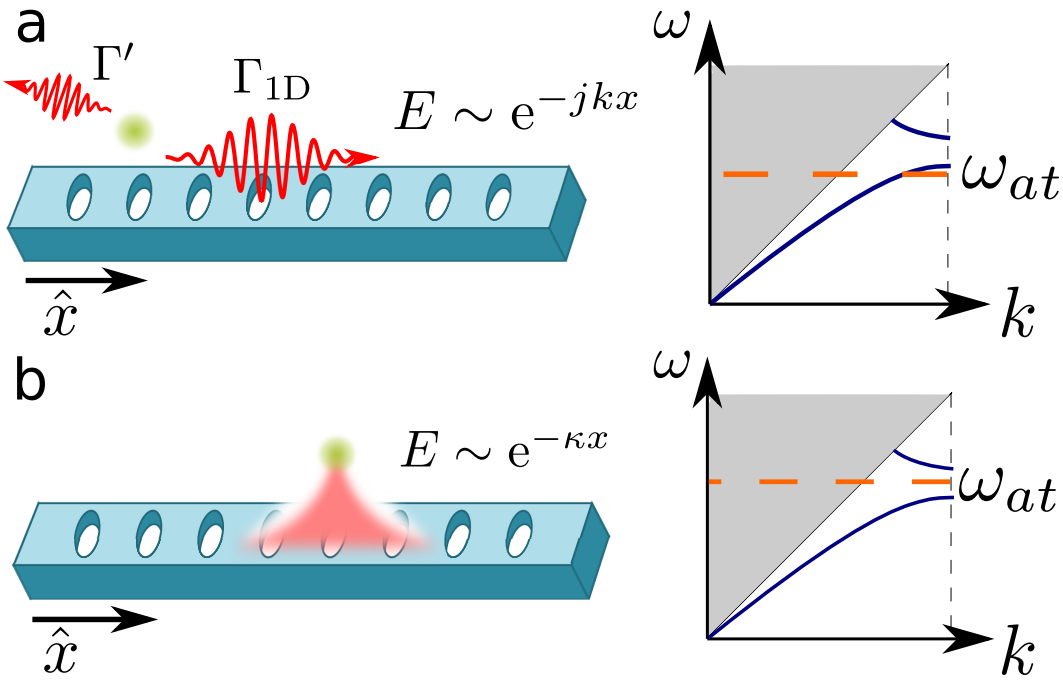

Figure 1.2: If the atomic transition is guided, outside the bandgap, as in (a), an atom near the photonic crystal waveguide can emit into a specific guided mode or into any other channel, with rates Γ_{1D} and Γ' respectively. If the atomic frequency is in the bandgap, then the atom can not decay into that photonic mode and it forms a bound state with the photonic excitation.

suppressed, depending on the characteristics of the structure, while the coherent exchange between atoms along the device is still present. Among the different states the atom and the photon can have, it is possible to form a bound state where the photonic component is localized around the atom.

The observation of such regime with cold atoms trapped near the APCW structure has been recently reported by Hood et al. [29]. In this regime, strong and variable-range interactions between atoms mediated by photons confined to one-dimensional photonic crystal waveguides, or two-dimensional photonic crystal membranes [31], can be engineered. The tight confinement of the guided modes favors strong interactions between atoms and localized photons, while control over the interaction length is provided by the presence of the photonic bandgap and its tunable dispersion properties, making photonic crystal systems a unique platform to test many-body systems of photons and atoms.

If the atomic transition frequency is guided, it is outside the bandgap, as shown in Fig. 1.2(a), the atoms can see their spontaneous emission rate into the guided

mode enhanced by slow-light effects as reported in Goban et al. [39]. The atoms are then considered to be in the dissipative regime. An array of atoms can exhibit superradiance emission into the guided mode, as collective interaction manifest in this case [40].

It remains possible to trap more than ~ 3 atoms as reported in those works. The worked carried out in Lab 2 points towards that direction. In this experiment, the delivery of atoms occurs by creating a standing wave pattern with two counter-propagating beams polarized perpendicular to the APCW, such that the reflection from the device can be minimized. The standing wave works as a conveyor belt if the relative phase of the two beams are different. This allows the atoms to move in a controlled manner. As the atoms, localized into the standing wave pattern, arrive to the APCW, as shown in Fig. 1.3, the guided mode probe transmission signal is modulated at the same pace as the arriving atoms. Recently, this signal has been observed and is still being analyzed, paving the way to load and cool atoms into the nanoscopic atomic lattices formed by the APCW guided modes.

This thesis focuses on several aspects of the project. On the experimental side, it concentrates on the assembly of the experimental apparatus, its characterization, and the measurements performed using the APCW devices. On the theoretical/applied side, the design of these traps, starting from the design and requirements of the APCW structure, the use of external illumination light, and the extension of the schemes in 1D to 2D are described.

The second chapter serves as a brief introduction to the majority of the nanophotonic aspects of the project, focusing on the description of light-matter interactions in arbitrary systems, with particular emphasis on photonic crystal waveguides. The AMO toolbox is described in the third chapter. Additionally, some fundamental limitations related to loading atoms in optical dipole traps are discussed, keeping in mind how they might, or already do, affect the performance of the experiment. An extensive description of the APCW is found in the fourth chapter, with emphasis on the design and fabrication challenges found along the way.

The following two chapters describe the core ideas behind the trapping schemes employed. Both schemes developed in Lab 11 and Lab 2 are explained. The search for a fringe sensitive signal in the probe transmission is discussed in chapter five. The experiment is thoroughly explained in chapter six. Experimental results up to this point are shown there.

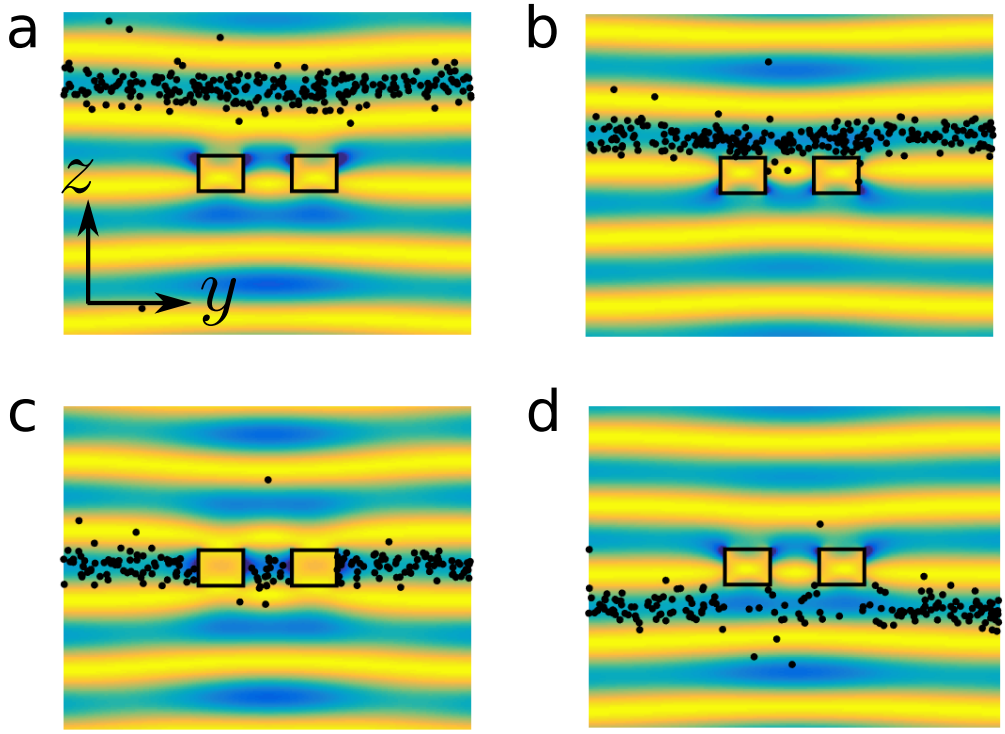

Figure 1.3: Transport of atoms in a standing wave near the APCW. As The phase between two counter-propagating beams changes, from (a) to (d), the atoms move with the intensity pattern of the standing wave. The APCW axis is along the x-direction. The color plot represents the potential, and the black dots the atoms. Details on this figures will appear later in the text.

Finally, the design of a 2D photonic crystal slab device can be found in the last chapter. The design is based on a simple square lattice array of holes, where efficient input and output coupling can be performed by means of another photonic component that collimates light along the slab.

Chapter 2

LIGHT-MATTER INTERACTION IN 1D SYSTEMS

In general, microscopy can be imagine to just report the position of certain emitters, by for example, collecting the light scattered by them with a microscope objective. Superlative advances had been made in the last two decade towards using new optical technologies and methods, from super-resolution fluorescence microscopy to identify and study 3D living sub-cellular organelles [41, 42, 43] to adaptive optical techniques in the Keck observatory to map the NIR and IR sky with higher resolution and power [44].

However, an essential idea already present in early works on light-matter interaction reveals light emitters also probe their local environment. These ideas can be traced back to the original Weisskopf-Wigner theory for spontaneous emission [45] or even, later, in the extraordinary work by Purcell [46]. These properties can be exploited by the recently new field of nanophotonics, because it is possible to design and fabricate structures that support electric field modes, propagating or not, that can excite emitters in ways that were not possible before [47, 1, 37].

Here, the coupling between a single emitter to the electric field that propagates into those structures will be described. The problem will be treated using some of the most powerful tools applied in the nanophotonics field: the Green's function formalism to describe light-matter interactions. In this section, the Green's function tensor will be introduced and used to obtain the total spontaneous emission rate of a dipole emitter in an arbitrary environment as well as some general features of nanophotonic systems, with emphasis in the adequate treatment for a photonic crystal waveguide.

2.1 Dipoles and modes

In a broad class of experimental situations, it is accurate to approximate certain emitters as point-like sources, for example, when a piece of matter is small compared to the relevant wavelength. This is the so called *dipole approximation*, usually invoked in the standard quantum electrodynamics treatment of light-matter interactions [48, 49, 50]. These point-like emitters can be thought as a small dipole emitting radiation with their characteristic spatial distribution. This is the most elementary treatment;

other corrections might need to be considered if necessary, but for now the treatment will be limited to this easier case.

The Green's function for the electric field

Maxwell's equations define the field generated by currents and charges in any material [51]. The wave equation follows from them, and shows how electric fields can be generated from time varying current densities. In a linear medium, the electromagnetic field can be written as a superposition of monochromatic fields of the form

$$\mathbf{E}(\mathbf{r}, t) = \mathbf{E}(\mathbf{k}, \omega) \cos(\mathbf{k} \cdot \mathbf{r} - \omega t). \tag{2.1}$$

In general, the main interest is to study the spectral representation of time-dependent fields, so only the time variable is going to be transformed. In this case, the spectrum $\hat{\mathbf{E}}(\mathbf{r}, \omega)$ of an arbitrary field $\mathbf{E}(\mathbf{r}, t)$ is defined by the usual Fourier transform

$$\hat{\mathbf{E}}(\mathbf{r}, \omega) = \frac{1}{2\pi} \int \mathbf{E}(\mathbf{r}, t)\, \mathrm{e}^{i\omega t} dt. \tag{2.2}$$

Back to the monochromatic fields, Eq(2.1) can be rewritten as

$$\mathbf{E}(\mathbf{r}, t) = \mathrm{Re}\left\{\mathbf{E}(\mathbf{r})\, \mathrm{e}^{-i\omega t}\right\} = \frac{1}{2}\left[\mathbf{E}(\mathbf{r})\, \mathrm{e}^{-i\omega t} + c.c\right]. \tag{2.3}$$

An important tool in field theory is the Green's function, which reflects the spatial impulsive response of the media [51, 52]. The physical intuition behind it is that if the solution for a point-like source for any position is known, a linear differential equation admits as solution for an extended source the appropriate superposition of solutions by many point-like sources. The Green's function carries the information of the solution at a point $\mathbf{r}$ from a point-like source at the position $\mathbf{r}'$.

In the case of the electric field, the wave equation for a monochromatic field in homogeneous space can be written as

$$\left[\nabla \times \nabla \times -k^2\right] \mathbf{E}(\mathbf{r}) = i\omega\mu_0 \mathbf{j}(\mathbf{r}), \tag{2.4}$$

where $\mathbf{j}(\mathbf{r})$ is the current density, μ_0 is the relative vacuum permeability of the medium, and $k = \omega/c$ is the wavevector. For each component, the Green's function for Eq(2.4) is defined as the solution to a localized point source

$$\left[\nabla \times \nabla \times -k^2\right] \mathbf{G}_i(\mathbf{r}, \mathbf{r}') = \mathbf{n}_i \delta(\mathbf{r} - \mathbf{r}'). \tag{2.5}$$

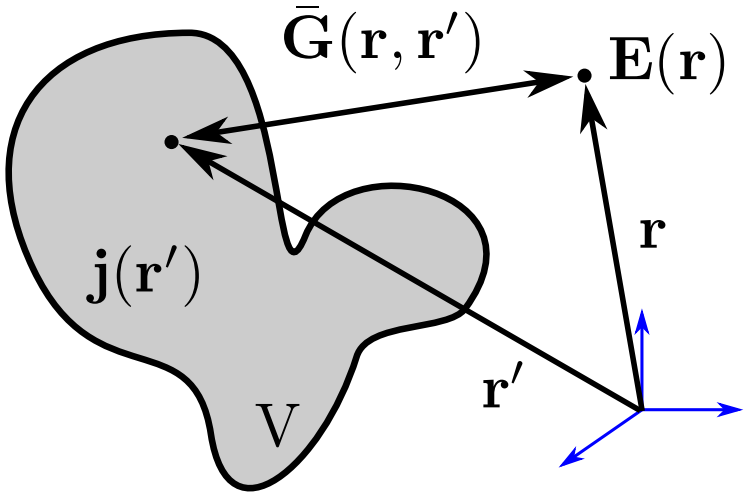

Figure 2.1: Sketch of the Green's function $\bar{\mathbf{G}}(\mathbf{r},\mathbf{r}')$. The electric field at position $\mathbf{r}$ due to a single point current source at position $\mathbf{r}'$ is determine by the Green's function $\bar{\mathbf{G}}(\mathbf{r},\mathbf{r}')$. A simple integration over the extended source $\mathbf{j}(\mathbf{r})$ renders the final result.

The Green's function must be a tensor, as it might allow the possibility that, for instance, a linear current density along the x axis generates an electric field along the y axis. This can be captured by writing

$$\left[\nabla\times\nabla\times-k^2\right]\bar{\mathbf{G}}(\mathbf{r},\mathbf{r}')=\bar{\mathbf{I}}\delta(\mathbf{r}-\mathbf{r}'), \tag{2.6}$$

where the bar on top of the bold vector now represents a tensor or dyad, and $\bar{\mathbf{I}}$ is the unity tensor. In this case, the first column of the tensor $\bar{\mathbf{G}}(\mathbf{r},\mathbf{r}')$ represents the electric field at a position $\mathbf{r}$ from a point-like source at $\mathbf{r}'$ in the x-direction. Figure 2.1 gives an idea of how the Green's function propagates the point-like source solution to an extended media case.

A rigorous analysis can be done to get from Eq(2.4) and Eq(2.6) the electric field $\mathbf{E}(\mathbf{r})$ generated from a current density $\mathbf{j}(\mathbf{r})$ in terms of the Green's function:

$$\mathbf{E}(\mathbf{r})=\mathrm{i}\omega\mu_0\int_V\bar{\mathbf{G}}(\mathbf{r},\mathbf{r}')\,\mathbf{j}(\mathbf{r}')\,dV'. \tag{2.7}$$

An oscillating dipole is the most elementary source of radiation, because it represents a localized harmonic current source. For example, consider a distributions of charges q_n at positions $\mathbf{r}_n$, centered around $\mathbf{r}_0$, such that the current density is defined as

$$\mathbf{j}(\mathbf{r},t)=\sum_n q_n\dot{\mathbf{r}}_n(t)\delta(\mathbf{r}-\mathbf{r}_n(t)), \tag{2.8}$$

and if the charges oscillate at some frequency ω, it is possible to write the current density as $\mathbf{j}(\mathbf{r},t) = \mathrm{Re}\left\{\mathbf{j}(\mathbf{r})\,\mathrm{e}^{-i\omega t}\right\}$ with

$$\mathbf{j}(\mathbf{r}) = -\mathrm{i}\omega\mathbf{p}\delta(\mathbf{r}-\mathbf{r}_0), \tag{2.9}$$

where the it is possible to recover the classical dipole moment of the distribution $\mathbf{p} = \sum_n q_n\left[\mathbf{r}_n - \mathbf{r}_0\right]$.

Now, after having introduced the Green's function treatment of current sources, Eq(2.7), and determining that an oscillating dipole can be represented as a localized current source, Eq(2.9), the electric field generated by an oscillating dipole is just

$$\mathbf{E}(\mathbf{r}) = \omega^2\mu_0\bar{\mathbf{G}}(\mathbf{r},\mathbf{r}_0)\cdot\mathbf{p}. \tag{2.10}$$

Therefore, the electric field at $\mathbf{r}$ generated by an oscillating dipole located at $\mathbf{r}_0$ is determined by the Green's function $\bar{\mathbf{G}}(\mathbf{r},\mathbf{r}_0)$ in Eq(2.6).

For a linear, homogeneous and isotropic medium, the Green's function can be written as [51]

$$\bar{\mathbf{G}}(\mathbf{r},\mathbf{r}_0) = \left[\bar{\mathbf{I}} + \frac{1}{k^2}\nabla\nabla\right]G_0(\mathbf{r},\mathbf{r}_0), \tag{2.11}$$

where $G_0(\mathbf{r},\mathbf{r}_0)$ is just

$$G_0(\mathbf{r},\mathbf{r}_0) = \frac{\exp(ik|\mathbf{r}-\mathbf{r}_0|)}{4\pi|\mathbf{r}-\mathbf{r}_0|}. \tag{2.12}$$

It is interesting to think about the Green's function as a way to simplify some problems. For example, if the total power emitted by a dipole is needed, one can use the Poynting's theorem to calculate it by integrating the Poynting vector over a surface enclosing the emitter, needing to know the electromagnetic field everywhere on the surface [51]. This can be rather complicated in real cases, like atoms in cavities, next to dielectric surfaces, etc. But there is a roundabout this option, which is to invoke the Green's function formalism just introduced, which might turn latter to be accessible for numerical simulations. From the Poynting's theorem the rate of energy radiated by a current source in a volume V is

$$\frac{\mathrm{d}W}{\mathrm{d}t} = -\frac{1}{2}\int_V \mathrm{Re}\left(\mathbf{j}^*\cdot\mathbf{E}\right)\mathrm{d}V. \tag{2.13}$$

For the dipole case the current source was described in Eq(2.9) and the electric field at any position in Eq(2.10). After those substitutions, the dissipation rate is

$$\frac{\mathrm{d}W}{\mathrm{d}t} = \frac{\omega^3|\mathbf{p}|^2}{2c^2\epsilon_0\epsilon}\left[\mathbf{n}\cdot\mathrm{Im}\left\{\bar{\mathbf{G}}(\mathbf{r}_0,\mathbf{r}_0,\omega)\right\}\cdot\mathbf{n}\right]. \tag{2.14}$$

Therefore, the power radiated by the dipole is calculated by only knowing the field at the dipole's position, that is the Green's function at *one point* $\bar{\mathbf{G}}(\mathbf{r}_0, \mathbf{r}_0)$. Intuitively, the Green's function knows as much about the environment as the electric field does. Not only does it takes into account the dipole electric field (primary field) but also the field scattered by the environment (secondary field), including multiple scattering events.

Although this treatment is based on a classical description for the dipole and field, in the spirit of the nanophotonics community [52], these results will be used later to understand how the photonic bath properties determine the way light-matter interactions are described for emitters coupled to arbitrary modes of the electromagnetic field, for example, the guided modes of nanostructures. To get a better intuition about these changes, the spontaneous emission rate calculation for a dipole in an arbitrary environment will be considered next.

Spontaneous emission rate in terms of the Green's functions

Atomic systems are complex, encompassing several degrees of freedom, selection rules for different transitions, levels and sublevels, energy shifts dependent on internal and external factors, single atoms, and maybe even molecules or bounded states. It is sometimes useful to idealize these systems slightly in order to get a superficial understanding of some of the properties one is interested in exploring. To begin with, the real atoms can be replaced by simpler *two-levels system* with one ground state and one excited state, in many cases an exact case [48, 49, 50]. The excited state is unstable, and an atom in the excited state will eventually decay to its ground state, even without driving. In isolated atomic ensembles, this happens by emitting a photon at the atomic transition frequency.[1]

An atom in its excited state will couple with the electromagnetic field, driving the atom to decay to its ground state[2]. The intention of this section is not to revisit the full calculation that the reader can find elsewhere. The derivation will put an emphasis on the use of the Green's function to determine the spontaneous decay rate in inhomogeneous environments. It will be based on the book of Novotny and Hecht [52].

[1] It is possible to have different decay channels, referred as non-radiative decay, very important in solid-state quantum emitters [47], but in this work we will only focus on the radiative decay case.

[2] As noted in Kimble and Mandel [53], spontaneous emission in the vacuum and the rate of fluorescence in an external field do not depend on quantum properties of the electromagnetic field, whereas the correlation functions do.

To begin with, a two-levels system is placed at position $\mathbf{r}_0$. It has a ground state $|g\rangle$ and an excited state $|e\rangle$ that differ in energy by $\hbar\omega_0$. The atomic system and the electromagnetic field can be described by their usual Hamiltonians $\hat{H}_{atom}$ and $\hat{H}_{field}$, respectively. The interaction terms between the atom and the electric field is described by the *minimal coupling Hamiltonian* [48, 49] in the dipole approximation $\hat{H}_I = -\hat{\mathbf{p}} \cdot \hat{\mathbf{E}}$. The quantum states describe the joint state of the electric field and the atom. Removing the dust from the reader's favorite quantum mechanics textbook [48], perturbation theory says that the transition rate Γ between two states of the system $|i\rangle$ and $|f\rangle$ is

$$\Gamma_{i\to f} = \frac{2\pi}{\hbar^2} \left|\langle f| \hat{H}_I |i\rangle\right|^2 \rho_f(E), \tag{2.15}$$

where $\rho_f(E)$ is the density of final states $|f\rangle$ with energy $E = E_i - E_f$. This is the so-called Fermi's Golden Rule. The transition element $\left|\langle f| \hat{H}_I |i\rangle\right|^2$ represents the probability that the Hamiltonian $\hat{H}_I$ couples the states $|i\rangle$ to $|f\rangle$, and the density of states $\rho_f(E)$ considers the possibility that there are several possible degenerate final states $|f\rangle$. In the case described here, the initial state $|i\rangle$ represents the atom in its excited state and no excitation in the field ($|i\rangle = |e, \{0\}\rangle$), while the final state $|f\rangle$ is a set of states $|g, \{1_{\mathbf{k}}\}\rangle$ with the atom in its ground state and the field with a single excitation in any of the possible modes $\mathbf{k}$ with frequency ω_k.

The electric field can be quantized following an appropriate recipe, even in arbitrary dielectric media, and it holds true that it can be quantized and described in terms of annihilation and creation operators. In general the quantized field is

$$\hat{\mathbf{E}}(\mathbf{r}, t) = \sum_{\mathbf{k}} \left[\mathbf{E}^+_{\mathbf{k}}(\mathbf{r})\hat{a}_{\mathbf{k}}(t) + \mathbf{E}^-_{\mathbf{k}}(\mathbf{r})\hat{a}^\dagger_{\mathbf{k}}(t)\right], \tag{2.16}$$

and $\hat{a}_{\mathbf{k}}(t) = \hat{a}_{\mathbf{k}}(0)\mathrm{e}^{-i\omega_k t}$ is the annihilation operator, and $\mathbf{E}^+_{\mathbf{k}}(\mathbf{r})$ and its complex conjugate are the negative and positive frequency parts of the field $\mathbf{E}_{\mathbf{k}}(\mathbf{r})$. In the process of quantizing the field for lossless media, it is possible to use the normal modes expansion

$$\mathbf{E}^+_{\mathbf{k}}(\mathbf{r}) = \sqrt{\frac{\hbar\omega_k}{2\epsilon_0}}\mathbf{u}_{\mathbf{k}}(\mathbf{r}), \tag{2.17}$$

with the orthogonality condition $\int_V \mathbf{u}_{\mathbf{k}}(\mathbf{r}, \omega_k) \cdot \mathbf{u}^*_{\mathbf{k}'}(\mathbf{r}, \omega_{k'})\, \mathrm{d}V = \delta_{\mathbf{k},\mathbf{k}'}$. This indicates that $|\mathbf{u}_{\mathbf{k}}(\mathbf{r})| \propto 1/\sqrt{V}$.

After some algebra, using the orthogonality relations for the field mode functions

and the fact that $\rho_f(E) = \sum_{\mathbf{k}} \delta(\omega_k - \omega_0)$, the transition rate as in Eq(2.15) is

$$\begin{aligned} \Gamma_{i\to f} &= \frac{2\pi}{\hbar^2} \sum_{\mathbf{k}} \left[\mathbf{p} \cdot \left(\mathbf{E}_{\mathbf{k}}^{+}\mathbf{E}_{\mathbf{k}}^{-}\right) \cdot \mathbf{p}\right] \delta(\omega_k - \omega_0) \\ &= \frac{\pi\omega_k}{\hbar\epsilon_0}|\mathbf{p}|^2 \sum_{\mathbf{k}} \left[\mathbf{n} \cdot \left(\mathbf{u}_{\mathbf{k}}\mathbf{u}_{\mathbf{k}}^{*}\right) \cdot \mathbf{n}\right] \delta(\omega_k - \omega_0), \end{aligned} \tag{2.18}$$

where the dipole moment was written as $\mathbf{p} = |\mathbf{p}|\mathbf{n}$, $\mathbf{n}$ being a unity vector colinear with $\mathbf{p}$.

A step forward can be taken by expressing Eq(2.18) in terms of the Green's function. It can be shown [52, 54], again by expanding $\bar{\mathbf{G}}$ in the normal modes of the field and using their orthogonality, that

$$\bar{\mathbf{G}}\left(\mathbf{r}, \mathbf{r}', \omega\right) = \sum_{\mathbf{k}} c^2 \frac{\mathbf{u}_{\mathbf{k}}^{*}\left(\mathbf{r}', \omega_k\right) \mathbf{u}_{\mathbf{k}}\left(\mathbf{r}, \omega_k\right)}{\omega_k^2 - \omega^2}. \tag{2.19}$$

As in Eq(2.14), for the purpose of spontaneous emission rate the imaginary part of $\mathbf{G}$ needs to be taken into account. After properly integrating by contours it can be shown that

$$\lim_{\eta\to 0} \mathrm{Im}\left\{\bar{\mathbf{G}}\left(\mathbf{r}, \mathbf{r}, \omega + i\eta\right)\right\} = \frac{\pi c^2}{2\omega} \sum_{\mathbf{k}} \mathbf{u}_{\mathbf{k}}^{*}(\mathbf{r}, \omega_k)\mathbf{u}_{\mathbf{k}}(\mathbf{r}, \omega_k)\delta(\omega_k - \omega). \tag{2.20}$$

After substituting in Eq(2.18) the total decay rate of the dipole is

$$\Gamma = \frac{2\omega_0^2}{\hbar\epsilon_0 c^2}|\mathbf{p}|^2 \left[\mathbf{n} \cdot \mathrm{Im}\left\{\bar{\mathbf{G}}(\mathbf{r}_0, \mathbf{r}_0, \omega_0)\right\} \cdot \mathbf{n}\right], \tag{2.21}$$

comparable to the classic electrodynamics result in Eq(2.14).

The imaginary part of the Green's function evaluated at its origin and at the right transition frequency determines the spontaneous emission rate, providing a direct link with the properties of the photonic bath (modes of the electric field).

A separate note can be done on how the density of states that appeared in Fermi's Golden Rule is present on the last expression. The density of states represents the number of modes per unit volume and frequency of modes of the electromagnetic field, and hence it should be associated with the Green's function component of Eq(2.21). In the literature [47, 52], the *local density of states* (LDOS) is often defined as

$$\rho_p(\mathbf{r}_0, \omega_0) = \frac{6\omega_0}{\pi c^2} \left[\mathbf{n} \cdot \mathrm{Im}\left\{\bar{\mathbf{G}}(\mathbf{r}_0, \mathbf{r}_0, \omega_0)\right\} \cdot \mathbf{n}\right], \tag{2.22}$$

as it contains the dependence of the transition rate on the location of the source within its environment, the frequency, and its orientation. In an isotropic and homogeneous

medium, like free space, it is possible to show the equality between the LDOS and the more common total density of states. For example, carrying out the previous calculations for the free space Green's function, Eq(2.11), leads to the well know blackbody radiation density of states $\rho = \frac{\omega_0^2}{\pi^2 c^3}$.

2.2 One dimensional systems

As presented in the previous section, the case of spontaneous emission can be treated by using the classical electromagnetic Green's function formalism. A more extended analysis of the light-matter interactions can be also develop with the Green's function toolkit. The richness of this paradigm lies in the possibility to capture single and collective phenomena in terms of the classical Green's function. The analytic solution is known for a handful of cases, but Maxwell equations can be efficiently solved numerically as will be shown later.

The experimental platform described in this work is *quasi-unidimensional* (quasi-1D), meaning that a single guided mode that propagates along one direction can be isolated, despite its transverse spatial profile, and construct an effective model that captures the interaction of the emitter with the mode. There are other guided and non-guided modes that might be weakly coupled to the emitter and need to be taken into account as well.

In this section, the interaction of atoms with quasi-1D systems will be described within the master equation formalism of open quantum systems [49, 55] and a few well known examples will be presented. It will be specially shown how collective phenomena might arise due to photon-mediated interactions as described by the Green's function formalism.

The master equation and the Green's function

The relations derived in the previous section, Section 2.1, depend on the electromagnetic field quantization. This is usually the first step towards describing light-matter interaction in any quantum system. Generally, one starts decomposing the electromagnetic field into its normal modes and associates them with the corresponding bosonic creation and annihilation operators [48, 49]. This recipe works fine in lossless, homogeneous systems, where $\epsilon(\mathbf{r}, \omega) = \epsilon$, or approximately closed systems with a few relevant eigenmodes, like high-Q cavities. However, the problem becomes more complicated as quantization techniques are considered in arbitrary dielectric structures, even lossy ones. A powerful way to solve this problem was developed only about 20 years ago in works by Welsch and coworkers and extends

the Green's function formalism developed before to arbitrary $\epsilon(\mathbf{r}, \omega)$ [56, 57, 58, 59, 60, 61].

It starts with the classical Green's function defined as the solution of the electromagnetic wave equation for a localized source in a medium where the dielectric constant changes in space and in frequency

$$\left[\nabla \times \nabla \times -\frac{\omega^2}{c^2}\epsilon(\mathbf{r}, \omega)\right] \bar{\mathbf{G}}\left(\mathbf{r}, \mathbf{r}', \omega\right) = \bar{\mathbf{I}}\delta\left(\mathbf{r} - \mathbf{r}'\right). \tag{2.23}$$

The fluctuation-dissipation theorem establishes that the noise operator for the material polarization should be associated with the material properties described by the complex dielectric function, and it is usually the starting point to quantize the field in any medium [58].

The paradigmatic problem is to find the self-consistent solution for the electric field and the polarizability of a set of atoms [29, 30, 32]. The atoms, treated as dipoles, generate their own field but also respond to external fields. As seen in the previous sections, the re-scattered field can be expressed in terms of the Green's function. To be more explicit, let's consider an input field $\mathbf{E}_0(\mathbf{r}, \omega)$ and a set of N dipoles at positions $\mathbf{r}_j$ with a frequency dependent dipole moment $\mathbf{p}_j(\omega)$. The linearity of the field equations and Eq(2.10) implies that the total electric field is

$$\mathbf{E}(\mathbf{r}, \omega) = \mathbf{E}_0(\mathbf{r}, \omega) + \mu_0\omega^2 \sum_{j=1}^{N} \bar{\mathbf{G}}(\mathbf{r}, \mathbf{r}_j, \omega) \cdot \mathbf{p}_j(\omega). \tag{2.24}$$

As pointed out by Asenjo-Garcia et al. [30, 32], a way to think about the complex quantization requirements that dielectric structures might pose is to realize that the propagation of the quantum fields is the same as their classical counterpart. That is, the propagator of the classical field, namely the Green's function, also defines the propagation of the quantum fields. The quantum nature of the fields lie in their fluctuations and occupancies, associated with the noise operators mentioned before. Hence, Eq(2.24) is still valid in the quantum domain if the dipole moments and electric fields are replaced by their corresponding quantum operators. In several relevant cases, the correlations in the photonic bath decay in much shorter time than the correlations in the atomic system, a regime where it is possible to apply the Born-Markov approximation, meaning that in the frequency domain the Green's function is more or less flat at the scale of the atomic linewidth. Taking this into

account, one can rewrite the quantum version of Eq(2.24)

$$\hat{\mathbf{E}}^{+}(\mathbf{r}) = \hat{\mathbf{E}}_0^{+}(\mathbf{r}) + \mu_0\omega_0^2 \sum_{j=1}^{N} \bar{\mathbf{G}}(\mathbf{r}, \mathbf{r}_j, \omega_0) \cdot \mathbf{p}\hat{\sigma}_{ge}^{j}, \tag{2.25}$$

where the dipole operator is $\hat{\mathbf{p}}_j = \mathbf{p}\hat{\sigma}_{ge}^{j} + \mathbf{p}^{*}\hat{\sigma}_{eg}^{j}$ with the atomic coherence $\hat{\sigma}_{ge}^{j} = |g\rangle\langle e|$ and $\mathbf{p} = \langle g|\hat{\mathbf{p}}|e\rangle$.

In general one is interested in solving for the atomic system $\hat{\rho}_A$, as the electric field follows from the input-output relation just derived in Eq(2.25). Therefore, the evolution of the atomic system is given by the master equation, taking into account the incoherent evolution with the Lindbland super-operator [49, 55, 30]:

$$\dot{\hat{\rho}}_A = (-i/\hbar)[\hat{H}, \hat{\rho}_A] + \mathcal{L}[\hat{\rho}_A]. \tag{2.26}$$

As before, the interaction between the electromagnetic field and the atom is through the dipolar properties of the latter, so it follows the form $\hat{H}_{int} = -\hat{\mathbf{p}} \cdot \hat{\mathbf{E}}$ [48]. The total electric field, Eq(2.25), has information about the field scattered by the other dipoles meaning that collective interactions mediated by the electric field can create energy shifts, manifested in the Hamiltonian, and modify the incoherent evolution of the system, introduced by the Lindblad super-operator. Neglecting the driving field, it is possible to write

$$\hat{H} = \hbar\omega_0 \textstyle\sum_{j=1}^{N} \hat{\sigma}_{ee}^{j} - \hbar \sum_{i,j=1}^{N} J^{ij}\hat{\sigma}_{eg}^{i}\hat{\sigma}_{ge}^{j}, \tag{2.27}$$

$$\mathcal{L}[\hat{\rho}_A] = \textstyle\sum_{i,j=1}^{N} \frac{\Gamma^{ij}}{2}\left(2\hat{\sigma}_{ge}^{i}\hat{\rho}_A\hat{\sigma}_{eg}^{j} - \hat{\sigma}_{ge}^{i}\hat{\sigma}_{eg}^{j}\hat{\rho}_A - \hat{\rho}_A\hat{\sigma}_{ge}^{i}\hat{\sigma}_{eg}^{j}\right), \tag{2.28}$$

with the coherent and incoherent interactions rates being

$$J^{ij} = \tfrac{\mu_0\omega_0^2}{\hbar}\mathbf{p}^{*} \cdot \mathrm{Re}\left\{\bar{\mathbf{G}}(\mathbf{r}_i, \mathbf{r}_j, \omega_0)\right\} \cdot \mathbf{p}, \tag{2.29}$$

$$\Gamma^{ij} = \tfrac{2\mu_0\omega_0^2}{\hbar}\mathbf{p}^{*} \cdot \mathrm{Im}\left\{\bar{\mathbf{G}}(\mathbf{r}_i, \mathbf{r}_j, \omega_0)\right\} \cdot \mathbf{p}. \tag{2.30}$$

The field re-scattered by each dipole creates dipole-dipole coupling terms between distant atoms, as represented by the (resonant) photon-mediated coupling strength J^{ij}. On the other hand, incoherent terms arise due to collective spontaneous emission as represented by the term Γ^{ij}, also determined by the properties of the field Green's function.

The interest for the work presented in this thesis is to study the case of quasi-1D systems, where one can isolate a single field mode that is effectively coupled with the atoms and propagates in a well defined direction [30]. In this case, it is possible

to separate the contribution of the selected mode by writing the Green's function as $\bar{\mathbf{G}}(\mathbf{r},\mathbf{r}',\omega) = \bar{\mathbf{G}}_{1D}(\mathbf{r},\mathbf{r}',\omega) + \bar{\mathbf{G}}'(\mathbf{r},\mathbf{r}',\omega)$. The Green's function $\bar{\mathbf{G}}_{1D}(\mathbf{r},\mathbf{r}',\omega)$ takes into account only the selected guided mode, while the other contribution $\bar{\mathbf{G}}'(\mathbf{r},\mathbf{r}',\omega)$ includes other guided and non guided modes of the electromagnetic field that couple to the atomic system. It is hard to account for collective phenomena arising from non-guided modes or guided modes that are not of special interest, so a further approximation is going to be made[3]. That is, the effects of $\bar{\mathbf{G}}'(\mathbf{r},\mathbf{r}',\omega)$ are only significant at an individual atom level as energy shifts or decay rates corrections and it is possible to write $J^{ij} = J^{ij}_{1D} + J'\delta_{ij}$ and $\Gamma^{ij} = \Gamma^{ij}_{1D} + \Gamma'\delta_{ij}$. In fact, Γ' can be different than just the free space decay rate Γ_0 by changing the dielectric structure geometry and frequency response $\epsilon(\mathbf{r},\omega)$, and by placing the atom in a specific position. The J' term accounts for spatial dependent energy shift on each atom, generalizing the free space Lamb shift [48].

Now that all the photon-mediated terms have been included in the Hamiltonian and Lindbland super-operator, a driving field $\mathbf{E}_L(\mathbf{r})$ with frequency ω_L can be added. In the rotating-wave approximation respect to the driving field it is possible to write the Hamiltonian

$$\hat{H} = -\hbar\Delta_A \sum_{j=1}^{N} \hat{\sigma}^j_{ee} - \hbar \sum_{i,j=1}^{N} J^{ij}\hat{\sigma}^i_{eg}\hat{\sigma}^j_{ge} - \sum_{j=1}^{N}\left(\mathbf{p}\cdot\hat{\mathbf{E}}^-_L(\mathbf{r}_j)\hat{\sigma}^j_{ge} + \mathbf{p}^*\cdot\hat{\mathbf{E}}^+_L(\mathbf{r}_j)\hat{\sigma}^j_{eg}\right), \tag{2.31}$$

with $\Delta_A = \omega_L - \omega_0$. Solving for the mean atomic coherences $\sigma = <\hat{\sigma}>$, according to the Heisenberg equations Eq(2.26)

$$\dot{\sigma}^j_{ge} = i\left(\Delta_A + i\frac{\Gamma'}{2}\right)\sigma^j_{ge} + i\Omega_j + \sum_i \left(J^{ij}_{1D} + i\frac{\Gamma^{ij}_{1D}}{2}\right)\sigma^i_{ge}, \tag{2.32}$$

where the driving field Rabi frequency for the atom j is as usual $\Omega_j = \mathbf{p}\cdot\mathbf{E}^-_L(\mathbf{r}_j)/\hbar$, makes it possible to study the atomic system in detail, specifically looking for collective phenomena.

Examples of quasi-1D systems

Now that the general framework was introduced, it is useful to examine some special cases. Some of the most paradigmatic cases in the literature are the free space case, a high-Q cavities and waveguides. The case of the photonic crystals will be introduced in the next section.

[3] It is interesting though to keep in mind that one can also target these quantities by designing a suitable nanophotonic structure

Free space

Although not a quasi 1D system, for the free space case, $\epsilon(\mathbf{r}, \omega) = 1$, the Green's function was already found in Eq(2.11). In this case there is no single preferred mode, so the distinction between $\bar{\mathbf{G}}_{1D}$ and $\bar{\mathbf{G}}'$ is not necessary.

From Eq(2.21) the spontaneous emission rate Γ_0 is found to be

$$\Gamma_0 = \frac{\omega_0^3 \mathrm{p}^2}{3\pi\hbar\epsilon_0 c^3}. \tag{2.33}$$

The additional shift J' renormalizes the atomic transition frequency ω_0, and is usually absorbed in its definition. This term can be associated with the well known Lamb shift.

Waveguide QED

The case of an invariant waveguide is of interest in different experimental platforms like superconducting circuits [62, 63], solid state systems [64, 65] and neutral atoms [66, 67, 23, 68, 69, 70]. It is also simple enough to study more exotic cases such as atom-atom entanglement generation, dissipative driven entanglement, or photon mapping [71, 72, 73, 74, 75].

In the case of a translational invariant waveguide, the guided modes usually take the form of $\mathbf{E}_n(\mathbf{r}, t) = \mathbf{f}_n(\rho)\mathrm{e}^{-i(\omega t + k_n(\omega)z)}$, where the index n identifies each mode, the mode function $\mathbf{f}_n(\rho)$ depends only on the radial position and $k_n(\omega)$ is the propagation constant along the waveguide. In the tapered nanofiber for example, the waveguide can be operated in the single-mode regime, although due to the spatial symmetry this mode is degenerate. Moreover, the properties of the field and the emitter at its position determines the coupling to each of the modes [76].

The fact that the electric field has a simple dependence on the space coordinates allows a clean expression for a selected guided mode contribution $\bar{\mathbf{G}}_{1D}$. Given any two points along the waveguide, the guided mode electric field at those points just differ by an accumulated phase and a radial dependent function. In fact, a dipole close to the structure can source a propagating field, like the guided mode seen before. Therefore, the Green's function should take the form

$$\bar{\mathbf{G}}_{1D}(\mathbf{r}, \mathbf{r}', \omega) = g_{1D}(\rho, \rho')\mathrm{e}^{ik_{1D}(\omega)|z-z'|}, \tag{2.34}$$

with $g_{1D}(\rho, \rho')$ a function of the radial coordinates and $k_{1D}(\omega)$ the propagation vector of the selected guided mode. It is possible to demonstrate [30] that $\bar{\mathbf{G}}_{1D}$ can

be simplified as

$$\bar{\mathbf{G}}_{1D}(\mathbf{r}, \mathbf{r}', \omega) = \frac{i\Gamma_{1D}}{2} e^{ik_{1D}|z-z'|}, \tag{2.35}$$

where Γ_{1D} depends on the radial coordinates.

As defined in Eq(2.29) $J_{1D}^{ij} = -\frac{\Gamma_{1D}}{2}\sin(k_{1D}(\omega_0)|z_i - z_j|)$ and Eq(2.30) $\Gamma_{1D}^{ij} = \Gamma_{1D}\cos(k_{1D}(\omega_0)|z_i - z_j|)$ determine the range of the photon mediated interactions between atoms. On one hand, there is a spin-exchange position dependent term between atoms, characterizing coherent dipole-dipole interactions. On the other hand, the atoms can cooperatively enhance the spontaneous emission rate into the waveguide mode. By setting the distance between the emitters one can totally suppress the spin-exchange dynamics or the decay one, although Γ_{1D}^{ii} is always present.

A special case happens when atoms are spaced by d_n satisfying $k_{1D}(\omega_0)d_n = n\pi$, n an integer. Therefore there is no spin-exchange term $J_{1D}^{ij} = 0$ and each pair decays at the same rate $\Gamma_{1D}^{ij} = \Gamma_{1D}$. The emission into the waveguide is maximized such that each dipole contribution constructively interferes to reflect as much light as possible. In this case, with all the Γ_{1D}^{ij} identical, the coherences evolve like

$$\dot{\sigma}_{ge}^{j} = i\left(\Delta_A + i\frac{\Gamma'}{2}\right)\sigma_{ge}^{j} + i\Omega_j + i\frac{\Gamma_{1D}}{2}\sum_i \sigma_{ge}^{i}. \tag{2.36}$$

Assuming the driving is the same for every atom, $\Omega_j = \Omega$, the collective operator $\hat{S} = \sum_i \sigma_{ge}^{i}$ satisfies

$$\dot{S} = i\left(\Delta_A + i\frac{\Gamma'}{2}\right)S + iN\Omega + iN\frac{\Gamma_{1D}}{2}S. \tag{2.37}$$

The total spin operator evolves driven by a collective Rabi frequency $\Omega_N = N\Omega$, and decays at a rate $\Gamma_N = \Gamma' + N\Gamma_{1D}$. This observation is important for creating decoherence free subspaces, or subrradiant states, where the state does not dissipate through the waveguide. There are proposals to build many-body entangled states using the decoherence free subspace, then map it to a dissipative superradiant state and reconstruct the atomic correlations from the observed photonic correlations [73].

Optical resonator cQED

It is also instructive to consider the case of an optical resonator, composed of two highly reflective and low-loss mirrors [77]. This case has been extensively studied under the Jaynes-Cummings model [49, 78] in different coupling regimes. Here, a

review of the well known results in the literature will be obtained using the Green's function paradigm [79]. In the context of this thesis, the evolution of the light-matter system occurs under the Markovian approximation. For atoms that decay with a rate Γ' and photon losses at a rate κ_c, the Markovian approximation means that $\Gamma' \ll \kappa_c$.

From Eq(2.19), the Green's function must have a spatial dependence of the form $\cos(k_c x_i)\cos(k_c x_j)$ as it can be represented in terms of products of normal modes [30]. To be concrete, the resonator has length L and transversal mode area A, which accounts for the radial extent of the Green's function. Taking two points along the cavity axis, at the same radial distance, the one-dimensional problem reduces to take into account properly the propagation phase in the cavity, considering multiple reflections from the cavity mirrors. After taking into account waves that propagate in both directions, the one-dimensional Green's function is [29, 79]

$$\bar{\mathbf{G}}_{1\mathrm{D}}(x_i, x_j, \omega_0) = \frac{ic}{2A\omega_0}\sum_{n=0}^{\infty}\left(\mathrm{e}^{i2k_0L}r^2\right)^n\Big[\mathrm{e}^{ik_0(x_i-x_j)} + r\mathrm{e}^{ik_0(L-(x_i+x_j))} + r\mathrm{e}^{-ik_0(L+(x_i x_j))} + r^2\mathrm{e}^{ik_0(2L-(x_i-x_j))}\Big], \tag{2.38}$$

where k_0 is the wave-vector at frequency ω_0, r is the complex cavity mirror reflection, and it was assumed that $x_i > x_j$. Close to a high-Q cavity resonance, the wavevector needs to be close to a resonant one, such that $k_0 \approx k_c^m + \delta k$, where $k_c^m L = 2\pi m$, and the mirrors are low loss ($r \approx 1$). In this case the one-dimensional Green's function is just

$$\bar{\mathbf{G}}_{1\mathrm{D}}(x_i, x_j, \omega_0) \approx -\left(\frac{c^2}{V\omega_0}\right)\frac{1}{\Delta_c + i\kappa_c/2}\cos(k_c x_i)\cos(k_c x_j), \tag{2.39}$$

where $V = LA$ represents the effective cavity volume. As in the Jaynes-Cummings model, the single atom-light coupling strength is $g_i = g_i^0\cos(k_c x_i)$ with $g_i^0 = |\mathbf{p}|\sqrt{\frac{\omega_c}{\hbar\epsilon_0 V}}$. Therefore, the collective spin-exchange and decay rates are, respectively,

$$J_{1\mathrm{D}}^{ij} = -g_i^0 g_j^0 \frac{\Delta_c}{\Delta_c^2 + \kappa_c^2/4}\cos(k_c x_i)\cos(k_c x_j), \tag{2.40}$$

$$\Gamma_{1\mathrm{D}}^{ij} = g_i^0 g_j^0 \frac{\kappa_c}{\Delta_c^2 + \kappa_c^2/4}\cos(k_c x_i)\cos(k_c x_j). \tag{2.41}$$

The Jaynes-Cummings model under the Markovian approximation and in weak coupling limit can be described by a Hamiltonian, like the one in Eq(2.31), and the corresponding Lindbland super-operator for the cavity field and the atomic system, with the one dimensional spin-exchange and decay rates as in Eq(2.40) and Eq(2.41), respectively.

2.3 Photonic crystals in a nutshell

Photonic crystals are complex structures that have a specific way to propagate light [80, 81]. They occur naturally, from precious stones like opals to peacock feathers. In the current era where the semiconductor industry and research continue to push for miniaturization and high-speed performance, integrated photonic circuits seem to have advantages over its electronic counterpart. Central to these advantages is the nature of light propagation in dielectric media.

Despite some of the advantages optical circuits might have, the commercialization of those is still something that has not happened, partially because a new architecture needs to be developed to design multipurpose devices. An appealing scheme to build photonic circuits is to use a novel class of materials known as photonic crystals. Within the complexity of all optical circuits, photonic crystals help to direct light through different paths. Photonic crystals exhibit a position dependent dielectric function, that helps to shape the way light propagates through them. Early ideas originate in works by Yablonovitch [82] and John [27, 83]. Both of them suggested that materials where the dielectric constant is modulated in a periodic way will affect the structure and dispersion of their photonic modes. Photonic crystals structures fundamentally relay on the appearance of photonic bandgaps to guide light.

In semiconductors, the crystalline lattice formed by the localized atoms creates a periodic electromagnetic potential, such that electrons propagating through the material are described by normal modes that follow the Bloch theorem [84]. Depending on the properties of the material, there are gaps where electrons with certain energies cannot propagate in any direction. In the case of photons, the spatial periodicity of the dielectric function constitutes a periodic potential, enabling the appearance of photonic band gaps where the light will not propagate through the crystal for a specific frequency range.

The fabrication of such photonic crystals is rather challenging as the features in the dielectric function need to be on the order of the wavelength. For the optical and near-infrared regime, this means that the lattice constant needs to be around 400nm. Only state-of-the-art lithography techniques are able to access this regime. For more information the reader can look into Su-Peng Yu's and Andrew McClung's thesis.

In this section, a brief description of the general properties of photonic crystals will be presented, although a more detailed section for the specific device design will appear later.

Generalities

It is often assumed when studying light propagation in certain medium that the medium is somehow homogeneous on the length scale of its wavelength. The details at the atomic scaled are averaged out because the field usually varies slowly at scales bigger than the small constituents. The absence of irregularities are associated with the lack of scattering from that medium. A different situation happens once some (random) irregularities at the material happen at scales bigger than the wavelengths. In this case, the scattering can be incoherent.

The realm of the photonic crystals lie somewhere in between these two regimes. In the photonic crystals, typical features happen at scales below the free-space wavelength λ_0 of the light. Despite the well known similarity with electrons in a crystalline lattice, light propagation in photonic crystals can be easily understood in terms of coherent scattering. For example, consider the case of a perfect invariant waveguide where light propagates according to some specific dispersion relation $\omega(k)$. Then at some position along the waveguide a defect, a hole for example, is extruded in the waveguide. Light incident on the hole is partially transmitted, some fraction is reflected, and eventually there could be some scattered out of the waveguide. Furthermore, when these defects are positioned in a periodic array, the scattered fields coherently add, modifying also the dispersion relation and spatial modes of the electromagnetic field inside the waveguide.

This coherent scattering can have dramatic consequences. For some frequencies, in a very long system, the periodic array of scatterers will reflect all the light. This propagation prohibition means that light can not propagate inside a photonic crystal if the light frequency is inside the bandgap. Depending on the dimensionality of the crystal, complete photonic bandgaps can be, and have been, observed. Moreover, a defect in the otherwise perfect crystal, leads to localized modes in the gap. For instance, a point defect can lead to a very well localized mode, or cavity; a line defect in a two dimensional array creates a 1D waveguide, and a 2D defect can create a planar mirror [80].

The propagation of light in photonics crystals is also studied by solving the Maxwell's equation. An important difference between electrons moving in a crystal and photons is that many-body effects are not present in the latter[4]. Numerical solvers, or analytical solutions if available, accurately describe the properties of light in the medium. A special and interesting property of Maxwell's equation is that it is scale

[4]For low intensities where non-linear processes can be ignored.

invariant. The periodicity of the dielectric function and its appearance on the wave equation implies that the electromagnetic field satisfy the Bloch theorem.

The Bloch theorem establishes that the solutions for the field should have the form $\mathbf{E}^n_{\mathbf{k}}(\mathbf{r}) = \mathbf{u}^n_{\mathbf{k}}(\mathbf{r})e^{i\mathbf{k}\cdot\mathbf{r}}$, where the mode function (Bloch function) $\mathbf{u}^n_{\mathbf{k}}(\mathbf{r})$ inherits the potential periodicity (lattice constant) and n identifies the band. The Bloch mode expresses the consequences of the coherent scattering that was mentioned before. The wavevector lies in the so called Brillouin zone and the solutions can be grouped in sets characterized by the band index. If all possible dispersion relations $\omega^n(\mathbf{k})$ are plotted on the same layout one obtains the structure's *band diagram*. The bandgaps appear in the frequency domain when there is a lack of field modes for any value of the wavevector inside the Brillouin zone for that given frequency range.

Photonic crystals waveguides

Initial works by Yablonovitch and John focused on the properties of photons in dielectric materials. The former was interested in inhibiting the spontaneous emission of a solid state emitter by designing the appropriate photonic bandgap in the embedded material [82], while the latter was keen on studying photon localization by defects on the dielectric lattice [27]. Both works are extremely relevant for the work developed in our group, as photonic bandgaps offer this unique and interesting regime to control light-matter interactions. Before them, effects of subwavelength cavities on spontaneous emission of atoms in the cQED context were analyzed by Kleppner [85, 12].

Most of the work described in this thesis describes a set of emitters interacting with photonic crystal waveguides, that is, a dielectric waveguide where the cross section instead of being invariant is modulated with some periodicity. As initially pointed out by the quantum dot community [47, 86], there are two fundamental reasons why these waveguides are interesting from the point of view of their applications in quantum optics. First, their ability to suppress the coupling to guided radiation modes due to the photonic band gap. Second, an emitter close to the photonic crystal waveguide will see its coupling to specific guided modes enhanced due to the slow light effect.

A common cases is a rectangular cross section waveguide where holes are etched through it, as seen in Fig. 2.3(a). This design, with several variations, has been widely popular among several groups, specifically in its use in optomechanical experiments done in Painter's group [87] influenced our work. These waveguides

can be characterized by their symmetry with respect to a specific plane. To be concrete, the $z = 0$ and $y = 0$ are symmetry planes in the case of the structure shown in Fig. 2.3(a). These symmetries are mapped into the allowed guided modes, which are often classified with respect to the $z = 0$ plane symmetry. The transverse electric (TE-like) family has polarization mainly in that plane, while the transverse magnetic (TM-like) has its electric field polarized mostly perpendicular to that plane.

In the one-dimensional waveguide, the only translational symmetry is along the propagation direction x. That means that the k_x component is conserved, while the other components are not, and it is usual to just refer to k_x as k. The family of guided modes with frequencies $\omega^n(k)$ that propagate along the waveguide is referred as the *projected band structure* respect to k. The modes where $\omega \geq ck$ are not guided, and that region on the band diagram is referred to the light cone (line) for $\omega > ck$ ($\omega = ck$). Furthermore, since the photonic crystal waveguide modes appear below the light line in the dispersion diagram, light in an ideal photonic crystal waveguide can propagate without loss. In reality, unavoidable fabrication imperfections will favor light leakage into non guided modes, and hence loss out of the waveguide.

The band structure for both TE-like and TM-like modes can be calculated using numerical methods. The result is shown in Fig. 2.3(b). There is a bandgap for the TE-like and bandgap for the TM-like modes; however, there is not a complete bandgap, a common feature in one-dimensional systems [80]. It is typical that the bands above and below the bandgap have a distinct intensity distribution in each unit cell. The lower band has lower energy as most of the light concentrates in the regions where the average dielectric constant $\bar{\epsilon}$ is bigger, while the higher band has higher intensity in regions where $\bar{\epsilon}$ is lower, as shown in Fig. 2.3(c). This is the reason why usually the lower and higher bands are referred to as dielectric and air band, respectively.

As it happens in standard waveguides, the electromagnetic energy is transported through the waveguide at a speed determined by the *group velocity* v_g, defined for the n-th band as $\mathbf{v}_g^n(\mathbf{k}) = \nabla_{\mathbf{k}}\omega^n(\mathbf{k})$. As seen in the band diagram showed in Fig. 2.3(a), each of the bandss tend to flatten as they approach the edge of the Brillouin zone, meaning that the group velocity decreases. This can be understood in terms of the forward and backwards propagation interference ideas that were described before. Frequently the dispersion relation has a parabolic-like shape, meaning that the slower light happens close to the band edge $k = \pi/a$, where a is the lattice constant. A drawback in this design is that it also increases the dispersion

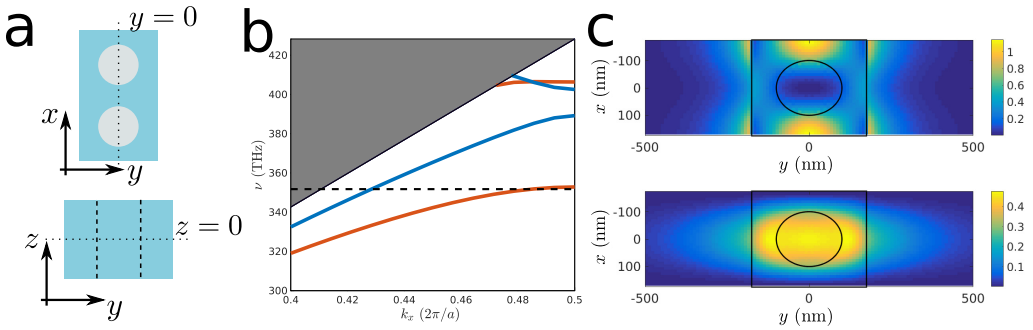

Figure 2.2: Single nanobeam waveguide with an etched hole. The waveguide has dimensions: thickness $t = 200$nm, width $w = 350$nm, hole radius $R = 100$nm and lattice constant $a = 350$nm and an sketch of its dielectric function is shown in (a). The band structure for the TE-like (red) and TM-like (blue) is shown in (b). The black trace indicates the Cs D2-line frequency. In (c), the intensity pattern $|\mathbf{E}(\mathbf{r})|^2$ at the $z = 0$ is shown for the dielectric and air band at the X-point.

$(d^2\omega/d^2k)^{-1}$, a feature that might not be desirable for some applications.

A different regime can be found as the frequency is further away from the band edge. As the mode lies further away from it, in the forward and backwards picture, these components start to be slightly out of phase, such that the mode loses contrast, i.e. it is no longer a standing wave. Even further away, they are completely out of phase and the mode resembles a waveguide. As a side note, it is possible to have waveguides where the slow light regime happens at different points from the band edge [88].

Fabrication imperfections have a major role in everyday use of photonic crystals. The lithographic patterning and the etching techniques are subjected to several imperfections, which might cause several problems. Apart from losses, random imperfections can create localized modes in the subwavelength regime due to very strong contrast in the dielectric constant. In general, one can classify the main effect into two classes [47, 89]. The first class is backscattering, that is, a defect might scatter light back into the guided mode. The associated decay length with this propagation loss mechanism has been shown to be quadratic with the group velocity $L_{backsc} \propto v_g^2$, which has been shown to lead to Anderson localized modes on the scales of 10μm [90]. The second class is associated with out-of-plane losses, related with coupling to non-guided modes in the light cone. In general, it is hard to associate a specific scaling for the out-of-plane losses.

Decay rate of an emitter close to a photonic crystal waveguide

Nanophotonic waveguides can enhance light-matter interactions. Two fundamental reasons are behind this statement. On the one hand, the local electric field is confined to sub-wavelength scales, providing big single-photon electric field magnitude, an important parameter to characterize an atom-photon coupling in cQED [78]. On the other hand, the low group velocity enhances the light-matter coupling between selected guided photonic modes and the emitter. Intuitively, the slower the group velocity the higher the density of states is for a given frequency range, as there are more modes where is possible to decay.

In the following paragraphs, a complete argument based on the Green's function theory presented before will be provided to account for the modification of the spontaneous emission rate of an atom in the vicinity of a photonic crystal waveguide. The general theory for this calculation can be found in several articles with a more detailed presentation [47, 86, 91, 92].

The Green's function determines the scattering rate of an emitter into any mode of the structure. Here it will be assumed that the system is quasi unidimensional as before, such that the focus will be on a specific guided mode. The electric field for the selected guided mode can be decomposed in terms of normalized modes, which should have the familiar Bloch theorem form:

$$\mathbf{u}_k(\mathbf{r}) = \sqrt{\frac{a}{L}}\mathbf{b}_k(\mathbf{r})\mathrm{e}^{ikx}, \tag{2.42}$$

where $\mathbf{k} = k\mathbf{n}_x$ is the Bloch vector, $\mathbf{b}_k(\mathbf{r})$ is the Bloch function with the photonic crystal periodicity a, and L is the waveguide length. The Green's function tensor for this mode from Eq(2.19) is

$$\bar{\mathbf{G}}(\mathbf{r}, \mathbf{r}', \omega) = c^2 \sum_k \frac{\mathbf{u}_k(\mathbf{r})\mathbf{u}_k^*(\mathbf{r}')}{\omega_k^2 - \omega^2}. \tag{2.43}$$

The evaluation of this sum is done in a few steps. First, the sum over the modes can be replaced as usual by an integral over the k vector, correcting by the state density $\sum_k \rightarrow (L/2\pi)\int dk$. Moreover, to integrate this expression an infinitesimal parameter δ, that in the end will be taken to go to 0, is introduced in the denominator. It is possible to write

$$\bar{\mathbf{G}}(\mathbf{r}, \mathbf{r}', \omega) = \frac{c^2 L}{2\pi} \lim_{\delta\to 0} \int \frac{d\omega_k}{v_g} \frac{\mathbf{u}_k(\mathbf{r})\mathbf{u}_k^*(\mathbf{r}')}{\omega_k^2 - (\omega + i\delta)^2}, \tag{2.44}$$

where the dispersion relation $\omega(k)$ and its derivative, the group velocity, was invoked. To simplify this expression, the renormalized Bloch expansion in Eq(2.42) and only

positive frequencies are considered, such that the it is possible to approximate the Green's function as

$$\bar{\mathbf{G}}(\mathbf{r},\mathbf{r}',\omega) \approx \frac{c^2 a}{4\pi\omega}\lim_{\delta\to 0}\int \frac{d\omega_k}{v_g} \mathrm{e}^{ik(x-x')}\frac{\mathbf{b}_k(\mathbf{r})\mathbf{b}_k^*(\mathbf{r}')}{\omega_k-(\omega+i\delta)}. \tag{2.45}$$

Taking the imaginary part and the limit, one obtains

$$\mathrm{Im}\left\{\bar{\mathbf{G}}(\mathbf{r},\mathbf{r}',\omega)\right\} \approx \frac{\pi c^2 a}{4\pi\omega}\lim_{\delta\to 0}\int \frac{d\omega_k}{v_g} \mathrm{e}^{ik(x-x')}\mathbf{b}_k(\mathbf{r})\mathbf{b}_k^*(\mathbf{r}')\delta(\omega_k-\omega). \tag{2.46}$$

The spontaneous emission rate for an emitter at position $\mathbf{r}_0$ and transition frequency ω_0 given by Eq(2.21) is written in terms of the imaginary component of the Green's function $\bar{\mathbf{G}}(\mathbf{r}_0,\mathbf{r}_0,\omega_0)$. After some algebra, we can write the spontaneous emission rate into the guided mode of the structure[5]

$$\Gamma_{1\mathrm{D}}(\mathbf{r}_0) = \Gamma_0 n_g \frac{a\sigma_0}{2V_{eff}(\mathbf{r}_0)} = \Gamma_0 n_g \frac{\sigma_0}{2A_{eff}(\mathbf{r}_0)}, \tag{2.47}$$

where Γ_0 is the spontaneous emission rate in free space (the Einstein A coefficient) defined in Eq(2.33), $n_g = c/v_g$ is the group index, $\sigma_0 = 3\lambda^2/2\pi$ is the free space scattering cross section, and $V_{eff}(\mathbf{r}_0) = aA_{eff}(\mathbf{r}_0)$ is the effective mode volume and area of the field at a position $\mathbf{r}_0$ defined as

$$V_{eff}(\mathbf{r}_0) = \frac{\int_{cell}\epsilon(\mathbf{r})|\mathbf{u}_k(\mathbf{r})|^2 dV}{\epsilon(\mathbf{r}_0)|\mathbf{u}_k(\mathbf{r}_0)|^2}. \tag{2.48}$$

The expression for the decay rate of the atom into specific guided mode, Eq(2.47), shows how different terms contribute to the enhancement of that rate respect with the free space rate. The effective mode volume is a position dependent term that accounts for the location of the dipole and how intense the field is at that position; the relevant enhancement over free space rates is obtained once the mode volume is smaller than $(\lambda/n)^3$. In photonic crystal waveguides, it is usually the case that $V_{eff} \sim a(\lambda/n)^2$. Another term accounts for the slow light effects, where the enhancement is given for the group index. Apart for specific design properties, fabrication imperfection might limit the group velocities achieved.

Pioneering experiments carried out in Lukin's group in Harvard achieved the trapping of a single atom near a nanophotonic crystal cavity with mode volume λ^3, a remarkable advance [19].

[5] In this case we explicitly average over all dipole orientations

Finally, a relevant remark is that the structure might affect the spontaneous emission into all the other possible modes, guided or not guided. By properly designing the structure, it is possible to inhibit or directionally enhance the scattering rate Γ' into those modes.

2.4 Numerical tools for the calculation of scattering rates in dielectric structures

For every nanophotonic system designed to interface light and matter, lies the basic estimation on how well or bad the interface might work. In general, the employed geometries do not have simple analytical electric field modes that might facilitate the calculations. Even in situations where those modes are analytical, explicit calculations can be challenging. A powerful tool to address this problem is a set of numerical techniques that allows to calculate the Green's function and estimate relevant coefficients. In this section, we will briefly introduce them and make the connection with the final physical problem we are trying to solve. Most of the work on FDTD relevant for our experiment can be connected with the research performed by the Hughes group in Ontario, Canada and Johnson and collegues at MIT. The interested reader can look up their work.

FDTD methods

The finite-difference time-domain algorithm (FDTD) has been applied in a wide range of situations and its use has been increasing since the development of the method by Yee in the 60's [93]. Numerically, the method is efficient as it runs in order N, where there are N nodes in the grid, because it does not use linear algebra techniques such as matrix diagonalization. It is accurate and robust and can be parallelized, offering a major advantage over other methods where bounds are beyond computational power. Physically, it can deal with Cartesian grids in space, non-linear media, impulsive sources, and complicated dielectric structures like lithographic patterned materials.

The FDTD method starts by considering the time dependent Maxwell equations in a sourceless medium and discretizing space in rectangular cells, called Yee cells. The electric field $\mathbf{E}$ and magnetic field $\mathbf{H}$ are defined in the Yee cell and in time following a specific procedure. The $\mathbf{E}$ field is defined on integer space steps along the cell edges and half integer time steps, while the $\mathbf{H}$ field is defined on half integer space and integer time steps. Furthermore, the fields components are defined at specific positions along the cell, such that if for example the cell is centered at $(0, 0, 0)$ and

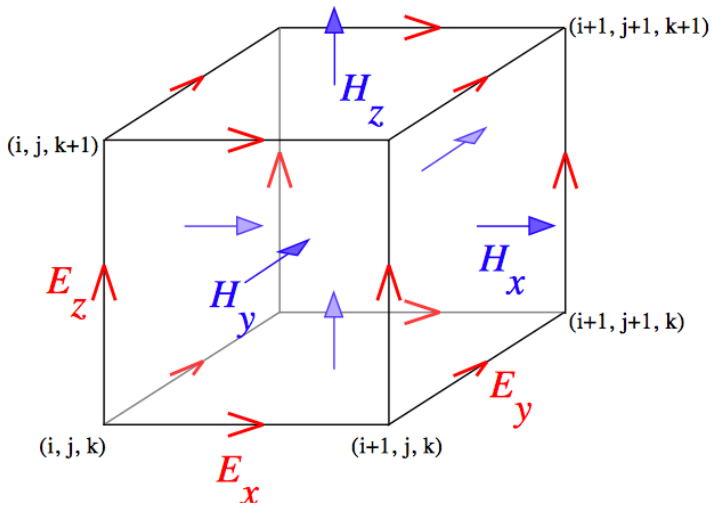

Figure 2.3: The Yee Cell. The cell is centered at $(0, 0, 0)$ and each edge has length a. The electric and magnetic field components are defined at specific position along the cell edges. Figure extracted from Wikipedia.

each side length is a, the electric field component E_x is defined at $(a/2, 0, 0)$ while the other components follow an analog rule. The magnetic field components are shifted half a grid cell, such that the H_x component is defined at $(0, a/2, a/2)$. As innocent as it looks, this is the main advantage of the method, as it means that the curl of a component, a vital part of the Maxwell's equations, can be calculated in terms of other components defined in a single plane. Typical problems due to discretization are usually not relevant, as the grid can be made smaller than the typical length scale of the fields.

There are a number of commercial and open software that can be used. In our group, we usually use the commercial software Lumerical - FDTD solutions [94] and the open software developed by the MIT groups Meep [95]. For an excellent reference regarding the use of FDTD techniques in number of situations can be found in Cole P. Van Vlack's doctoral thesis work [96]. In this work, the use of these methods towards obtaining spontaneous decay rates of dipoles close to nanophotonic structures will be described.

Scattering rate of dipoles in inhomogeneous media

The Green's function can be found exactly[6] by using FDTD techniques. As FDTD solves the time and spatial dependent Maxwell equations, obtaining the field $\mathbf{E}(\mathbf{r}, t)$,

[6]Upon numerical accuracy and computer power

the only requirement to obtain the Green's function for a specific medium $\epsilon(\mathbf{r}, \omega)$ is to solve for the appropriate current density.

As shown before, Eq(2.9), an oscillating electrical dipole at position $\mathbf{r}_0$ can be represented by a current density $\mathbf{j}(\mathbf{r}) = -i\omega\delta(\mathbf{r} - \mathbf{r}_0)$. For a dipole with dipole moment magnitude $|\mathbf{p}| = 1$ at position $\mathbf{r}'$, it is enough to define the current source at a specific position in space such that $\mathbf{j} \propto \delta(\mathbf{r} - \mathbf{r}')$. That can be performed in both the softwares described above. One is usually interested in a frequency broadband simulations as the media can have different properties for some wavelength ranges, for example the band gap in a photonic crystal waveguide. For that purpose, the source takes the form $\mathbf{j} \propto \delta(\mathbf{r}-\mathbf{r}')\delta(t-t_0)$. The specific normalization factor depends on the specific software.

The time dependent electric field can be recorded at any position inside the simulation volume. Using Eq(2.7), which describes the relationship between the dipole source and the electric field at any position through the Green's function, the Green's function can be obtained from

$$\bar{\mathbf{G}}_{ij}\left(\mathbf{r}, \mathbf{r}', \omega\right) = \frac{\mathbf{E}\left(\mathbf{r}, \omega\right) \cdot \mathbf{n}_i}{i\omega\mu_0 \mathbf{j}(\mathbf{r}, \omega) \cdot \mathbf{n}_j} = \frac{\mathcal{F}\{\mathbf{E}(\mathbf{r}, t) \cdot \mathbf{n}_i, \omega\}}{\mathcal{F}\left\{i\omega\mu_0 \mathbf{j}(\mathbf{r}, t) \cdot \mathbf{n}_j, \omega\right\}}, \tag{2.49}$$

where $\mathcal{F}\{\mathbf{E}(\mathbf{r}, t) \cdot \mathbf{n}_i, \omega\}$ is the Fourier transform at frequency ω of the i-th component of the output field $\mathbf{E}(\mathbf{r}, t)$. This allows to perform accurate calculations of spontaneous emission rates of dipoles near photonic structures, as seen in previous sections.

A few analytical solutions exist for simple geometries and they are used as a benchmark test of accuracy. For a dipole in free space, the real part of the Green's function diverges as can be seen from Eq(2.11). On the other hand, the imaginary part does not diverge, and averaging over orientations

$$\mathbf{n} \cdot \mathrm{Im}\left\{\bar{\mathbf{G}}(\mathbf{r}_0, \mathbf{r}_0, \omega_0)\right\} \cdot \mathbf{n} = \frac{1}{3}\mathrm{Im}\left\{\mathrm{Tr}\left[\bar{\mathbf{G}}(\mathbf{r}_0, \mathbf{r}_0, \omega_0)\right]\right\} = \frac{\omega_0}{6\pi c}, \tag{2.50}$$

such that the spontaneous emission rate takes the well known expression

$$\Gamma_0 = \frac{\omega_0^3 |\mathbf{p}|^2}{3\pi\epsilon_0\hbar c^3}. \tag{2.51}$$

In most cases presented along this work, the ratio between the imaginary part of the Green's function found through the simulation and corresponding value for free space is plotted.

Chapter 3

THE AMO TOOLBOX IN A NUTSHELL

Our experiment brings together two different worlds: on the one hand, the nanophotonic side of the project that involves fundamental and technical challenges discussed in Chapter 2 and Chapter 4, and on the other hand, the challenges of AMO experiments, such as delivering a cold sample of atoms towards the device or trap atoms close to the structure. Apart from the specificities of the structure design, it is necessary to realize new ways to cool and trap atoms using the properties of the nanophotonic structure [97]. That is where the two core concepts need to work together.

This chapter describes briefly some basic concepts regarding the cooling and trapping of atoms in bigger and smaller optical dipole traps. Laser cooling techniques and optical trapping are described in order to address some of the important steps of the experiments. Furthermore, a brief description of steps that allow efficient loading and cooling into optical lattices is described. In the end, some important considerations regarding trapping in small traps are discussed. The incorporation of this technique into the current experiment is probably the best way to trap much more than one atom near the structure.

3.1 Laser cooling

Modern laser cooling is a well established field [97]. Alkali atoms are historically the favorite group of the periodic table in experiments. Some of the reasons are the existence of closed cycling transitions and the availability of lasers at the relevant transitions. Cesium (^{133}Cs) is a heavy alkali metal atom, and is specially well suited for these experiments due to its atomic weight and associated small photon recoil. The benefits of using slow atoms for precision spectroscopy, quantum optics, and the emergent field of quantum simulations have been recognized for many years [98]. Relatively simple experimental setups allow cooling large Cs samples to a few μK in vacuum environments.

Alkali metals have very simple electronic configurations, with a closed shell and a single valence electron. For instance, the electronic structure of Cs is [Xe]6s^1. Since there is only a single valence electron, the total orbital angular momentum

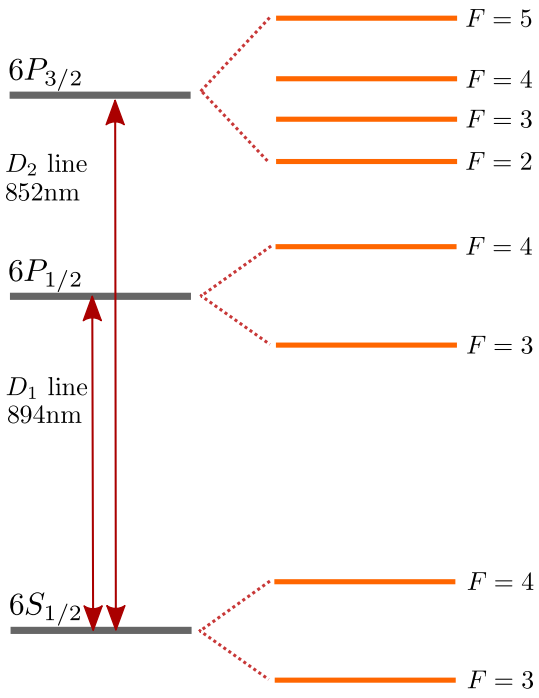

Figure 3.1: Fine (left) and Hyperfine (right) structure for ^{133}Cs and details on the D1 and D2 lines.

(**L**) and total spin angular momentum (**S**) depend solely on this valence electron. The total angular momentum quantum number of the atom J can take values in the range: $|L - S| \leq J \leq L + S$. For Cs, the spin-orbit interaction $\mathbf{L} \cdot \mathbf{S}$ splits the first excited level with $L = 1$ into two states $6P_{3/2}$ and $6P_{1/2}$. Both transitions lie in the near infrared regime, where diode lasers are available.

The Cs nucleus has total nuclear spin $I = 7/2$ and the hyperfine interaction makes it necessary to consider the total angular momentum of the atom $\mathbf{F} = \mathbf{J} + \mathbf{I}$. Each F state is split into substates labeled by m_F, referred to several times as $|F, m_F\rangle$. In the ground state of cesium, the $F = 3$ and $F = 4$ levels are split into 7 and 9 substates, respectively, and in the absence of magnetic fields the frequency separation is the Cs clock transition $\Delta_{HFS} = 9.192631770$GHz. Fig. 3.1 shows the hyperfine structure of Cs and the relevant splittings [99].

Cycling transitions are extremely beneficial for laser cooling, as usually many photons need to be scattered during the process. The selection rules guarantee the existence of such transitions, but the closeness among different hyperfine levels can create off-resonant scattering, making some a priori closed transitions slightly open. For instance, in Cs the $6S_{1/2}\ F = 4,\ m_F = 4 \rightarrow 6P_{3/2}\ F = 5,\ m_F = 5$ is a closed transition if driven by pure σ^+ light, but it can off-resonantly drive the population

to the $6S_{1/2}$ $F = 3$ state if the polarization is not perfectly pure for example. In most cases, an additional laser can repump the population to the $6S_{1/2}$ $F = 4$ state, returning them to the cooing cycle.

Doppler and sub-Doppler cooling

When an atom absorbs a photon, the state of the atom changes. Not only is it excited, increasing its energy by $\hbar\omega_0$, but it also recoils from the light source with momentum $\hbar k$. The atom stays in its excited state until it decays, emitting a photon and recoiling again. The main difference between the two processes described above is that absorption is directional, and the laser imprints its momentum on the atom; meanwhile in the the spontaneous emission process the photon is emitted in a random direction, such that the mean momentum transfer is zero. The change in momentum can be characterized by a force depending on the photon scattering rate, R_{sc}, and the momentum transfered per event $\hbar k$, such that $\vec{F} = \frac{d\vec{p}}{dt} = R_{sc}\hbar\vec{k}$. The scattering rate depends on atomic and light properties,, as the excited state linewidth Γ (the free-space Einstein-A coefficient), light intensity I and associated Rabi frequency Ω, the saturation intensity I_s, and detuning from the resonance $\delta = \omega_L - \omega_0$ and can be written as [97]

$$R_{sc} = \frac{\Gamma}{2}\frac{I/I_s}{1 + I/I_s + 4(\delta/\Gamma)^2}, \tag{3.1}$$

where the saturation intensity is defined as $I/I_s = 2(\Omega/\Gamma)^2$. As the atom moves with some velocity $\vec{v}$, the light frequency seen by the atom is Doppler shifted by $\delta_D = -\vec{k}\cdot\vec{v}$ and it needs to be taken into account in the detuning, making the scattering force velocity dependent. That makes it possible to rewrite the scattering rate, Eq(3.1), as

$$R_{sc} = \frac{\Gamma}{2}\frac{I/I_s}{1 + I/I_s + 4((\delta - \vec{k}\cdot\vec{v})/\Gamma)^2}. \tag{3.2}$$

For a red detuned beam ($\delta < 0$), the atom will preferentially scatter light opposed to its velocity as it will be closer to the atom resonance in its rest frame. If two counter-propagating beams with same intensity and red detuned from the atomic resonance overlap with the atoms, the atom will be tricked to slowly stop. For example, if it moves towards the left, it will preferentially scatter photons from the beam coming from the left, while if it moves to the right it will preferentially scatter photons coming from the right. The force can be expanded around $v \approx 0$ and will be just a dragging force $F \simeq -\beta v$, where the dragging coefficient β depends on similar parameters as R_{sc}. This process is the so-called Doppler cooling mechanism. In

principle, the above argument can be extended to three dimensions using three pairs of orthogonal counter-propagating beams, called usually optical molasses [97].

Even though the energy and momentum transfer from the light field to the atoms happens as small kicks, associated with its quantum nature, the effect of a single photon has a negligibly small effect on the motion of thermal atoms at room T, but repeated cycles of absorption and emission can cause a large change of the atomic momenta and velocities. This is the reason why closed transitions are preferred for laser cooling.

Due to the random characteristics of the spontaneous emission, the Doppler cooling mechanism is not the only effect affecting the atoms. Each absorption event is followed by spontaneous emission where the photon can be emitted in any direction. The average momentum transfer of many spontaneous emission events is thus zero. However, its fluctuations are not zero. An instructive way to think about it is realize that each of this events causes a random walk in momentum space, with a step size $\hbar k$ and frequency $2R_{sc}$ because there are two beams in a given direction. The diffusion in momentum space is characterized by a diffusion coefficient $D_0 = 2\frac{(\Delta p)^2}{\Delta t} = 4R_{sc}(\hbar k)^2$. The competition between the dragging force and the random walk can be described by the same formalism as the Brownian motion or the Langevin equation, achieving a steady state temperature $T_D = \hbar\Gamma/2k_B$, the Doppler temperature [97]. For Cs, the Doppler temperature is $T_D = 125\mu$K.

Early experiments that tried to measure this limiting temperature in different atomic species found, for their surprise, that the temperatures were well below T_D [100]. In order to study real lab situations, where the atomic structure is a bit more complicated than the one in the simplified Doppler cooling scheme, Chu's and Cohen-Tannoudji's groups tried to explain these phenomena with a bit more realistic models [101, 102]. The key feature of these models was the inclusion of the hyperfine states of the atoms and details of the motion of the atom through the light fields, allowing optical pumping mechanisms to reduce the limiting temperatures below the Doppler temperature T_D.

While being cooled, the atoms move through the light field. The population among the different ground state sublevels is redistributed by the optical pumping caused by the light fields. Transitions among those levels can be achieved by exchanging angular momentum between the light and the atom, so polarization gradients can generate spatial redistribution of these populations. That is because different light polarization will favor different angular momentum transfers, reorienting the atoms.

However, not only optical pumping happens, but also light shifts are present as the atoms move. An interesting process happens in this case: the atoms move through a series of hills and valleys, while experiencing cycles of optical pumping. In each closed cycle a fraction of the potential energy is radiated in the pumping event. This happens several times, losing a bit of kinetic energy on each cycle in a process called Sisyphus cooling [97].

The temperatures that can be achieved with this cooling mechanism are only limited by the recoil temperature, $T_{rec} = 180$nK for Cs, making it relatively straightforward to achieve sub-Doppler temperatures. The sub-Doppler viscous force is much greater than the Doppler viscous force, but its capture range is smaller, making it really effective if atoms were already cooled to Doppler temperatures. In order to create polarization gradients, different configurations can be achieved. Two typical examples are lin$\perp$lin or $\sigma^+ - \sigma^-$ counter propagating beams. Further details can be found in several references, for example [97].

Trapping neutral atoms is a challenging task. For neutral atoms, trapping relies on, for instance, induced electric dipole moments or its magnetic dipole moments and the space variation of the electromagnetic field. In the case of optical dipole traps, the atom acquires certain polarizability near its resonance. The spatial trapping can be provided by changing the atoms potential energy in space, that is, creating spatial dependent energy shifts of its levels, affecting potentially the spectroscopic of the sample. A very standard technique to trap neutral atom is based on the magneto optical trap (MOT), pioneered by work of Chu and Pritchard in 1987 [103]. A brief description will be presented here, with not a lot of detail, but further details can be found elsewhere [97].

The MOT operates as an hybrid trap that uses inhomogeneous magnetic fields and light in order to exploit optical pumping and cooling due to the scattering force. Usually, the set up is relatively robust as it does not depend on very precise balancing light balancing, polarization, power, or strong magnetic fields, making it a very standard tool in most AMO labs. To be concrete, it can be assumed that the atoms move in one dimension called x. A magnetic field gradient with $B(x = 0) = 0$ is present and can be achieved by using a pair of coils in the anti-Helmholtz configuration. Furthermore, a pair of counter-propagating beams in the $\sigma^+ - \sigma^-$ configuration are present as in the optical molasses scheme. The presence of the magnetic field causes imbalance in the scattering force of the lasers, providing a position dependent contribution to the force near the center of the system. The

internal structure of the atoms and its Zeeman shifts, in conjunction with a pair of circular polarized and close detuned beams, generates not only the velocity damping seen before, but also a harmonic force localizing the cooled atoms in the center. Therefore, the effect of the field gradient and the optical molasses provides a force like

$$F_{MOT} \approx -\alpha x - \beta v. \tag{3.3}$$

The restoring force depends on the magnetic field gradient, the light intensity and detuning from resonance. Under normal conditions, the atoms in the MOT undergo over-damped oscillations: atoms that enter the volume where the beams overlap are slowed down by the optical molasses ($-\beta v$) while being pushed towards the center by the restoring force ($-\alpha x$).

The MOT can capture atoms within a certain velocity range and in a certain volume, therefore several schemes can be used to load atoms into a MOT. For some species, a high flux atomic beam is sent to the MOT region and collected in the MOT. Another approach is to have a moderate partial pressure of the specific species to cool and operate the MOT under normal conditions. The atoms will have a thermal distribution given by the temperature of its reservoir, implying that there is a small fraction of atoms whose velocity is relatively small, at the tail of the Boltzmann distribution where $v < v_c$, where v_c is the so-called capture velocity.

A straightforward calculation shows that the loading rate of the MOT based on this Boltzmann distribution argument can be written as $R_{MOT} = \frac{n_0 A}{\pi}(v_c^4/\bar{v}^3)$ where $\bar{v} \propto \sqrt{k_B T/m}$ is the mean thermal velocity, n_0 the Cs vapor density and A the associated trap area [104]. The performance of the MOT is then determined basically by the value of v_c, which might depend on, for example, the available distance to bring atoms at rest and the forces experienced. The scattering force in the optical molasses is linear for small velocities and saturates around $v = \pm\Gamma/k$ rolling off at higher speeds. Therefore, the competition between the MOT beam size and the scales of the scattering force might dominate the MOT performance. For big beams, it is found that the atom number increases only from the increased surface area for capture $R_{MOT} \propto L^2$.

3.2 Optical dipole traps

Position dependent forces that might trap or manipulate atoms can be also achieved using intense light fields. Atomic trapping is a well established and powerful technique [105, 106, 97]. Optical dipole traps rely on the electric dipole interaction

with far-detuned light, which is in general a much weaker mechanism than radiation pressure forces or magnetic confinement. The light pattern can be shaped using different techniques to create intensity arrangements with features at subwavelength scales. The most remarkable techniques developed are optical lattices and optical tweezers. In an optical lattice, the interference pattern of various coherent fields is used to create complex periodic intensity patterns in any spatial dimension. Some of the most common uses of these potentials are in quantum simulation regime [13, 98] and optical atomic clocks [107]. Optical tweezers, i.e. a tightly focus light beam, have been used to trap individual atoms and perform detailed control operations on them [108, 109, 110, 111].

Both techniques rely on the fact that optical dipole traps can produce deep potentials while keeping a low light scattering from the lattice beams that might cause heating or incoherent processes. For a two-levels atom with energy difference $\hbar\omega_0$ and a trapping laser with frequency ω_L, the scattering rate Γ_{sc} scales as [106]

$$\hbar\Gamma_{sc} = \frac{\Gamma_0}{\Delta}U, \tag{3.4}$$

where Γ_0 is the decay rate of the system, Δ is the trapping laser detuning $\Delta = \omega_L - \omega_0$ and U is the dipole potential[1]. Therefore, increasing the laser detuning improves the ratio between the trapping strength U to photon scattering Γ_{sc}.

A monochromatic optical field can be written as

$$\mathbf{E}(\mathbf{r}, t) = \frac{1}{2}\left[\mathbf{e}E(\mathbf{r})\,\mathrm{e}^{-i\omega t} + c.c\right], \tag{3.5}$$

where $\mathbf{e}$ indicates the field polarization and $E(\mathbf{r})$ its amplitude. The dipole potential associated to the field can be written is [112]

$$U(\mathbf{r}) = -\frac{1}{2}\alpha(\omega_L, \mathbf{e}) < |\mathbf{E}(\mathbf{r}, t)|^2 >= \frac{1}{4}\alpha(\omega_L, \mathbf{e})|E(\mathbf{r})|^2, \tag{3.6}$$

where the brackets indicate time average over one optical cycle and $\alpha(\omega_L, \mathbf{e})$ is the atomic polarizability.

For a given atomic state, the polarizability is can be found by applying second-order perturbation theory and summing over all the possible dipole-allowed transitions and its expression can be found elsewhere [112, 113, 114, 115, 116]. The polarizability is a tensor operator that depends on the light polarization and the wavelength:

[1] To be precise, corrections need to be done to this expression, but it is not relevant in our context [106].

$\bar{\alpha}(\omega_L, \mathbf{e}) = \alpha_{\mu\nu}(\omega_L)\mathbf{e}^*_\mu\mathbf{e}_\nu$. As the selection rules follow from different angular momentum ($\mathbf{F}$) properties, it is preferable to decompose this tensor in the spherical tensor base. In this case, the spherical tensor can be decomposed in three components: two symmetric components, one traceless (tensor) and the other diagonal (scalar), and one antisymmetric (vector) component.

Therefore Eq(3.6) can be written as [112, 113]

$$U(\mathbf{r}) = -\alpha_{\mu\nu}(\omega_L)E^-_\mu(\mathbf{r})E^+_\nu(\mathbf{r}), \tag{3.7}$$

where the electric field is separated in its positive and negative frequency components $\mathbf{E}^+(\mathbf{r}) = \mathbf{E}(\mathbf{r})/2 = (\mathbf{E}^-(\mathbf{r}))^*$. The mentioned splitting in the polarizability is achieved by writing it as [117, 113]

$$\bar{\alpha}(\omega_L, \mathbf{e}) = \alpha_s(\omega_L)\bar{\mathbf{I}} + \alpha_v(\omega_L)(\mathbf{e}\times\mathbf{e}^*)\cdot\frac{\mathbf{F}_z}{F} + \alpha_t(\omega_L)\frac{(3|\mathbf{e}\cdot\mathbf{e}_z|^2-1)}{2}\left(\frac{3\mathbf{F}_z^2-\mathbf{F}^2}{F(2F-1)}\right), \tag{3.8}$$

where the scalar $\alpha_s(\omega_L)$, vector $\alpha_s(\omega_L)$ and tensor $\alpha_s(\omega_L)$ polarizabilities are introduced, $\bar{I}$ is the identity operator, $\mathbf{F}_z$ the angular momentum operator for the z-direction, $\mathbf{F}$ the angular momentum operator.

For linearly polarized light only the the scalar and tensor components are relevant, while the vectorial component creates Zeeman-like shifts (dependent on m_F) if elliptical components on the polarization are present. All the trap calculations are performed using this expressions and the tabulated transitions are found elsewhere [116, 118].

3.3 Optical lattices

In our experiment optical lattices play a very important role. The ability to create localized optical dipole traps with low scattering rates favors the creation of dense and cold samples of atoms that can be transported over centimeters and stored in the lattice for hundreds of milliseconds. Those atoms can be moved to the nanometer size traps created with the guided modes of the structure [25]. Some numerical results and extensive experimental characterization will be discussed later in this thesis, but for now the case of a one-dimensional optical lattice formed by two counter-propagating laser beams will be described.

Gaussian beams optical lattice

For a single Gaussian monochromatic beam focused to a waist w_0, with optical power P_0 and propagating along the z-direction, the electric field amplitude [119,

106] is[2]

$$\mathbf{E}^{in}(\mathbf{r},t) = \frac{1}{2}E_0^{in}(\rho)\mathrm{e}^{-ikz-i\omega t}\mathbf{e} + c.c., \tag{3.9}$$

with $\mathbf{e}$ a norm one vector that denotes the field polarization and the transverse dependence is encoded in the radial position function

$$E_0^{in}(\rho) = \sqrt{\frac{4P_0}{\pi\epsilon_0 c w_0^2}}e^{-\rho^2/w_0^2}. \tag{3.10}$$

If there is a counter-propagating beam with the same optical power, frequency, and perfectly mode matched with the previous beam, the total electric field amplitude is

$$\mathbf{E}(\mathbf{r},t) = \frac{1}{2}[2\cos(kz)E_0^{in}(\rho)]\mathrm{e}^{-i\omega t} + c.c.. \tag{3.11}$$

Plugging this term into Eq(3.6), the optical dipole potential is given by

$$U(\mathbf{r}) = -\alpha(\lambda)\cos^2(kz)|E_0^{in}(\rho)|^2. \tag{3.12}$$

For a red detuned optical dipole trap ($\alpha(\lambda) > 0$), the trap minima occurs at the intensity maxima, that is each anti-node of the standing wave separated by $\lambda/2$ in the z-direction. Atoms loaded into a red detuned one dimensional optical lattice can be trapped and confined both axially and transversely, into a shape that resembles a pancake as seen in Fig. 3.2(a). At the bottom of the trap the potential can be expanded quadratically such that an atom with mass m oscillates with frequencies

$$\nu_z = \frac{1}{2\pi w_0\lambda}\sqrt{\frac{32\pi\alpha(\lambda)P_0}{mc\epsilon_0}} = \frac{1}{\lambda}\sqrt{\frac{2U_0}{m}}, \tag{3.13}$$

$$\nu_\rho = \frac{1}{2\pi w_0^2}\sqrt{\frac{16\alpha(\lambda)P_0}{\pi mc\epsilon_0}} = \frac{1}{2\pi w_0}\sqrt{\frac{4U_0}{m}}, \tag{3.14}$$

where the trap depth is

$$U_0 = \frac{4\alpha(\lambda)P_0}{\pi w_0^2\epsilon_0 c}, \tag{3.15}$$

and in the usual settings used in this thesis have magnitudes in between $k_B \times 1\mathrm{mK}$ and $k_B \times 10\mu\mathrm{K}$. For beams that are not focused near their diffraction limit, it is true that $\nu_z \gg \nu_\rho$. The harmonic approximation and its consequence on the quantization of the motion of the atoms along z is shown in Fig. 3.2(b).

Usually it is assumed that the atoms are cold enough compared to the trap depth that the harmonic approximation remains valid. In some cases this is no longer true, and

[2] By now, the curvature radius and Gouy phase are not considered to simplify the final expressions

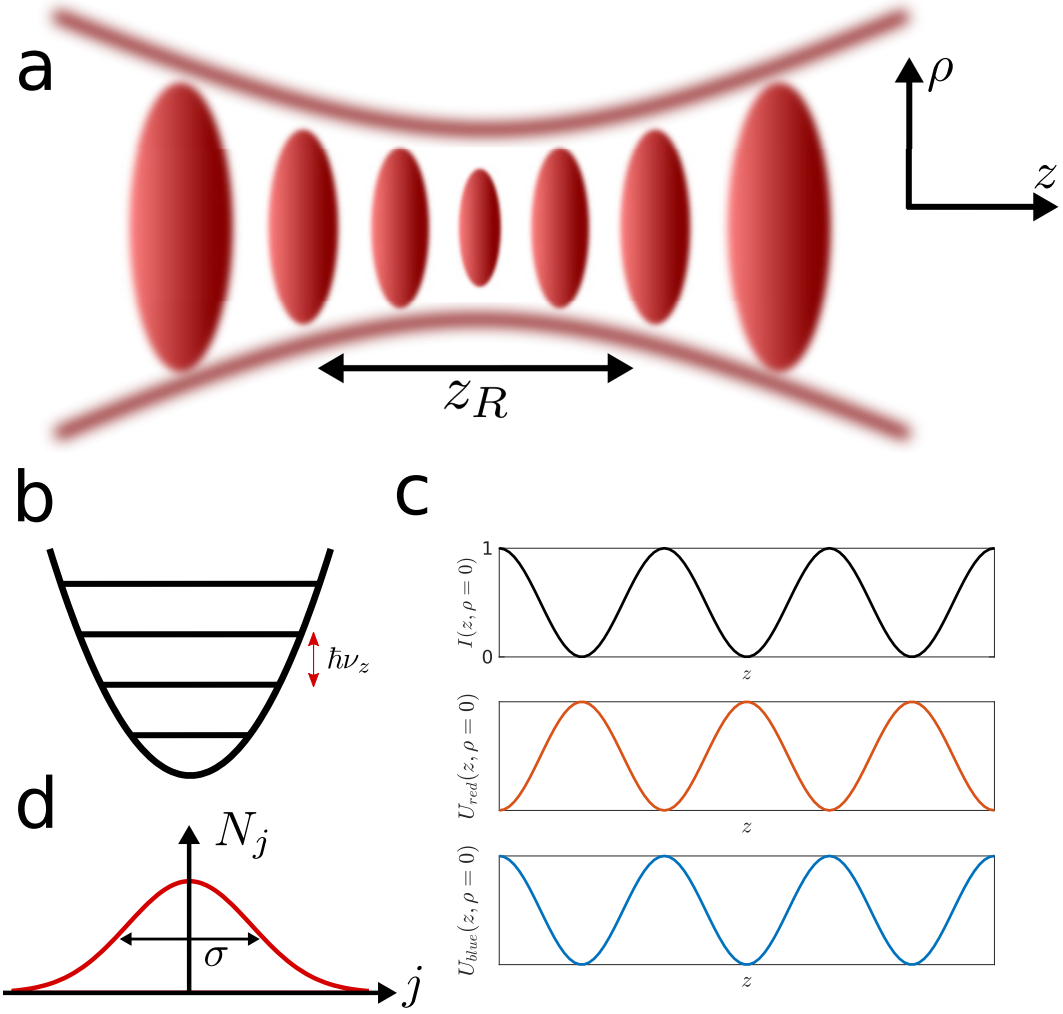

Figure 3.2: (a) Sketch of a few pancakes in a 1D optical lattice. Pancakes are separated by $\lambda/2$, upon corrections, and have a transversal waist w_0. Figure not on scale. (b) Under the harmonic approximation, the motion in the z-direction is described as an harmonic oscillator with its corresponding energy levels. (c) For a standing wave along the z-direction, the intensity oscillates (top). For a red trap (middle), the atoms are at the intensity maxima, while for a blue lattice (bottom), atoms are trapped along z at the intensity minima. (d) Each pancakes j have N_j atoms, whose width σ is characterized by the MOT and lattice overlap.

one needs to take into account further terms in the expansion [120]. Those terms can, for example, determine the thermalization rates for the whole sample if cooling is performed in a specific direction, as they mix the different degrees of freedom. Collisions might as well contribute to these processes.

For the lattice used in the experiment, two contrapropagating beams focused to $w_0 = 55\mu$m with an optical power $P_0 = 150$mW and detuned around $\Delta = -500GHz$ from the D2 transition are employed. Typically, oscillation frequencies are around $\nu_z = 300$kHz and $\nu_\rho = 500$Hz. More experimental details about our one dimensional optical lattice will be presented later in Chapter 6.

Blue detuned lattices are, by themselves, unstable as axial trapping is only provided at the intensity nodes but transversally the atoms are not confined as the intensity is zero. In order to overcome this, a collinear single red detuned beam can be used to create a deep trap that creates transverse confinement without destroying the blue longitudinal confinement. An plot showing a red and blue detuned lattice trap along the axial direction appears in Fig. 3.2(c).

Real Gaussian beams

In the previous section, the expression for the Gaussian beam was oversimplified. In the paraxial approximation [119], the electric field amplitude is

$$E(\mathbf{r}, t) = E_0 \frac{w_0}{w(z)} \mathrm{e}^{-\frac{\rho^2}{w(z)^2}} \mathrm{e}^{-i\left(kz + k\rho^2/2R_c(z) - \eta(z) - \omega t\right)}, \tag{3.16}$$

where $w_0 = w(0)$ is the waist radius, $z_R = \pi w_0^2/2$ is the Rayleigh length, $w(z) = w_0\sqrt{1 + (z/z_R)^2}$ is the waist at position z, $R_c(z) = z\sqrt{1 + \left(\frac{z_R}{z}\right)^2}$ is the radius of curvature for the beam's wavefront,, and $\eta(z) = \arctan(z/z_R)$ is the Gouy phase. When two identical beams are counter-propagated as before, the optical dipole potential is

$$U(\rho, z) = U_0 \left(\frac{w_0}{w(z)}\right)^2 \mathrm{e}^{-\frac{2\rho^2}{w(z)^2}} \left(1 + \cos\left(2kz + k\rho^2/R_c(z) - 2\eta(z)\right)\right). \tag{3.17}$$

For the parameters described before the curvature radius R_c at $z_c = 7$mm from the focus, the actual separation between the lattice focus and the chip's surface, is $R_c(z_c) = 2.5$cm and the Gouy phase is $\eta(z_c) = 0.36\pi/2$. The occurrence of this factor in the phase of the lattice potential implies that the intensity maxima are not separated by $\lambda/2$ as mentioned before, but rather by a different distance. According to the values calculated for z_c, the separation between intensity maxima

along $\rho = 0$ differs from $\lambda/2$ in 3pm. Therefore, it is safe to assume the distance between intensity maxima is $\lambda/2$.

Site occupancy in optical lattices

Usually the experiment starts by loading atoms into a one-dimensional optical lattice from a MOT, whose density profile is usually Gaussian. The density distribution inherits the Gaussian pattern imprinted by the original MOT, such that the site occupancy will follow certain spatially dependent distribution. The atoms loaded into each pancake are characterized by a thermal length that describes the spatial density profile of the ensemble at certain temperature [121].

To estimate those thermal lengths, that are important to understand the atomic distribution that arrives to the nanostructure in the optical lattice, as it will be discussed later, the real space density needs to be considered. The harmonic approximation of the optical potential at a given anti-node, in the case of a red detuned optical lattice, has the form

$$U(x, y, z) \approx U_0 + \frac{m\omega_z^2}{2} z^2 + \frac{m\omega_\rho^2}{2} y^2 + \frac{m\omega_\rho^2}{2} x^2. \tag{3.18}$$

In the experiment the atomic ensemble is not a degenerate gases, so it can be properly described by a Maxwell-Boltzmann distribution. However, it is certainly true that atoms can be cooled to the ground state of these potentials, at least along a specific direction, as will be shown later. In this case, the motion of a single atom in one of these pancakes can be described by a quantum harmonic oscillator Hamiltonian $\hat{H}_{HO}$

$$\hat{H}_{HO} = \hbar\omega_z \left(\hat{n}_z + \frac{1}{2}\right) + \hbar\omega_x \left(\hat{n}_x + \frac{1}{2}\right) + \hbar\omega_y \left(\hat{n}_y + \frac{1}{2}\right), \tag{3.19}$$

with $\omega_x = \omega_y = \omega_\rho$ as before.

The full quantum calculation can be performed using the analytical expression of the eigenfunctions of this Hamiltonian and assuming a Maxwell-Boltzmann thermal distribution. The density profile for a single pancake with N atoms, without considering the curvature of the wavefront, is Gaussian:

$$n_T(x, y, z) = N \times \frac{\mathrm{e}^{-(x/L_x)^2}}{\sqrt{\pi} L_x} \times \frac{\mathrm{e}^{-\left(y/L_y\right)^2}}{\sqrt{\pi} L_y} \times \frac{\mathrm{e}^{-(z/L_z)^2}}{\sqrt{\pi} L_z}, \tag{3.20}$$

where $L_i = \sqrt{\frac{\hbar}{m\omega_i}} \sqrt{\frac{1 + \mathrm{e}^{-(\hbar\omega_i/k_B T)}}{1 - \mathrm{e}^{-(\hbar\omega_i/k_B T)}}}$ for $i = x, y, z$. Both the classical limit for a harmonic oscillator or the quantum zero-point motion limit can be recovered

depending on the ratio between the energy of a quanta of vibration and the thermal energy. Usually, at achievable low temperatures in the experiment, the motion is cooled axially to a few quantums of oscillation but its not significantly cooled radially.

Now that the thermal distribution of a single pancake has been determined, the next step is to study the atom number change along the z-direction. The atom number along the lattice axis is assumed to be Gaussian with a width σ. The occupancy distribution can be used to calculate a properly weighted average of a certain quantity. A sketch of the distribution is shown in Fig. 3.2(d).

If there are N_{tot} atoms trapped among all the pancakes, the j pancake will have N_j atoms drawn from a Gaussian distribution

$$N_j = N_0 \mathrm{e}^{-(j\lambda/2\sigma)^2}, \tag{3.21}$$

where the pancake $j = 0$ is the lattice central pancake, loaded with N_0 atoms. Summing along all the pancakes it is possible to derive N_0 as function of N_{tot}

$$N_0 \approx N_{tot}\lambda/2\sqrt{\pi}\sigma. \tag{3.22}$$

In the experiment the distribution width σ is associated with the overlap between the MOT and the optical lattice. The width is estimated to be $\sigma \approx 500\mu$m, which is around $1/20$ of the Rayleigh length, z_R, of the lattice beams and over that distance the curvature of the wavefronts only change by 3%, so it is accurate to assume that the lattice waist is uniform along the atomic sample.

Close to the chip, the associated thermal length for each pancake is $L_x = L_y = 40\mu$m and $L_z = 18$nm for a lattice depth of $U_0^{chip} = 500\mu$K and temperature $T = 50\mu$K. With $N_{tot} = 1 \times 10^6$ atoms that make it to the chip, the central pancake has around $N_0 = 500$ atoms. A simple estimation of the ratio between the thermal area of the pancake and the transverse area between the alligator photonic crystal nanobeams allows a quick estimation of about 6 atoms near the device for the central pancake.

3.4 Loading, collisions, and cooling in an optical lattice

A basic step in the experiment is to load the one dimensional optical lattice with a high phase space density. Loading the optical lattice is a balanced process where the loading rate and losses rates, density dependent or not, determine the success of the given approach. In general, the loading rate depends on the cooling efficiency and the flux of atoms into the trapping volume, while the loss rate could be caused by

noise in the trap (intensity noise, phase noise, etc), excited state collisions induced by the MOT light, or ground state inelastic collisions for example. For the purpose of this thesis, the loading was optimized by adjusting the MOT-lattice spatial overlap, the repumper light intensity and the cooling parameters to take into account the spatial dependent energy shifts. A great reference to follow a systematic study of a large number of degrees of freedom can be found in the work of Kuppens et al. [122], and some of the discussion here is based on that work and how it applies to our experiment.

Initially a cold atomic cloud rapidly fills the lattice in the space that overlaps with it until loss mechanisms start to balance the initial growth and sets a set a limit for the number of loaded atoms. Meanwhile, the atoms that were not loaded will usually move due to the gravitational drag or any other force that could be present. The atomic flux into the trapping volume will eventually depend on the cloud density and temperature while any sort of cooling mechanism might be present to remove excess energy from the atoms in the trap and enhance the loading rate. The complexity of the light beams, the shape and depth of the optical potential,, and the intensity and detuning of the resonant fields are important to control the loading of the lattice.

For dipole-trap loading, the MOT is typically operated in two stages. First, the detuning of the MOT beams fields is set quite close to resonance, a few natural linewidths away, to optimize the capture by the resonant scattering force. Then, the MOT parameters are changed to optimize sub-Doppler cooling by further detuning the MOT beams, reducing their optical power, turning off the quadrupole magnetic field and nulling the residual magnetic field at the sample's position. The latter step usually reduces the temperature of the atomic sample, but the atom number is mostly influenced by the former stage of the loading. The dipole trap is filled by simply overlapping it with the atomic cloud in the MOT, before the latter is turned off. A key ingredient in the efficient loading that will be discussed later is the reduction of the $F = 4$ repumper intensity during the sub-Doppler cooling stage, such that the atoms spend more time in $F = 3$ avoiding the absorption and reabsorption of the near resonant MOT light, photoassociative collisions,, and ground state hyperfine changing collisions [122]. Further experimental details will be provided later.

On the other hand, losses can be naively caused by heating mechanisms and collisional processes. Spontaneous scatter of the trap light [106], background gas collisions [123], intensity fluctuations, and beam pointing instabilities [124, 125] generate significant heating and are usually density independent. The trap light

induces heating and is of paramount importance in optical dipole trapping to characterize these processes. Spontaneous scattering of trap photons in far detuned traps are elastic (almost elastic if a Raman transition changes the hyperfine ground state), as the energy of the scattered photon depends on the frequency of the field, although its associated fluctuations cause heating. At large detuning, the heating due to absorption followed by random recoil in the spontaneous emission process increases the total energy of the atom by twice a recoil energy $2E_{rec} = k_B T_{rec}$ per scattering event in a time scale $1/\Gamma_{sc}$ as described before in Sec 3.2. Atoms in the vacuum chamber (Pressure$\sim 10^{-9}$ Torr) can collide and expel trapped atoms, affecting not only the steady state numbers of atoms in the MOT but also the atom number in the dipole trap. In the current experimental system, background gas losses in the MOT are well understood and do not contribute significantly within the experiment timescale; however, local pressure close to the chip is still unknown, depending on the behavior of the chip surface and other components as the glue and the optical fibers in high vacuum. Furthermore, technical heating can occur due to intensity fluctuations and pointing instabilities in the trapping beams creating resonant parametric heating. In the first case, fluctuations at twice the characteristic trap frequencies parametrically drive the atomic motion in the trap. In the second case, a shaking of the potential at the trap frequencies increases the motional amplitude. Experimentally, these issues will strongly depend on the particular laser source and its noise spectrum.

Collisions, however, are density dependent [126, 127, 128, 129]. There are different classes of collisional processes that are important in this experiment, for example, photoassociation losses [130], spin exchange hyperfine changing collisions [131], and radiative escape [132, 133]. Photoassociative collisions are caused by the lattice field and ends in the production of untrapped molecular states. Although they happen at specific frequencies resonant with the molecular states potential, in Cs those frequencies are $\sim$ 40GHz apart and span tens of nm around the D1 and D2 transitions. Ground state hyperfine changing collision increases the atomic kinetic energy as much as the hyperfine splitting ($\sim 0.45K$ for Cs), more than enough to expel them from the optical dipole trap. Light assisted collisions or radiative escape, happen once a near resonant field is present. In the simple semiclassical picture [132] resonant light excites an atom and induces a long range dipole-dipole ($\sim$ 100nm) attractive molecular potential that accelerates the atoms towards each other. Meanwhile, the atom decays though having gained enough kinetic energy to leave the trap.

Pushed by the interest to create Cs BEC in optical and magnetic traps [128, 129] due to the low temperatures achieved by laser cooling alone and its apparently favorable scattering properties in the $|3,-3\rangle$ state, the study of cold and ultracold collisions is a well developed research area both theoretically and experimentally. These collisions are inherently dependent on the hyperfine state. Early measurements in Foot's and Dalibard's groups showed that the $|4,4\rangle$ state exhibit huge hyperfine-changing collisions, responsible of large two-body inelastic loss in magnetic traps, with measured rates of about $K_2^{|4,4\rangle} \simeq 1 \times 10^{-11} cm^3 s^{-1}$ at 30μK. Tiesinga's group performed measurements in optical dipole traps [134], measuring inelastic two-body losses characterized by a rate

$$K_2^{|4,4\rangle} = (1.1 \pm 0.1 \pm 0.2) \times 10^{-11} cm^3 s^{-1} \tag{3.23}$$

and hyperfine changing collisions between $F = 3$ and $F = 4$ characterized by the rate

$$K_2^{3-4} = (1.5 \pm 0.2 \pm 0.5) \times 10^{-12} cm^3 s^{-1}. \tag{3.24}$$

These high collisional loss rates have thwarted all attempts to attain BEC in Cs with magnetic trapping. Optically trapping cesium in the $|3,3\rangle$ lowest energy ground-state led to the production of a Cs BEC in the Innsbruck group [135].

The $|3,-3\rangle$ state does not have hyperfine changing collisions, but it has a complicated magnetic field dependent elastic and inelastic scattering properties. The first measurements on the elastic collision cross sections and two-body inelastic collision rates in spin polarized Cs was performed by Monroe et al. in 1993 [136]. An upper limit of $K_2^{|3,-3\rangle} \leq 5 \times 10^{-14} cm^3 s^{-1}$ was put on the two-body inelastic collision rate coefficient, significantly smaller than for the $|4,4\rangle$ state. That measurement was performed with a strong bias field present (50G) where other effects described in [137] can take place. However, the intricate structure of the Freshbach resonances close to zero field, determining a negative scattering length for $B \approx 1G$ implied the failure in Cs condensate experiments in magnetic traps at low fields [129]. A detailed analysis of this low field resonances can be found in works by Julienne's group [137].

Although the focus of many of these experiments is on the possibility of creating a Cs BEC and the implication of the losses in different stages of cooling, our interest has less restrictions. Most noticeably, the losses will limit the loading of the traps near the dielectric structure. Optical tweezers, deep in the so-called collisional blockade regime, can offer a different perspective about loading several atoms near

the device. A further analysis will be carried out at the end of this chapter and some more hints about the use of small optical dipole traps will appear along different sections of this thesis.

Apart from the sub-Doppler cooling stage briefly described before, a Degenerate Raman Sideband Cooling (DRSC) stage is performed after all the resonant MOT beams are completely extinguished. The method was developed by Chu's group in the late 90's and at the time achieved the highest PSD [138, 139]. This is a way to overcome density limitation in the standard sub-Doppler cooling stages, associated with reabsorption of spontaneously emitted photons and atom-atom interactions at high densities, meanwhile achieving significant population in the vibrational ground state. DRSC relies in the use of only the two lowest-energy ground states, suppressing different losses mechanisms specific to Cs. The method was first demonstrated for atoms trapped in a one dimensional lattice [138], although due to those collisions and trap characteristics, cooling among the three directions can be observed. In these traps, the ground state wave-package spread is much smaller that the optical wavelength of the cooling transition, $k\Delta x_0 \ll 1$, the so-called Lamb-Dicke regime.

The method is inspired in original work in Jessen's group [140]. The sample is initially polarized in the $|3, 3, n\rangle$ state, where n represents the vibrational quantum number in the tightly confined direction, in this case the z-direction along the lattice axis because $\nu_z \gg \nu_\rho$. An external magnetic field $\mathbf{B}$ is applied, such that the Zeeman splitting degenerates the consecutive vibrational levels for different hyperfine states in $F = 3$, therefore the state $|3, 3, n\rangle$ and $|3, 2, n-1\rangle$ are degenerate, as seen in Fig. 3.3. The cooling cycle is composed of a degenerate Raman transition from $|3, 3, n\rangle$ to $|3, 2, n-1\rangle$, followed by optical pumping back to $|3, 3\rangle$. As the atom is in the Lamb-Dicke regime, the photon recoil do not change the vibrational momentum, so the atom falls into the $|3, 3, n-1\rangle$ state removing one quantum of vibrational energy.

The Raman transition uses two photons with the same energy, and the biggest significance of Chu's group work was to realize how to use the trap light to perform these transition. A major advantage is the low heating associated with the spontaneous Raman scattering of the far detuned beams. To create the Raman coupling between these states that differ in one unit of angular momentum m_F, an angle α between the polarization directions of the counter-propagating beams that form the lattice will induce an effective ellipticity in the field, creating a vector shift in the lattice

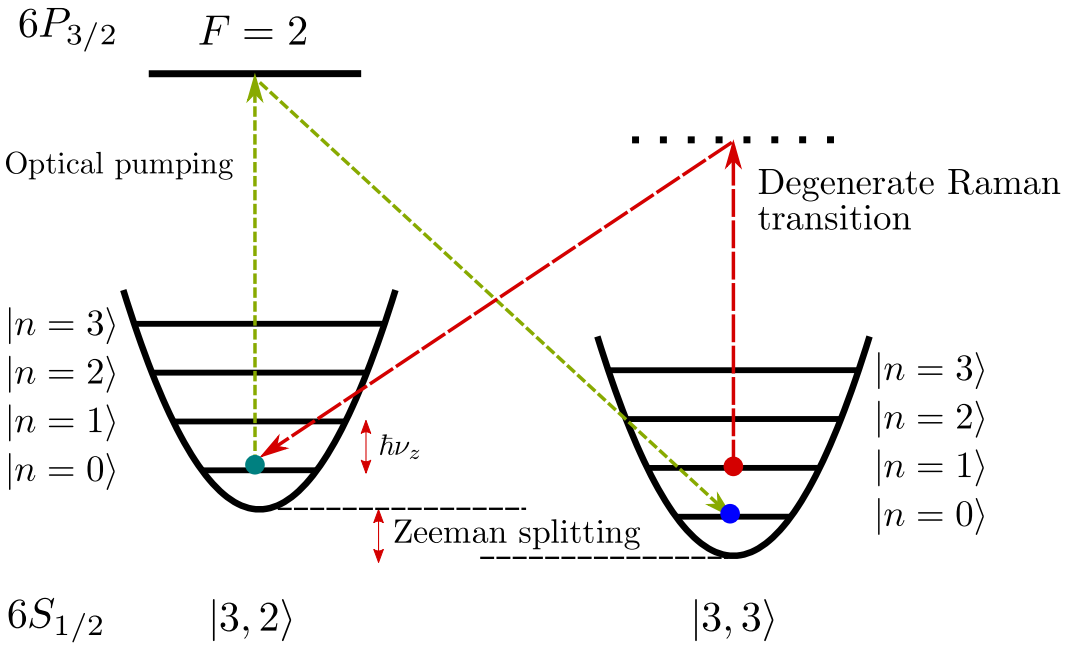

Figure 3.3: DRSC for an atom trapped in a tight trap. One cooling cycle uses a degenerate Raman transition (red) to reduce the vibrational quanta by one unit (red to green), followed by an optical pumping transition (green) that accumulates the atom in the ground and dark state $|3, 3, 0\rangle$.

potential. The corresponding coupling strength can be written as [117]

$$\langle 3, 2, n-1|\, U(\mathbf{r})\, |3, 3, n\rangle = \frac{(6n)^{1/2}}{2} \epsilon U_0 \eta \sin(\alpha) \sin(\beta), \tag{3.25}$$

where β is the angle between the external magnetic field $\mathbf{B}$ and the lattice wavevector $\mathbf{k}$, U_0 is the trap depth for linear polarized light, ϵ characterizes the strength of the Raman transition for the lattice detuning, and η is the Lamb-Dicke parameter.

In the experiment, the atoms loaded in the optical lattice are transported by a moving lattice over $\sim$ 1inch. Different processes contribute to the efficiency of this transport, but certainly cooling the sample to the ground state has been of great importance to deliver a high flux of atoms towards the device.

Small volume traps

To conclude this chapter, a few remarks about loading atoms in very small traps will be done. This might be taken into account specially in the JILA experiment as a few atoms in a very small volume trap can be trapped, as it will be discussed later. In the Lab 2 experiment, these effects might lead to collisional blockade while loading of each individual trap created along the APCW. The implication in both experiments

is currently under investigation.

Loading individual neutral atoms in small traps, as optical tweezers, has been achieved in different contexts [141, 109, 19, 110, 111]. By loading individual atoms in small volume optical traps, individual addressing with high resolution can be achieved. Because of the small trapping volume, only one atom can be loaded at a time. Consequently, the statistics of the number of atoms in the trap is strongly sub-Poissonnian because there could be either one or zero atoms in the trap with equal probabilities. In Schlosser, Reymond, and Grangier [142] the description of this process is given. Fundamentally, depending on the trap parameters there could exist a collisional blockade regime where the loading mechanisms as in Kuppens et al. [122], and very small volume traps determine the number of atoms in the trap and its statistics.

In the simple model [122, 142] where N atoms are in the trap loaded at a rate R, subjected to one-body losses $-\gamma N$ like background gas collisions and two-body losses $\beta N(N-1)$ the atom number changes as

$$\frac{dN}{dt} = R - \gamma N - \beta N(N-1). \tag{3.26}$$

As soon as two atoms are in the small volume trap collisions become the dominant loss mechanism. This is the so-called collisional blockade regime, as once the atoms collide, both are ejected of the trap. Consequently, in this regime the number of atoms is either zero or one, as every time an atom is trapped is the cause of either a loading or loss event. This plateau, as mentioned in [142], extends over a big range of loading rates. After the plateau, the strong loading regime allows a large number of atoms to be trapped in small volumes. However, reaching that regime is hard.

This is important for the experiments carried out in both labs and we begin to understand the implications and limitations of the collisional blockade mechanism in the small trapping volume systems that are used. Further research is performed on this issues.

Chapter 4

1D PHOTONIC CRYSTAL WAVEGUIDE DESIGN FOR STABLE TRAPPING AND STRONG PROBING

A promising frontier for optical physics would become accessible with the integration of atomic systems and nanophotonics, which have made remarkable advances in the last decade. Significant progress toward integration of atomic systems with photonic devices has progressed on several fronts, including cQED, where atom-photon interactions can be enhanced in micro and nanoscopic optical cavities, and nanoscopic dielectric waveguides, where the electric field is confined at sub-wavelength scales.

Beyond traditional settings of cavity QED and waveguides, fascinating paradigms emerge by combining atomic physics with photonic crystal waveguides. One- and two-dimensional photonic crystal structures formed from planar dielectrics offer a configurable platform for engineering strong light-matter coupling for single atoms and photons with high complexity. For instance, dispersion-engineered photonic crystal waveguides permit the trapping and probing of ultracold neutral atoms with commensurate spatial periodicity for both trap and probe optical fields that have disparate free-space wavelengths. Such systems can lead to atom-atom interactions efficiently mediated by photons within the waveguide. In photonic crystal waveguides, atom-photon coupling can be enhanced near the band-edge via slow-light effects and can be tailored to explore quantum many-body physics with atom-atom interactions that can be readily engineered.

The research in our group goes in that direction. In order to achieve such objectives, different group members made great efforts towards designing, fabricating, and characterizing the structures. Newer versions are being currently explored, and some of the recent advances can be found in Jonathan Hood's, Su-Peng Yu's and Andrew McClung's theses [143, 144]. In this chapter the focus will be in my personal contribution towards the alligator photonic crystal waveguide design and some other characteristics of the system. This material can overlap with other group thesis and published material [26].

4.1 Rights and obligations

Trapping atoms very close to dielectrics is not an easy task, neither for neutral atoms [145, 146] nor ions [147]. Several advances had been done on both fronts, with optical fibers the favorite platform to trap and probe atoms. In the last ten years, progress on creating very thin optical nanofibers where the propagating electric field is mostly evanescent has increased the interest toward trapping neutral atoms near dielectric surfaces [148, 149]. This important milestone was finally achieved in 2010 in Austria [23]. A two color trap scheme creates an array of stable optical nanoscopic dipole traps for neutral cesium atoms spaced by $\lambda_{red}/2$, where λ_{red} is the effective wavelength of the red detuned trap light. Around 2000 atoms can be routinely trapped, providing a very optical dense sample of cold atoms [23]; long coherences times were observed in those traps [150], magic wavelength traps were investigated [68], and multiple other phenomena like chiral emission were demonstrated [151].

Although nanofiber traps are an exciting platform, they have some limitations. Material properties of SiO_2 might limit the possibility of efficient production and detection of entangle states in atomic ensembles, as Raman scattering from the trapping beams into the resonant atomic frequencies is considerable. The fact that the trap longitudinal spacing is in general not commensurate with the probe wavelength means that collective effects are not manifested in their full possibilities. A major drawback of the nanofiber setup is that the light-matter coupling strength is fundamentally bounded, depending only the ratio between the fiber radius and distance of the atom to the fiber [24].

The ideas behind the nanofiber trap can guide the development of new hybrid atom-photon platforms for neutral atoms. The idea is to further use the properties of the guided mode not only to create stronger light-matter coupling as described in Chapter 2, but also to create traps that employ the strong subwavelength confinement. Photonic crystal waveguides are a good candidate to fulfill these requirements.

Significant technical challenges exist for developing these new platforms arising from the following requirements:

- the fabrication is sufficiently precise to match waveguide photonic properties to atomic spectral lines;
- atoms are stably trapped in the presence of substantial Casimir–Polder (CP) forces yet achieve strong atom-field interaction;

- coupling to and from guided modes of nanophotonic elements is efficient;
- sufficient optical access exits for external laser cooling and trapping;
- optical absorption is low, and the net device thermal conductivity is high, permitting optical power handling to support 1 mK trap depths.

The first device designed to fulfill at least some of these requirements was inspired by proposals in Chen-Lung Hung's work [25] and consists of two parallel silicon nitride (Si_3N_4) suspended nanobeams, each with a periodic array of circular holes. The atoms are trapped in the gap between the beams. The band edges of the dielectric and air bands for the TE-like modes are designed to be aligned with the Cs D1- and D2-line transitions at 894nm and 852nm respectively. Two reasons are behind this design:, the first one is to use low optical power to create strong optical traps with the guided modes, while the second is to enhance the light-matter interaction by having a band edge close to the relevant transition as described in Chapter 6. Light couples into the device from a single mode optical fiber and is routed out of the vacuum chamber with low loss. The light propagates through a long single mode nitride waveguide, about 1.4mm long, and then an adiabatic Y-junction ends in a double beam configuration. Each waveguide was designed to be 330nm wide and separated by a gap of 250nm. The photonic crystal had 30 nominal holes in each beam with radius 50nm and lattice constant is a = 365nm. A few more holes were placed before and after the nominal holes in order to impedance match the double nanobeam plain waveguide and the photonic crystal. There is another identical Y-junction that brings the double nanobeam waveguide to a single beam waveguide where bigger holes are etched to create a mirror for the TE-like modes by having a bigger bandgap that includes the two Cs transitions. Some of this details are captured in Fig 4.1.

Although this seemed a promising start, several things needed to improve. First and fundamentally, it was extremely hard to fully etch 50nm radius holes through the 200nm thick nitride. Some of the holes were not etched and the size of them fluctuated considerably. Several other features were improved in later designs, but the fundamental change was the adoption of a smooth modulation in the outer part of the nanobeams in order to make the fabrication easier and more robust. I designed and calculated the properties of the side modulation structures in 2013.

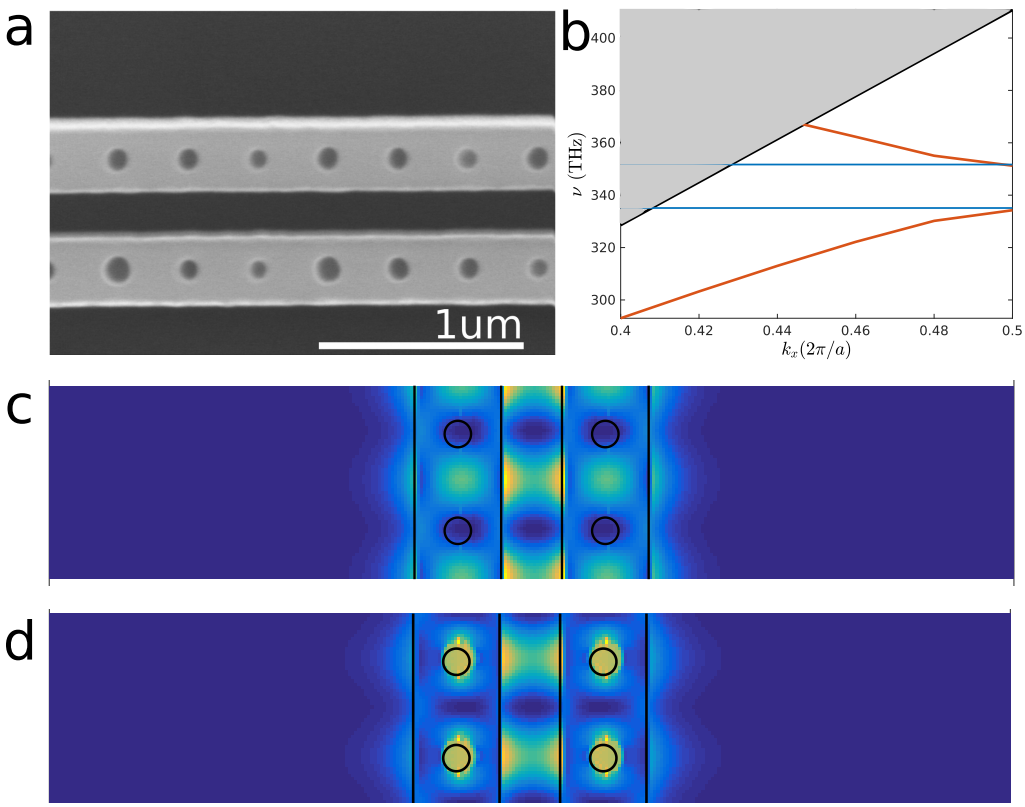

Figure 4.1: (a) SEM images from the original devices with holes (Fabricated by Su-Peng Yu). Note the big fluctuations in the hole size. (b) Band structure for the TE-like modes (red) with the Cs D1- and D2-line frequencies indicated (blue). (c) $|\mathbf{E}(\mathbf{r})|^2$ in the $z = 0$ plane for the the dielectric mode at $k = \pi/a$. (d) $|\mathbf{E}(\mathbf{r})|^2$ in the $z = 0$ plane for the the air mode at $k = \pi/a$.

4.2 Alligator photonic crystal waveguide

The central component of our next device is an *alligator photonic crystal waveguide* (APCW) region shown in Fig. 4.2(a). It consists of two parallel Si_3N_4 waveguides (refractive index $n = 2$) where a modulation on the waveguide width is imposed by changing the outer surface of the waveguide. This configuration is similar to the double nanobeam with holes introduced before, but without holes. Instead, these smooth modulationss can be fabricated with better detail and precision. In order to create good trapping and enhance the density of states for the atom to decay into the waveguide mode, the atoms can be trapped in the gap between the dielectrics and the band edges are aligned to the Cs D1- and D2-line transitions [25] as shown in Fig. 4.2(b). The TE-like modes of the structure have a significant intensity in between the beams as the field from each of the nanobeams evanescently leaks into the other beam. Around the structure the fields decay with $\sim$ 150nm decay length

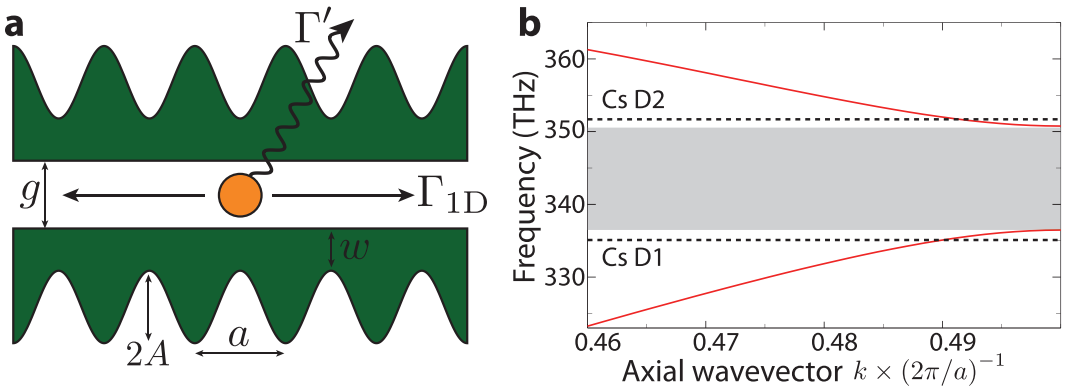

Figure 4.2: (a) Schematic of the APCW with dimensions: thickness t = 200nm, inner waveguide width w = 187nm, gap g = 260nm, lattice constant a = 371nm, and sinusoidally-modulated outer waveguide edge with amplitude A = 129nm. The decay rates into the selected guided mode for the atom (orange sphere) into the waveguide Γ_{1D} and into other modes Γ' are indicated. (b) Photonic band structure of the fundamental TE-like modes of the nominal APCW device calculated with the dimensions derived above from a typical fabricated device. Small adjustments are made to the waveguide parameters within the absolute uncertainty of the SEM ($< 5\%$) to obtain better agreement between measured band structures and those computed from SEM images. Figure adapted from [26].

for the intensity. Generally, the fabricated devices have about 150 unit cells (55μm) and about 30-40 unit cells at each extreme to provide proper impedance matching as described later.

Guided mode trapping in the APCW

One strategy for trapping and probing Cs atoms within the gap of the APCW is to use the dielectric band mode blue detuned from the Cs D1-line as a trapping beam and the air-band mode as a probe on the D2-line of the trapped atoms. In this scenario, Cs atoms are trapped between the parallel nanobeams where the dielectric-band mode has an intensity null in the $x-y$ plane, as in Fig. 4.3(a). To be precise, this is true exactly at the band edge, as the Bloch mode has maximum contrast in a given unit cell. However, for modes that are still close to the band edge, there is not an intensity null but rather a local minimum in the $x-y$ plane. Along the z-direction the blue detuned dielectric mode will slightly repel the atom from the $z = 0$ plane. The confinement in the vertical z-direction can be recovered by an additional guided mode red detuned from the Cs D2-line transition. Additionally, if the band structure is the one shown in Fig. 4.2(b), it is possible to reverse this configuration and use a D2 blue detuned guided mode in the air band to provide confinement in the intensity

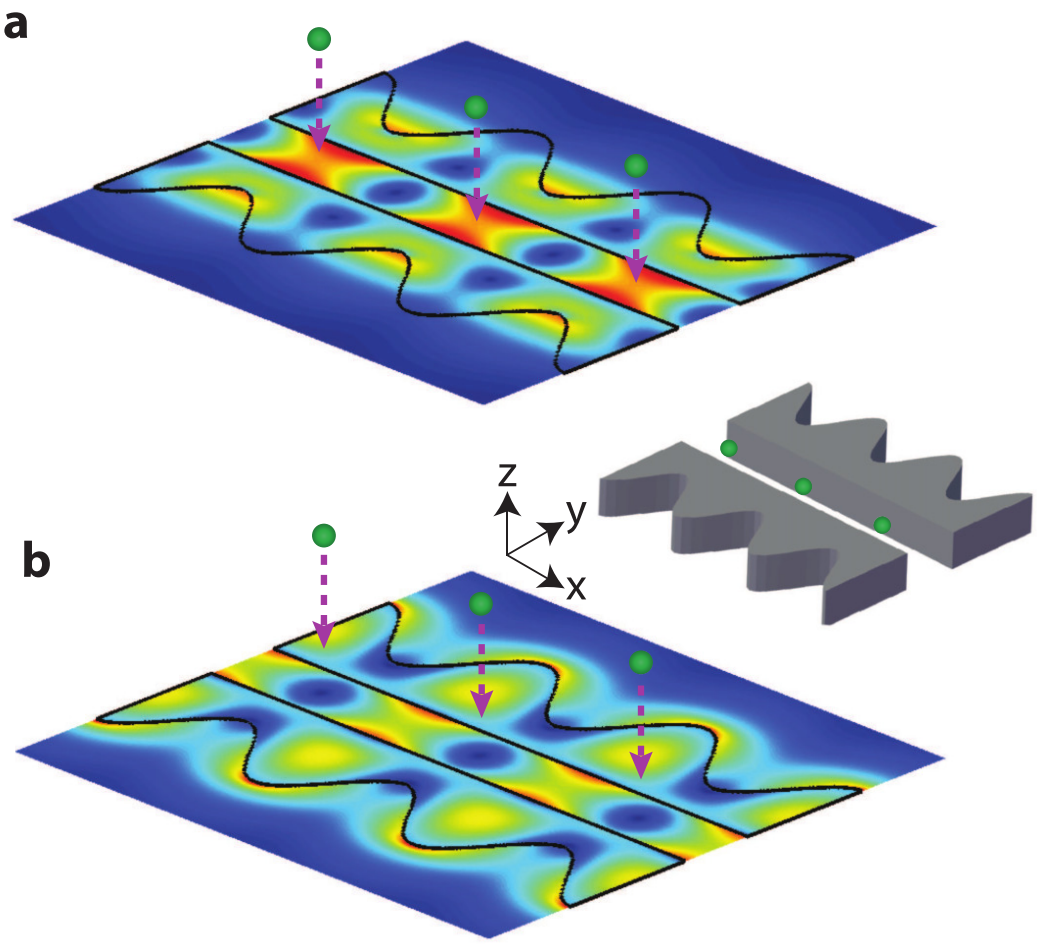

Figure 4.3: Finite-element-method (FEM) simulation of the guided mode electric field magnitudes $|\mathbf{E}(\mathbf{r})|$ near the band edge for the TE-like (a) dielectric and (b) air band. The optical frequencies correspond to the Cs D1- and D2-lines, and the corresponding band structure is shown in Fig. 4.2(b). Figure adapted from [26].

local minimum in the $x-y$ plane and use a D1 red detuned dielectric band mode to confine in the z-direction. In general, if a blue detuned mode is used in a given band to trap, the probing is done in the other band, such that the light intensity is stronger at the trapping positions as seen in Fig 4.3(b).

To be specific, for the band structure shown in Fig. 4.2(b) and with counter-propagating 30μW TE-like mode fields blue detuned 30GHz from the Cs D1-line $F = 4 \rightarrow F' = 4$ transition combined with 15μW of counter-propagating TE-like mode fields red detuned 300GHz from the D2 $F = 4 \rightarrow F' = 5$ transition, a ~ 5 mK deep trap can be created with trap frequencies of $\{\nu_x = 3.5, \nu_y = 1.4, \nu_z = 0.7\}$MHz. The actual optical power represented by the numerical solution is calculated by taking the numerically computed group velocity v_g and the electric field energy in

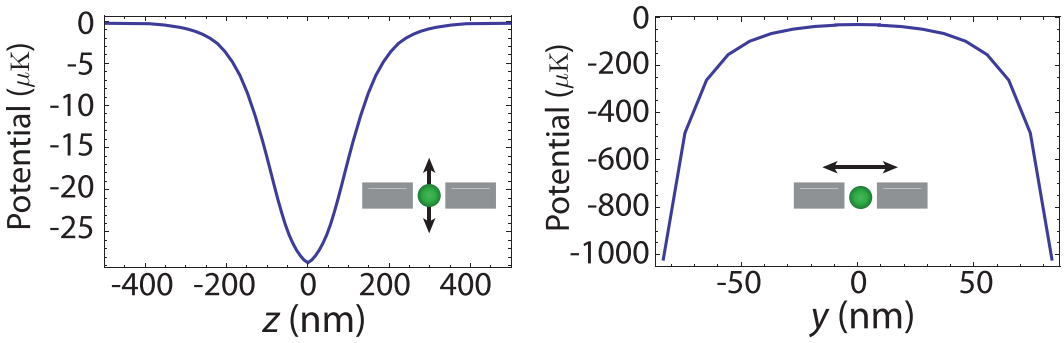

Figure 4.4: Numerically computed Casimir–Polder potential along directions (x_m, y_m, z) and (x_m, y, z_m) direction as indicated, where the (x_m, y_m, z_m) is the dielectric band intensity minimum as shown in Fig. 4.3(a). Figure adapted from [26].

a given unit cell U_E, and estimating the total power flowing through the waveguide as $P = \Delta U_E/\Delta t = U_E v_g/a$.

For this calculation, Casmir-Polder potentials were not taken into account. However, as shown in Hung et al. [25], surface forces are extremely strong at distances smaller than 100nm. That will weaken the confinement in the y-direction fundamentally. Furthermore, Casimir-Polder enhances the confinement in the z-direction, as it creates an attractive potential for ground state atoms [59]. For this specific design it creates a weakly 30μK trap by itself. The contribution of the surface potential is shown in Fig. 4.4. The use of Casimir-Polder forces in order to trap atoms very close to structures is an open topic that will probably be addressed in future research [25, 31, 34]. A good review on the effects of surface forces in nanostructures can be found in Rodriguez, Capasso, and Johnson [152].

Device engineering in the APCW

Although the heart of the experiment lies on the APCW device, there are several other elements along the entire structure to in- and out-couple light efficiently, as well as to provide mechanical support and to improve heat dissipation Fig 4.5. SEM images taken along the length of the SiN waveguide show the various sections of the device, including a waveguide-to-fiber coupling region, Fig. 4.5(b), mechanical support and thermal tethers, Fig. 4.5(c), a tapered region of the APCW, Fig. 4.5(d), and finally the central APCW region, Fig. 4.5(e).

The waveguide-to-fiber coupling in Fig. 4.5(b) consists of a slow tapering of the nanowaveguide from a nominal width of 300 nm down to an endpoint, the coupler,

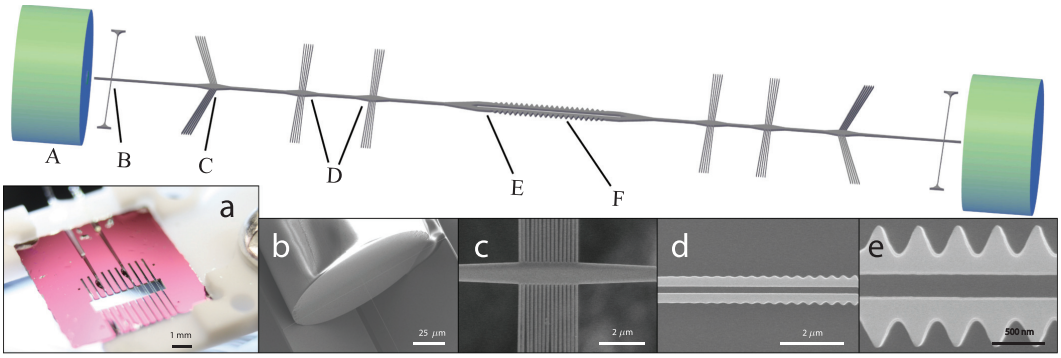

Figure 4.5: Center: Schematic of the waveguide chip, illustrating the various regions of the waveguide. Bottom: (a) Optical image of the fiber-coupled waveguide chip showing the through-hole for optical access. Zoom-in SEM image of (b) the adiabatic fiber-coupling region (A), (c) the alignment, mechanical support, and thermal heat-sink tethers (B, C, D), (d) the tapered region of the APCW (E), and (e) the central APCW region (F). The sinusoidal modulation facilitates high-precision fabrication. Other elements (not shown) are side thermal contacts which consist of a pair of 7.5μm wide SiN rails extending across the entire length of the waveguide and connecting to the substrate. Figure adapted from [26].

near the fiber facet of width 130 nm and provides efficient optical mode-matching to an optical fiber [153] (Nufern 780HP fiber; mode field diameter 5μm). The coupler size is really critical, as the coupling efficiency can be strongly wavelength dependent if the coupler is too big or too small. Theoretically, coupling efficiencies above 90% can be estimated [153]. Optical fibers are placed into the input and output v-grooves in the Si substrate, and they provide the most common way to characterize the optical properties of the device. The new free space coupling scheme, developed by Su-Peng Yu, is a very promising step towards maximizing the use of all the fabricated devices and creating more flexible science chamber designs.

To mechanically support the nanowire-waveguide, nanoscale tethers are run from the side of the waveguide either directly to the substrate or to side support rails of 7.5μm wide SiN that extend the entire waveguide length and connect to the substrate at either end of the waveguide (labeled sections B, C, and D of Fig. 4.5 show the tethers). The tethers are each 90 nm wide and consist of a single tether for fiber alignment at the ends of the waveguide and multi-tether arrays of 15 tethers, spaced at a 220 nm pitch. FDTD simulations show that the input coupling efficiency of the taper and single alignment tether is 75% for light near the Cs D2-line. The multi-tether supports provide anchoring against the high stresses within the device and increase device-substrate thermal contact. Optical scattering is minimized at the

multi-tether attachment points by tapering the waveguide width up to 1μm as seen in Fig. 4.5(c). FDTD simulation shows that the scattering loss at the multi-tether points is 0.5%, while at the fiber alignment tether can be 10%. New generations of 1D slots waveguides and 2D photonic crystals slabs have different mechanical support structures to accommodate new architectures. Details can be found in Su-Peng Yu's thesis.

The nanowire waveguides as shown in Fig. 4.5 are formed from a thin film of stoichiometric SiN 200nm in thickness, grown via low-pressure chemical vapor deposition on a (100) Si substrate of 200μm thickness. This sort of SiN has exhibited low optical loss in the near-infrared [154, 155, 156] and large tensile stress (1 GPa) [157]. A 1×5mm window opened through the Si substrate provides optical access for laser trapping and cooling, with the nanobeam extending across the length of window and into the v-grooves, spanning a total distance of about 2mm. Even with the extreme aspect ratio of the waveguides, the high tensile stress of SiN preserves mechanical stability and alignment. A key feature is angled tether label as C in Fig. 4.5.

The fabrication itself follows several well calibrated steps in order to produce clean devices that can go into the science vacuum chamber. Further success cannot be achieved without a careful and fully studied fabrication. Su-Peng, Andrew, and Jon have done an amazing job in terms of characterizing in detail all the steps. Here I will just provide a summary, based on published work [26]. In order to obtain smooth waveguide side walls of vertical profile and to avoid damage during the SiN etch, an inductively-coupled reactive-ion etch (ICP-RIE) of low DC-bias and optimized C_4F_8 and SF_6 gas ratios is employed. A similar etch has been used to create record high-Q SiN micro-ring optical cavities near 800 nm [154, 158] and verified again by creating the in-house design so-called 'fishbone' cavities where the mirrors are created using external modulations as in the APCW design.

Fabrication of the waveguide chip begins with a UV lithography step to define the back window region. Then a single e-beam lithography step defines the fine features of the waveguide and sets the fiber v-groove position and width (which ultimately determine the fiber-waveguide alignment). A piranha clean removes any resist residue prior to a potassium hydroxide (KOH) wet etch, which opens a through-hole in the Si substrate defined by the two SiN windows on back and front. After additional nanostrip cleaning, the chip is transferred to an isopropyl alcohol solution where it is dried using a critical point drying step to prevent stiction of the

double nanobeam APCW section. The last cleaning stage involves an O2 plasma clean to remove any residual particles on the waveguide surface. Due to observed Cs contamination in the devices, in current devices an alumina (Al_2O_3) coating is used by performing a controlled single atomic layer deposition procedure on the APCW structure. Usually about 10nm of alumina is deposited on each device.

Device characterization

Once fabricated, anti-reflection coated optical fibers are mounted into the input and output v-grooves in the Si substrate. The fiber-waveguide separation is set for optimal coupling (typically 5μm) before the fibers are affixed in place with low degassing thermal cured epoxy. The Si chip and fibers are then attached to a vacuum compatible Macor mount (see Fig. 4.5(a)) and loaded into a vacuum chamber (reaching 10^{-9} Torr) with optical fiber teflon feedthroughs [159].

In order to measure the broadband reflectivity and transmission of the APCW, a broadband superluminescent diode optical source and optical spectrum analyzer is used. The measured normalized reflection R and transmission T spectra over a frequency range of 320–360THz for a typical APCW waveguide is shown in Fig 4.6(a). These data sets provide substantial information about the optical properties of the whole device. The measured spectra reflects the position of the photonic bandgap for each device. For the example in Fig 4.6(a), the fabricated APCW has the desired photonic bandgap, with the dielectric and air band edges closely aligned with the Cs D1- and D2-lines, respectively, and in reasonable agreement with the numerically calculated spectra, Figs. 4.6(c)-(d), based on the device characteristics derived from the SEM images. From the average reflection level within the photonic bandgap, the estimated total single-pass coupling from optical fiber to APCW is $\simeq (60 \pm 5)\%$. The high-frequency oscillatory behavior of the reflected and transmitted intensities is due to parasitic reflections from the AR-coated input fiber facet (0.1% reflection) and the input tether (0.2%). Based upon previous measurements for similar waveguides, the power loss coefficient of the unpatterned nanobeam sections is ~ 4 dB/cm.

Because of the finite length of the APCW reported in this work, the spectral regions near the bandgap exhibit slowly oscillating fringes in transmission and reflection which can be interpreted as low-finesse cavity resonances of the APCW section. FDTD simulations reproduce the oscillatory behavior, as shown in Figs. 4.6(c)-(d). As noted by Purcell, these cavities should affect the spontaneous emission rate into the waveguide. In the APCW cavities, the enhancement due to these cavities is

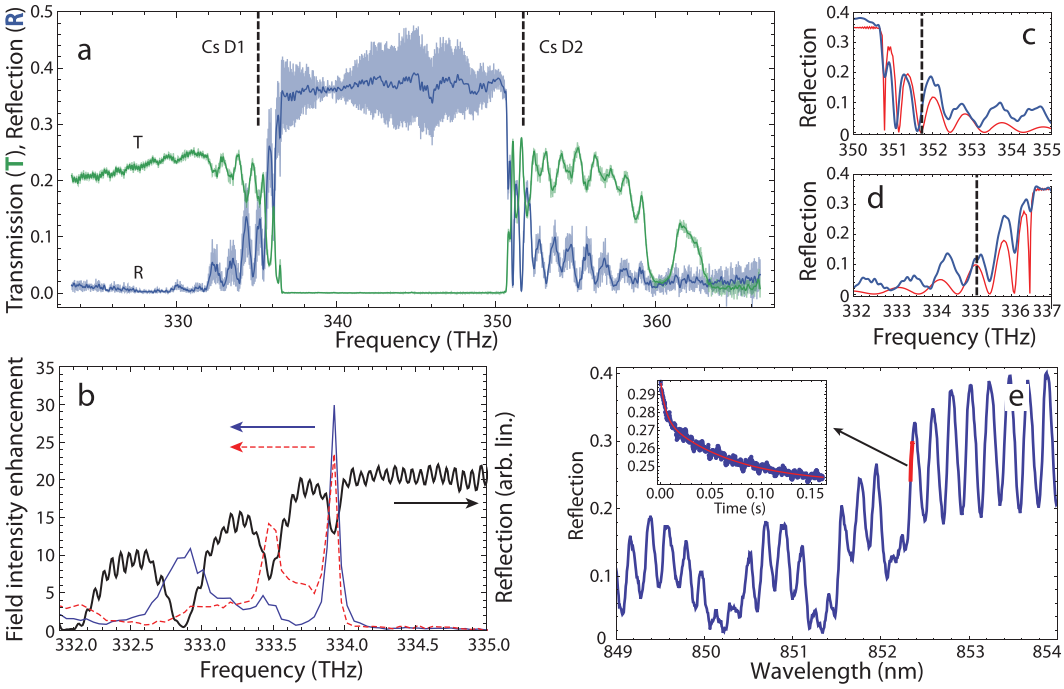

Figure 4.6: (a) Plot of the measured reflection and transmission spectra of the complete device, with the input polarization aligned to excite the TE-like mode. A smoothing filter is applied to the raw (transparent curves) reflection measurement, yielding the solid lines. Within the bandgap, the transmitted optical power is 30dB below the reflected power, consistent with the optical spectrum analyzer noise floor. (b) Intensity of the scattered light imaged from a region near the center (blue) and 1/3 from the end (red) of the photonic crystal section, and (black) reflected optical power as functions of the frequency of an incident probe laser. ((c) and (d)) FDTD simulation (red) and measurements (blue) of the reflection spectra near the air (c) and dielectric (d) band of the device. (e) Thermal tuning of a waveguide reflection spectrum (red line) with respect to the device reflection spectrum (blue) and time domain response of the device reflectivity (inset) to a step function input for which the intra-device power is 60μW. The time-domain response is fit with a double-exponential function with time constants of 70ms and 5ms. Figure adapted from [26].

generally ≤ 10, and peaks at the cavity resonance that is closer to the band edge. The scattered light is imaged with a microscope objective positioned above the waveguide as the frequency of a laser source is scanned across the slow fringes at the band-edge. As shown in Fig. 4.6(b) (red and blue traces), the scattered radiation from the APCW section is modulated as the input frequency is scanned from resonance to antiresonance. The resonances are associated with super-modes along the structure, so they have a smooth position dependence. The blue trace in Fig. 4.6(b) is taken for a scatterer in the center of the crystal, so it is expected to excite the first super-mode, the third, etc., but not the even ones. The red trace, however, refers to a scatterer positioned closer to the end of the device and shows the second super-mode. Based upon the measured enhancement of intensity within the APCW (normalized with respect to illumination several THz from the bandgap where no enhancement should be present) of $\simeq 30$ (i.e., a cavity finesse of $\simeq 10$), at the reflection minimum nearest the bandgap the enhancement on the spontaneous emission into the guided mode can be estimated to be $\Gamma_{1D}/\Gamma_0 \simeq 20$ for a Cs atom in the $6^2P_{3/2}\,|F = 5; m_F = 0\rangle$ excited state.

The optical power handling capabilities of the APCW ultimately limit the trapping schemes. Figure 4.6(e) shows the time and frequency dependent reflection signal of a single mode laser, with frequency tuned close to the band edge of the APCW. In this measurement, a heating laser, with frequency of 335THz, is abruptly switched on at the input fiber port using an acousto-optic modulator for a 200ms interval. The increase in the temperature for a device in ultrahigh vacuum can be estimated by measuring the shift of the fast fringe shown in Fig. 4.6(a). For an input power of 95μW, which corresponds to an intra-device power of approximately 60μW, the wavelength shift of the reflection spectrum is measured to be $\delta\lambda = 40$pm. For a thermo-optic coefficient of SiN of $dn/dT = 2.5 \times 10^{-5}$ [158], and an estimated average energy density overlap $\eta_E \approx 0.85$ of the guided mode within the SiN nanobeams, the wavelength shift in the spectrum corresponds to an average temperature rise of $\delta T = 2°$C. This rise is roughly an order of magnitude smaller than the temperature rise of the APCW devices without thermal rails, which serve as thermal bath at room temperature for the device. The many node tethers described before are able to conduct a limited amount of energy to the rials, effectively cooling down the device. A very clean device and testing setup is essential to obtain this improved result. Just as a reference, for the tapered optical nanofibers we experimented with in our group, more than 200mW in vacuum had been employed without damage, and in the case of the APCW in air several mW can be sent without

deteriorating the device.

Impedance matching in the APCW

The nominal photonic crystal structure described in this chapter is really hard to fabricate indeed. The band edges are required to be really close to the Cs transition frequencies. Depending on the purpose of the experiment, devices whose bands are 1nm or less away from the desired atomic wavelength might be employed. This requires a very precise and accurate photonic device where the properties are as constant as possible over the 150 cells that compose the nominal crystal structure. Challenges are found at almost every fabrication and design step, and many of them are described in the thesis of other members of the group. A problem we tried to track at the initial stages of design was to understand all the features that appear in the optical spectrum.

Near both band edges there are a series of about 5 resonances with a decreasing separation between each other as they approach the band edge, seen in Fig. 4.6(a). It is also true that the spacing depends on the device's total length. These features seem to reflect two things. First, they are associated with a structure that captures the whole device, not like the Bloch mode that has the lattice constant a periodicity. Furthermore, they seem to reflect the fact that the group velocity decreases near the band edge. These features are consequences of the device finite extent and the change on the dispersion relation as the side modulations on the device grow from zero amplitude, the blank double nanobeams, and the nominal design described before.

In a finite array of coupled elements, it is common to consider collective excitations of the system, the so-called normal modes, where the dynamical coupled degree of freedom has a common phase relation. For example, a unidimensional array of masses coupled by springs has a lower frequency mode where the central elements experience a bigger displacement from their equilibrium position than the elements closer to the end of the array. The second mode envelope has instead a node in the system's center, while there are two positions along the array, between the center and both extremes, where the displacement maximizes. Our system exhibits similar characteristics, as many other photonic systems.

Moreover, the photonic crystal represents only about 50μm in a 2mm device. There are several reasons for its small size: fundamentally the unavoidable defects and disorder that can induce localized modes [89, 160]. In the context of the discus-

sion presented here this is relevant because before the photonic crystal the light is propagating in a double beam unpatterned waveguide. The dispersion relation in both waveguides has very different structure. In principle, that means that if the two sections are simply butted together, apart from the discontinuity on the dielectric function, the group velocities, the wavevector, and the mode function will also be different. These issues will create backscattering and losses into non guided modes [89]. A different option is to adiabatically modify the unpatterned waveguides until the modulation grows to the nominal value. This option has the advantage of reducing the difference in the dielectric function cell to cell, and consequently, the dispersion relation changes less abruptly reducing undesired effects. An SEM image of this section in a fabricated device is shown in Fig 4.7(a).

In any case, it is really hard to design and fabricate a perfect adiabatic taper region. Certainly, each taper region will be a reflector, with a strong wavelength dependence, that will contain in the middle a strongly dispersive medium. The full APCW is now partially a cavity, implying that the light-matter interaction picture needs to be further modified by its presence. The first direct consequence of this can be observed in the optical spectrum of the device is the appearance of some cavity resonance on near both band edges, as shown in Fig 4.6(a). As the intercavity medium is dispersive, $\omega(k)$, the free spectral range is proportional to the group velocity v_g and it decreases as the resonances approach the band edge. Besides, the accumulated phase in a single pass increases π between every consecutive resonance. For the resonances close to the dielectric band edge, the wavevector can be written as $k \approx \pi/a - \delta k$, such that the previous condition considering the phase over N units cell gives $\delta k = \pi/Na$. This first collective mode is bright in the central section, while the second mode is dark at the middle while it has two bright spots between the center and the extremes of the crystal.

In order to reduce the effect of the cavity enhancement into the atomic signal, the reflectivity of the mirrors that surround the APCW needs to be as small as practically possible. The idea towards this is shown in Fig 4.7(b). At the nominal photonic crystal for the TE-like modes, both band edge frequencies ν_{diel} and ν_{air} for the dielectric and air bands respectively, sets the range of frequencies that do not propagate through the APCW. To avoid unwanted reflection for the range of frequencies that will propagate through the APCW, the band structure of each unit cell that composes the taper must propagate those same frequencies. For instance, if each unit cell has a TE-bandgap centered at the very same frequency

$\nu_c = (\nu_{diel} + \nu_{air})/2$ and its span increases slowly until reaches its nominal value $\Delta_0 = \nu_{air} - \nu_{diel}$, the frequencies outside the nominal bandgap will always propagate. This will indeed reduce the unwanted reflection, but not totally eliminate them. To center the bandgap, the initial width of the double blank nanobeam is the central parameter to accommodate for. In fact, the width is chosen such that $\omega_{blank}(k = \pi/a) \approx 2\pi\nu_c$.

The taper section length is an important parameter in order to have a smoother transition, so it can also be used for the purposes discussed here. Nonetheless, what seems more relevant in our design is the way the cells change in a given length. In the side modulation design, the band structure does not open a significant gap until the modulation is $\sim 70\%$ of what it is in the nominal APCW. That means that only a few sites along the taper with small modulations ($\leq 0.7A$) are enough to adiabatically open the gap. However, as the modulation approaches to the nominal one, the band edge frequencies quickly approaches their final values. Therefore, if there are more site with dimensions closer to the nominal one, the changes can happen at a slower pace. Keeping in mind that the structure is meant to be short, the taper section usually will not take more than 30-40 sites on each side, with the first ten or so sites quickly increasing the amplitude of the modulation and the rest of the sites, 20 or so, slowly approaching the nominal size. This is the so-called exponential taper.

In order to implement this the amplitude A of the modulation and width w with the adequate length constant are changed at an exponential pace along the device length. Fig 4.7(c)-(d) shows the band structure midgap frequency and its span for different amplitudes and widths, with the values for each unit cell along the taper represented by a red dot. The taper is designed to keep its bandgap central frequency aligned with the nominal APCW bandgap central frequency and its bandgap span always smaller than the APCW bandgap. Device to device fluctuations make it difficult to analyze the different taper designs in detail. At the beginning Su-Peng Yu fabricated several devices with this taper, however, later modifications opted for a linear ramping on the modulation constant A and careful bandgap opening alignment as described. FDTD simulations on the whole device where done to get the reflection and transmission for different taper cases and are shown in Fig 4.7(e)-(f). A noticeable reduction in the size of the resonances is observed for the exponential taper.

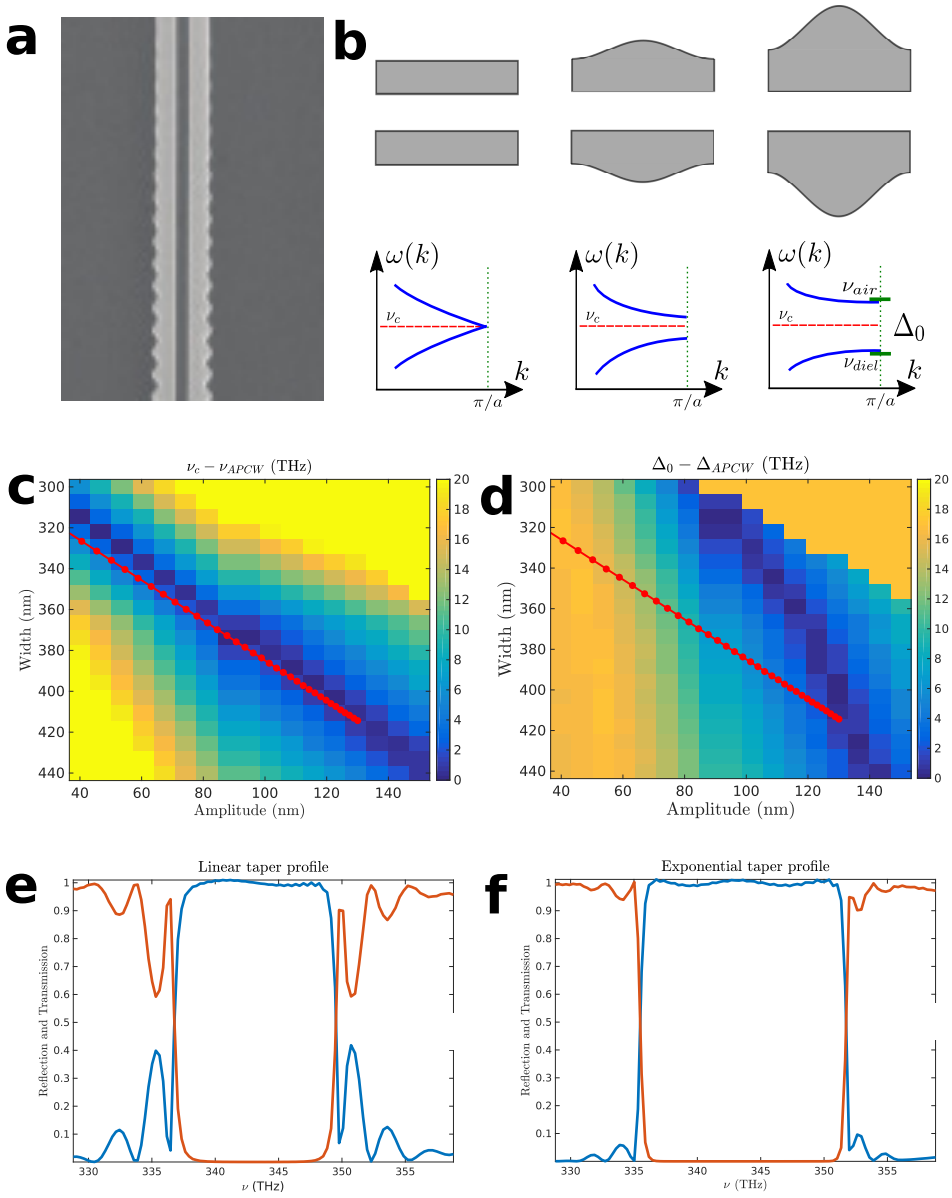

Figure 4.7: Impedance matching in the APCW. (a) SEM image from taper section (b) Transition from unpatterned double beam waveguide to nominal APCW structure. Different unit cells and associated band structure in the B.Z. defined by the lattice constant a are sketched showing the bandgap centered at ν_c. (c) Midgap frequency ν_c, with respect to the ideal midgap ν_{APCW}, for different amplitude A and width w. The red circles represent the values for each unit cell along the designed exponential taper. The red line is just a interpolation. (d) Gap span Δ_0, respect to the desired nominal span Δ_{APCW}, for different amplitude A and width w. Red circles are the values along the designed taper. Reflection (blue) and transmission (red) from FDTD simulation of the (e) linear and (f) exponential taper section (30 unit cells in each extreme) and nominal device (100 sites), as indicated in the red trace in (c) and (d).

APCW modes and symmetries

Given that the APCW design is symmetric with respect to the $y = z = 0$ planes, the modes can be classified according to these symmetries as described in Chapter 2. There are two classes for each plane, even or odd, and can be combined between them. The TE-like mode is y-odd-z-even, following the classification criteria from [80]. The two lower bands for each symmetry is shown in Fig. 4.8. In terms of design and fabrication, the photonic crystal waveguide strategy followed here is more prone towards modifying the properties of the TE-like modes, as it is easier to affect the structure of the waveguide in the $x - y$ plane and harder to modified the structure in the z-direction. However, in the APCW design and others, it is still possible to modify the properties of the TM-like mode (y-even-z-odd). In our experiment, the TM-like mode is important for observing effects that are not affected by the photonic crystal properties of the systems, as the Bloch mode contrast and band structure details are less relevant and resemble a normal non-patterned waveguide.

There are two more modes present in the APCW that do not couple to the single mode waveguides and optical fibers present along the system. Moreover, unavoidable defects along the waveguide can mix different modes. Some details regarding this in the current design can be found in Andrew McClung's thesis and related work in the slot waveguide in Su-Peng Yu's.

Although some more work on the characteristics of the TE-like and TM-like modes will be discussed later, Fig. 4.8 summarizes some of the characteristics of the different symmetries in the APCW. The full band structure for the APCW is shown in Fig 4.8(a), where two bands for each symmetry are shown. Noticeably, the TM-like bandgap is placed at higher frequencies and the y-even-z-even mode has a bandgap that overlaps with the TE-like gap, being probably responsible for causing some of the inter-bandgap features seen in Fig 4.6(a). The spatial structure of these modes is really different for each mode. Fig. 4.8 (c) to (f) shows the intensity of the lower band for each symmetry at $k = \pi/a$ in the $z = 0$ and $x = 0$ planes.

4.3 Coupling in the APCW

In past sections, a detailed analysis of the coupling of the emission to the photonic bath of an infinite photonic crystal waveguide was presented, Sec 2.3. The spontaneous emission rate of the emitter into the waveguide, Γ_{1D} was expressed in terms of a properties of the atom and the waveguide in Eq(2.47). Form the full band

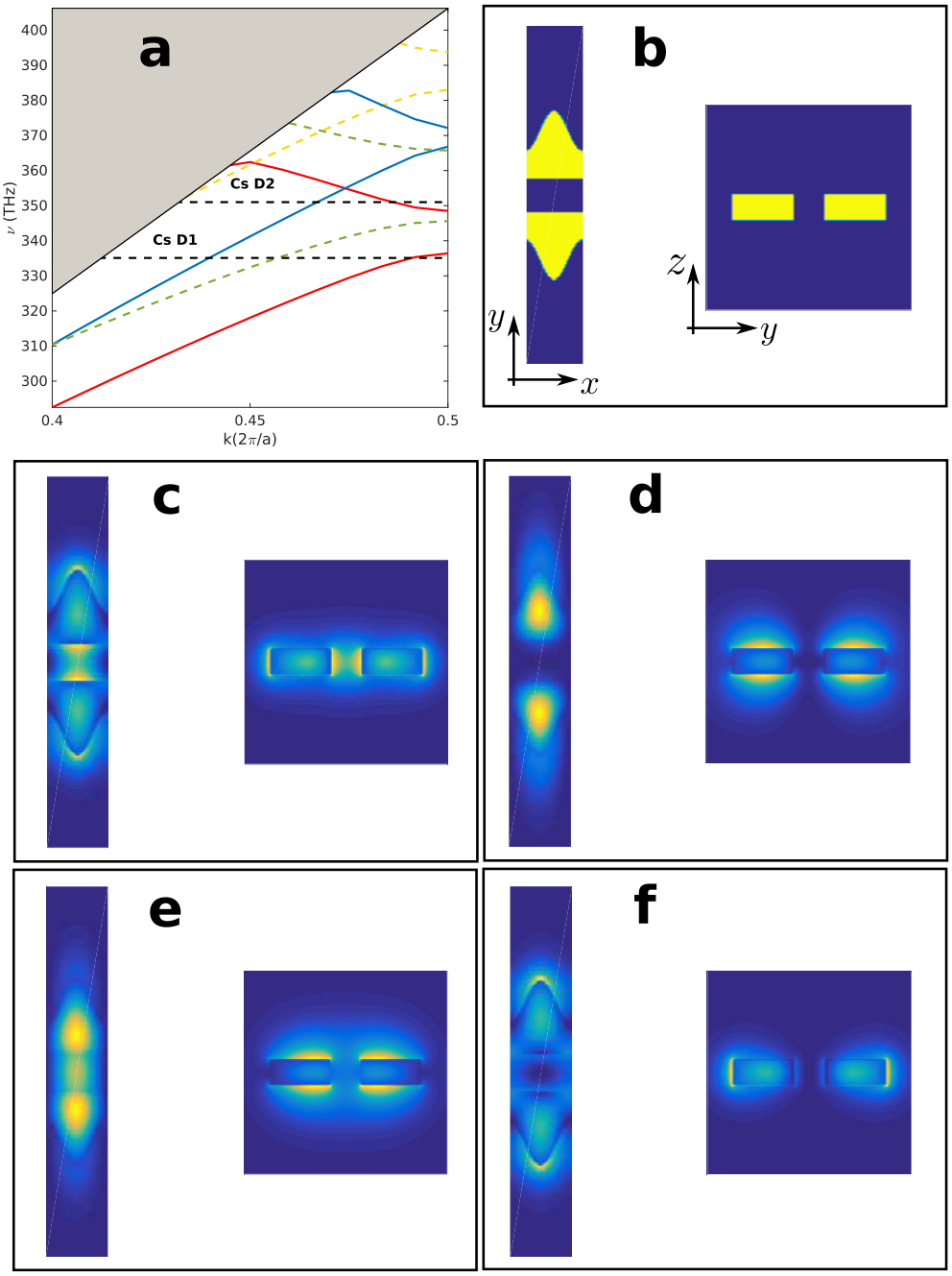

Figure 4.8: (a) Full band structure for the APCW taking into account all the symmetries. The normal TE-like mode is in solid red (y-odd-z-even) and the normal TM-like mode is shown in solid blue (y-even-z-odd). The other hybrid antisymmetric modes are shown in dashed yellow (y-odd-z-odd) and dashed green (y-even-z-even). Two dielectric function plane cuts are shown in (b) for the $z = 0$ plane (left) and $x = 0$ plane (right) where the modulation is larger. Plots for $|\mathbf{E}(\mathbf{r})|^2$ are shown for these planes, in particular for the lower band at $k = \pi/a$ and (c) y-odd-z-even (TE-like), (d) y-odd-z-odd, (e) y-even-z-odd (TM-like), and (f) y-even-z-even.

structure presented above in Fig. 4.8(a), both atomic frequencies are crossed by several bands, enabling couplings to these guided modes. Furthermore, coupling to these modes will depend on the position of the atom in the unit cell, its orientation as a dipole and the local photonic properties at that frequency for example. In order to account for these details, in this section the coupling of some of these modes to the atom will be analyzed.

Optical depth model for uniform density atoms

To begin with, one can imagine that the atoms are not trapped and represent a dilute sample around the device. This case is described in free-space by the Beer's law. The atoms are inhomogeneously coupled to the device mode as the local intensity at different positions is different. An average Γ_{1D} can be assigned according to a uniform density of atoms in the vacuum section along the whole device according to

$$\bar{\Gamma}_{1D}^{N} = \frac{\Gamma_0 n_g N \eta}{2}, \tag{4.1}$$

where Γ_0 is the free space decay rate, n_g the group index, $N = nL\sigma_0$ represents an effective atom number, n is the uniform density, σ_0 the radiative atomic cross section, L is the device length, and η is the fraction of the field that interact with the atoms

$$\eta = \frac{\int_{vacuum} \epsilon(\mathbf{r})|\mathbf{E}(\mathbf{r})|^2 dV}{\int_{cell} \epsilon(\mathbf{r})|\mathbf{E}(\mathbf{r})|^2 dV}. \tag{4.2}$$

In the same way, according to the Beer's law the optical depth, OD, can be written as $OD = \eta N n_g$ and will determine the medium absorption. The two tables below show the values of some of these parameters for the modes that cross the Cs D2- and D1-lines transition, respectively. These are numerical values based on the calculated band structure and the spatial modes, not capturing effects that appear in finite structures, which will be explained in the next section. Moreover, the atom density is not uniform close to the structure because there are strong surface potentials that disturb and deplete the density close to the device ($\leq$ 100nm).

Mode symmetry	Band	$k(2\pi/a)$	η	n_g
y-odd-z-even (TE-like)	Air	0.486	0.55	2.9
y-even-z-odd (TM-like)	Dielectric	0.465	0.27	1.45

Table 4.1: Contribution from each mode that crosses the Cs D2 line.

Mode symmetry	Band	$k(2\pi/a)$	η	n_g
y-odd-z-even (TE-like)	Dielectric	0.495	0.52	6.2
y-even-z-odd (TM-like)	Dielectric	0.442	0.23	1.35
y-even-z-even	Dielectric	0.458	0.54	2.1

Table 4.2: Contribution from each mode that crosses the Cs D1 line.

Γ_{1D} for guided modes: group index and effective mode area

There are two properties of the APCW that determine the coupling strength of the atom to the waveguide. First of all, the group velocity directly relates to the dispersion relation as the slope changes the local density of states. Although it is possible to calculate the band structure from the dimensions inferred from the SEM images, the device's optical spectrum provides the most relevant information to characterize the structure. The resonances described before near the band edges have a regular spacing in the k-space, such that it is possible to map out the local dispersion relation $\omega(k)$ [40]. The second component to determine the device's influence on the coupling is the spatial structure of the mode. The fact that the mode is confined to scales smaller than $\sim \lambda$ means that the local intensities are much higher than for free-space beams, reflected in the small effective volumes or areas for the mode.

Mapping the band structure from the optical spectrum of the device is not straight forward but is a powerful quantitative tool to characterize the device properly. The simplest model involves a cavity with a dispersive medium inside and symmetrical wavelength dependent mirrors, as described in Sec 4.2 and [40]. The dispersive medium, given the quasi-parabolic description of the bands, can be captured by the dispersion relation of the form $\omega(k) = \omega_c \pm \sqrt{\Delta_g^2 + \alpha^2 \Delta k^2}$, where $\Delta k = k - \pi/a$ is the distance of the wavevector to the band edge, Δ_g is half the gap span, $\omega_c = 2\pi\nu_c$ is the midgap frequency and α is a parameter that characterizes the behavior close to the band edge and far from it. Expressing the curvature in a slightly different way, the wavevector can be written as

$$k(\nu) = k_0 \left(1 - \sqrt{\frac{(\nu_c - \nu)^2 - \Delta_g^2}{\nu_{far}^2 - \Delta_g^2}} \right), \tag{4.3}$$

where $k_0 = \pi/a$ and ν_{far} parametrizes the group velocity far from the band edge ($2\pi\nu_{far}/k_0$). The phase acquired in a single pass through the structure is just $\phi(\nu) = N_{cell} a k(\nu)$, where the crystal has a total number of units cells of N_{cell}. The inner material is surrounded by symmetric mirrors with reflectivity R_{tapper},

associated with the imperfect impedance matching section as described in Sec 4.2. The cavity transmission is [119]

$$T(\nu) = \frac{1}{1 + F \sin^2(\phi(\nu))} \tag{4.4}$$

with the cavity finesse $F = 4R_{tapper}/(1 - R_{tapper})^2$. The positions of the cavity resonances are fitted to Eq(4.3). In general, the midgap frequency ν_c is extracted from the distance between the first resonances at each side of the bandgap, while the gap span Δ_g and frequency ν_{far} can be fitted. After that, the cavity transmission can be fitted to the data, using the accumulated phase $\phi(\nu)$ and an empirical polynomial expansion of the cavity finesse F of the form $(F)^{-1/2} = A_1(\delta\nu/\Delta_g) + A_1(\delta\nu/\Delta_g)^2 + A_3(\delta\nu/\Delta_g)^3$ where $\delta\nu = \nu - \nu_{edge}$.

At this point, no loss has been added, but as observed by the resonances' associated linewidth and peak level, Fig 4.6(a), there is loss present in the system. Loss can be added by assigning a small imaginary component to the frequency $\nu \rightarrow \nu(1 + i\kappa)$, going back to Eq(4.3), taking $\phi(\nu) = N_{cell}a\mathrm{Re}\{k(\nu)\}$ and modifying Eq(4.4) to

$$T(\nu) = \frac{1}{1 + L + F \sin^2(\phi(\nu))} \tag{4.5}$$

with $L = (1 - R_{tapper}\mathrm{e}^{-2\zeta})^2/\mathrm{e}^{-2\zeta}(1 - R_{tapper})^2 - 1$ and $\zeta = N_{cell}a\mathrm{Im}\{k(\nu)\}$ parameterizing the single-pass transmission $\mathrm{e}^{-2\zeta}$.

Some of these results are shown in Fig 4.9(a), where the optical spectrum for device 10 in Lil 2 is shown. By using a tunable monochromatic source, it is possible to study in detail the structures near the band edges. For the dielectric band at the first resonance, Fig 4.9(b), the group index is $n_g \approx 6$ and the cavity enhancement is estimated to be $\mathcal{E} \approx 8$, the single pass-transmission is above 90%. For the air band, Fig 4.9(c), the group index is $n_g \approx 10$ and the cavity enhancement is estimated to be $\mathcal{E} \approx 10$, the single pass-transmission is just below 90%. This model is very limited as it does not take into account the fact that the two bands can have different curvatures, the mirrors might not be symmetric, long range disorder can change the band structure of the unit cells at different positions along the APCW. Further methods that combine imaging the hole device as the input wavelength is tuned can provide better information [29]. However, it seems that, by several methods, the group index at the first resonance can be $n_g \simeq 5 - 10$. In [40] a group index $n_g \simeq 11$ and intensity enhancement $\mathcal{E} \simeq 4$ was reported, meaning that the taper has lower reflectivity for that specific device.

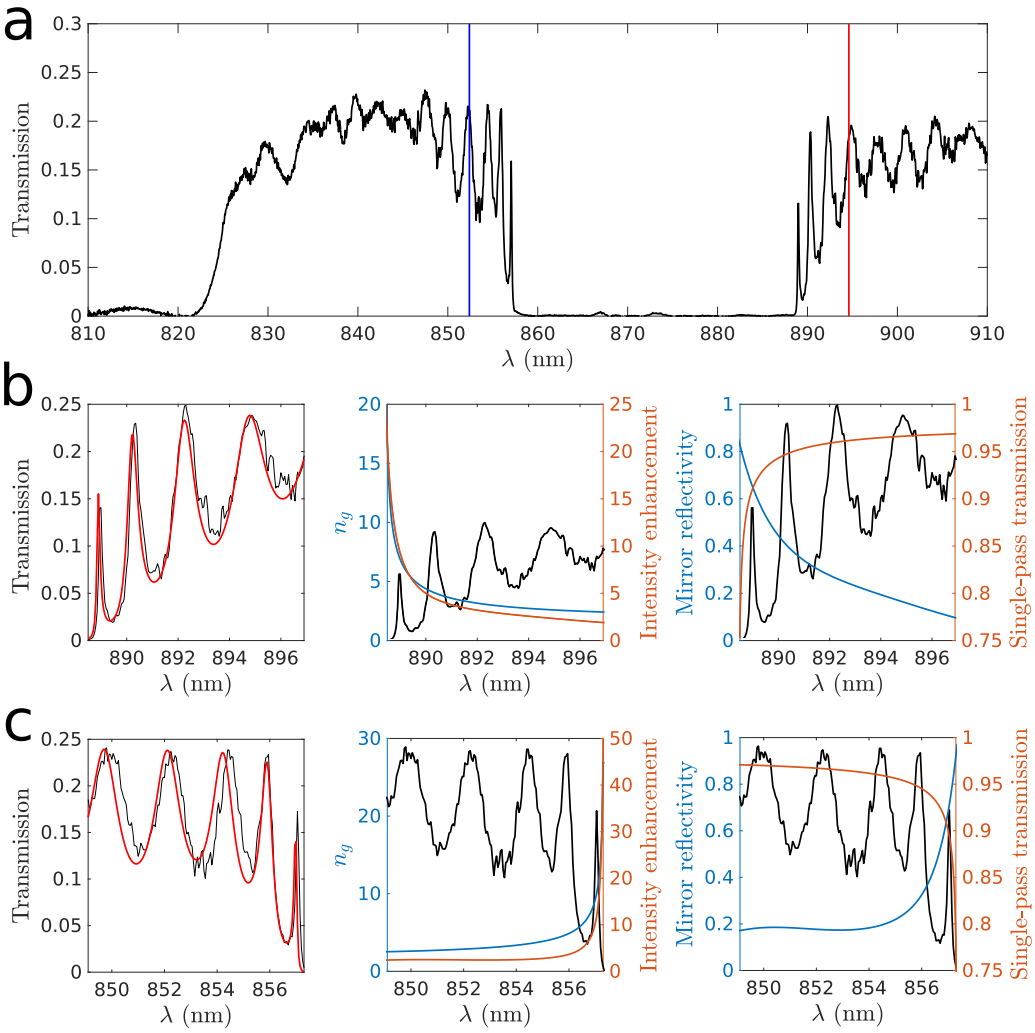

Figure 4.9: APCW optical characterization. (a) Optical spectrum from a device (Lil2, device 10 fabricated and characterized by Andrew McClung - Winter 2016). Fitting in the (b) dielectric and (c) air band: transmission fit (left), group index and intensity enhancement (middle), and mirror reflectivity and single-pass transmission only through the APCW nominal section (right).

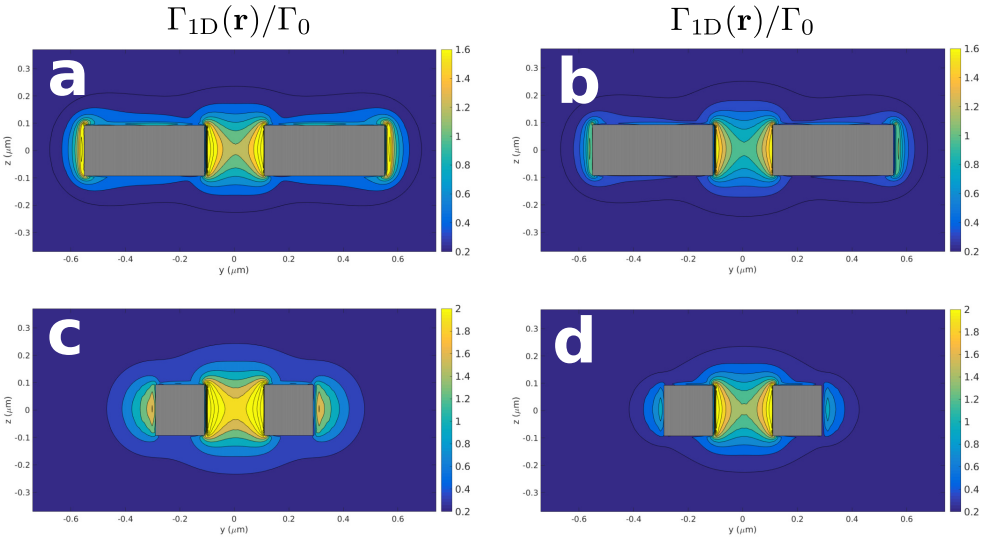

Figure 4.10: Ratio $\Gamma_{1D}(\mathbf{r})/\Gamma_0$ with $n_g = 2$ for (a) TE-like dielectric band at $x = 0$ and $k = \pi/a$, (b) $k = 0.9\pi/a$, (c) the TE-like air band at $x = \pm a/2$ and $k = \pi/a$, (d) $k = 0.9\pi/a$.

On the other hand, the spatial structure of the modes is really important. As seen in Fig 4.3, in a given unit cell the modes go dark and bright, modulating the light-matter coupling $\Gamma_{1D}(\mathbf{r})$. Without taking into account the effect of the group velocity, the effective area $A_{eff}(\mathbf{r})$ determines the coupling to the guided mode. Focusing on the TE-like modes and the trapping schemes described earlier on Sec 4.2, the atom can be trapped at $(x_1, y_1, z_1) = (0, 0, 0)$ or $(x_2, y_2, z_2) = (\pm a/2, 0, 0)$. Fig. 4.10 shows the ratio $\Gamma_{1D}(\mathbf{r})/\Gamma_0$ with $n_g = 2$ as calculated from Eq(2.47) for: (a) the TE-like dielectric band at $x = 0$ and $k = \pi/a$, (b) $k = 0.9\pi/a$, (c) the TE-like air band at $x = \pm a/2$ and $k = \pi/a$, (d) $k = 0.9\pi/a$. The further from the band edge, the lower the contrast inside each unit cell, meaning that the peak $\Gamma_{1D}(\mathbf{r})$ is smaller. In this specific case, the difference between $k = 0.9\pi/a$ and $k = \pi/a$ could be between 20% to 40%.

The evanescent nature of the fields is manifested in strong changes of the coupling in relatively small distances. For example, the coupling is 5.5 times bigger at the center of the nanobeams $y = z = 0$ than above the nanobeams ($y = 0$, $z = 250nm$). The fact that the coupling varies so abruptly is a big complication in current experiments, as it makes it harder to estimate the atom number and its coupling if atoms are not trapped at precisely known positions.

Furthermore, the TM-like mode couples to the optical fibers, so there is a straight-

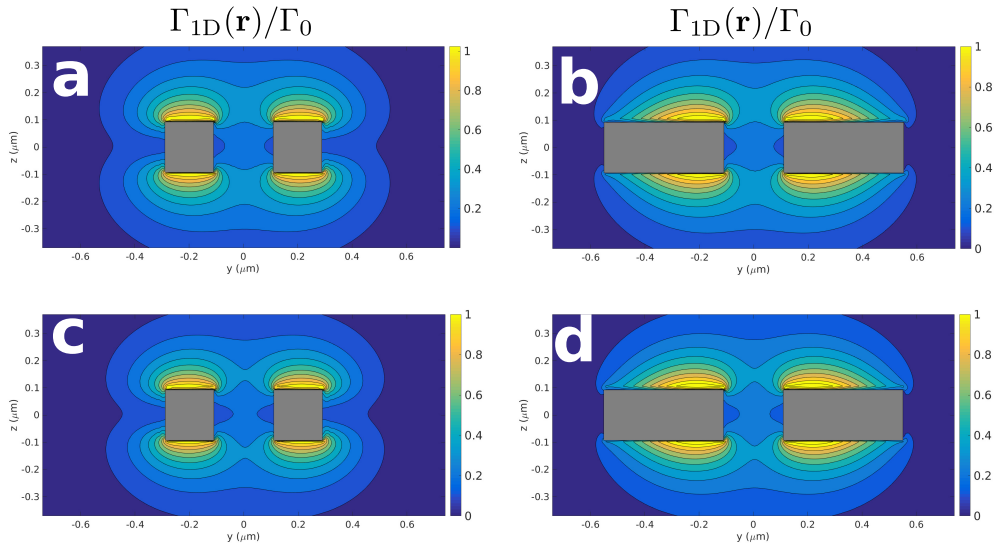

Figure 4.11: Ratio $\Gamma_{1D}(\mathbf{r})/\Gamma_0$ with $n_g = 2$ for the TM-like dielectric band D1 crossing at $k = 0.88\pi/a$ and (a) $x = \pm a/2$, (b) $x = 0$; TM-like dielectric band D2 crossing at $k = 0.93\pi/a$ and (c) $x = \pm a/2$, (d) $x = 0$.

forward readout of the signal from this mode. As the TM-like dielectric band crosses the D1 and D2 frequencies at $k = 0.88\pi/a$ and $k = 0.93\pi/a$ respectively, the photonic crystal resembles more to a waveguide, without a high contrast spatial modulation across the unit cell, meaning a more uniform $\Gamma_{1D}(\mathbf{r})$ along the structure. This is captured in Fig. 4.11, where the ratio Γ_{1D}/Γ_0 is plotted for the D1 and D2 TM-like modes at sections $x = 0$ and $x = a/2$. Clearly, the TM mode has lost contrast as it is really far from its band edge at the D1 and D2 frequencies.

Although is quite direct to characterize the coupling of the emitter to a given guided mode as shown above, the atom will couple to several guided and non-guided modes. As discussed through Chapter 2, all these details are captured in the calculation of the total emission rate $\Gamma_{tot}(\mathbf{r})$. In the following, this point is discussed.

Calculation of $\Gamma_{tot}(\mathbf{r})$ in the APCW using FDTD techniques

To quantify the modification in the radiative coupling due to the presence of the dielectric structure, the spontaneous emission decay rate $\Gamma_{tot}(\mathbf{r}_0)$ is determined for a point dipole located at $\mathbf{r}_0$ for a structure with N_{cells} unit cells. Finite-difference-time-domain (FDTD) calculations are performed to evaluate the classical Green's tensor $\bar{\mathbf{G}}(\mathbf{r}_0, \mathbf{r}_0, \omega)$ and thus $\Gamma_{tot}(\mathbf{r}_0)$ as described in Section 2.4 and [25, 61, 161, 162].

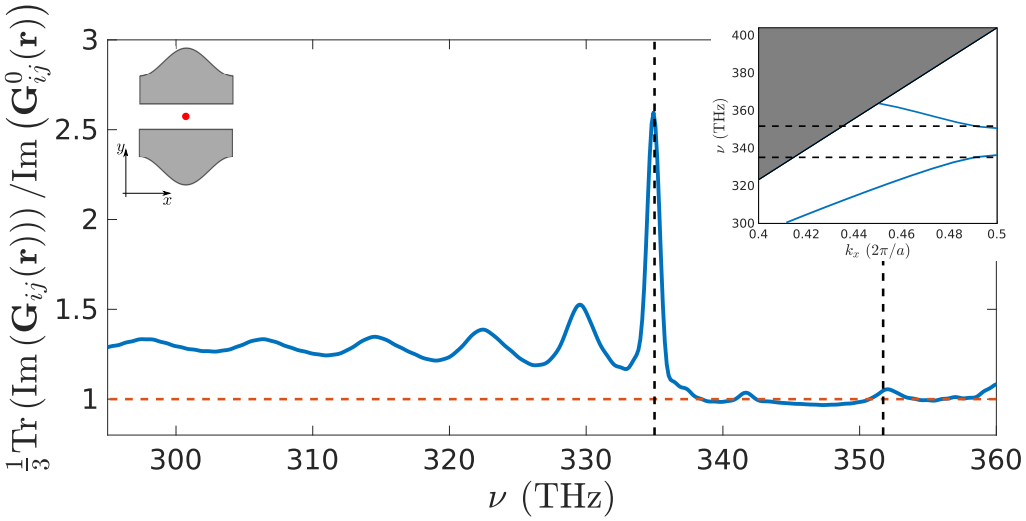

Figure 4.12: Total spontaneous emission rate $\Gamma_{\mathrm{tot}}(\mathbf{r}_0)/\Gamma_0$ calculated using FDTD techniques. The structure has $N_{cells} = 60$ unit cells. The dipole is positioned in center of the unit cell as indicated by the red circle in the left inset. The right inset shows the calculated band structure. The vertical black lines indicate the Cs D1- and D2-line transitions.

In this case, the calculation for a small structure with $N_{cell} = 60$, and additional 3 taper sites at each side, is shown for a dipole positioned at $\mathbf{r}_0 = (0, 0, 0)$, where the cross section is the widest as seen in the left inset in Fig. 4.12. The biggest contribution to the Green's function is the yy component, as the dipole can radiate in the dielectric TE-like mode polarized along the y direction. In Fig. 4.12, the total decay rate is shown for this position. The inset shows the band structure for the TE-like modes, where the two bands are aligned with the Cs D1- and D2-line. Due to the small intensity of the air band modes near that position, the enhancement for frequencies above the Cs D2-line is not significant. Inter-bandgap features are associated with other modes, as seen in the band structure in Fig. 4.8(a).

Near the dielectric band edge, aligned with the Cs D1-line transition, a significant enhancement is observed. The peaks observed near the Cs D1-line transition are associated with the boundary conditions for finite structures, as also seen in the reflection and transmission optical spectrum of the structure. Their position in the k_x-space is determined by $k_x^n \simeq \pi n/N_{cell}a$, with $n = 1, 3, 5, \ldots$ as the dipole is at the center of the APCW, and each resonance is associated with an mode envelope with periodicity $2N_{cell}a/n$ [25].

Chapter 5

TRAPPING A FEW ATOMS USING NEAR-FIELD DIFFRACTION

Trapping neutral atoms in arbitrary systems other than free space is challenging. It took about ten years until atoms were finally observed, trapped, and cooled in high-Q optical cavities for a couple of seconds [77, 163, 164, 165] and trapping neutral atoms very close to dielectric structures was only achieved using an optical nanofiber [23, 68]. In parallel, randomly flying Rydberg atoms in microwave cavities were used to perform exquisite control at the single quanta level [166, 167]. The interest towards creating subwavelength confinement of light with nanophotonic dielectric structures promises to combine the control protocols developed for atoms with subwavelength manipulation and strong light-atom interactions associated with tight light confinement.

Solid state systems, with their own advantages and disadvantages compared to neutral atoms, have shown a great flexibility when integrated in nanophotonic systems [168, 169, 9, 47]. Remarkably, fabrication techniques have evolved to the point that they are compatible with either a priori knowledge of the emitter's position or a posteriori spatial placement of the emitter into the photonic system. For atoms, the challenge of trapping within nanophotonics structures still remains.

On the other hand, trapping atoms in optical lattices has become a major field pushed by its use in precision measurements and quantum simulations, to name just two [170, 171, 172, 13]. Another remarkable technique developed nearly 15 years ago for trapping one or up to a few thousand atoms are the optical tweezers. Recent developments in optical tweezers makes it possible to trap single atoms with high efficiency [173, 109], create spatially complex arrays [110, 111], or observe tunneling induced interactions between two atom in two close traps [108]. Nevertheless, energy scales in the simulation of condensed matter models, for example Hubbard models or spin chains, can be substantially increased and long-range interactions in coherent and dissipative many-body systems can be engineered if atoms are trapped near nanophotonic structures with photon-mediated interactions [28, 31, 33].

Pioneering work in the Lukin-Vuletić collaboration in Cambridge demonstrated the

trapping and coupling of a single Rb atom to a nanoscale optical cavity with mode volume $\sim \lambda^3$ [19]. In this experiment, an optical tweezer trap and transports with exquisite control localize a single atom beside a nanophotonic cavity, where a small volume trap was created by its reflection on the structure. Inspired by this scheme, intuition on how to use the near field diffraction pattern in our structures was gained.

This chapter tries to explain the different trapping techniques I helped develop, discussing some generalities of the near field diffraction pattern in our structure. Then I will focus on one of the traps developed and where around 3 atoms were trapped above the nanostructure. Furthermore, I will describe a different scheme based on delivering atoms towards the structure using an optical lattice. This is the current experimental effort performed by my colleagues and me. Finally, some ideas about the loading of these nanosopic traps will be presented.

5.1 Scattering of light by thin and long dielectric structures

Understanding the consequences of having a dielectric patterned structure in the scattering of light is of paramount importance. Light is used for cooling and trapping atoms and how this is affected by having a nanostucture modifying its spatial pattern can be useful to develop a successful trapping scheme. For example, in the optical nanofiber case the traps are loaded from a polarization gradient cooled cloud, formed by usually 2cm wide beams close detuned to the atomic resonance. The evanescent traps are relatively open, sustaining a solid angle of $\sim 2\pi$ at $\sim$ 200nm from the dielectric surface, so the atoms that are loaded and cooled into these traps experience the near field scattering behavior of the MOT beams around the fiber.

The scattering of light by small structures, compared to the incident wavelength, is hard to interpret. Similarly as before when revisiting the Green's function formalism, the total field is the sum of the incident field and the electric field caused by the structure's induced electric polarization. In general, given the structure or particle orientation and dimensions, the polarizability can have tensorial characteristics. The scattering of light by small particles is a complicated field in optics [174] that has seen great advances since the incorporation of numerical techniques to solve the Maxwell's equations in its full form without approximations. Structures like the APCW resemble a long ($H \gg \lambda$) but narrow ($w \sim \lambda$) dielectric cylinder, that for the sake of simplifying the problem is homogeneous transversally. The easiest and most paradigmatic problem to solve is the scattering of a plane wave incident on such a cylinder. The problem turns to be quite comparable with the Mie problem

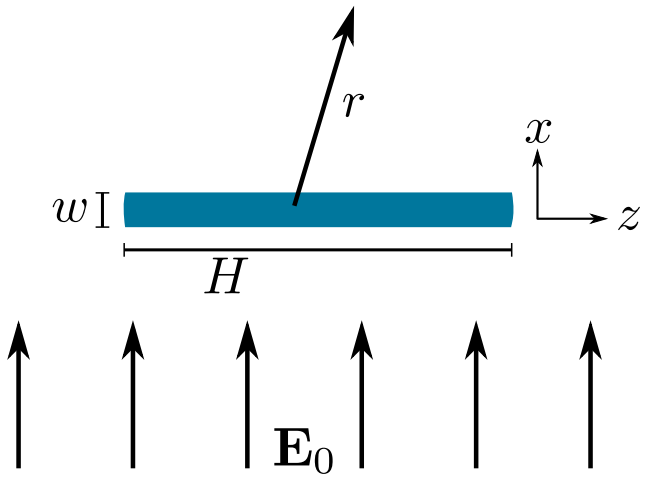

Figure 5.1: Scattering regimes for a long finite cylinder

for the scattering of light by homogeneous small spheres.

To be specific, the cylinder is longitudinally oriented along the z-direction, it has finite length and sees a plane wave incident propagating perpendicular to its axis, let's call that the x-direction, as seen in Fig. 5.1. The easiest solution is found for the forward scattering field and three characteristic regions can be detailed depending on the distance r from the structure:

1. for $r \ll w^2/\lambda$, the wave pattern is complicated, depending on the transversal length scale the field is very different. Wide cylinders have a shadow, and narrow cylinders induce a field in this region.

2. for $w^2/\lambda \ll r \ll H^2/\lambda$, the scattered field has the character of a cylindrical wave because the part of the cylinder that effectively contributes to the field has a length of the order $\sqrt{r\lambda} \ll H$ such that the cylinder is effectively infinite.

3. for $r \gg H^2/\lambda$ the scattered wave has spherical characteristics and its amplitude decays as $1/r$. This is due to its small size once the field is calculated at infinity.

From these observations a few things can be inferred. First of all, far from the device its influence might not be very relevant, as the scattered field quickly decays. Furthermore, relatively close to the device, the scattering can be significant and affect the properties of the local field even at distances comparable to its length H. For instance, if the cylinder is seen as infinite, its radiation pattern might have a field amplitude decaying as $r^{-1/2}$. Unfortunately, not much about the near field can be

known a priori. A few cases are well known in the literature. Relevant to our work, a thin optical nanofiber is able to focus light behind the incidence point [175], being a good candidate for atom trapping [176].

Traps for non-patterned single nanobeams

Before discussing the different trap schemes based on the APCW's scattering, a brief analysis on different trap configurations for non-patterned waveguides will be presented. A single rectangular cross section dielectric nanobeam with refractive index n can operate in the single mode regime, with a TE-like mode and a TM-like mode as seen in Fig. 5.2(a)-(b). As the nanofiber traps where a set of counter-propagating beams with significantly different evanescent decay lengths can create a three-dimensional optical dipole potential minimum for an atom near the fiber's surface [23, 68], confinement can be obtained using the guided modes of a rectangular cross section waveguide. As described before in Chapter 4, optical power limitations in a vacuum environment prevents the use of high optical power to create these guided modes traps. Therefore, to create sufficient deep traps, optical fields close detuned to the atomic transitions need to be used. This worked started as a joint project with Daniel Alton in 2012 [177].

A careful balance between repulsive and attractive potentials can create the desired trap minimum. A factor that always favors a more robust balance is the existence of modes with very different decay lengths D_L outside the dielectric. The decay length for the evanescent field is defined from $|E(r_i)| \propto \exp(-r_i/D_L)$, where r_i is one spatial coordinate, i.e. r_i is y or z. If only access to a given transition is possible, the red and blue detuned beams can excite modes with different polarizations, and hence a different decay length for a given direction. Fig. 5.2(c) shows the electric field decay length for different modes along different directions as the nanobeam changes its width. As shown in Fig. 5.2(c), a significant contrast can be achieved in the z-direction for $w \sim 300$nm between the TE-like and TM-like modes, and hence, a combination of red and blue detuned modes can create a trap as in Fig. 5.2(d). Furthermore, if two atomic transitions can be reached, like the Cs D1- and D2-lines transitions, additional enhancement can be achieved by having a larger difference between the wavelengths, and decay lengths, of the red and blue detuned beams.

Surface potentials are particularly challenging to overcome and calculate [178, 152]. However, simple approximations are valid in different regimes. Energy shifts for both ground and excited states have been carefully studied in some structures, for

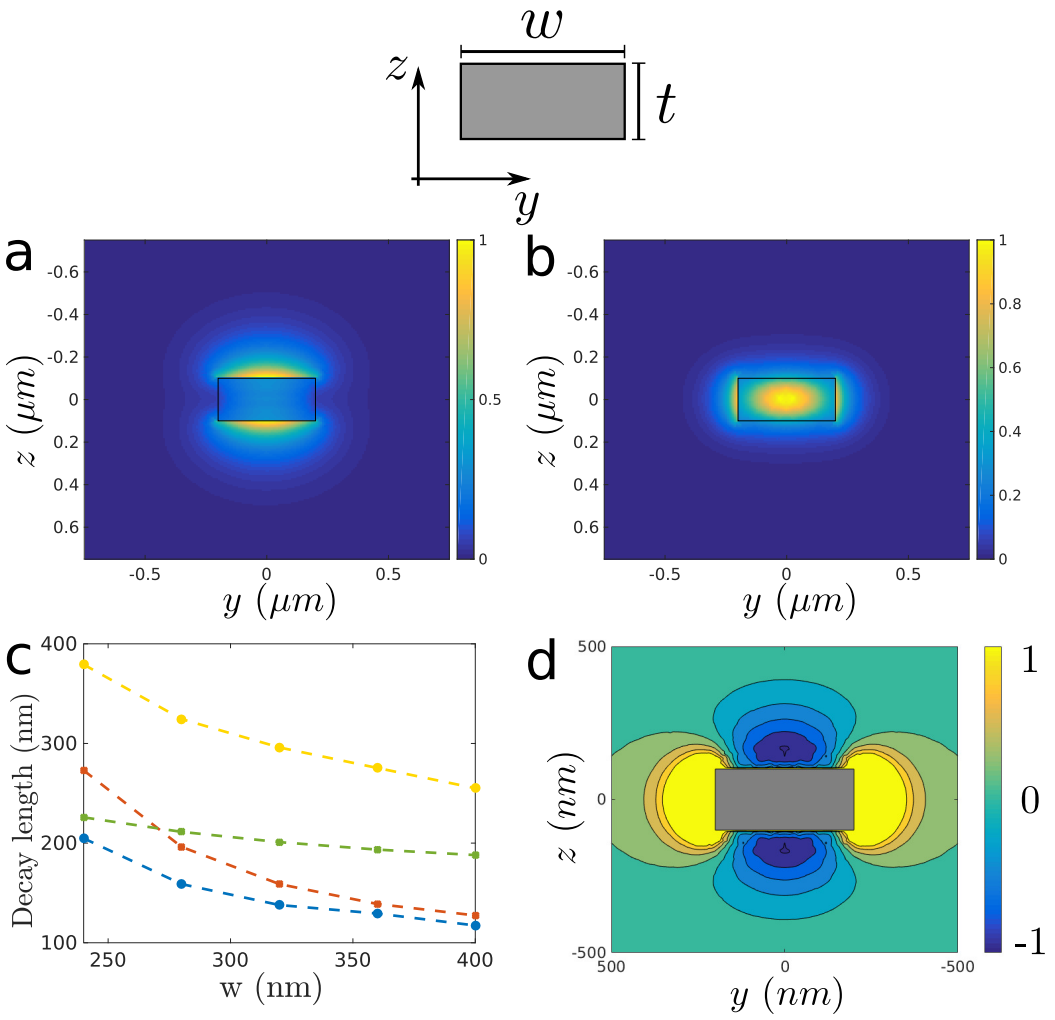

Figure 5.2: (a) TM-like and (b) TE-like mode intensity $|\mathbf{E}(\mathbf{r})|^2$ for a SiN (n=2) rectangular cross waveguide with $w = 400$nm and $t = 200$nm. The structure geometry is shown in the inset above (a) and (b). In (c) the decay length D_L for the evanescent electric field for different modes and directions, as the width of the waveguide w changes but the thickness is constant $t = 200$nm, is shown for: TE-like mode along the y-direction (blue circles), TE-like mode along the z-direction (red square), TM-like mode along the y-direction (yellow circle), and TM-like mode along the z-direction (green squares) (fits considered for fields up to $1\mu m$ from surface). (d) Optical dipole potential created by balancing blue repulsive potential in the TE-like mode and red attractive potential in the TM-like mode. Traps are created $\sim$ 100nm from the top and bottom surfaces. No surface forces were considered and the modes have the same optical frequency. Blue colors indicate lower potential values and yellow higher potential values

example microtoroids gallery cavities [179], and can be described for the ground state $6S_{1/2}$ by the van der Waals potential $U_g = -C_3/r^3$ with $C_3 = h1.99\text{kHz}\times\mu m^3$ if the atom is close to an infinite SiN half space. Because the retarded surface forces (r^{-4} scaling) decrease faster away from the surface than the van der Waals forces, using U_g overestimates the surface interaction at the trap location. In order to overcome the surface attraction, strong optical repulsive potentials keeps the trapped atoms far from it. Comparing with numerical calculations performed by Chen-Lung Hung while he was a postdoctoral scholar in our group, the dielectric half space results is relatively good at distances $d \sim 120\text{nm}$ after scaling the C_3 coefficient by $\sim 1/3$. Therefore, in the trap shown in Fig. 5.2(d), it is possible to overcome surface forces by employing sufficiently deep and balance optical potentials [177].

The scattering properties of a long single nanobeam can be used to trap atoms too. To be specific, if a plane wave propagates along the z-direction and impacts a nanobeam with an constant rectangular cross-section waveguide along the x-direction as shown in Fig. 5.2(a), part of the field will reflect, interfering with the incoming wave and producing a short range standing wave near the device. Remarkably, the first intensity maximum of this interference pattern can have big contrast, providing a single isolated intensity maximum suitable for a red detuned optical dipole trap. The scattering pattern depends on the incident polarization: if the plane wave is polarized along the length of the nanobeam it will excite a bigger component of the dipole polarizability, while if the polarization is perpendicular to its length it will not reflect as much. Other ideas were studied beforewhere auxiliary structures will create additional reflection in order to place the intensity maximum closer [177].

Below, Fig. 5.3 shows the intensity patterns $|\mathbf{E}(\mathbf{r})|^2$ for different beams dimensions and incident polarization. The influence of the thickness is quite notorious, as drastic changes on how close the intensity maximum is to the surface can be observed for small increases. In the APCW the thickness is given by the SiN substrate, and is therefore hard to modify. Recently, alumina deposition has been used,, increasing the device's thickness, and in the past, CF_4 etchings were performed to reduce the device's thickness. More details on the scattering properties for different polarizations will be discussed later.

In order to develop some intuition regarding the position of the standing wave intensity maxima, a simple model can be consider as done by Thompson et al. [19]. The distance from the closest lattice site to the nanostructure surface depends on

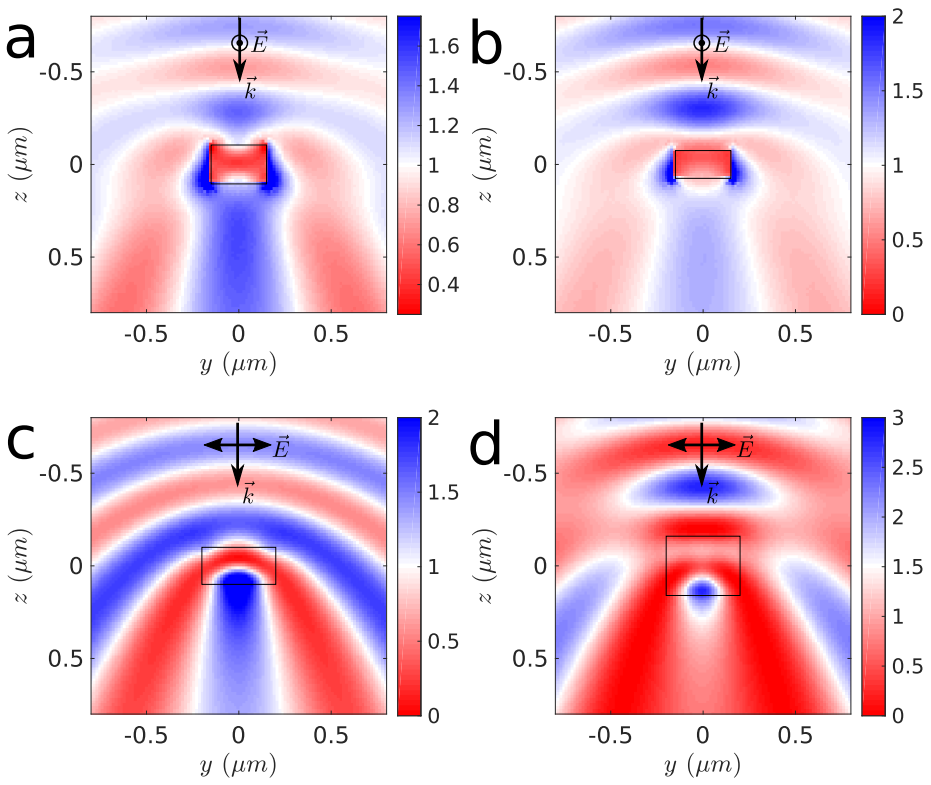

Figure 5.3: Scattering in the single nanobeam case for incident field with **k** along the z-direction. The input polarization could be along the x-direction (a) and (b), or perpendicular to the device along the y-direction (c) and (d). Different thicknesses are considered and the intensity $|\mathbf{E}(\mathbf{r})|$ is plotted: (a) $(w, t) = (300, 210)$nm, (b) $(w, t) = (300, 150)$nm, (c) $(w, t) = (400, 200)$nm,, and (d) $(w, t) = (400, 320)$nm. In all cases the input beam has the same amplitude and is focused to $w_0 = 15\mu$m at the device position.

the phase of the scattered light. This phase depends strongly on the dimensions and dielectric properties of the nanostructure, and can be changed by fabricating different structures in principle. For a plane wave with normal incidence on a single dielectric-vacuum interface at $z = 0$, the Fresnel relations [51] give an amplitude reflection coefficient $r = (1 - n)/(1 + n)$ such that on the vacuum side the intensity maximum happens at $z = \lambda/4$. If there is a second interface, replacing the dielectric half-plane by a dielectric slab of thickness L, the reflection coefficient is

$$r = \frac{(1 - n^2)\sin(nkL)}{i2n\cos(nkL) + (1 + n^2)\sin(nkL)}, \tag{5.1}$$

such that the trap position and depth now depends on the thickness L and are coupled in a nontrivial way as shown in Fig. 5.4. The trap can be closer to the surface, and hence a bigger light-matter coupling is achieved, at the expense of reducing

the trap depth. For the wavelength used in our experiments, the inferred position is at $z_0 \approx 200$nm. Fig. 5.4 compares the results of fully vectorial three-dimensional FDTD simulations for different polarizations and the predictions from the above equation. Remarkably, the model and the actual simulations are in reasonable agreement for thicknesses $L < 400$nm in their prediction of the intensity maximum created by the device reflection.

There are differences between the two polarizations, but in general they behave in a similar fashion as the slab case. The perpendicular polarization (purple trace) trap's position (Fig. 5.4(a)) follows the shape of the slab. It oscillates around $\lambda/4$ with excursion of amplitude $\lambda/4$ and periodicity of about $\lambda/2n$. The excursion for the parallel case (red trace) is significantly smaller. There periodicity seems to grow as the device thickness changes. The trap depth (Fig. 5.4(b)) shows similar characteristics, for example oscillations with more or less similar contrast and with an increasing period.

In terms of the angular spectrum of the scattered field, analytical analysis can be done assuming cylindrical symmetry [174]. The scattered field can be decomposed in terms of partial waves with azimuthal dependence $e^{im\phi}$, with ϕ the usual angle in the cylindrical coordinate system. For small cylinders, $w < \lambda$ as before[1], only the first partial wave $m = 0$ is reflected, producing a cylindrical symmetric scattered field. Moreover, the mapping from a free space tweezer (no reflection) to a reflection trap as discussed here and in Thompson et al. [19] work is possible because only the $m = 0$ partial wave is excited, otherwise, more complicated variations on the transverse nature of the scattered field make difficult the loading. Furthermore, that could be the fundamental reason for the existence of an intensity maximum in the case of the APCW or a non-patterned double nanobeam, as will be discussed later.

Another difference between the scattering for the two incident polarizations is the fact that the induced polarizability has tensorial characteristics when the polarization is along the y-direction. That is because the scattered field contains components in the z-direction too. As seen in Fig. 5.5 these scattered components can acquire an additional phase, creating a complicated elliptical polarization pattern near the device. This induced ellipticity creates m_F dependent/Zeeman-like shifts in the atoms, so-called vector shifts.

[1] It is challenging to realize this in the current setup, where $w \ll \lambda$.

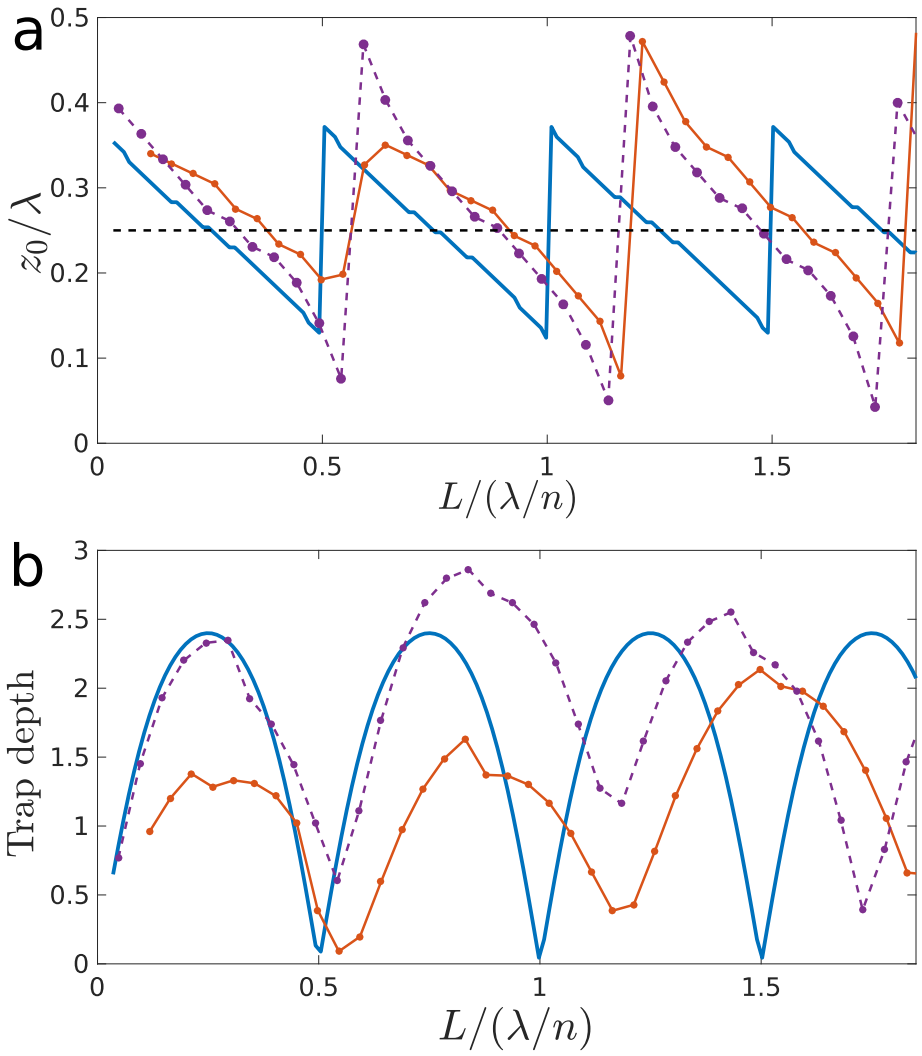

Figure 5.4: Scattering characteristics of the slab model and the numerical simulations. (a) Distance along the z-direction from the trap minimum to the surface according to the dielectric slab model described by Eq(5.1) (blue) or from numerical simulation for a Gaussian beam focus to $w_0 = 15\mu m$ polarized along the waveguide longitudinal axis x (red) or transversal direction y (purple). (b) Trap depth for the closest trap site, taken as the contrast between the intensity maximum and its closest intensity minimum. The input field is the same in every case: the slab and waveguides has refractive index $n = 2$, and the infinity long waveguides have width $w = 350$nm and changing thickness L. The incident vacuum wavelength is 852nm.

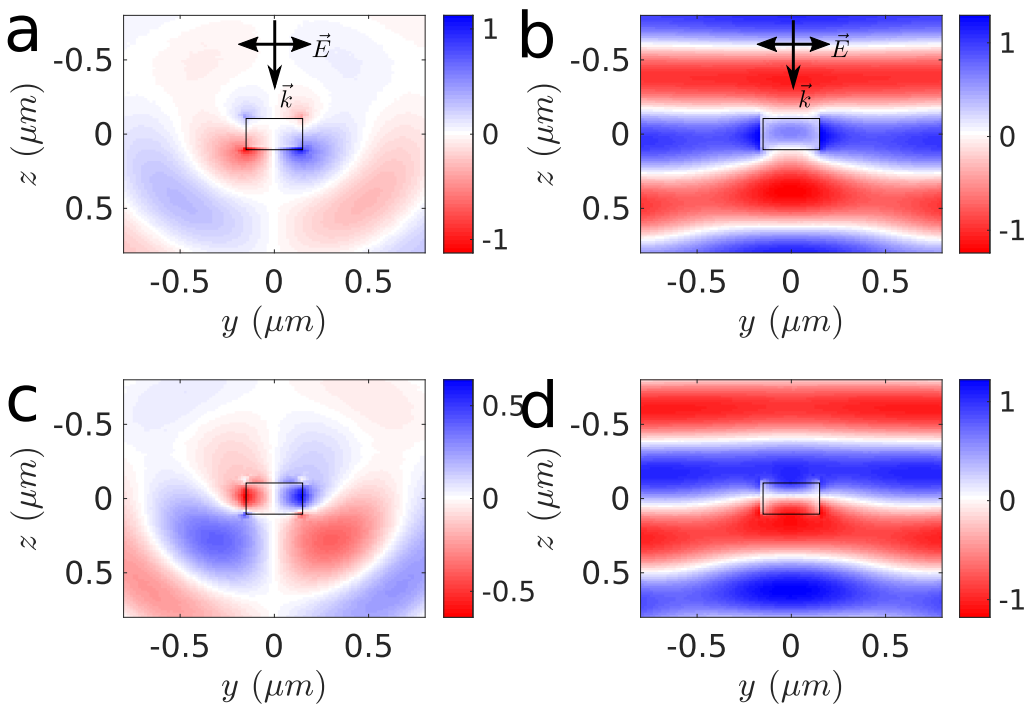

Figure 5.5: Real and imaginary components of scattered field for an input Gaussian beam polarized along the y-direction and propagating along then z-direction for a single SiN nanobeam with width w and thickness t $(w, t) = (300, 210)$nm. The field components are (a) Re(E_z), (b) Re(E_y), (c) Im(E_z), and (d) Im(E_y). In all cases the input beam has the same amplitude and is focused to $w_0 = 15\mu m$ and for the same phase.

Traps for non-patterned double nanobeams

The scattering pattern for a double blank nanobeam depends also on the separation between them. The relevant dimensions are described in Fig. 5.6(a). The scattered fields of each single beam interfere again to create an intensity maximum just above the gap between two structures as shown in Fig. 5.6(a). If the distance between the two nanobeams is much larger than the free-space wavelength λ, that effect will not be present. As further discussion will be presented for the APCW structure, some details will be skipped. However, in Fig. 5.6(c)-(d) the trap depth and position of that maximum is plotted against the separation g between the beams.

A scheme that will be described here is based on the illumination of two incoherent beams incident from the y-direction. The reflections in the different interfaces create, in the near field of the waveguide, a strong intensity maximum if the scattering from each beam is considered independently, hence the incoherent assumption. For our

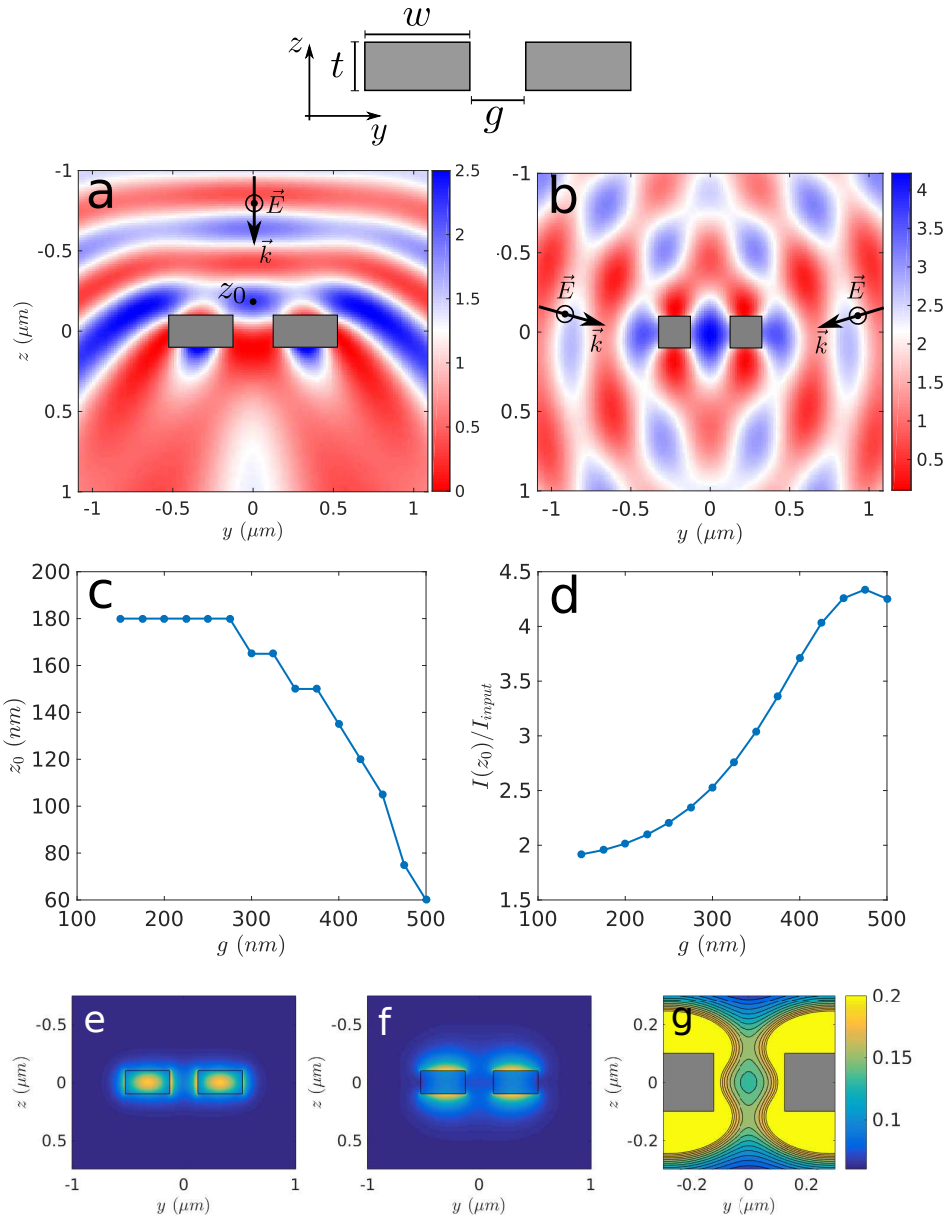

Figure 5.6: Scattering in the double nanobeam waveguide for fields polarized along the x-direction. The top inset shows the relevant dimensions and dielectric structure. (a) Intensity pattern for a Gaussian field ($w_0 = 15\mu m$) propagating along the z-direction. The nanobeam has $(w, t) = (400, 200)$nm and the field is polarized along x. The position of the standing wave maximum on top of the beams, z_0, is indicated. (b) Incoherent intensity sum for two beams propagating with a 10° angle with the y direction. The input field configuration is shown. (c) Position z_0 of the trap minimum and (d) intensity $I_0(z_0)$ for the intensity maximum closer to the surface along $y = 0$ as in (a) for different nanobeams distances g and same dimensions as in (a). (e) TE-like mode, (f) TM-like mode,, and (g) optical dipole potential for a combination of both.

chip architecture, this situation is extremely complicated. However, small angles ($< 15°$) are tolerated for the incidence of the two beams. The main problem in this case, as seen in Fig. 5.6(b), is the appearance of multiple intensity maximums. In principle, atoms can be loaded in each site, but the interaction strength with the guided modes decays exponentially with the distance.

Another similar scheme is based on the use of guided modes, as seen in the case of the single nanobeam. Using a combination of TE-like, Fig. 5.6(e), and TM-like, Fig. 5.6(f), guided modes with positive and negative detuning with respect to the atomic transition, it is possible to create a tight trap in the center of the system with the usual repulsive-attractive combination. Fig. 5.6(g) shows one of these combinations and the resultant trap potential in between the nanobeams.

Hybrid traps in the non-patterned double nanobeam system

For a double nanobeam system with dimensions similar to the APCW, the guided modes offer the possibility to create a high intensity region in between the beams because the single beam modes hybridize and occupy the region in between them. For the TE-like mode, a saddle point with non-zero intensity exists at the center of the nanobeam system. If used as an optical dipole trap, confinement will be provided along one direction while the other will provide a rolling potential creating an escape channel from that region. A similar situation arises in quadrupole ions traps [180]. However, the solution ion trappers found is to change the electric field configuration (electrodes polarity) in time in order to create an average confining force in all three directions. To do so, the confining and anti-confining directions are switched at a rate faster than it takes the particle to escape the trap, such that on average the ion sees a restoring force along each direction. The traps are also called "radio frequency" traps because the switching rate is often in the radio frequency range.

In particular, as far as we know, there is not a similar scheme for neutral atoms using optical dipole traps with fields in the optical regime. It has been demonstrated that, for example, the fast motion of a blue detuned beam moving in circles around some point P creates effectively a circular wall around P, providing confinement [181]. Furthermore, time-varying inhomogeneous electric fields with micron sized electrodes can be applied to trap spinless neutral atoms like ^{88}Sr [182]. We propose that a fast and continuous switching between blue and red detuned fields of the same guided mode, i.e. TE-like, can provide confinement in alternate directions as

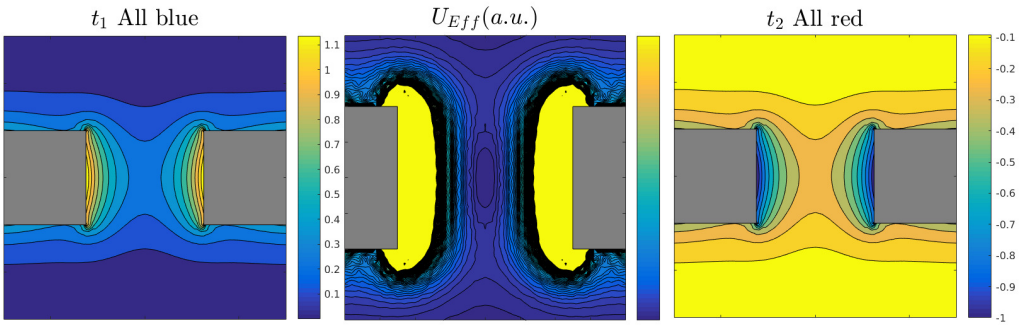

Figure 5.7: Field switching trap. The potential for two different time instances are shown. The blue potential is slightly bigger than the red one. The effective potential is also shown. A very tight minimum appears in the center, as a consequence of the saddle point structure of the intensity profile.

in the quadrupolar ion trap. The switching frequency and strength of the potential are usually bounded in order to provide stable trapping and they are related to the stability regions of the Mathieu equation that describes the motion of the atoms in the oscillating potential.

To be specific, lets consider the motion of an atom in the transversal plane $y-z$ as the system is totally invariant along the waveguide axis x and its motion along that direction is straightforward. The blue and red harmonic potentials for the mentioned mode are $U_B = m(\Omega_{By}^2 y^2 - \Omega_{Bz}^2 z^2)/2$ and $U_R = m(-\Omega_{Ry}^2 y^2 + \Omega_{Rz}^2 z^2)/2$ respectively, such that the time varying potential is $U(y,z,t) = U_B(y,t)\cos^2(\Omega_{RF}t) + U_R(y,t)\sin^2(\Omega_{RF}t)$ where Ω_{RF} is the RF switching frequency. The time varying part of this potential can be written as $U_{RF}(y,z,t) = 1/2(U_B(y,z) - U_R(y,z))\cos(2\Omega_{RF}t)$ and gives rise to a pseudo-potential $U_{eff} = \frac{1}{4m(2\Omega_{RF})^2}|\nabla U_{RF}|^2$ that describes the so called secular motion, while the micro-motion is assumed to be just a small perturbation. In the last expression, the gradient is taken on the time independent part of the potential. Fig. 5.7 shows different instances in time of the switching potential and the effective potential $U_{eff}(y,z)$.

Small waists beams

A subject that will be probably studied in the new JILA-Caltech collaboration will be the possibility to incorporate optical tweezers into the APCW and future designs. In addition to the threats posed by confining an atom in very small volume like an optical tweezer trap does, significant challenges can be encountered by loading one of these side illumination traps if created by an optical tweezer reflecting from a

nanostructure. Pioneering work by Thompson et al. [19] demonstrated that starting from a single atom trapped in a tightly focus optical tweezer, adiabatic loading to the closest trap site in a similar nanostructure can be performed. The ideas are similar to the ones presented above, except that further requirements due to the fact that the beam is so tightly focus ($w \sim \lambda$) need to be taken into account.

For instance, the diffraction patter changes considerably, as can be seen in the fully 3D vectorial FDTD simulation [183] for an actual APCW structure presented in Fig. 5.8(a)-(b) for waist radius $w = 1\mu m$ and $w = 0.5\mu m$ beams polarized along the APCW axis, where the waist is defined as half the FHWM for the central field intenisty lobe. Again, this simulation is not performed under the paraxial approximation. Partial wave arguments can be made to analyze the properties of the scattered light in similar situations, and is currently interesting for a big community studying trapping very small spheres with optical tweezers close to different structures [184, 174], but as far as we are aware, there is not any systematic study in the literature to refer to.

Another characteristic property of tightly focus beams is the appearance of longitudinal components in the electric field. Naively, in a charge free space $\nabla \cdot \mathbf{E} = 0$ meaning that the spatial components should relate like $|\mathbf{E}_T|/w = |\mathbf{E}_L|/\lambda$, where the subindex T and L indicate transversal and longitudinal components respectively. When used to create a trap, these components can cause Zeeman-like shifts, inhomogeneous broadening, and significant heating. As an example, the strength of each of the components for a beam focused to $w = 1\mu$m and $w = 0.5\mu$m and impacting on the APCW wider section is shown in Fig. 5.8(c)-(d).

Precision in the relative positioning between the beam and the structure now becomes very relevant, as the scattering is highly dependent on where the device is located relative to the nanostructure since the reflected light will leave the structure forming a bigger angle with the incoming beam. Fig. 5.8(e) and (f) captures the cases for incident angles 20° and 40° in the APCW for $w = 1\mu$m radius beam. In these plots, the incident beam is still focused on the APCW center $y = z = 0$, but small deviations become relevant if they are on the scale of the beam's waist. Moreover, it can be seen that adiabatic transport for an atom trapped in a tweezer that rotates around the structure's axis can be complicated as the field pattern acquires several angular components, creating wavelength scale distortions.

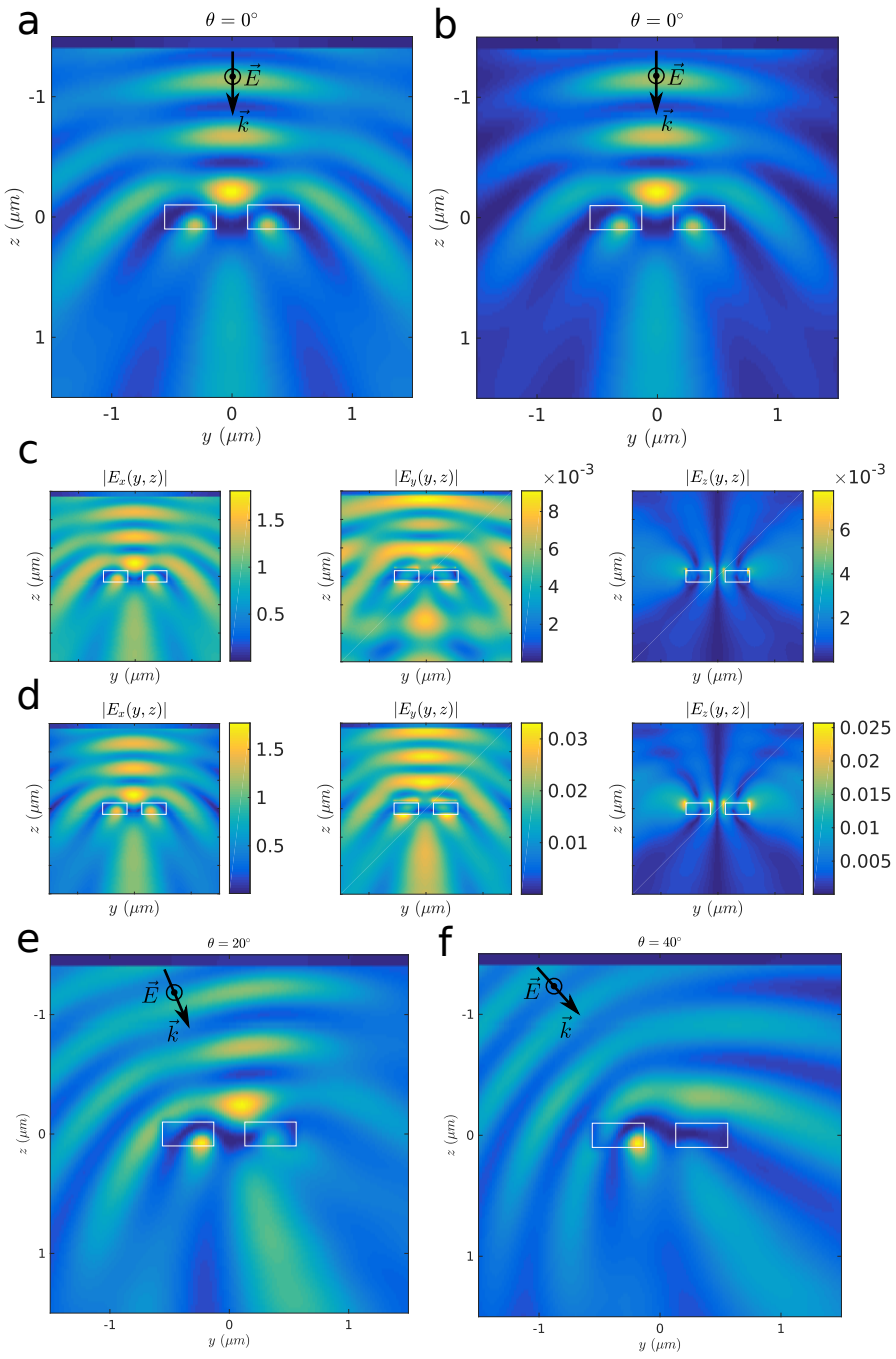

Figure 5.8: Scattering in the APCW structure (FDTD simulation) for very small waist beams. Fully 3D vectorial numerical model showing the intensity pattern $|\mathbf{E}(y,z)|^2$ at the widest part of the APCW for a waist radius $w = 1\mu$m and $w = 0.5\mu$m in (a) and (b) respectively and normal incidence. As the beam is so tightly confined, the paraxial approximation is no longer valid and different components appear in the total field as seen in (c) for $w = 1\mu$m and (d) for $w = 0.5\mu$m. For different incident angles, (e) $\theta = 20°$ and (f) $\theta = 40°$,, the intensity profile $|\mathbf{E}(y,z)|^2$ is shown for $w = 1\mu$m.

5.2 Creating atomic traps with external illumination in the APCW

As pointed out in the previously, Section 5.1, external illumination can create strong traps near dielectric structures. Naturally, due to the small size of these traps they are hard to fill. Therefore, in order to maximize the filling efficiency, a very specific and truthful knowledge of the nanophotonic device and light scattering properties is required. Despite this, they might offer some advantages over the guided mode traps presented in Chapter 4. For example, they are relatively open as they are usually above the devices and not in the small space between the beams, as seen in Fig. 5.3 and Fig. 5.6. Surface forces might be less, although somewhat, important than in the guided mode traps as surfaces are further away from the trap position. Furthermore, they might depend mostly on parameters that are easier to control in the laboratory as the design of the free space optical delivery of light to the structure. But those are supposition, and it takes a lot of effort and time to verify each of them. Fortunately, at some point in 2014 Aki Goban and Chen-Lung Hung figure out how to load a few atoms into these traps created with external illumination after they were proposed and studied by Chen-Lung and me [40]. In this section, details on the trap design, characterization, and experimental results will be discussed.

Scattering properties of the APCW for parallel incident polarization

Motivated by the scattering properties of the double non-patterned nanobeam structure, the same effect on the APCW device was investigated. In the experiment reported in [40] and [29], the atoms can be trapped in the tight optical potential created by the interference pattern of a side-illumination beam and its reflection from the surface of the APCW. The polarization of the external beam is aligned parallel to the x-direction of the 1D waveguide to maximize the reflected field. With a red-detuned external beam, cold atoms can be localized at any of the intensity maxima around the structure. However, because of the exponential falloff of the guided mode intensity, only those atoms sufficiently close to the APCW can interact strongly with guided photons of the input field.

The trap site with the strongest atom-photon coupling is located at $(y_1, z_1) = (0, 220)$nm, closest to the center of the unit cell and $\Delta z \sim 120$nm from the plane of the upper surfaces of the APCW, as seen in Fig. 5.9(d)-(e). Other locations are calculated to have coupling to the fundamental TE-like mode less than 1% of that for site z_1 (e.g., the sites at z_{-1} on the other side across the device and the second maximum z_2 have probe intensity ratios $I(z_{-1})/I(z_1) = 0.01, I(z_2)/I(z_1) = 0.005$).

Along the x axis of the APCW, the dipole trap $U(x, 0, z_1)$ is insensitive to the dielectric corrugation within a unit cell and is nearly uniform to within $< 2\%$ around the central region of the APCW as seen in the detailed numerical simulation plot in Fig. 5.9(c), so atoms are usually not confined along the x-direction for the temperatures achieved in the experiments to date. By contrast, atom emission into the fundamental TE-like mode is strongly modulated with $\Gamma_{1D}(x, 0, z_1) \simeq \Gamma_{1D} \cos^2(kx)$ due to the Bloch mode function near the band edge of the APCW ($k = \pi/a$). Thus, even for atoms uniformly distributed along the x axis of the trapping potential, only those close to the center of a unit cell, i.e. $kx = p\pi$ for $p = 0, 1, 2, ...$, where the probe is stronger, can strongly couple to the guided mode, greatly facilitating phase-matched symmetric excitation of the atoms. In the experiment, the external beam has power $P = 60$mW and waist $w_{trap} = 25\mu$m (radius),, providing weak confinement along the x axis, with atoms localized near the central region ($\Delta x' \pm 10\mu$m) of the APCW for the estimated temperature $\sim 30 - 50\mu$K from a time-of-flight measurement in free space of the atomic cloud trapped in the several pancakes forming above the structure. The external beam for dipole trapping is 220GHz red-detuned with respect to the D2 line and has a total power of 50mW for all measurements reported.

In order to calculate the trap potential for the reflection trap formed by the 50μm diameter beam, a 3D FDTD calculation needs to be performed. Details of this kind of simulation are shown in Fig. 5.9 for a long APCW structure and a Gaussian beam with waist $w = 20\mu$m. Given the size of the Gaussian beam, the simulation volume is usually really big. The trap is weakened along the directions closer to the nanobeams because of Casimir-Polder forces, creating a lower barrier around the optical potential minimum. Fast atoms can leave the trap through these directions, most probably crashing into the SiN surfaces. As seen in the case of the non-patterned double nanobeam (Fig. 5.6) the position of the intensity maximum can be really sensitive to the gap between the beams. Mechanical deformation of the long $\sim 60\mu$m suspended double nanobeam probably modulates the gap by $\sim 10 - 20$nm, as is described in Andrew McClung and Su-Peng Yu's theses, creating an additional modulation on the trap distance to the nanobeams Δz_1.

The small modulations over the $w \sim 20\mu$m scale envelope for $I(x, 0, z_1)$ seen in Fig. 5.9(b) correspond to the lattice constant scale changes on the dielectric function. The depth of the modulation is really small, such that the trap above the structure can be considered as a long cigar shaped dipole trap. However, as seen in Fig. 5.9(d)

and (e), there are significant changes in the scattering pattern near the external modulation of the beams, i.e. the sinusoidal profile wrote in the structure.

Although the trap depth can be modified by changing the dipole trap detuning from the atomic transition or the optical power, as a matter of fact the number of atoms loaded in the trap do not seem to be more than three. Different loading routines, cooling techniques as bright- and gray-molasses, and the use of guided modes, just to name a few examples, were tried by Aki and Chen-Lung, although no further improvement was observed. The reason why this loading is limited might be the appearance of light induced collisions between the atoms in the trap. The trap volume is extremely small $V \sim (100\text{nm}) \times (100\text{nm}) \times 10\mu\text{m} \sim 1 \times 10^{-13}\text{cm}^3$, such that "densities" above $1 \times 10^{13} cm^{-3}$ can be reached. These densities are not only huge in terms of MOT loaded traps, but also any kind of light induced collisions as discussed in Chapter 3 might turn on in really short time scales and equilibrate the number of trapped atoms. Further investigation are being performed in the experiment at JILA.

Superradiance

In the experiment performed in lab 11 by Aki and Chen-Lung, cold atoms from a MOT that surrounds the APCW are loaded into the dipole trap described before during an optical molasses phase ($\sim$ 5ms) and then optically pumped to $6S_{1/2},\ F = 3$ ($\sim$ 1ms). For the APCW used in the experiment [40], the TE-like fundamental mode band edge is close to the Cs D1-line at 894.6 nm, such that it is ideal to probe the atoms with a resonant $6S_{1/2},\ F = 3 \rightarrow 6P_{1/2},\ F = 4$ TE-like excitation. Atoms are held in the dipole trap for a time t_m and then a short free-space absorption image is taken in order to measure the atom number. As shown in Fig. 5.10(a), a free-space measured trap lifetime $\tau_{fs} = 54 \pm 5$ms and a peak density $\rho_0 \simeq 2 \times 10^{11} cm^{-3}$ near the APCW is measured.

From the normalized probe transmission, T/T_0 with T_0 is the transmission without atoms, measured against different holding times, the lifetime can be also be measured by observing the time-dependent guided mode transmission when atoms are trapped near the device, as can be seen in Fig. 5.10(b). The signal T/T_0 gradually reaches $T/T_0 = 1$ as t_m increases, with a fit to the data giving a $1/e$ time of $\tau_{gm} = 28 \pm 2$ms.

Given that in the employed APCW device the Cs D1-line transition is guided for the TE-like mode, it serves as a great scenario to study the properties of the so-called dissipative regime, where propagating fields mediate the atom-atom interactions.

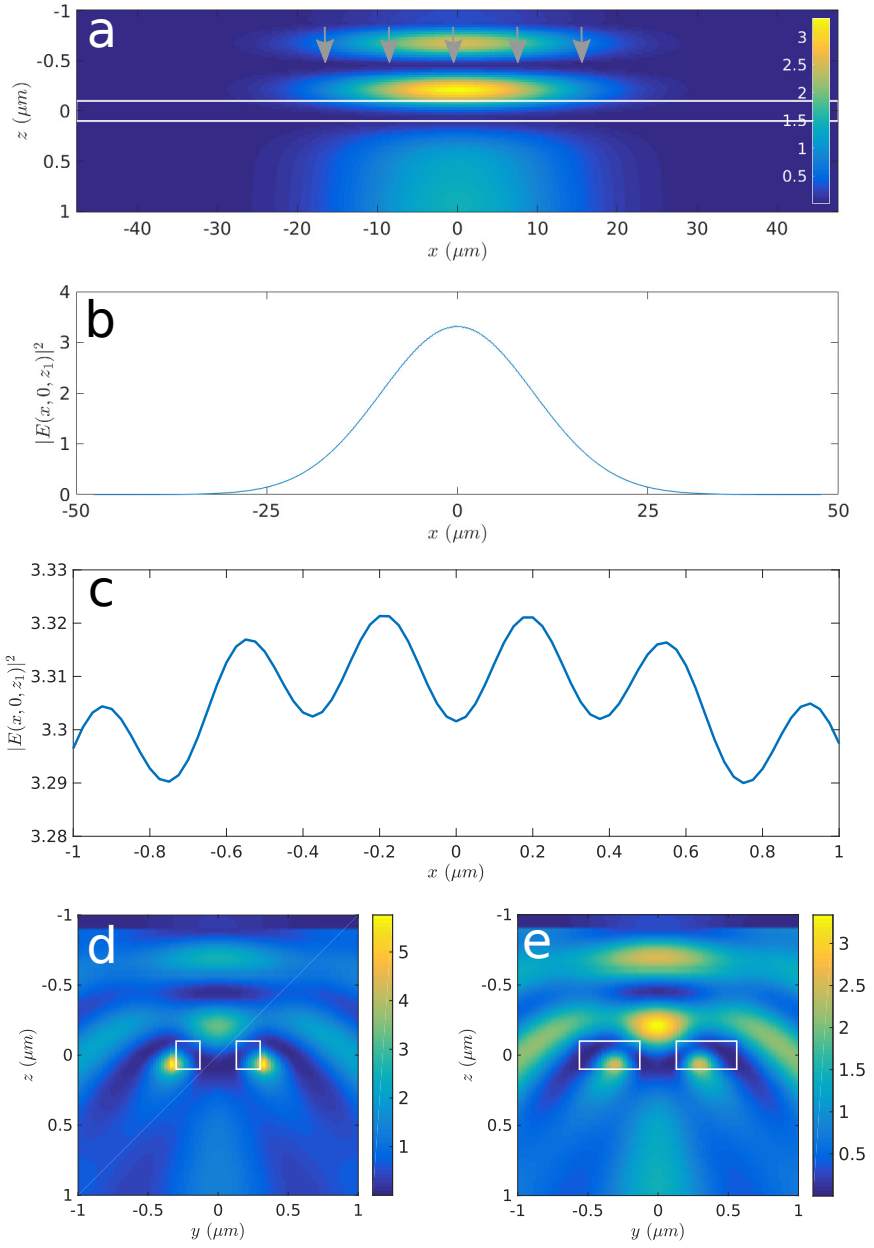

Figure 5.9: Scattering in the APCW structure - FDTD simulation. A $w = 20\mu m$ waist Gaussian beam propagating along the z-direction and polarized along the x-direction. (a) Intensity pattern $|\mathbf{E}(x, 0, z)|^2$ in the $y = 0$ plane a 100μm long APCW with 30 taper sites on each site. The gray arrows indicate the incident direction and the white rectangle the outline of the long waveguide. (b) Intensity pattern $|\mathbf{E}(x, 0, z_1)|^2$, notice the very small modulations on the lattice constant scale and the beam waist scale envelope. (c) A detail of (b) with the $< 1\%$ intensity modulation near the device center $x = 0$. The transversal pattern $|\mathbf{E}(x_i, y, z)|^2$ at the (d) narrow ($x_i = 0$) and (e) wider ($x_i = a/2$) APCW sections closer to APCW center.

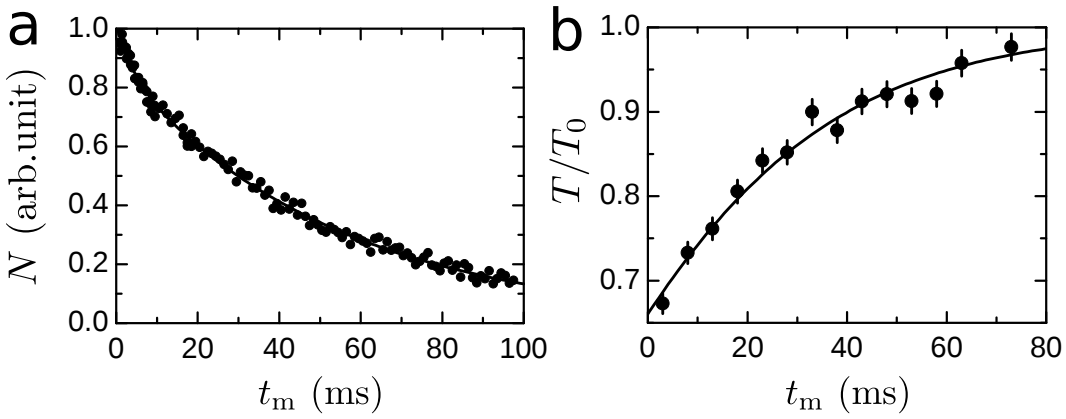

Figure 5.10: Lifetime of trapped atoms near the APCW determined by (a) free-space absorption imaging of the cloud $\tau_{fs} = 54 \pm 5$ms, (b) observed from the normalized transmission T/T_0 of a resonant GM probe $\tau_{gm} = 28 \pm 2$ms. Figure reproduced from Goban et al. [40].

The main observation of this work is then on the dissipative characteristics of the set of atoms trapped above the crystal. The observation of superradiance involves monitoring the transient decay of both forward and backward emission from atoms trapped along the APCW. The excitation is provided by a weak and short pulse (FWHM 10ns) with an average photon number $N_{ph} \ll 1$ per pulse, ensuring that a small degree of excitation can be uniformly shared among all ground-state atoms. For a collection of $N > 1$ atoms, superradiance is heralded by a total decay rate $\Gamma_{\mathrm{tot}} = \Gamma_{\mathrm{SR}} + \Gamma'$ that is enhanced beyond the total decay rate for one atom $\Gamma^1_{\mathrm{tot}} = \Gamma_{\mathrm{1D}} + \Gamma'$ as described in Chapter 2. Γ_{SR} is the N-dependent superradiant rate operationally determined from Γ_{tot} and Γ^1_{tot}. As before, Γ' is the radiative decay rate into all channels other than the TE-like guided mode. In this experiment Γ' is evaluated numerically and determine to be $\Gamma' = 1.1\Gamma_0$ for an atom at the trap site z_1, where Γ_0 is the Einstein-A coefficient for free space [48].

Two different kinds of measurement are performed in order to study the nature of the emission properties. A time-domain measurement records the emission into the guided modes following the mentioned short pulse excitation. Repeated cycles of the excitation are performed in order to accumulate data after the high-extinction edge of the excitation pulse over a total time much shorter than the observed lifetimes. The total decay rate Γ_{tot} is extracted from exponential fits as shown in the inset of Fig. 5.11(a). By changing the holding time t_m, the atom number in the trap changes and differences in the observed total decay rate Γ_{tot} are observed. Asymptotically, only the single atom contribution is observed such that the single atom decay can

be extracted from measurements for long holding times, giving $\Gamma^1_{\rm tot}/\Gamma_0 \approx 2.0$. Fig. 5.11(a) shows the measured decay rate for different hold times, while Fig. 5.11(c) shows the same rate as a function of the mean number of trapped atoms N. In this case, N is adjusted by changing the trap hold time (red) or atom loading time (blue). The black line is a linear fit to the combined data sets giving $\Gamma_{\rm SR} = \eta\Gamma_{\rm 1D}\bar{N}$ with $\eta = 0.34 \pm 0.06$.

A second set of measurements is performed in order to observe the superradiant behavior, this time in the frequency domain. Steady-state transmission spectra $T(\Delta)$ measured at $t_m = 3$ms for 5ms is shown in Fig. 5.11(b) for different MOT densities. The measured linewidths Γ_m are significantly broader than the free-space width $\Gamma_0 = 2\pi \times 4.56$MHz, and they are also affected by the atom number, as shown here in Fig. 5.11(d) as a function of the loading MOT density. The shift in the line center for the transmission spectra is induced by the red optical dipole trap. Furthermore, trapped atoms should suffer small inhomogeneous broadening in the spectra, since the light shift induced by the dipole trap is small (< 1 MHz) for the $6P_{1/2}$ excited states, and the atoms are well localized around the trap center due to their low temperature. In Fig. 5.11(d), a linear interpolation allows to estimate the single-atom linewidth as $\Gamma^1_m/\Gamma_0 = 2.1 \pm 0.1$ and hence single atom decay rate into the TE-like guided mode $\bar{\Gamma}_{\rm 1D}/\Gamma_0 = 1.1 \pm 0.1$. The mean number of atoms for the highest density used can be estimated from $\bar{N}_m = (\Gamma_m(\rho_0) - \Gamma')/\bar{\Gamma}_{\rm 1D} = 2.4 \pm 0.4$ atoms.

5.3 Transporting atoms towards the device using an optical lattice

In the process of investigating the scattering properties of the non-patterned single and double nanobeams, the effect of different incident polarizations was discussed. A few examples where shown and the main differences described before in this chapter. The limitations in the Lab 11 experiment and the difficulties to reliably generate a long lived small MOT pushed us to look for different ways to deliver atoms near the device. While investigating the several different combinations of external illumination and guided modes, the use of coherent fields combinations near the device proved to be a possibility.

To begin with, consider the scattering of light by a double nanobeam waveguide as described before. In fig. 5.12(a) the intensity pattern $|\mathbf{E}(\mathbf{r})|^2$ is shown for the input polarization along the y-direction. The incoming wave has amplitude 1. The features along the propagation direction have mostly the same length scale as the nanobeams

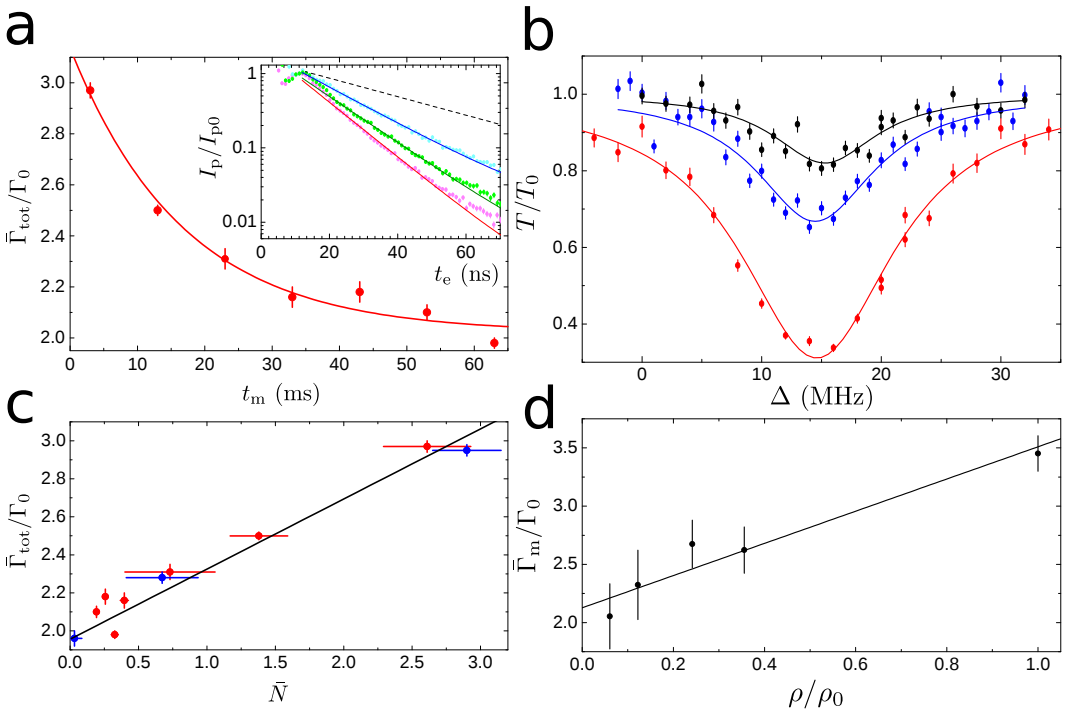

Figure 5.11: Superradiance experiment. Time-domain measurements fitted total decay rate vs. (a) holding time, with inset with different decay traces and (d) inferred atom number based on asymptotic value. Frequency-domain measurements for the transmission spectrum $T(\Delta)$ for different MOT densities (b), and its linewidth dependence on the density (d). Figures reproduced from Goban et al. [40].

and they are more or less flat transversally. The power reflection coefficient based on the amplitude of the first maximum is $R_{perp} = 0.033$. For an incoming beam polarized along the x-direction and propagating along the z-direction as indicated in Fig. 5.12(b), the scattering pattern changes significantly as seen in Fig. 5.12(b). The central feature is on top of the gap center and bigger contrasts are observed. The associated reflection coefficient is $R_{para} = 0.20$, six times bigger than for the other polarization. The question now is how these fields would affect the transport of atoms to the device.

A set of counter-propagating Gaussian beams propagating along the z-direction can create interesting near field patters. Disregarding its input polarization, the near field diffraction scattering modifies the usual interference arrangement found when identical light beams counter-propagate in space. Furthermore, the total field intensity depends on a number of factors, such as the phases between the two beams and the relative position of APCW. For example, if the phases are such that the lattice anti-nodes are close to the dielectric structure, it is reasonable to suppose

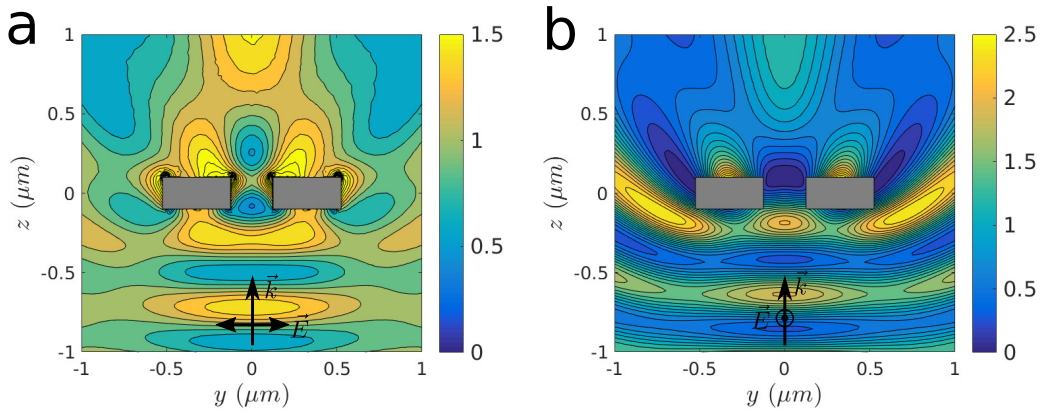

Figure 5.12: Scattering of light by a double nanobeam waveguide for two different polarizations. The field intensity $|\mathbf{E}(\mathbf{r})|^2$ for an incoming plane wave is plotted for two polarization of the field. In (a) the electric field is polarized along the y-direction, while in (b) it is polarized along the x direction.

that the light will preferentially leak into the dielectric. But if the nodal plane is closer, the lattice will not be so distorted locally. Besides, as the structure is really long and not very wide, the induced polarizability for light polarized along x might be bigger than for light polarized along y. Therefore the y-polarized case might resemble more to the free space and no-dielectric case. Finally, note that scattering near yhe APCW edges, as the ones in the waveguides before, usually induce high electric fields that might extend in space for a few tens of nanometers.

The following figures, Fig. 5.13 and Fig. 5.14, show the intensity pattern for two incident plane waves on a double beam non-patterned waveguide with polarization along the device axis x and along the transversal direction y respectively[2]. Both cases show that the local maxima and minima on the lattice intensity move towards the device although affected by the diffraction effects of the device. The cycle in these figures shows consecutive steps of $\pi/2$ in the relative phase between the beams, such that $t_5 = t_1$.

On the one hand, if the incoming beams are polarized along the x direction the intensity maximum along $y = 0$, indicated with purple circles in each frame on Fig. 5.13, approaches the nanobeams but splits, just before it gets too close to them, into two maximums that move towards the sides and impact onto their surface. For example, starting in the t_3 frame, the maximum at $z = 0.5\mu$m, indicated with a purple circle, moves closer to the structure in frame t_4 and splits into two maxima

[2]This is usually a good approximation as the field just above the device does not really change for different beams width as seen before in Fig. 5.9, for example.

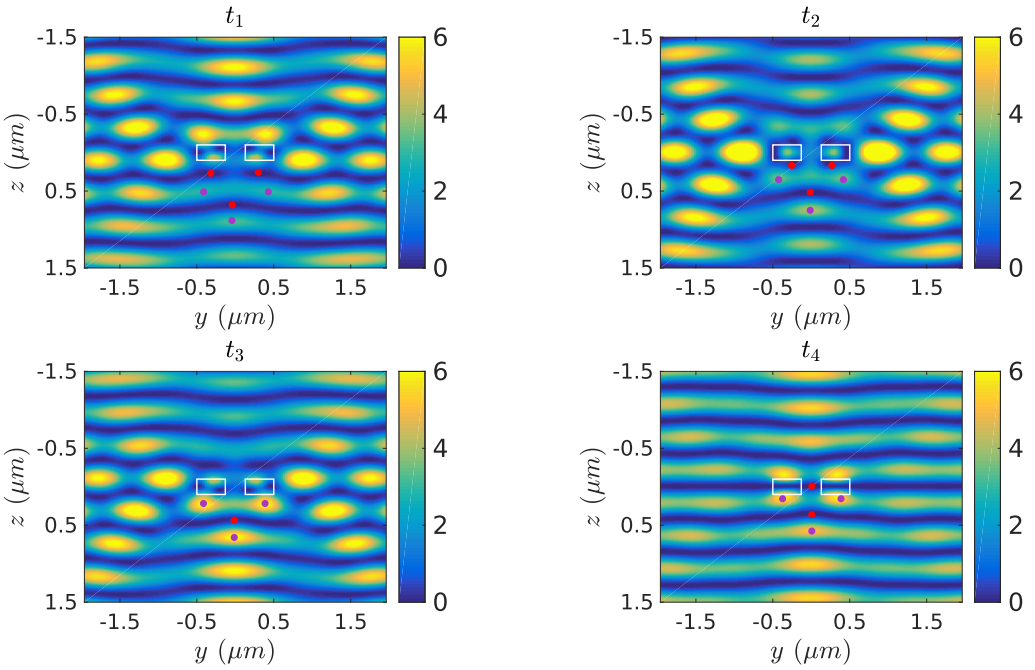

Figure 5.13: Side illumination for a standing wave propagating along the z-direction and polarized along x. Each frame t_i represents the total intensity $|\mathbf{E}(y,z)|^2$ for consecutive $\pi/2$ steps between the relative field phases. Some relevant maxima and minima are marked with purple and red circles, respectively.

in t_1 and t_2 that appear back in t_3 and t_4, hitting the beams' surface. If used as a trap, the atoms will adiabatically follow the intensity maximums and crash into the surface. Likewise, the intensity minimums indicated with red circles also split, although there is clearly a minimum that goes through the center of the beams. For example, the red circle at $z = 0.5\mu$m in the frame t_1 it approaches the beams until t_4, but it splits again at t_1 colliding with the beams' surface at t_2. In contrast with the intensity maximums, an intensity minimum at $y = z = 0$ can be seen in frame t_4, but it is not continuously connected to any of the other minimums in the vacuum region for different time frames.

On the other hand, if the beams are polarized along the y-direction, the pattern is less distorted by the structure diffraction and more resembles a normal lattice interference pattern, as seen in Fig. 5.14. For example, there are multiple high intensity points around the device in Fig. 5.13 but those do not appear in Fig. 5.14 because the diffraction from the device is not so strong. Particularly, the intensity nodal planes continuously move through the beams gap. Therefore, if an atom is localized in the intensity minima along the $y = 0$ direction, indicated by red circles,

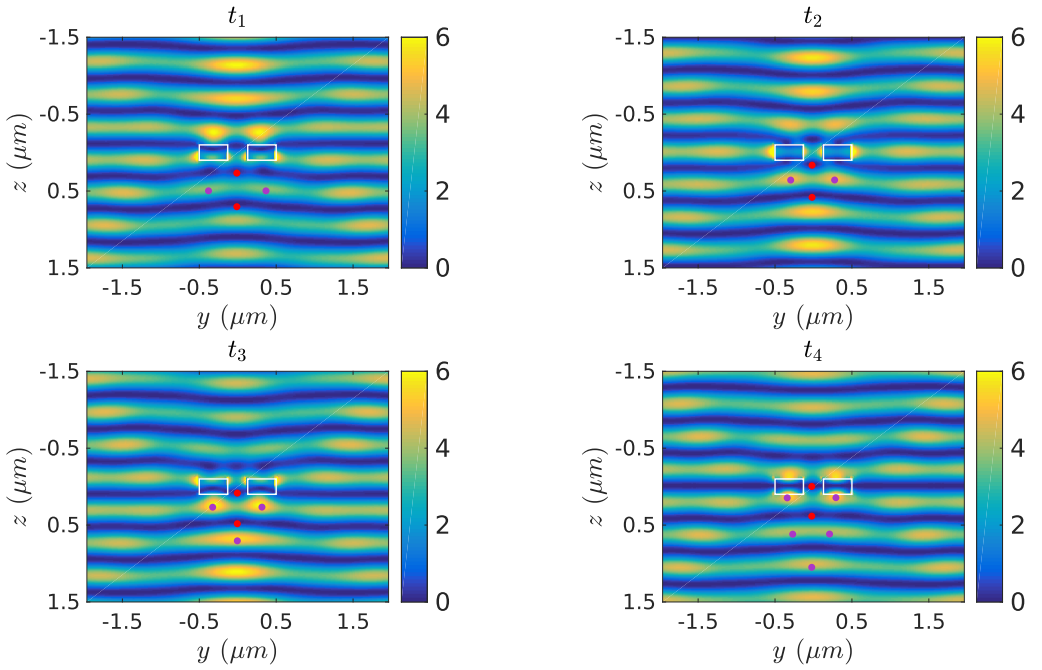

Figure 5.14: Side illumination for a standing wave propagating along the z-direction and polarized along y. Each frame t_i representss the total intensity $|\mathbf{E}(y,z)|^2$ for consecutive $\pi/2$ steps between the relative field phases. Some relevant maximums and minimums are marked with purple and red circles, respectively.

as the lattice moves towards the device the atom will go through the beams. That can be seen following the red circles through the different consecutive frames in Fig. 5.14, ending in the t_4 frame where the nodal plane is in between the nodes. The intensity anti-node planes behave similarly as before, with the central maximum splitting just before they arrive to the nanobeams.

An optical lattice can be loaded far from the device and atoms can be transported as depicted in Fig. 5.13 and Fig. 5.14 by carefully controlling the phase between the two beams. In the laboratory, the optical phase between the two beams can be modified by shifting their frequency with an acousto-optical modulator (AOM) for example. This frequency shift can be controlled with great accuracy using digital synthesizers. Several parameters enter in the efficiency of the transport sequence like the lattice trap depth and vibration frequency, technical noise, the lattice transport velocity, temperature, etc. In the last year, Lucas Peng, following initial efforts by Michael Martin at the end of his postdoctoral period in the group, has been performing an extensive numerical study of the transport properties far and near the device. It has been very useful to have the numerical tools that Lucas optimized

with great effort as an efficient comparison tool with the experiments.

Some of his results and the experimental results will be shown in the next chapter. However, as a way to introduce some basic ideas, the transport of atoms near the device is shown in Fig. 5.15. A red detuned lattice polarized perpendicularly to the device axis as seen in Fig. 5.15(a) can transport atoms in its intensity anti-nodes, as can be seen in the transport simulation snapshots in Fig. 5.15(a) to (d). Each snapshot represents a different relative phase value between the two fields. Notably, a fraction of the atoms crash into the beams' top surface, while a significant number of them move smoothly through the nanobeams gap. The two events happen at slightly different times and have different time span, marked by different phases between the two beams, so any atomic signal dependent on $N \times \Gamma_{1D}$, the resonant light transmission for example, will exhibit modulation that follows the amount and position of the atoms near the device. When this happens, we say the signal exhibits *fringe sensitivity*. The device usually scatters into its guided mode some small amount of the lattice light that oscillates with the lattice optical phase. A narrow frequency filtering allows to collect this light and trace back the lattice as it passes through the device.

Additional information comes from the density distribution among areas with different AC-shifts. Therefore, a common tool to analyze the simulation and its fringe sensitivity is to plot the normalized probe transmission $T(\Delta)$ as a function of detuning Δ and time, at the scale that resolves each pancake arriving. For a simulation consisting of 5 pancakes, the transmission is shown in this way in Fig. 5.15(e). Oscillation in the transmission signal are observed for different detunings as the atoms arrive and leave transported by the lattice. On the other hand, when atoms are transported with a blue detuned lattice polarized parallel to the device axis, the atoms crashing and going through the device center produce time modulated signals with bigger contrast. Recent experimental results will be shown in the next chapter.

5.4 Loading a single trap site

Even though the atoms can transit through the gap between the beams, trapping them is another story. Guided mode traps can be present, but the transfer between atoms trapped in the lattice and the guided mode trap sites is not straightforward. Numerical simulation allows us to perform extensive studies on the different parameters like trap frequencies, lattice detuning, temperature, and lattice speed, but its dependence are rather complex. For example, in a one-dimensional system where a moving

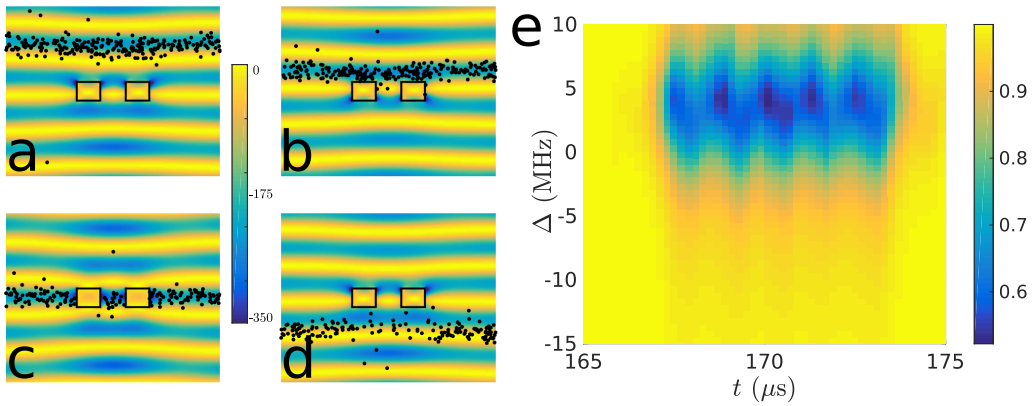

Figure 5.15: Transport of atoms in the conveyor belt near the device. A single pancake, black dots, trapped in the lattice formed by two counter-propagating red detuned beams polarized perpendicular to the device's axis as shown in (a), is shown as it approaches the device in (a), (b), (c), and (d). The color scale in the figure represents the lattice potential in μK. In (e) the time-detuning transmission signal for 5 pancakes is shown.

lattice transports atoms towards a deep localized trap (dimple) the lattice speed (frequency) can be resonant with the dimple's trap frequency. In particular, if the lattice moves twice as fast as the dimple's oscillation frequency the lattice helps to create an effectively deeper trap, helping to confine the particle for some cycles until it dephases and escapes.

The main problem is whether it is possible to perform any kind of procedure that allows one to increase the trapping efficiency. In principle two different procedures are of interest. The first involves loading without removing energy from the atom by, for example, creating deeper traps that confines the atom. The second scheme, more ambitious, involves cooling the atom into the localized trap. Normal cooling techniques, like Doppler or polarization gradient cooling, usually needs several scattering events and motion along a few wavelengths to remove significant energy. However, the transport discussed in Sec. 5.3 might pose serious constrains in terms of performing conventional schemes for loading and cooling because the trap volumes, travel distances, and transit times can be quite small. Therefore, we have been thinking about different schemes that might allow cooling and loading into guided mode traps.

Single photon loading and state sensitive traps

Optical dipole traps are state dependent,, as discussed in Chapter 3, due to the fact that the dynamical polarizability tensor depends on the angular momentum operators $\bar{\alpha}(\lambda, F, m_F)$. Fields that are not linearly polarized generate Zeeman-like shifts and tensor shifts have a quadratic dependence on the azimuthal total angular momentum number m_F. Far from resonance, the scalar polarizability for different ground states $6S_{1/2}$, $F = 3$, and $F = 4$ is almost identical, but for near resonant they can differ significantly. For example, for a detuning of $\Delta = 30$GHz the scalar polarizabilities are significantly different with a ratio $|\alpha_s(F = 3, \Delta)/\alpha_s(F = 4, \Delta)| = 1.5$. Even differences of $\sim 1\%$ in traps with depths of 100μK can be easily observed in a microwave spectrum and used to calibrate the trap depth, for example.

As atoms are transported in the lattice towards the device, they will posses a big kinetic energy component associated with the motion of the lattice, with typical speeds $v \approx 0.35$m/s giving $K_{lattice} \approx 1$mK in our experiment. If the atoms are going to be loaded into a static lattice site, all this energy needs to be removed in some way or at least transformed into potential energy. In case the latter is chosen, deep traps $U_0 \sim K_{lattice}$ are required such that usually very close detuned light fields are needed.

An example that tries to exploit the internal state sensitivity of the traps could be a simple 1D problem where an atom trapped in a lattice with depth U_{lat} is transported towards $z = 0$ where a tight close detuned optical trap is created. The trap actually is non degenerate for the different ground states, such that one of them, F_s, sees a shallower lattice with depth U_s and the other, F_d, sees a deeper trap with depth U_d. The atom is in the state F_s while transported in the lattice and once it arrives to the tight trap at $z = 0$ it will transform a big part of its total energy into potential energy. If the lattice depth is not as big as the localize trap depth, the motion inside the static tight trap will be dominated by the restoring force of the dimple potential, and the atom will oscillate in the trap or escape from the trap depending on its initial energy. If spatially selective pumping can be applied, by for example exciting the correct guided mode in the APCW, the atom can be pumped to F_d near $x = 0$ with high probability. In this deep trap, the atom will be trapped as its total energy will be smaller than the trap depth. In Fig. 5.16 a diagram depicting this situation is shown, inspired by the work realized in Mark Raizen's group [185, 186].

In the real APCW case, there are some factors that need to be taken into account. The problem is not unidimensional, having consequences on the lattice transport

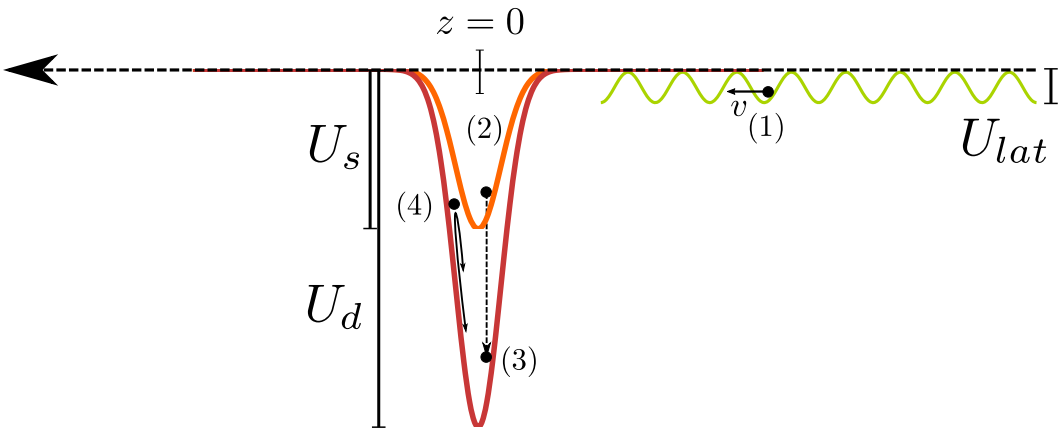

Figure 5.16: Single photon loading scheme in the state sensitive trap. An atom trapped in an optical lattice with depth U_{lat} is transported by it towards $z = 0$ with velocity v in (1) in the state F_s. Once the atoms starts to move through the localized trap (2) it can be optically pumped to a different state F_d that sees a deeper trap with depth U_d (3). The atom oscillates in the trap U_d and remains in the state F_d (4).

near the device, as seen in Sec. 5.3, and the oscillation in the localized trap created by the guided modes, as seen in Chapter 4. In between the nanobeams surfaces forces can perform an important role in reducing the confinement in the y-direction and effectively reducing the strength and spatial region around $y = 0$ where confinement can be achieved. Furthermore, to have significant trap depths and differences between them, it is necessary to go close detuned. In principle, only $|U_d| \geqslant K_{lattice}$ is required, but the difference between the two state dependent traps is an important difference to favor the final confinement. In order to reduce the kinetic energy of the transported atoms, which reduces the required trap depths, slower lattices can be used and have been tested in our laboratory. Further studies in single photon cooling and loading schemes are found in works from Mark Raizen's group, for example [185, 186].

Another possible modification on this scheme is to use a detuning in between the two ground states $F = 3$ and $F = 4$. In this case, one state will see a blue detuned beam and the other a red detuned beam. If the atom approaches in the lattice and sees a localized potential hill, it will slow down and eventually roll back. However, a single optical pumping event can drive the atom to the other trapped state. The speed reduction in this case favors the use of lower optical powers and hopefully avoids significant heating schemes. Again, spatial selective optical pumping is relevant to enhance the effect of state dependent traps.

Sisyphus cooling in localized traps

A mechanism that allows to cool atoms into these traps also depends on the existence of state dependent potentials and was proposed by Zoller and Cirac in 1994 [187]. Their scheme is based on the interaction between a far detuned trapping laser, which forms a standing wave, and an auxiliary near resonant laser that will help to cool and localize the atoms in the lattice. They were thinking mostly on two-level atoms, such that one level was the ground state and the other the excited state, although generalization to a Λ system is discussed in terms of a Raman cooling scheme, similar to the one performed in ion traps.

However, the important difference between laser cooling of neutral atoms in optical potentials and laser cooling in an ion trap is that for an ion trap the ground and excited state potentials are identical, while for a neutral atom the dependence on the internal state quantum numbers and selection rules create different potentials. For the model studied by Taïeb et al. [187] it is shown that laser cooling can only be obtained if the excited state is more tightly confined than the ground state. For alkali atoms the two ground states are typically Zeeman levels (m_F states) belonging to the $6S$ hyperfine structure manifold and in this case the optical potential for the two ground states are identical for far detuned lattices. This leads to a Raman cooling mechanism in complete analogy to ion traps.

The basic idea of the scheme is shown in Fig. 5.17, although for specific details please refer to [187]. An atom in the state F_2 oscillates in the more tighter confined potential $U_2(x)$ around $x = 0$, while it is selectively pumped to the other state F_1 at a distance x_a at a rate Γ_a, where $\Delta U_a = U_1(x_a) - U_2(x_a) < 0$. The atom oscillates in its new potential $U_1(x)$ until it reaches $x = 0$ again and is pumped to F_2 with a rate Γ_0. This time, the energy difference $\Delta U_0 = U_2(0) - U_1(0) > 0$. If the difference $\Delta U_{cycle} = \Delta U_a + \Delta U_0$ is negative, the atom lost that potential energy in the cycle. Successive oscillation cycles create a Sisyphus mechanism that can cool down the atom. The APCW system can, potentially, be ideal to perform those kind of mechanisms as very strong and spatially selective fields can propagate through the photonic structure. Ground state cooling can be achieved if the pumping rates are smaller than the oscillation frequencies, similarly to standard sideband cooling.

Importantly, schemes similar to this have been already performed in neutral atom traps like works by Miller, Dürr, and Wieman [188]. In their case an rf-induced Sisyphus cooling in a circularly polarized far detuned trap, is demonstrated. An optical dipole trap is formed by a single circularly polarized laser beam, exhibiting

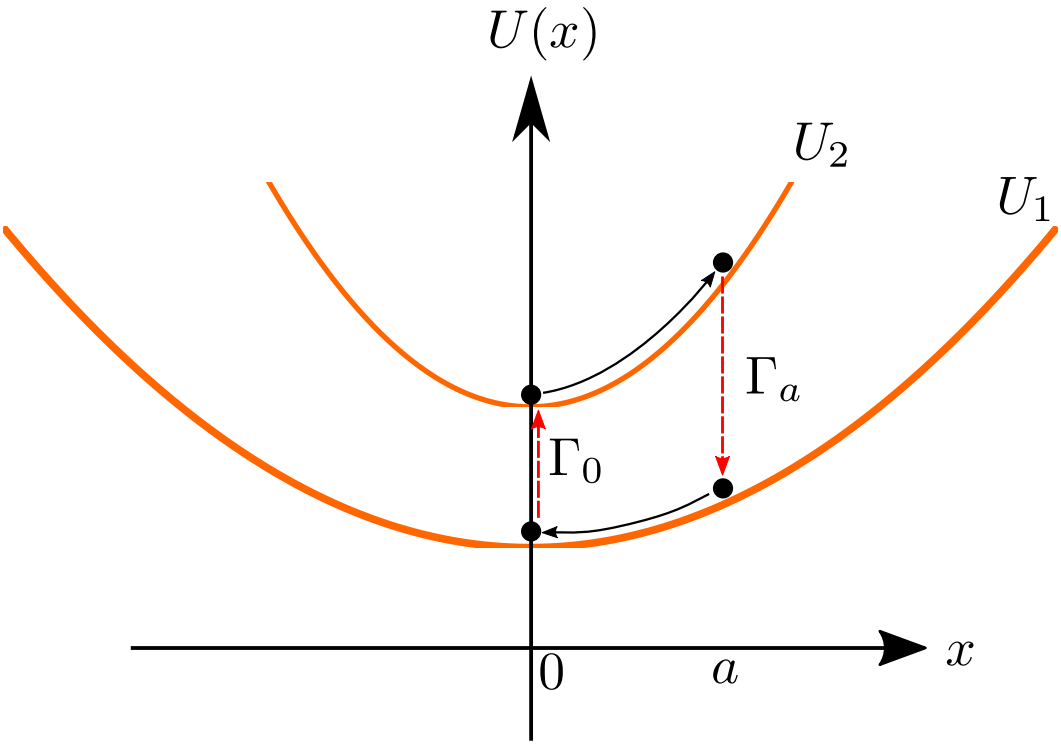

Figure 5.17: Sisyphus cooling into guided mode traps. An atom oscillates in state dependent potentials and is pumped to different states at specific locations. In each cycle the atom loses energy if the potentials are as shown in the figure. Figure adapted from [187].

a Zeeman state dependent trap with is eventually spin polarized by the off resonant scattering of the trap beam. An rf field, microwave pulse, can couple the different Zeeman potentials inducing rapid cooling as before. As far as I am aware, the only other reference that applies to a scheme similar to this one is on Page 72 of Thibault Peyronel's doctoral dissertation [189] in reference to a hollow-core fiber atom trap.

In order to perform a scheme similar to this, microwave π-pulses could be an option, but usually they take $\sim 10\mu$s in our setup, probably limited by the radiation intensity at the atoms position. A two photon Raman transition could be a good option, as it will allow to be depend strongly on the light shifts at the atoms position. The main challenge is to limit the entire scheme to happen in a couple of μs, as that is the timescale it takes the atoms to transit the gap between the nanobeam. Probably, a scheme where the atoms can be slowed down and then have a cooling scheme applied is a more promising case to try.

Chapter 6

DELIVERING ATOMS TO THE APCW

The two legs of this experiment, the nanophotonic one and the atomic one, need to complement each other in order to succeed in trapping several atoms in the vicinity of photonic crystals and observing photon-mediated interactions. The experimental apparatus needs to satisfy all the requirements required. Standard laser cooling and trapping, experimental control of the parameters, and characterization of the different processes that can attempt to destroy the expected signal are key ingredients to trap several atoms near the APCW.

The following chapter explains in detail the performance of the apparatus, focusing on the lattice trapping characterization. At the end of this section, relevant experimental results are discussed. Currently, there is strong evidence that fringe sensitive signals have been observed. The characterization and comprehension of these signals is being performed at the time this thesis is written in collaboration with my colleagues.

6.1 Experimental apparatus

The experimental apparatus for Cs is relatively simple, as usually reasonable size MOTs can be loaded from background gas, and high power laser diodes are available. The setup used in the experiments described in this thesis and others in our group is similar. The main characteristic is the existence of multiple MOTs in different stages and positions of the system, in order to protect the nanophotonics devices from a high cesium partial pressure environment. Exposure of silicon nitride surfaces to low cesium vapor pressure has been reported in earlier experiments carried out at Caltech in the Painter-Mabuchi collaboration [154]. In their case, a micro-resonator was placed in a low pressure environment and one of its resonances was followed after the Cs reservoir was opened (10^{-9} Torr). Remarkably, the resonator's resonance shifts after being exposed to Cs, exhibiting a power-law dependence with time. Similar experiments performed in Pfau's group [190] recently shown that rubidium also sticks on nitride resonators generating losses. However, they found that by coating the structure with 9nm of alumina by means of an atomic layer deposition technique the "resonances remain visible, although their linewidth is still increased after rubidium exposure"[190]. This observations, and a set of our own in the

nanofiber experiment [68], showed that is was important to keep the structures in an environment as clean as possible. To mitigate this problem a separated two-chamber system was built, where atoms are transported from a high partial pressure environment to a very low partial pressure environment where the nanophotonic device is placed, as was done in the microtoroid experiment[1] [18, 177, 179]. There, atoms need to be captured, cooled, and transported towards the dielectric structure. In the rest of this section some of the technical details of the system built in the laboratory will be described.

To begin with, the vacuum system and the transport of atoms from the first chamber (source chamber) to the second chamber (science chamber) is described. Technological developments for this purpose have been tested under different circumstances and different methods exist to separate the two chambers and obtain a high flux of slow atoms. Among them, we adopted a method similar to the one described by Wohlleben et al. [191]. Two vacuum chambers, each with its corresponding ion pumps, are placed 70cm from each other. The source chamber is a small 2.75" stainless steel spherical hexagon pumped by a 35L/s ion pump. The chamber is connected to a Cs reservoir kept at room temperature ($\sim 20^{\circ}$) by a small valve and an angle valve is used to pump the whole source chamber system if needed. The science chamber is a standard 6.0" stainless steel spherical octagon (Kimball Physics - MCF600-SphOct-F2C8) that is connected to its own 50L/s ion pump and to the source chamber by a long 50cm nipple-in-line valve-short bellow-nipple section. The in-line valve between the two chambers is closed every time there is a chip transfer and the science chamber system is exposed to ambient pressure. The science chamber is also connected to an angle valve that is used to pump every time it is needed. The system is horizontal and the distance between the center of each chamber is 70cm and both at the same height. A sketch of the system is shown in Fig. 6.1

The element that actually isolates the two chambers is a small tube positioned close to the source chamber. That tube, usually called differential pumping tube, effectively creates a large pressure gradient between the two chambers. The tube used here is 8" long with 4mm ID. The Cs reservoir vapor pressure [99], the ion pumps, and the conductance between the different elements in the system determine the Cs pressure in the source and science chamber.

[1] Even with two chambers, resonances in the high-Q microtoroid resulted from the Cs deposition.

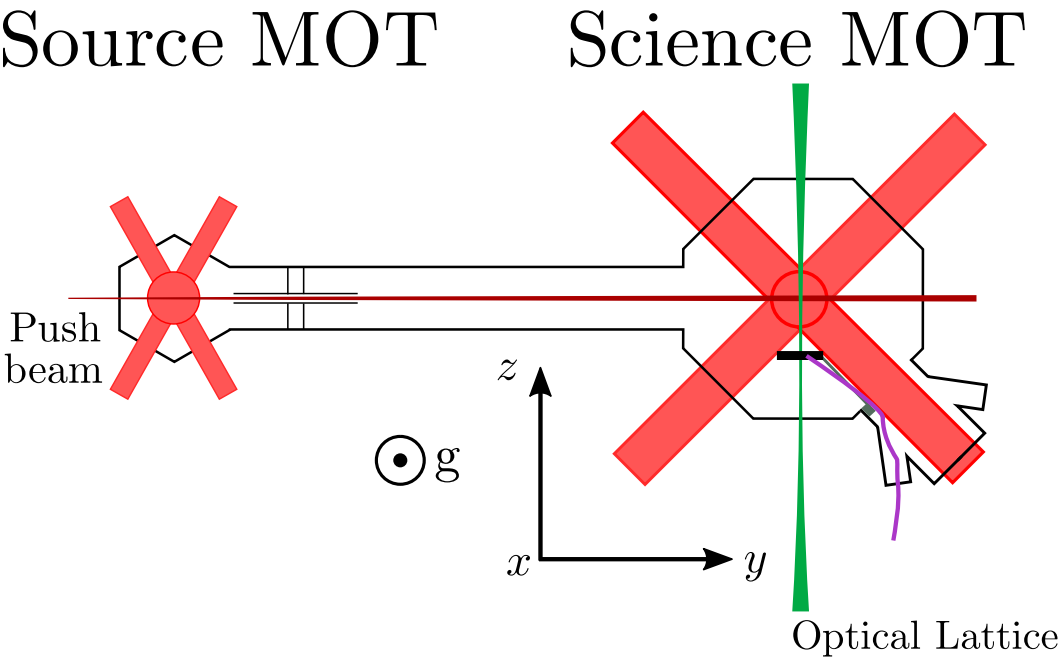

Figure 6.1: Sketch of the experimental system. The two chambers, source and science, are separated by a differential pumping tube that keeps a pressure difference between them. The source MOT formed from Cs vapor pressure due to the Cs reservoir connected to the source chamber (not shown) is pushed and recaptured in the science chamber. A 1D optical lattice (green) goes through the MOT and chip (black). Optical fibers (purple) are connected to the chip and threaded through a multiplexer.

Pushing beam

In the source chamber a big MOT is loaded by capturing and cooling atoms from the low velocity part of the Maxwell-Boltzmann distribution at room temperature. This MOT traps approximately 1.5×10^8 atoms, based on calibrated fluorescence measurements. The MOT loads quickly, with a $1/e$ time below 500ms that allows fast loading in order to shorten the experiment cycle. The three orthogonal MOT beams have different characteristics. The horizontal beams have a waist of 1cm and are partially clipped by the 17mm viewport windows before being retro-reflected. Each beam has 10mW of optical power. The horizontal beams form a 120° angle between them, and each of them forms a 30° angle with the chamber-chamber direction. Meanwhile, the vertical beam has 15mW of power and a 1" waist[2] as the top and bottom viewport are bigger. Each beam is derived from the same optical path after a tapered amplifier , its polarization is the usual $\sigma^+ - \sigma^-$ configuration, and

[2]All the waist indicated in the thesis are represent $1/e^2$ drops in its intensity, unless otherwise stated.

it is usually detuned by −10MHz from the $F = 4 \rightarrow F = 5$ transition. Additionally, there is a 1 inch almost resonant $F = 3 \rightarrow F = 4$, 5mW repumper beam colinear with the vertical beam. A set of coils whose axis is aligned with the vertical direction produces a magnetic quadrupole field with a gradient of 10G/cm near the chamber center. Furthermore, three pairs of coils aligned with each of the orthogonal spatial axis, oriented as indicated with the orthogonal system in Fig. 6.1, produce a uniform magnetic field in the center of the chamber where the atoms are trapped.

From this MOT, a small laser beam aligned along the chamber-chamber direction and close detuned to the $F = 4 \rightarrow F = 5$ transition extracts a significant amount of the trapped Cs atoms. Different configurations were tested. Most of the existent works propose the use of a time-continuous beam that creates a radiation pressure imbalance in the MOT [191], but a significant enhancement is observed if a short pulsed beam is used. A remarkable difference between our work and most of the papers is that our system is horizontal while many of the other systems were vertical or inclined. In general the beam is linearly polarized and focused close to the source MOT, with a waist of about $\sim$ 1mm. This pushing beam is pulsed usually every 23ms for 450μs and it almost destroys the whole MOT after every flash. The atoms are not cooled along the transversal directions, so the trapped cloud expands ballistically.

The MOT and pushing beam are centered by first observing the pushing beam going through the differential pumping tube and then moving the source MOT with the bias magnetic coils. At the other end of the vacuum system, there is a viewport that makes it possible to monitor the beam profile of the pushing beam slightly after the science MOT. First and foremost, monitoring the intensity profile of the pushing beam at that viewport is used to easily determine if the beam clips on the differential pumping tube, or not. The first aperture of the tube is at 12cm from the source MOT, holding an angle of about 20mrad. At the source MOT the pushing beam has a $1/e^2$ waist radius of 1.1mm while at the science MOT is 4mm. Therefore, the radiation pressure produced by this beam at the science MOT is at least 16 times smaller than at the source MOT. The smaller intensity at the science MOT is needed to avoid destabilizing the recaptured MOT, while at the source MOT the imbalance on the radiation pressure creates an escape channel.

Atoms arrive at the recapture MOT in the science chamber 30ms after being pushed, as detected by the fluorescence signal at the science chamber as the MOT starts to load, traveling then at a mean velocity of 23m/s. As is the case here, atoms traveling

the 70cm distance between the two MOTs will experience the gravitational pull down. To be specific, they will fall 1cm if they do not have any initial velocity component along the vertical direction. In order to avoid the cloud crushing inside the differential pumping tube, the pushing beam angle with the horizontal plane is changed by tilting a mirror, increasing the recapture efficiency.

While the atoms are being pushed the source MOT light beams are on as well as the quadrupole magnetic field. Therefore the atoms are continuously kept in the $F = 4$ ground state by the repumper beam. The atoms will scatter light mostly on the closed $F = 4 \longrightarrow F = 5$ transition but occasionally will off resonantly scatter and fall into the $F = 3$ ground state where the radiation pressure will be extremely small. As the atomic cloud moves through the illuminated region where the repumper is present, the radiation pressure force will continuously accelerate the atoms. After they escape that region, the atoms will be quickly pumped to $F = 3$ and remain there without being accelerated, only subjected to gravitational forces until reaching the recapture region. Despite the transversal characteristics of the cloud, if the acceleration is too big atoms can move very fast once they arrive at the science MOT, region reducing the capture efficiency. If they go too slow, they will impact on the differential pumping tube.

A very simple semiclassical model can capture some of these features. The force acting on an atom in this multiple beam configuration is a priori very complex. For simplicity, a two level system will be assumed with two levels $|g\rangle$ and $|e\rangle$ with an energy difference $\hbar\omega_0$ and spontaneous emission rate Γ_0. The radiation pressure force is

$$\mathbf{F} = \hbar\mathbf{k}\frac{\Gamma_0}{2}\frac{s(\mathbf{r},\mathbf{v})}{1+s(\mathbf{r},\mathbf{v})}, \tag{6.1}$$

where the saturation parameter is

$$s(\mathbf{r},\mathbf{v}) = \frac{I}{I_{sat}}\frac{1}{1+4\left(\dfrac{\delta-\mathbf{k}\cdot\mathbf{v}\pm\mu B/\hbar}{\Gamma_0}\right)^2}, \tag{6.2}$$

and takes into account the interaction with the magnetic field and the Doppler shift. The nature of this force in the MOT environment is really complicated. While the pushing beam is on, the intensity I is well above saturation I_{sat}. A quick approximation shows that $s \approx (500 I_{sat}/I_{sat}) \times 1/(1+4\times 2^2) \sim 30$[3], and therefore it can be assumed that $\mathbf{F} \approx \hbar\mathbf{k}\Gamma_0/2$. Notice that at the science MOT this number is

[3]Here $\delta \approx 2\Gamma_0$, $\mathbf{k}\cdot\mathbf{v} \approx 0$ at the beginning and $\mu B/\hbar \approx 0.5\Gamma_0$.

estimated to be 16 times smaller, and hence $s \approx 2$ and probably can be overcome by the additional MOT beams. Once the atoms start to accelerate towards the observed velocity and further from the quadrupole center, $s \approx 5$ at the source chamber. It is safe to assume the pushing force is more or less constant over the whole transit through the MOT beams region, accelerating at a rate $a_{push} \simeq 5900g$, with g the standard acceleration due to gravity. Starting from rest and accelerating at the mentioned rate a_{push}, it will take 830μs to transit through the 2cm distance where the repumper is present in the current experiment. However, as mentioned before the push beam is on only during 450μs. This indicates that the final velocity should be v_{push} = 26m/s in good agreement with the observed velocity of 23m/s.

The main limitation found in the experimental efforts is the fact that the atomic cloud expands significantly before arriving to the differential pumping tube, probably because it is too big to completely go through the whole tube. To check this, a camera was placed near the source MOT as it was pushed. A series of images as the atoms flight through the chamber are taken and enable the characterization of the cloud as it travels through a 1cm distance. The position and spread of the cloud gives information about the velocity, acceleration, and temperature of the cloud. A Gaussian fitting performed on each image gives information about the center of the cloud. The displacement as function of time t_p is plotted in Fig. 6.2(a) and its extracted derivative, which represents the velocity, is shown in Fig. 6.2(b). Clearly for short times ($t < 450\mu$s) the displacement is quadratic in time and for longer times is linear equilibrating at a velocity of ~20m/s, reflecting some of the observations made before in the simple model.

A number of parameters change the velocity with which the cloud moves. As discussed in the simple model, if the pulse is shorter the final velocity is smaller, and we have observed this for a set of pulse widths. For pushing pulses $\leq 200\mu$s the cloud elongates along the pushing beam direction, some atoms are not really pushed away and remain in around the MOT position. Furthermore, spatially redistributing the power on the near resonant MOT beams and the repumper changes slightly the final velocity. A configuration where most of the repumper is in the vertical direction, the widest beam, was adopted. Slower velocities can probably enhance the recapture efficiency, but are also more susceptible to experiencing larger falls due to gravity and crashing inside the differential pumping tube.

The measured temperature is an important parameter to characterize the spreading of the cloud. In continuous push schemes, the push beam can serve other roles along

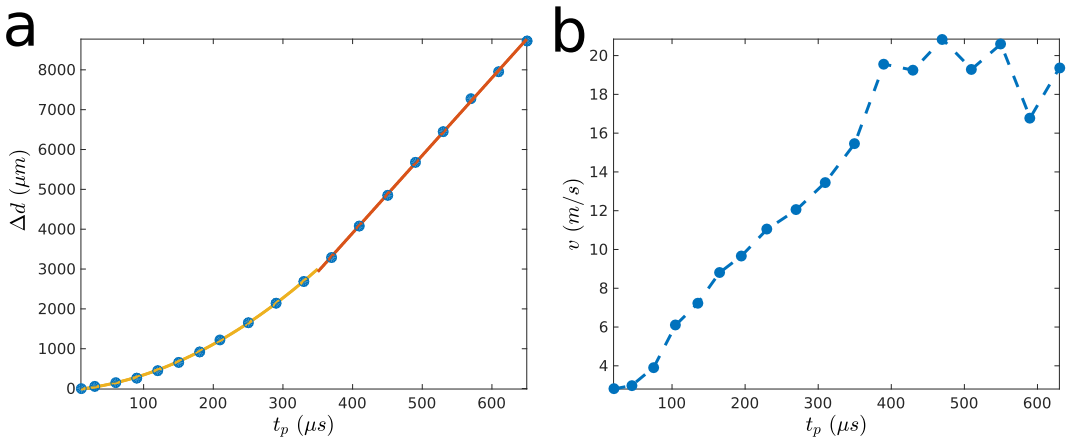

Figure 6.2: Tracking the flying cloud in the source MOT. A 450μs wide pulse moves the MOT and is monitored using florescence images. During the pushing, the MOT beams, the repumper, and quadrupole are on. Before the 50μs resonant pulse to image, all the laser beams are switched off. The linear displacement of the cloud center is shown in (a). An initial quadratic increase is associated with a constant force, followed by a constant velocity motion after the pulse is switched off. A quadratic and linear fits help to guide the eye in those two regimes. The extracted velocity is shown in (b). The camera calibration might not be ideal, probably causing the small discrepancy on the observed final velocity of 23m/s.

with pushing. A red detuned beam can provide enough radiation pressure force to push the atoms while it also provides gently dipole guiding to avoid transverse spreading. However, the pushing scheme we adopted seems to just propel the whole MOT without significant guiding and deforming the flying cloud. The $1/e$ width of the cloud along the longitudinal and transversal direction, σ_L and σ_T, respectively, evolves quadratically in time as shown in Fig. 6.3(a). In the usual time of flight measurements, the spreading is associated with the sample's temperature. From these measurements the fitted longitudinal temperature is $T_L = 200$mK while the transversal temperature is $T_T = 15$mK, both measured after the 450μs pulse is finished. The big difference between the two directions is caused by the preferential direction of the pushing mechanism, and the fact that the MOT beams probably contribute to transversally cool the cloud.

As discussed before, as the push beam is strongly saturation the cloud, $s \gg 1$, m the scattering rate is maximized $R_{sc} = \Gamma_0/2$. The total number of scattered photons is $N_{ph} = R_{sc} t_{push} \approx 7.5 \times 10^3$. Spontaneous emission causes the mean square velocity to increase as $\bar{v^2} = N \times v_r^2$ or along a specific axis $\bar{v_z^2} = \eta N \times v_r^2$, where $v_r = 3.4mm/s$ is the recoil velocity for Cs and $\eta =< \cos^2(\theta) >$ is the angular

average for the spontaneous emitted photon. Additional fluctuations associated with the absorbed number of photons leads to an increase in the velocity spread by $\bar{v_z^2} = N \times v_r^2$ assuming Poissonian statistics. Therefore, if only the pushing beam is acting and the scattered photons are isotropically distributed ($\eta = 1/3$) the spread in velocity is $\bar{v_z^2} = (1+\eta)N \times v_r^2$ associated with a temperature $T_{push} = m\bar{v_z^2}/k_B \approx 2$mK. There is a huge difference with the measured temperatures along the two directions. This model is a simplification, as during the push cycle the MOT beams are on, presumably cooling, and the magnetic field gradient is also present. We were not able to find any reasonable mechanisms that produce this discrepancy.

The measured temperatures pose a big limitation in the transport efficiency. At the entrance of the differential pumping tube the transversal spread is $\sigma_T \approx 4$mm, comparable with the tube ID. Without taking that into account, at the science MOT the longitudinal spread is almost 10cm and the transversal one is almost 3cm, comparable to the size of the MOT beams. Although there does not seem to be a major drop in the recapture efficiency if the science MOT beams are changed from 2.5cm diameter beams to 1.5cm diameter beams, further reductions decrease the atom number. Smaller temperatures were observed for shorter pulses and different detunings of the push beam, although the recapture efficiency is smaller.

Finally, a curious observation is about the detuning of the pushing beam. As seen in Fig. 6.3(b) the atom number at the science MOT is optimized for a blue detuned ($\delta_p = 10\text{MHz} \sim 2\Gamma_0$) push beam. As a reminder, $\delta = \omega_L - \omega_A$. A blue detuned push beam will enhance the pushing efficiency as it will compensate for the Doppler shift. A small peak near $\delta = -12$MHz is also observed. In principle, it is possible to argue that if the push beam detuning is negative and bigger than the MOT beam detuning ($|\delta| > |\delta_{MOT}|$), assuming similar intensities, the trap is only decentered and no flux is established between the two MOTs. Also, there exist some negative detuning were the trapping and pushing force are comparable, and some local maximum can be expected. The work by Wohlleben et al. [191] explains the fact that there is a decrease in the recapture efficiency near the free space resonance $\delta = 0$ associated with an increase in the jet divergence. For a positive detuning the trapping and pushing forces are comparable and there is a higher efficiency in the recapture process, probably associated with an increase in the source MOT transversal cooling efficiency[191].

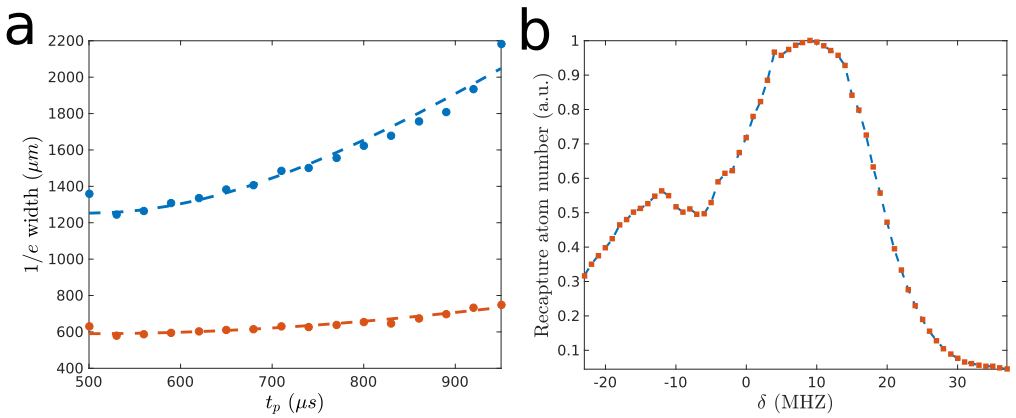

Figure 6.3: From the same measurements described before, the cloud width can be extracted, indicating the transversal and longitudinal temperatures. In (a) the blue (red) dots and dashed line indicate the longitudinal (transversal) measurements and TOF fits, respectively. The temperatures are higher than expected. In (b) the recapture efficiency (normalized to the maximum) is shown for different pushing beam detunings. Two peaks near $\delta \approx \pm 10$MHz are observed, while a drop near the free space $F = 4 \longrightarrow F = 5$ resonance is shown.

Science MOT

The second chamber helps to recapture the atoms and form a second MOT, the so-called the science MOT. The optical access in this chamber provides better imaging of the MOT in the horizontal and vertical plane. The six 1" circularly polarized MOT beams come from the same source and are split into three pairs that are retro-reflected. The horizontal beams form 90° between them and usually have about 35mW of power each. The vertical beam propagates normally to the horizontal plane and carries about 50mW of power. The repumper co-propagates with the vertical beam and usually carries about 10mW of power. The magnetic quadrupole is generated by a big 14cm radius anti-Helmholtz coils pair, each of them with 150 turns and generating a 15G/cm gradient at the center of the system. Each direction also has three different coil pairs in the Helmholtz configuration to produce different uniform magnetic fields. Along each direction, the three pairs have have 50, 25, and 10 turns in case bigger or faster fields are needed. The quadrupole field current though the coils turns off in 3ms, but parasitic currents in the system extinguish in about 15ms.

Under normal conditions, the science MOT loads about 30×10^6 atoms from the atomic flux coming from the source MOT. The $1/e$ loading time is about 1s, while the time constant once the pushing beam is turned off is usually 3s, indicating that

the base pressure is around 10^{-9} Torr. That is pretty good considering that the chamber is opened once every 4 months and has not been baked since the beginning (Fall 2012). Every time the system is opened, it is purged with high purity N_2. Once the chip transfer has been performed, it is pumped with a turbo pump for 12 hours before the ion pump is turned on and the turbo pump is turned off slowly while the system closes. After 48 hours, the science MOT is close to its steady state size with lifetimes around 3s.

The atoms are usually loaded at certain position in the science chamber, slightly away from the push beam as the recapture efficiency is bigger. This is done by moving the minimum of the quadrupole field by adding a bias field. After the loading is concluded, the bias field is changed and the atoms move towards the center of the chamber where the cooling works a bit better.

One of the science chamber viewports chip is used to position the chip and its fibers inside the vacuum environment as seen in Fig. 6.4 (a). The viewport has attached a 2.75" conflat flange adapter that allows to mount a conflat flange multiplexer that serves the purpose of housing different instruments. This multiplexer has grooves machined in its inner surface that allows to lock a small groove-grabber plate where a long arm that positions the chip close to the chamber center is attached Fig. 6.4(b)-(c). The multiplexer housing also has a normal 2.75" flange at its other end that allows to have significant optical access in that viewport Fig. 6.4(e). Additionally, it has four smaller 1.33" ports where four vacuum Swagelok fitting adapters can house a machined teflon feedthrough where the optical fibers enter the vacuum system. The teflon pieces are pressed once the fitting is closed and the fibers-teflon interface isolates the vacuum system from the exterior. Each feedthrough was able to house up to 4 fibers so far, so while no significant changes in the base pressure, fiber transmission or strain-induce birefringence were observed. Hitherto, the record has been 16 fibers out of the vacuum chamber.

The transfer usually takes two working days. The first day is used to glue the optical fibers to the chip in Lab 11A. The chip is glued to a Macor or aluminum chip mount, a thin flat piece with a 8mm×8mm hole in the center. Cleaved AR-coated single mode optical fibers are positioned and glued to each device V-groove and the chip holder, which is kept hot ($\sim 100°$) in order to accelerate the curing. The final result is seen in Fig. 6.4(d). After the gluing process concluded, the chip plate is screwed to a clean and long aluminum angled arm that helps position the chip closer to the chamber center. The arm is attached to the groove-grabber in the multiplexer

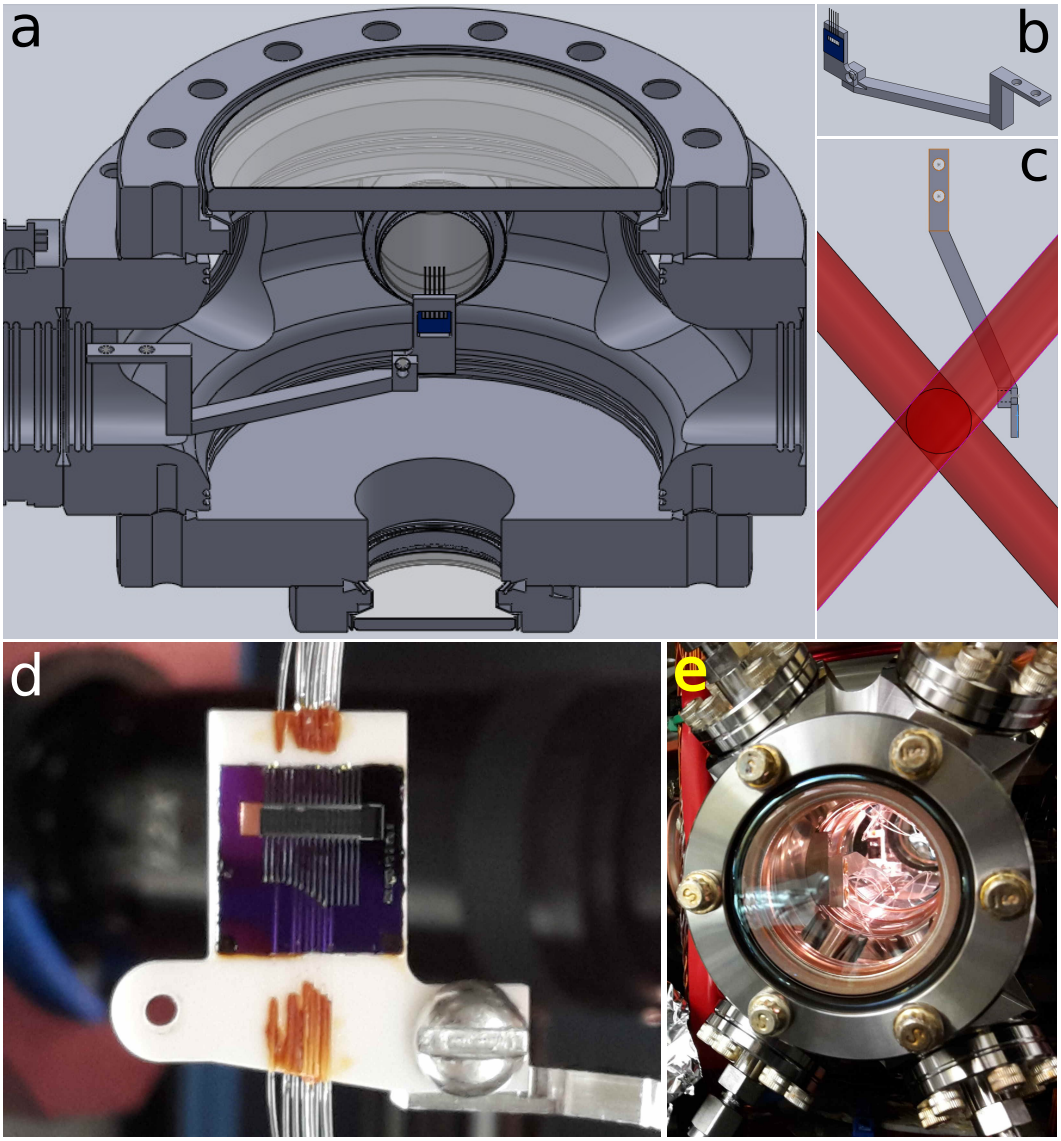

Figure 6.4: Components on the science chamber. The science chamber sketched in (a) with the chip (blue square) recessed from the center by means of the extension arm attached to the grooves near the multiplexer flange. (b) A sketch of the arm-chip pair. (c) Relative position with the 1" horizontal MOT beams. (d) Photograph of the Macor holder and the chip with 16 fibers glued. The brown regions are the cured glue. Note on the bottom right corner the screw that held the mount to the arm. The multiplexer attached in the chamber viewport can be seen in (e). In the back the mounted chip and the arm are seen, while some of the fibers that go through the feedthrough are seen near the window.

flange, the fibers are carefully cleaned and fed through the full teflon feedthrough system, and then the multiplexer is inserted in an acrylic N_2 purged box. The chip-multiplexer system is transported to Lab 2, where the recently opened chamber awaits. After the multiplexer and all the other conflat flanges are tight, the system is pumped as described before.

The chip is finally positioned parallel to the vertical direction, normal to the horizontal science MOT beams bisector, as seen in Fig. 6.4(c). The chip surface is about 1" away from the MOT. A valid concern is to know the local pressure near the devices. Even if the science MOT decays in time scales of 3s without the pushing beam flux, the pressure could be significantly higher near the chip. Indeed, it has been observed that if near infrared light heats up the chip substrate, the science MOT disappears and the pressure gauge increases its registered value. Probably, the rise in pressure is a result of material degassing from the chip surface or glue when it is heated up. Therefore, it might be the case that material is continuously coming out of it at any given temperature, modifying the pressure and probably the lifetime of any trapped atomic system.

Once mounted, the chip motion has been studied a couple of times using a version of a Twyman–Green interferometer. There, a beam is spatially split in two orthogonal polarizations using a polarizing beam splitter (PBS). One beam is reflected normally on the chip and the other is reflected on a mirror in the optical table, each of them passing twice through a $\lambda/4$ waveplate. After that, the beams are combined in the same PBS, the common polarization is filtered by a rotated PBS and a photodiode detects the intensity as seen in Fig. 6.5(a). The intensity can be analyzed in a spectrum analyzer and its power spectrum measured. Different acoustic resonances can sometimes be observed that change every time the chip is replaced. The amplitude is not immediately calibrated by just observing the power spectrum. The time trace is relatively quiet, with some noticeable oscillations at ~65Hz as seen in Fig. 6.5(b). When the chamber is shaken by hitting it rhythmically with a screwdriver, the amplitude of the oscillations increases, as seen in Fig. 6.5(b). This is attributed to a fringe wrapping in the interferometer, meaning the chip moved more than half a wavelength. That intrusion changes the voltage at the photodiode output by about 0.1V. When the system is quiet, the voltage intrusions are only about 0.05V. Therefore, the chip shakes only a fraction of a wavelength when it is not forced. It is hard to draw any further quantitative conclusion, as other parts of the system might shake, so there could be higher frequency oscillations in principle

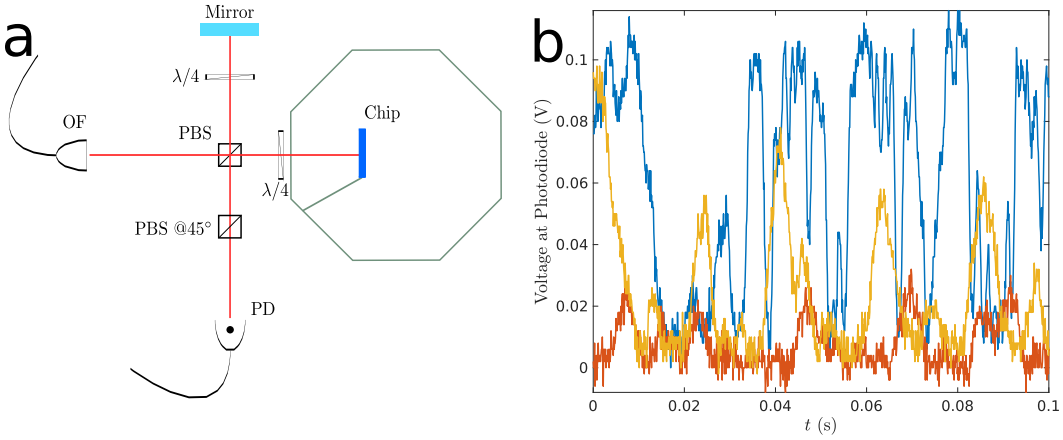

Figure 6.5: Twyman-Green interferometer to measure chip vibrations. In (a) the optical setup for the interferometer is shown. In (b) different time traces measured at the photodiode (PD) reflect the vibration of the chip. The red and yellow trace are two traces taken under quiet conditions, amd indicate that all the equipment is on and the system left by itself. The blue trace was taken while tapping the science chamber (indicated in green in (a)).

not taken into account or we could just have been lucky that no one was trying to park near the lab, but if the chip shakes it happens with time scales of 20ms. New measurements will be taken soon, as it might be a relevant source of phase noise and it changes every time the device is changed.

MiniMOT

In order to position atoms close to the nanostructure, different procedures where used during my time in the group. At the beginning, an additional set of six almost orthogonal MOT beams with 1mm diameter were threaded through the chip's window. The science MOT with tens of millions of atoms was cooled into a moving frame by quickly changing the magnetic field, through a two-photon process called velocity selective resonance [97]. The atoms were recaptured in the new miniMOT. Usually around 2×10^6 atoms would be recaptured and cooled to 40μK. This new MOT is a bit more particular than its cousins (science and source), as it is formed near the dielectric structure and by small beams.

The size of the MOT beams is relevant to determine the trapping volume and the capture velocity. When the beams are small, the atoms might be able to escape the trapping volume resulting in a small lifetime for the MOT. In most of our group experiments, the cooled atomic cloud has decay times of 50ms. During that time, guided mode traps were placed as in [40, 29], and different cooling techniques were

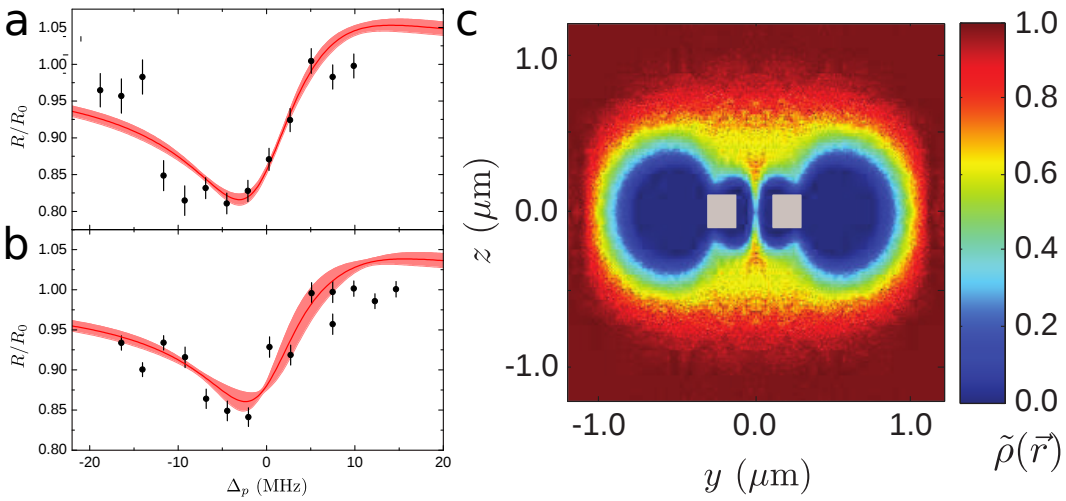

Figure 6.6: Cold atomic cloud around the APCW. Measured reflection spectra and theoretical fit for the APCW in (a) and (b). In (b) the miniMOT density is reduced by 25%. The fits are based on transfer matrix models. (c) Simulated relative density of atoms around the device considering surface forces and the blue detuned guided mode excitation. Figure adapted from Goban et al. [39].

employed to try to load the APCW nanotraps, as in the nanofiber case.

Noticeably, by using a single blue detuned guided mode detuned $\Delta = 10$GHz from the D1 transition and with less than 1μW of power, the reflection of a weak resonant probe guided mode caused by the atoms was enhanced [39]. Numerical simulations showed that the blue detuned guided mode favors the atoms to localize near the center of the cell, 30nm away from the surfaces. This localization is just temporal; the atoms transverse that region and stay there a significant time to scatter some guided mode probe photons. The blue guided mode still prevents the atoms from entering the gap between the beams, as there is a significant intensity there which repels them. On the other hand, trajectory simulations showed that the atom density above the APCW gap is significantly increased when the guided mode is present. From the information gained from the simulations and reflection measurements, we determined that an average of 1.1 ± 0.4 atoms were present at every time around the structure with an average coupling $\Gamma_{1D}/\Gamma' = 0.32 \pm 0.08$, already significantly bigger than in the nanofiber experiments. Details of the density around the device and reflection measurements can be found in Fig. 6.6.

For the measurements in [68], the device architecture was not as developed as it is now. Furthermore, working with the miniMOT became remarkably complicated. The miniMOT characteristics were extremely dependent on several parameters,

like beam alignment, scattering on the chip window, power, and science MOT positioning. Additionally, it was clear that these kind of procedures were going to be inadequate as new structures were designed and new ways to load and cool atoms near the device were needed. For that reason, two different schemes were developed. First, Lab 11 developed the single beam external illumination trap loaded from the miniMOT as discussed in Chapter 5. On the other hand, Lab 2 started to develop a new way to deliver high density cold atoms to the structures, based on the optical lattice schemes shown in Chapter 5, that does not depend on the miniMOT.

Laser and optical system

The laser system used is straightforward. The near resonant light to the $6S_{1/2}\ F = 4$ ground state is derived from a home made ECDL laser, locked to the $6P_{3/2}F = 3'$-$6P_{3/2}F = 4'$ crossover by means of a saturation absorption spectroscopic signal[4]. About 40mW of power are used to injection lock another laser and seed a tapered amplifier (TA) that outputs around 600mW of power. A series of polarization elements and double pass AOMs sifts the frequency of the TA output closer to the desired transition. In particular, near resonant light to the $F = 4 \rightarrow F = 5'$ transition is taken from here to form the source MOT, the science MOT, the pushing beam, and the imaging beam. An additional beam near resonant with the $F = 4 \rightarrow F = 4'$ is used to depump the atoms to the $F = 3$ ground state. The TA output has a significant ASE pedestal that carries spectral power at different wavelengths and spreads above 50nm around the seed's wavelength. In order to avoid resonant heating, the TA is not used to create optical dipole traps. An additional homemade ECDL laser is phase locked to the master and used to interrogate the atoms around the structure.

An additional ECDL laser is locked around the $6S_{1/2}\ F = 3$ resonant frequency, specifically at the $6P_{3/2}\ F = 3' - 6P_{3/2}\ F = 4'$ crossover. This light is properly shifted and acts as a repumper in both MOTs. An injection locked laser is used to have enough power. Furthermore, an $F = 3 \rightarrow F = 2'$ optical pumping beam is taken from this laser and used in the DRSC scheme discussed in this thesis.

Having covered the D2 transitions, lasers to cover the D1 line are needed. There are few companies that sell diodes at that frequency, and only large batch requests are subject to production. As a solution, two DBR lasers were bought to operate at the desired wavelength. As the excited state manifold is quite sparse, with two hyperfine states separated by 1GHz, a the crossovers usually do not appear and it is required to

[4]Here, the prime in the angular momentum value appears only on excited states.

lock to the transitions. One of the lasers is locked to the $6S_{1/2}\ F = 3\text{-}6P_{1/2}\ F = 3'$ transition and the second laser is phase locked to the master. The phase lock can be done either at a beat note of 1GHz or at 9GHz, but it is more convenient to just lock to the other ground state transition $6S_{1/2}\ F = 3\text{-}6P_{1/2}\ F = 4'$. This light is usually used to probe the atoms in the D1 transition.

The guided mode trap lasers are two commercial ECDLs, one near the D2 and the other near the D1 transitions, that can be tuned over a 20nm range by rotating the diffraction grating. The free-space optical lattice light is the output of a Solstis M2-Lasers Ti:Sapphire laser that can be also scanned automatically from 700nm to 980nm. This laser is sometimes used to study the optical properties of the device, specially if it is inside a vacuum environment.

Frequency filtering is usually done by using lithographically patterned volume Bragg gratings (VBG) that can be aligned to reflect with high efficiency ($> 95\%$) light in a 40GHz range around the center wavelength λ_0 for any polarization. The central wavelength can be easily adjusted by changing the VBG incidence angle. Transmission across the VBG is almost lossless for light not in the filtering range, so light with different frequencies can be combined with high efficiency using a VBG. For example, the probe and guided mode trap beams need to be combined before they are sent to the device and in some cases only a 300GHz ($\sim$ 1nm) difference between the probe and one of the trap beams frequencies exist, making it challenging to succeed. A simple set of VBG can do the task.

Imaging is an important part of the daily characterization and measurements of the system. Fluorescence from the atoms is hard to use as atoms need to be observed usually from certain distance and the signal strength depends on the collected scattered photons. In the current system, the closest an objective can be to the atoms is about 6cm, although the off-angle is large ($\sim 40^\circ$). A more convenient family of methods to use are the absorption imaging techniques. Absorption imaging is done by illuminating the atoms with a laser beam and imaging the shadow cast by the atoms onto a CCD camera. Because cameras are not sensitive to phase, the absorption image shows the spatial variation of sample's transmission. A good review on imaging methods is [192]. Absorption imaging is sensitive to energy shifts, so for big traps its topography can be resolved by a combination of images at different detunings of the probe. For small traps, the trap shift can be manifested as an enhancement in the total signal for different detunings.

The imaging procedure is simple: the atoms can be released from the trap or not,

and at any given time a pulsed resonant light beam is sent to the atoms. Usually, in order to increase the signal a cycling transition is used. In the spatial profile of the output beam the atoms leave a hole that can be imaged in a detector. A single image does not reveal all the useful information as it also contains all the information of the spatial profile of the imaging beam and the imaging system. A second image without the atoms can be subtracted to the first in order to normalize the first image. The sample's optical density is just $OD(x_i, y_j) = -\ln\left(I_{atoms}(x_i, y_j)/I_{noatoms}(x_i, y_j)\right)$ which can be easily inferred from the data. To collect the light and focus the image onto the CCD camera we use an Infinity long working distance microscope with a IF-3 objective and a doubling tube that gives a resolution of about 5.5μm at a working distance of 170mm. Different setups with standard camera objectives that offer a much lower resolution (1/8th of the mentioned resolution) are also used. Usually the probe beams for absorption imaging are 1 inch waist beams.

Most of the optics in the system is designed to have the two MOTs working at the same time, while having the possibility to perform different kind of cooling techniques and image at different positions. The 1D optical lattice has its own optical system and propagates normally to the chip surface. Atoms are loaded in the lattice and moved towards the chip as described in Chapter 5. In the same path, an optical pumping beam and imaging beam are aligned.

The experimental control happens in the central computer. A LabVIEW code controls a series of analog outputs and inputs (AO/AI) as well as different digital PFI ports. The whole sequence is stored as a big MATLAB matrix where the indexes represent the corresponding analog or digital channel and the timing array, while the entries are their values. Most of the digital outputs work as TTL ports to control RF switches, camera triggers and any other timed action. The timing resolution is $10\mu s$ and it is usually enough to control most of the tasks. The set of AOs are usually used to set different RF frequencies and powers by using commercial VCOs and VCAs.

The data acquisition for probing atoms near the APCW is mostly based on time precise photon counting. The photon counts are usually recorded in a single photon counting module (SPCM) whose output goes through a gated photon counter that outputs an analog signal. These pulses are finally digitalized by a commercial multiple-event time digitizer card (FAST ComTec MCS6A). For every single cycle of the experiment, a time trace with 200ps resolution is generated and saved as a binary file that can be read later.

6.2 Optical lattice for atomic transport

The optical lattice 1'' away from the chip

Having described most of the characteristics of the experiment apparatus, the next step is to describe the measurements. The experiment starts by loading a one dimensional optical lattice near the center of the science chamber, following some of the tips mentioned in Chapter 3. The optical lattice light is derived from a Ti:Sapph laser with 2W of output power, pumped with a Verdi G-10 laser. The laser is connected to a wavemeter with 600MHz resolution and has a software interface that locks the laser frequency using the etalon and reference cavity. Most times, the red optical lattice is red detuned and the laser frequency is locked around 853.5nm, which is 1.3nm below the atomic transition ($\Delta = -2\pi \times 500$GHz). The laser is located in the room adjacent to Lab 2 and a 20 meters long optical fiber delivers around 800mW of power to Lab 2. It has been observed that for longer fibers the transmission efficiency drops significantly as the input power increases. By monitoring the damping port of the optical isolator placed before the fiber input, a fast flash is observed in that port when the input power increases above 1W. That could be associated with stimulated Brillouin scattering (SBS) [193] from the fiber material. In this case, Stokes backreflected optical power is initiated by thermal phonons and there exists a threshold where the nonlinear gain is significant enough to reflect the input beam into the backwards direction. The gain depends on different material parameters, but it is also a function of the fiber length. The observations made in Lab 2 seems to reflect that dependence.

The light is then divided into two paths with similar power and orthogonal polarization. Each path goes through an 80MHz double pass AOM that shifts both frequencies in the same direction. Each beam is coupled to a 1 meter polarization maintaining optical fiber that is launched on the optical table using a 15mm molded aspheric lens that collimates the beam to a waist of 1.5mm. Two dielectric mirrors are used to modify the beam pointing, and polarization elements are used to align the polarization of both beams parallel to the horizontal plane. Before each side of the chamber, a 300mm achromatic doublet lens mounted on a 3-axis translational stage is used to focus each lattice beam inside the chamber. The two beams are focused to the same point, usually about 7mm away from the chip and 1.8cm from the science MOT. Using the edges of the chip's window, a knife edge measurement allows to measure the beam waist. At the focal point, the beam is focused to 55μm with a Rayleigh length of $z_R = 11.1$mm. Just before the chamber's viewport a 1" polarization beam-splitter is placed. Usually, after all the optics each beam has a

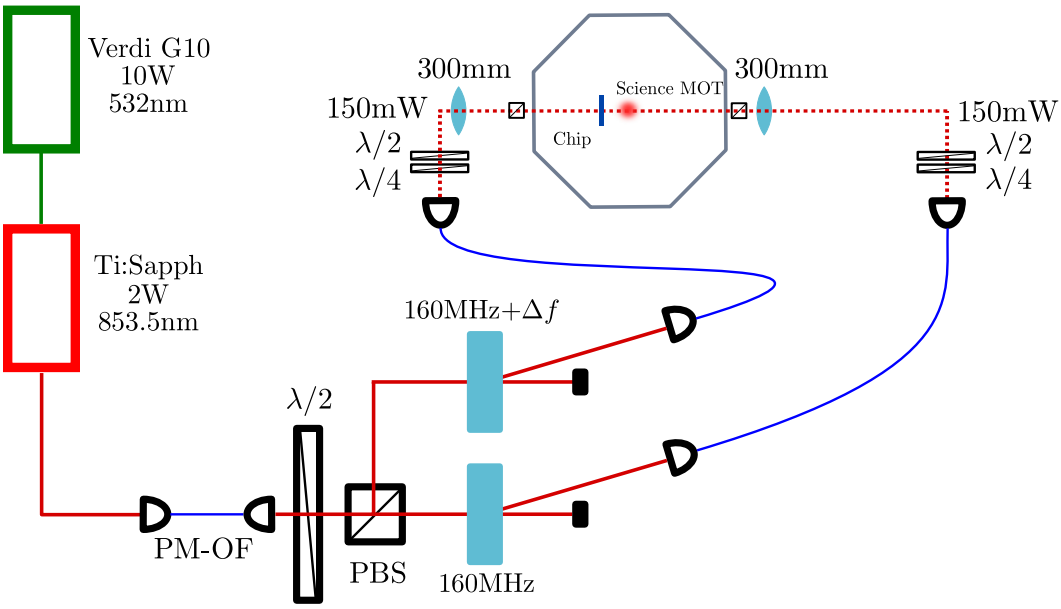

Figure 6.7: Optical lattice setup. The light derived from a Ti:Sapph is split in two paths whose frequencies are shifted in a controlled way and then are interfered in the the science chamber. The frequency ramp $\Delta f(t)$ controls the motion of the conveyor belt.

150mW of power before entering the chamber. The beams are aligned to a device and usually a good backcoupling efficiency is observed. The laser light path that creates the lattice is shown in more detail in Fig. 6.7.

The RF driving signal for each AOM causes the atoms to move towards the chip. One of the AOMs is driven by a 80MHz signal generator that also outputs a 10MHz signal used to phase lock other generators. The other AOM is driven by mixing a 70MHz phase locked signal and a 10MHz signal generated by a commercial DDS (AD9854). This DDS is clocked by a 200MHz signal, phase locked to the others, and is able to store in its internal memory an arbitrary frequency ramp. A band-pass filter (5MHz bandwidth) removes the additional frequency components generated in the mixing process. The frequency ramps are programmed on an Arduino microprocessor and transmitted to the DDS through a serial SPI bus.

Transfer of atoms from the MOT into the optical lattice with a high efficiency is of paramount importance for the experiment. A prerequisite for a successful loading is a thorough alignment of the dipole trap laser onto the MOT. The overlap is controlled by changing the current in the science chamber bias coils. The lattice beams are turned on and the MOT operates for 35ms. During that time, the MOT beams power and detuning are changed and the quadrupole is on. The repumper

power is significantly reduced, almost to its minimum ($\sim 20\mu$W total), increasing the time atoms remain in $F = 3$, in order to avoid resonant light re-scattering and inelastic collisions that turn on at higher densities as seen in Sec. 3.4. After that, the quadrupole is turned off and the bias field is dynamically changed, trying to keep the atomic cloud around the lattice beams. Usually, the correction on the magnetic field is performed mostly along the quadrupole axis. The change in the magnetic field lasts about 10ms and coexists with the changes in the MOT beams parameters. At this point the lattice is loaded almost to its full capacity and the sample thermalizes close to its Doppler temperature (125μK).

After that stage, the current in each of the bias coils is set to cancel any residual magnetic field at the lattice position. To set this values a microwave scan is performed, usually every few weeks. The MOT beams and repumper beams are turned off and a 1ms depumper beam pumps all the atoms to $F = 3$. Subsequently, the atoms are prepared among all the 7 m_F states, with its specific distribution given by tyhe details of the optical pumping process. A residual magnetic field will create a Zeeman-like shift of the form $g_F|\mathbf{B}|$, where the g_F coefficient determines the sensitivity to the magnetic field. For $F = 3$ ($F = 4$), the g_F coefficient is $g_F = -350$kHz/G ($g_F = 350$kHz/G). A microwave field with frequency around the ground states hyperfine splitting can coherently transfer atoms between $F = 3$ and $F = 4$ and in the presence of a magnetic field there will be several frequencies where transfer between different m_F states can happen. A π-pulse transfers most of the atoms to $F = 4$ where the atoms can be imaged as described before. As the microwaves are not polarized, every possible transition among the 15 is usually excited. The splitting between two consecutive peaks is proportional to the magnitude of the magnetic field. By changing the bias coils settings and repeating the microwave scan around resonance the peaks can merge into a single peak around resonance, indicating that the magnetic field is nulled as seen in Fig. 6.8(a). When all the peaks merge and absent power broadening, the width of the spectrum determines the residual magnetic field. For the yellow trace in Fig. 6.8(a), the peak is about 40KHz wide, giving a residual field $B_{res} \approx 10$mG. Given the microwave power at the atoms location, a π-pulse can be found by changing its duration and maximizing the transfer, as seen in Fig 6.8(b). For the experiment, that time is about 55μs and the associated Rabi frequency is $\Omega_{Rabi}^{\mu-\text{wave}} = 2\pi \times (4.5 \pm 0.2)$kHz.

Once the field has being nulled, polarization gradient cooling further cools the atoms in the lattice. Temperatures as low as 10μK for non-trapped atomic clouds have

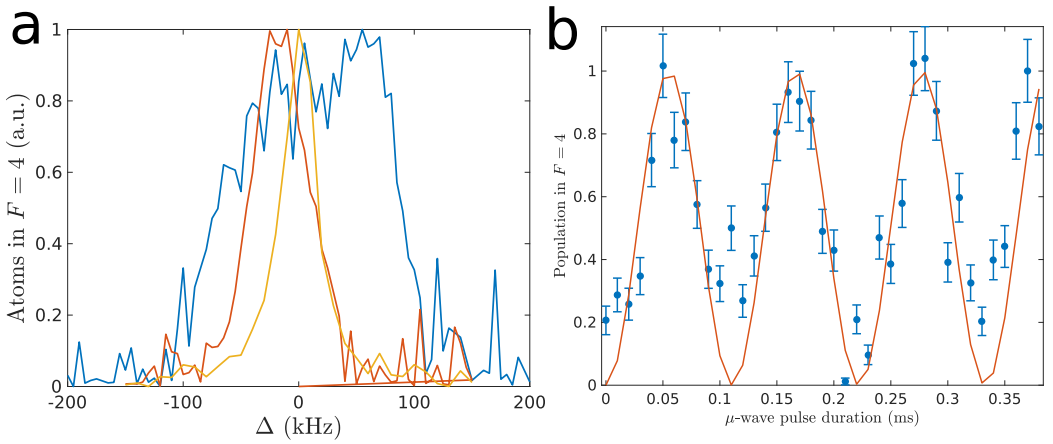

Figure 6.8: Microwave spectroscopy of untrapped atoms. The atoms are exposed to a π microwave pulse that pumps them from $F = 3$ to $F = 4$. If residual magnetic fields are present, the different sublevels broaden the central peak or are completely separated if the field is too big. In (a) the transition from the blue-red-yellow scan represent the transition from a bigger field to a smaller one as the bias coils are changed. The duration of the π-pulse is extracted from (b).

been measured by means of time of flight measurements, but in order to maximize the atom number loaded in the trap the temperatures measured are around 40μK. Atom number in the lattice is usually measured after waiting at least 50ms in order to get rid of the non trapped science MOT atoms. For deep traps, where a few million atoms are loaded, significant difference between the lifetime for samples that are pumped to $F = 3$ and samples that remain in a balanced mixture between $F = 3$ and $F = 4$ are observed. When the atoms are polarized to $F = 3$, after holding them in place for 100ms usually the lattice contains 2×10^6 atoms with an axial and radial Gaussian rms width of $\sigma_{latt-ax} = 450\mu$m and $\sigma_{latt-rad} = 80\mu$m, respectively.

At the science MOT the optical dipole potential has a depth

$$U_0^{MOT} = 400\mu\text{K},$$

with trap frequencies

$$\nu_z^{MOT} = 262\text{kHz},$$
$$\nu_\rho^{MOT} = 374\text{Hz},$$

for the corresponding waist radius $w_{MOT} = 135\mu$m, $P = 150$mW, $\lambda_{trap} = 853.57$nm and $\alpha_s = 85500$ a.u.[5] (the difference between the scalar polarizabilities for the two

[5]In atomic units (a.u.) the atomic unit of electric polarizability is $e^2a_0^2/E_h = 4.64877 \times 10^{-41}\text{C}^2\text{m}^2\text{J}^{-1}$ according to the CODATA value.

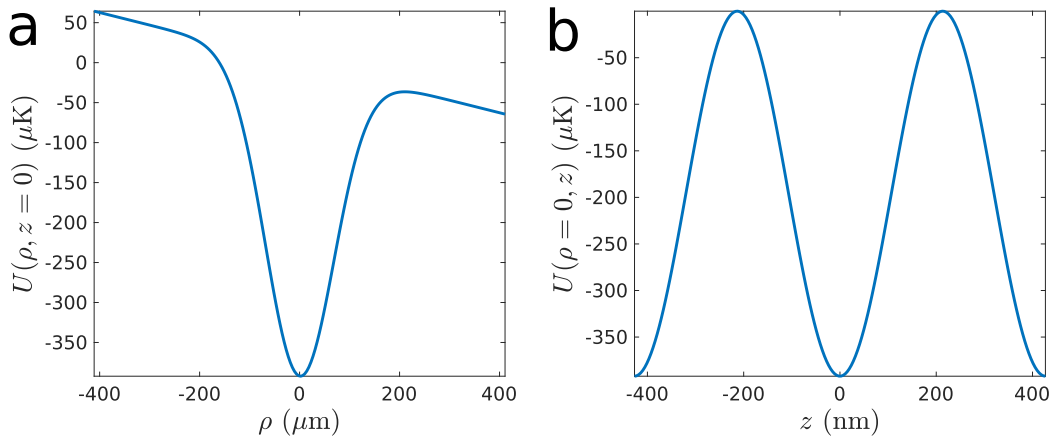

Figure 6.9: Optical dipole trap at the science MOT. In (a) the radial confining potential with the effect of gravity is shown while in (b) the axial dependence over a wavelength space is shown.

ground state is about 1.7% of its mean value at this detuning). Each pancake is characterized by a radial thermal length $L_\rho = 46\mu$m and axial thermal length $L_z = 17$nm. Along the z-direction gravity reduces the trap depth by 35μK. The off-resonant scattering rate is $\Gamma_{sc} = 2\pi \times 88$Hz. Once the atoms move towards the chip, the trap volume reduces significantly. For the same power, the trap depth is

$$U_0^{chip} = 2.43\text{mK},$$

with trap frequencies

$$\nu_z^{chip} = 646\text{kHz},$$
$$\nu_\rho^{chip} = 2.26\text{kHz},$$

and the scattering rate is $\Gamma_{sc} = 2\pi \times 510$Hz. For these calculations, as the lattice light is still close to the Cs D2-line transition, the trap is calculated using the atomic polarizability. The simple two level approximation tends to overestimate the trap strength by almost 50%. Fig. 6.9 shows the trap along different axis at the MOT position, considering gravity.

Further cooling for the trapped atoms is performed by the DRSC technique introduced in Section 3.4. In order to cool the atoms to its vibrational axial ground state, the polarization between the lattice beams is rotated by 15°. That weakens the trap depth, but creates the desired Raman coupling. An additional circularly polarized $F = 3 \rightarrow F = 2'$ optical pumping beam is introduced along the y-direction. Usually it is operated at very weak intensities with just about 200nW in its 1mm waist

($\sim 0.01 I_{sat}$) and detuned about $-\Gamma$ from resonance, in order to avoid broadening in the $|3,2\rangle$ state. Higher powers tend to decrease the efficiency of the cooling and result in atom loss. A bias magnetic field produced by a fast switch in the current through the bias coils along the y direction is introduced to create a degeneracy of the Zeeman sublevels and vibrational levels as described before. Usually, after the DRSC is successfully applied the atoms are polarized in the $|3,3\rangle$ state. A fraction in $|3,2\rangle$ can remain as a small π polarized component is needed in the optical pumping beam.

In the interest to find the actual value of the applied bias magnetic field for DRSC, the current through the y-coils is scanned in small steps and the atoms are held in the trap for 100ms before being released and imaged 8ms later. An increase in the total number of atoms, accompanied by a reduction in the cloud size, and hence denser (peak OD), is the symptom of cooling. For the opposite current direction, heating is observed although it exhibits a much broader resonance than the cooling. By monitoring the OD for different B_y fields, usually a couple of resonances are observed once the Zeeman shifts equals the energy of one and two vibration quanta as seen in Fig. 6.10(b). Free space imaging techniques usually measure an axial temperature $T_{ax} = 20\mu$K and radial $T_{rad} = 45\mu$K, although the latter tends to reduce as cooling extends for longer times, probably associated with thermalization due to non-harmonic trap characteristics, small though, and collisions. The observed cooling along the axial direction is fast, and usually 10ms is more than enough. The Rabi frequency associated with the Raman coupling calculated from Eq(3.25) is $\Omega^n_{DRSC} = \sqrt{n}2\pi \times 440$kHz. As a consequence, even smaller angles between the two polarization directions can provide significant cooling. However, the main limitation in the cooling rate is the small optical pumping rate.

After DRSC most of the atoms are pumped to the $|3,3\rangle$ state. If the trap is turned off and a microwave pulse is applied as before, there will be a few narrow resonances associated with atoms populating certain m_F states as shown in Fig. 6.10(a). There, the blue trace hows the resonances associated with atoms populating $|3,3\rangle$ and $|3,2\rangle$ for an unpolarized microwave pulse. However, if the trap is on during the microwave pulse information about the trap can be also obtained. In Fig. 6.10(a) the red trace indicates a widening of the peaks, associate with the trap potential and the sample temperature. Furthermore, it is possible to excite transitions between different vibrational levels manifested as sidebands around the carrier. For example, an atom can be excited from state $|3, m_F, n\rangle$ to the state $|4, m_{F'}, n \pm 1\rangle$

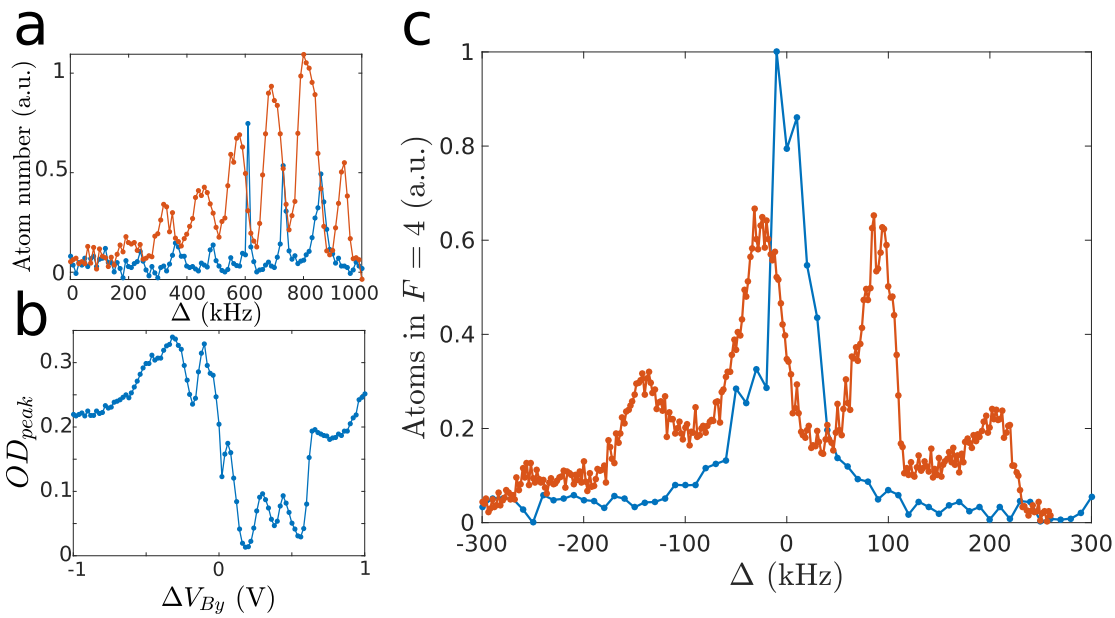

Figure 6.10: Degenerate Raman sideband cooling in a 1D optical lattice. In (a), for the applied bias magnetic field, a microwave spectrum revels the distribution of the atoms among the different sublevels for the lattice on (red) and off (blue). The lack of a specific polarization for the microwave pulse excites several transitions. In (b) the results of the absorption imaging analysis shows the peak optical depth increasing as the voltage that controls the current through the bias coils in the y-direction is applied. Heating is observed for a different direction. Finally, in (c) a microwave spectrum is taken after applying a big magnetic field in order to isolate a single Zeeman sub-level with the trap on (red) and off (blue). When the lattice is off (blue), the carrier is narrow and centered in the free-space expected position. Once the trap is on (red), the vibrational sidebands are reveled showing that the sample is significantly cooled to the ground state. Peaks at $\Delta = -140$kHz and $\Delta = 100$kHz correspond to the red and blue sideband respectively. The carrier for the red trace is located at $\Delta = -20$kHz. The trap is different to the one described in the text (bigger waist), and hence the resolved vibrational frequency is smaller ($\nu_z = 120$kHz). The difference between the carrier centers for the blue and red trace (20kHz) is a consequence of the different polarizability for the two ground states.

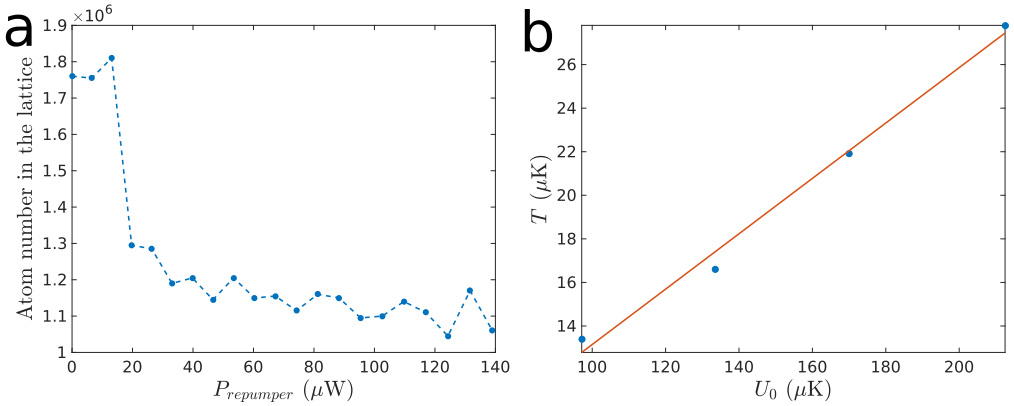

Figure 6.11: (a) Repumper power influence in the lattice loading. (b) Trap filling after DRSC considering the radial temperature vs the trap depth U_0.

if the microwave frequency is shifted by $\pm\nu_z$ with respect to the carrier, exciting a vibrational sideband. The asymmetry in the sidebands is associated with the fraction of atoms that occupy the vibrational ground state as those atoms can not undergo a transition that reduces its vibrational quantum number. A big blue sideband and a disappearing red sideband is usually a good indication of ground state cooling. It can be also used to estimate the temperature, as in equilibrium the ratio between the sidebands should be $e^{-\frac{\hbar\nu_z}{k_B T_{ax}}}$. A measurement of the sidebands is shown in Fig 6.10(c). The width and asymmetrical characteristics of the sidebands are associated with the radial motion and temperature and are hard to resolve in this case. For a beautiful thermometry analysis the work of Blatt et al. [120] is recommended.

The dependence of the atom number loaded into the one dimensional lattice as function of the repumper power is shown in Fig. 6.11(a). As observed by Kuppens et al. [122], low values of the repumper power enhance the loading efficiency. In that way, the atoms remain more time in the $F = 3$ ground state, where resonant light re-scattering and inelastic collisions are suppressed as explained in in Section 3.4.

Other measurements where performed to study the distribution and localization of the atoms in the trap. In particular, in order to estimate the magnitude of different heating processes the ratio between the atoms total energy E and the trap depth U_0 is necessary. The measurement is simple, the power is reduced and the trap depth reduced proportionally. For each power the temperature of the sample is measured. At the science MOT position before DRSC, the ratio is about $E/U_0 \approx 0.3$ but after DRSC the ratio can decrease to $E/U_0 \approx 0.13$. That means that the atoms are really

localized in the trap. The measurement can be seen in Fig. 6.11(b).

Optical conveyor belt

By carefully controlling the RF driving source, submicron precision in a few centimeters distance can be achieved for transporting atoms [194, 195, 196]. As described before, the dipole trap formed by the two counter-propagating beams with waist w_0 and Rayleigh length z_R produces a time and position dependent optical dipole potential[6]

$$U(z,t) = U_0 \frac{w_0^2}{w^2(z)} \mathrm{e}^{-2\frac{\rho^2}{w^2(z)}} \cos^2(\pi \Delta f t - kz), \tag{6.3}$$

where $w(z) = w_0\sqrt{1+(z/z_R)^2}$ is the beam radius with waist w_0 and Δf is the frequency difference between the two beams imprinted by the two AOMs. In the laboratory frame, this pattern corresponds to a moving standing wave along the optical axis with velocity $v_{lattice} = \frac{\pi\Delta f}{k} = \frac{\lambda\Delta f}{2}$.

After the atoms are loaded and cooled into the lattice by 40ms of DRSC, the lattice is ready to move. Over a big range of final velocities, $10m/s < v_{lattice} < 1m/s$, it was verified that short acceleration times were ideal to avoid losses. In most cases the lattice accelerates from 0 to $v = (1\mathrm{MHz})\lambda/2 \approx 0.43\mathrm{m/s}$ in 100μs. This acceleration a_{latt} is significant, about $4.3 \times 10^3 \mathrm{m/s^2} \simeq 440g$. In the accelerated frame the potential is the sum of the standing wave one $U_{latt}(z) = U_0 \cos^2(kz)$ and the contribution of the acceleration force $U_a(z) = ma_{latt}z$. The result is a tilted $\lambda/2$ periodic potential with an smaller effective potential depth. The atom remains trapped as long as the acceleration potential does not create a force larger than the lattice force, that is the same as the existence of a potential local minimum. The acceleration is thus fundamentally limited by the trap depth U_0, such that the maximum acceleration is $a_{max} = U_0 k/m = 2.3 \times 10^5 \mathrm{m/s^2} \simeq 2.35 \times 10^4 g$, which is about 50 times bigger than the accelerations used in the experiment. For the accelerations used in the Lab 2 experiments, this effect weakens the lattice depth by $ma_{latt}\lambda/2 \approx k_B 30\mu\mathrm{K}$.

In this work, bigger accelerations are hardly ever used, although we have experimented with 1.6MHz and 2MHz moving lattices. Experimenting with faster lattices have problems apart from what was just discussed. A common technical problem is

[6]Here the intensity profile is assumed to be transversally flat according to the discussion in Section 3.3.

the AOMs bandwidth that limits the use of lattices faster than 10MHz at the expense of reducing efficiency significantly.

When the acceleration starts, it is rapidly switched on from 0 to a_{latt}. The equilibrium position of the accelerated potential is shifted by the amount $\Delta z = -\frac{\arcsin(a_{latt}/a_{max})}{2k} \approx -13\text{nm}$. These sudden changes of the potential, either heat or cool the atoms depending on the relative position in the potential. If before any change in the potential the atom has a significant potential energy, a sudden change in the potential, that results in a weaker barrier, might not be able to confine the atom. As in the experiment $a_{latt}/a_{max} \ll 1$, the maximum energy gained due to an abrupt jump is insignificant. As described before, the initial thermal energy distribution of the atoms in the trap corresponds to $0.2U_0$. A slow change in the acceleration would avoid this heating because the atoms would then adiabatically follow the motion of the potential well, but at expense of trap loss due to the finite lifetime of the atoms in the optical lattice.

Losses in the moving optical lattice

As described before, the lifetime of the atoms in the lattice is limited by several different mechanisms. Here, a more detailed analysis of the different losses mechanisms is presented. As a note to the reader, many of the heating models considered here are just that, simplifications of the real and more complex problem.

Cold Collisions

For short times, very big state dependent losses are observed. The measurements performed prepare atoms in *(i)* a balance mixture of $F = 3$ and $F = 4$ or *(ii)* every atom in $F = 3$ by turning on a depumper beam. Among all the mechanisms that can take place and generate losses, the only one that can explain such a difference between the two ground states are state dependent collisions. Along with absorption imaging measurements, the procedure developed in Section 3.3 gives peak densities of $\sim 1 \times 10^{12}$ atoms/cm^3, which is enough to start showing two-body losses for both states over the time of transport our lattice to the APCW. This has implications not only in the fast atom number decays, but also on the observed long term lifetime as seen in Fig. 6.12. It has also being verified that if a smaller number of atoms is loaded, by for example reducing the efficiency of the push beam scheme, the two lifetimes become more comparable. In order to reduce the effect of this loss, the atoms are continuously pumped to $F = 3$ during the cooling and transport to the

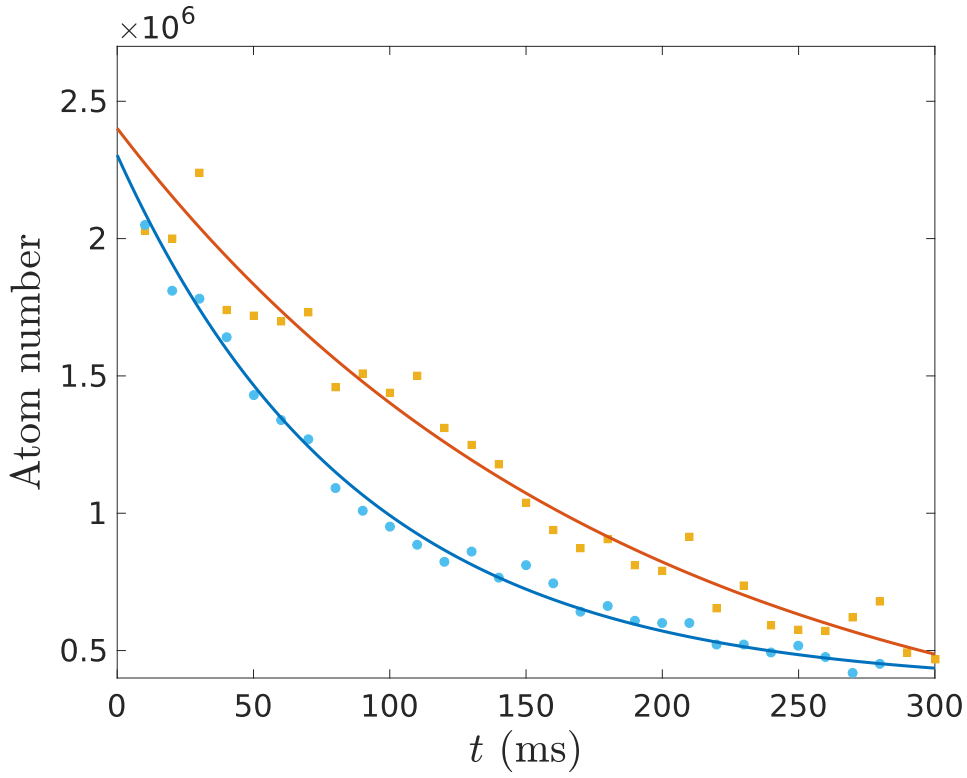

Figure 6.12: Lifetime for different sample preparations. The red trace is the exponential decay fitting for the orange square measurements when the atoms are pumped into $F = 3$ (case *(ii)* in the text) with $\tau = 200$ms, while the blue trace is the fitting for mixed state preparation in $F = 3$ and 4 (case *(i)*) with $\tau = 80$ms.

chip. If the atoms are further cooled continuously observed lifetimes can exceed 500ms.

Recoil heating

The observed lifetime could be explained by big contributions due to off resonant scattering from the lattice beams. The scattering rate at the MOT position $\Gamma_{sc} = 2\pi \times 88$Hz means that a photon is scattered every 1.8ms. The atom oscillates many times while absorbing and emitting photons such that the momentum transfer averages to zero. In the best case, each absorption and emission process increases the atomic energy by the one-photon recoil energy E_r[7]. The energy of the atom increases then at a rate $\dot{\bar{E}} = E_r\Gamma_{sc}/2$, where the factor of two comes from applying the virial theorem. Therefore, only n_{heat} photons are needed to heat the atom out of

[7]If vector shifts are present, the recoil energy is higher, as additional energy is carried away in every scatter event.

the trap with

$$U_0 = 2n_{heat}E_r. \tag{6.4}$$

This gives $n_{heat} \approx 9.7 \times 10^2$ photons which limits the lifetime to about 4s, and 2.5s considering that the atoms fill the trap to about a third of its depth. From the MOT decay measurements, the background gas collisions might will limit the trap lifetime to about 3s. There is still almost a tenfold difference between the projected lifetime and the observed one. It has been verified that, the lifetime depends on the power used to load the lattice, and hence the trap depth.

Excited-ground state dipole force fluctuation

For a two level system the polarizabilities have opposite signs, therefore, at the potential minimum for the ground state, the excited state has a local maximum. Over several excitations, the randomly fluctuating dipole force causes heating. Cs atoms and their trap potentials are more complex than just this two level approximation, but it is at least a simple model to develop intuition about the scaling and magnitude of this effect. A great review on this topic is presented by Dalibard and Cohen-Tannoudji [197].

The idea is to consider the momentum transfer that results from a fluctuation in the dipole force. In the ground state, an atom experiences a position dependent force with magnitude $F_g(\mathbf{r}) = |\nabla U_g(\mathbf{r})|$, while in the excited state the force is $F_e(\mathbf{r}) = |\nabla U_e(\mathbf{r})|$. As a consequence of the different sign for the polarizabilities and hence the optical dipole potentials[8], at the same position the forces for ground and excited state have, approximately, opposite direction as can be seen in Fig. 6.13. As the excited state has lifetime $\tau = 1/\Gamma_0 \approx 30$ns, much shorter than the oscillation period in the trap, and the momentum transfer if an atom is excited to the ground state for that time is

$$\Delta p = \tau(F_e(\mathbf{r}) - F_g(\mathbf{r})) = \tau\Delta F. \tag{6.5}$$

This instantaneous momentum transfer, associated with a kick force, is identical to the Langevin equation treatment discussed before in Chapter 3. Therefore, the kicks in momentum space drive a random walk with steps

$$E_{kick} = \frac{(\Delta p)^2}{2m}. \tag{6.6}$$

[8]This remark is true for the $6P_{3/2}$ excited state family, as there are not appreciable light shifts in the $6P_{1/2}$ excited state manifold due to the lattice potential.

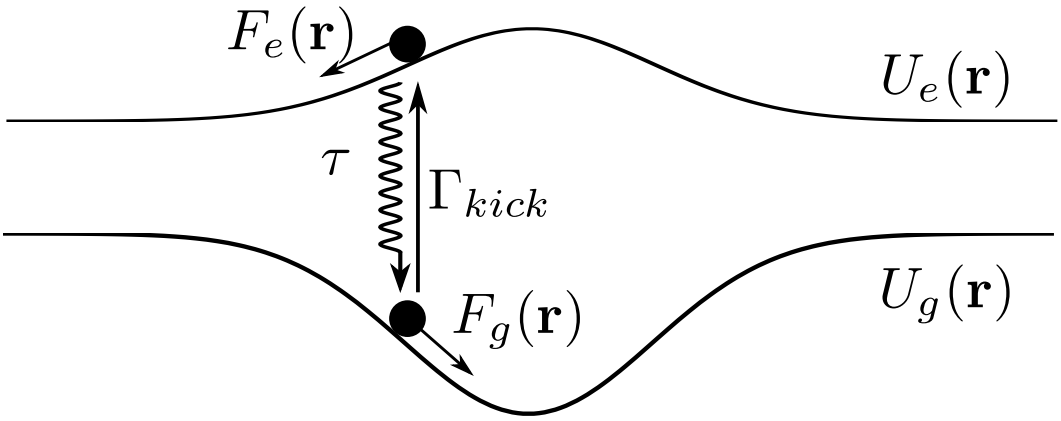

Figure 6.13: Optical dipole force fluctuations as the atom can be pumped to the excited state where the force is different.

For a ground state trap with $U_0 \approx k_B \times 400\mu K$ and considering its variation over a lattice period the force can be estimated as $F_g \sim U_0/(\lambda/2) \approx m \times 6 \times 10^3 g$ and the associated energy step is $E_{kick} \approx 105$nK. The rate at which these kicks happen, $\Gamma_{kick}/2\pi$, is a bit more tricky. It is not immediate that it is the lattice scattering rate, because in the dressed state picture the dipole potential mixes ground and excited state components and the lattice photons absorbed do not necessarily describe changes in the shape of the potentials that lead to these fluctuations. Instead the rate at which this excitations happen is given by [197]

$$\Gamma_{kick} = \frac{\Gamma_{sc}^2}{\Gamma_0} \approx 2\pi \times 2\text{mHz}. \tag{6.7}$$

This process has therefore a negligible effect on the atomic motion giving a heating rate of $\dot{\bar{E}} = 1.23$nK/s.

However, near resonant light can contribute to this form of heating in a more significant way, as associated rate is higher. For a periodic cosine potential, the maximum force F_{max} is experienced at the turning points if the energy is half of the depth of the potential ($E = U_0/2$) where the force varies linearly with the displacement. If the atom energy is significantly smaller than the potential depth, under the harmonic approximation the maximum force is $F_{max}\sqrt{2E/U_0}$, and therefore the heating rate is

$$\dot{\bar{E}} = \Gamma_{kick} \frac{\tau^2 F_{max}^2 E}{m U_0}. \tag{6.8}$$

Along the axial direction, for $E = U_0/2$, the maximum force is

$$F_{max}^{ax} = kU_0 \approx 4\frac{\hbar k \Gamma_0}{2}, \tag{6.9}$$

and along the radial direction a similar argument follows because near the bottom the two potentials are harmonic such that

$$F_{max}^{rad} = \frac{U_0}{w_0}\frac{2}{\sqrt{e}} \approx 0.007\frac{\hbar k \Gamma_0}{2}, \tag{6.10}$$

where both comparisons are made with the maximum force due to resonant light scattering. The axial heating rate is significant $\dot{\bar{E}} = 2.6$K/s. As the radial heating rate is greatly suppressed, axial temperatures could be larger than radial temperatures during continuous illumination. This case does not apply to our experiment, as the only near resonant light present during the transport is the depumper beam, but it only acts if the atoms is pumped to $F = 4$.

Lattice fluctuations

The previous heating mechanisms discussed here have origins in different atomic properties. But very important sources of noise have technical causes that need to be characterized and suppressed as much as possible. Two of these technical noises associated with the laser light and its propagation system can cause fluctuations in the trap depth and position. In the one dimensional lattice, fluctuations of the laser optical power lead to changes in the trap depth, therefore changing the oscillation frequency. Beam pointing instabilities can transversally move the trap, but the phase noise is more important in our interference pattern traps.

Fluctuations in the laser intensity have been proven to heat up atoms trapped in optical dipole traps [124]. In this model, fluctuation in the intensity changes the trap frequencies which, in the quantum picture, drives transitions towards different trapped states, causing heating and cooling. Using perturbation theory and assuming the intensity fluctuations are small the energy increases exponentially ($\dot{\bar{E}} \propto \bar{E}$), where the heating rate associated with a trap frequency ν_0, is [124]

$$\Gamma_I(\nu_0) = \pi^2 \nu_0^2 S_I(2\nu_0), \tag{6.11}$$

and $S_I(\nu)$ is the spectral density of the relative intensity noise defined as the normalized variance of the intensity in a spectral band $d\nu$ around the frequency ν,

$$S_I(\nu)d\nu = \frac{< (\Delta I)^2 >_{d\nu}}{< I >^2}. \tag{6.12}$$

This effect is similar to the classical parametric heating effect, where fluctuations or driving at twice the motion frequency increases the amplitude of the oscillations. Due to the factor ν_0^2, high oscillation frequencies are more critical than low frequencies.

By measuring the power of the laser with a photodiode (Si photodiode), the relative intensity noise $S_I(\nu)$ of the Ti:Sapph in the lab can be determined. The power spectrum of the photodetector output (bandwidth from DC to 10MHz) can be determined in an spectrum analyzer (SRS-760 and HP-E4403B) and by dividing by the DC voltage one obtains the relative intensity noise $S_I(\nu)$. Details are shown in Fig. 6.14(a), where $S_I(\nu)$ is shown over different detection windows, hence the different color traces. At low frequencies, $1/f$-noise and the power line frequency (60Hz) and its harmonics dominate. A series of strong peaks at (2,4,8,12,16,20)kHz dominate the acoustic regime. The fundamental cause of these peaks could be on intrinsic laser noise, electronic noise (power supplies, etc) and noise in the pump laser. At high frequencies the noise becomes flat with the exception of a broad peak around 75kHz and reaches the theoretical shot noise of the photocurrent determined from the DC output voltage. At some point an AOM was used to remove acoustical range noise on the laser intensity, but it never had a significant impact on the lifetime of the trapped atoms, although the laser systems has been updated since that then. A significant fraction of the acoustical noise is due to polarization fluctuations and vibration in the optical elements and in principle can be improved.

The characteristic $1/e$ time constant $\tau_I = 1/\Gamma_I(\nu)$ described in Eq(6.11) is shown in Fig. 6.14(b). If an oscillation frequency of the atom in the lattice coincides with one of the large peaks in the noise spectrum, significant heating is expected. For the calculated trap frequency at the MOT $\nu_z^{MOT} = 260$kHz, the time constant is $\tau_{I,z}^{MOT} = 10$s.

Shifts in the trap position resemble the application of a stochastic force that can induce a random walk in phase space and therefore heating. Transversal position fluctuations of the lattice beams can be caused by acoustical vibrations of the optical elements or by pointing instability of the laser beams. With $S_z(\nu)$ being the relative spectral density of the position fluctuations, the associated heating is given by [124]

$$\dot{\bar{E}} = \pi^3 m \nu_0^4 S_z(\nu_0). \tag{6.13}$$

The spatial stability of the standing wave dipole trap inside the vacuum chamber is not known. At the science MOT position, the waists w of the lattice beams have been changed over a wide spectrum, from 30μm to 150μm. Due to the dependence of the trap frequencies on the waist w and the strong influence the trap frequencies has on the heating, Eq(6.13), it is fair to believe that this is not a relevant heating mechanism in the experiment.

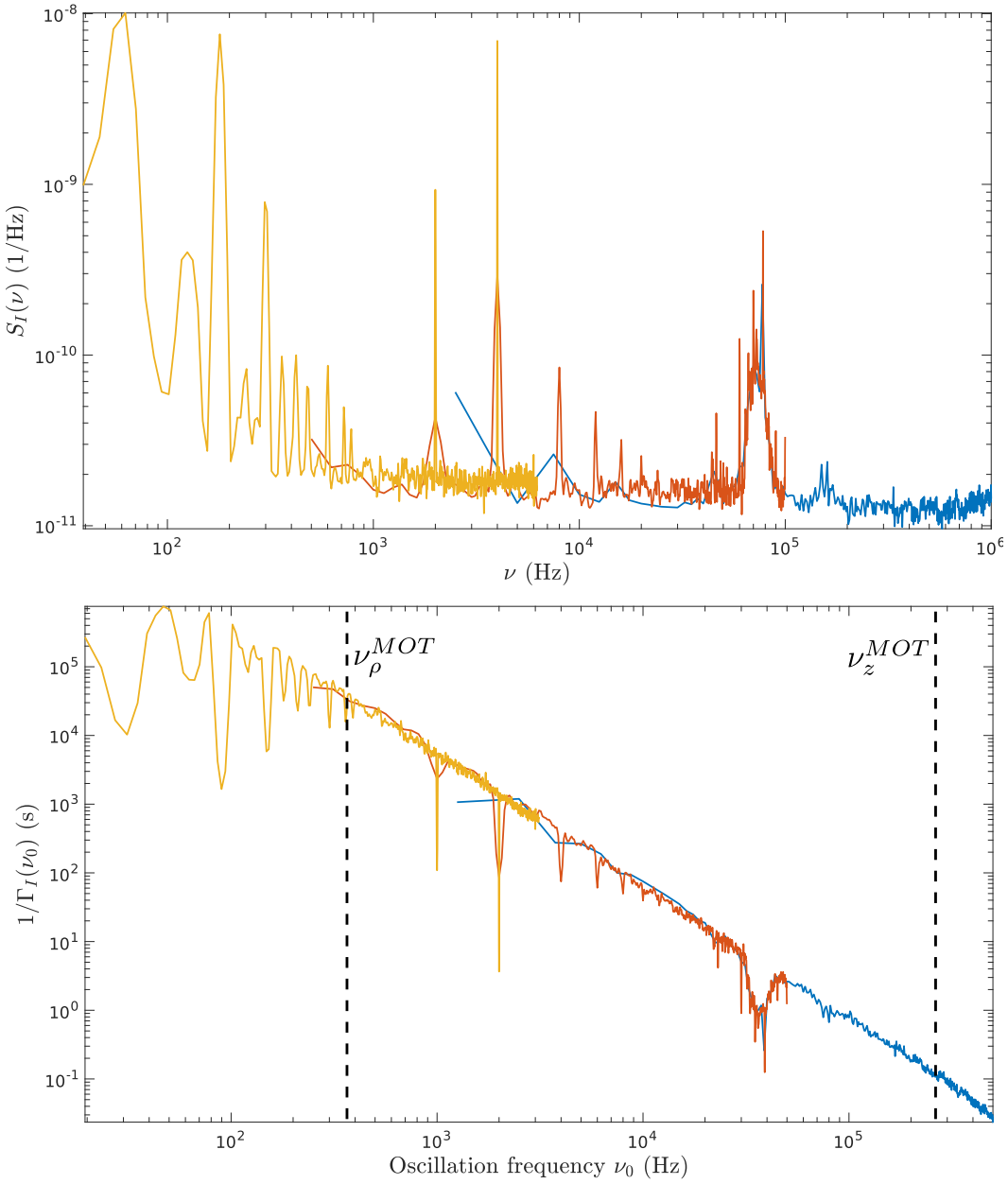

Figure 6.14: Laser intensity noise. In (a) the relative intensity noise $S_I(\nu)$ is shown. The different traces correspond to the use of different spans and bandwidths in the spectrum analyzer. Every trace is normalized accordingly to estimate the relative intensity noise. Several peaks and its harmonics appear in the spectrum. In (b) the corresponding $1/e$ time constant $\tau_I = 1/\Gamma_I(\nu)$ is shown.

The optical phase noise is really relevant for the unidimensional lattice and the operation of the optical conveyor belt. As the two counter-propagating beams are derived from the same laser light and frequency shifted by two AOMs that cause the motion of the standing wave pattern. For a change $\Delta\phi$ in the optical phase between the beams, the atoms will move axially by $\Delta z = \Delta\phi/2k$ according to Eq(6.3). The phase noise can have different causes: the mirrors shake, the temperature or strain in the optical fibers changes, and also electronic noise in the AOMs driving system to name a few examples. The electronic noise is relevant as it can have serious consequences on the expected probe transmission in the APCW.

The noise on the RF signals can be studied by doing an heterodyne measurement on a phase detector. The idea here is to characterize the phase modulation of an oscillating signal by comparing that signal with a reference oscillation that would have a fixed offset in frequency and phase from the signal if no modulation were present. The phase difference between the two electronic signals, $\Delta\phi_{el}$, is encoded in the voltage output of the phase detector $V_{\phi_{el}} = V_0 \cos(\Delta\phi_{el})$. If the two signals are set in quadrature, such that $< V_{\phi_{el}} >= 0$, the output voltage is proportional to the phase difference: $(V_{\phi_{el}})_{rms} = V_0(\Delta\phi_{el})_{rms}$. As both AOMs are in a double pass configuration, the position fluctuation is

$$< \Delta z^2 >= \frac{< \Delta\phi_{el}^2 >}{k^2}. \tag{6.14}$$

Therefore, the relative position noise is derived from the relative phase noise $S_z(\nu) = S_\phi(\nu)/k^2$ and from Eq(6.13) the associated heating rate is derived. The measurements performed are shown in Fig. 6.15. At high frequencies the heating rates can be on the order of a few mK/s. Two peaks at $\nu_0 = 545$kHz and $\nu_0 = 410$kHz with heating rate 350mK/s and 4mK/s respectively could be significant. A possible effect associated with Eq(6.13) is the fact that as soon as the atoms start to heat up, the harmonic approximation is no longer valid and the effective trap frequency can drop significantly when atoms filling a large fraction of the trap depth, meaning that the phase noise is no longer relevant. The integrated phase noise is $\Delta\phi_{rms} = 3\times10^{-3}$rad, which is quite small. Further improvements can be done and are being discussed.

Adiabatic compression of the lattice

As the atoms move towards the chip, the waist, the intensity and the trap depth change. This variations in the trap characteristics can create more complicated effects. If these changes happen slowly, the trap will deform and the atoms will

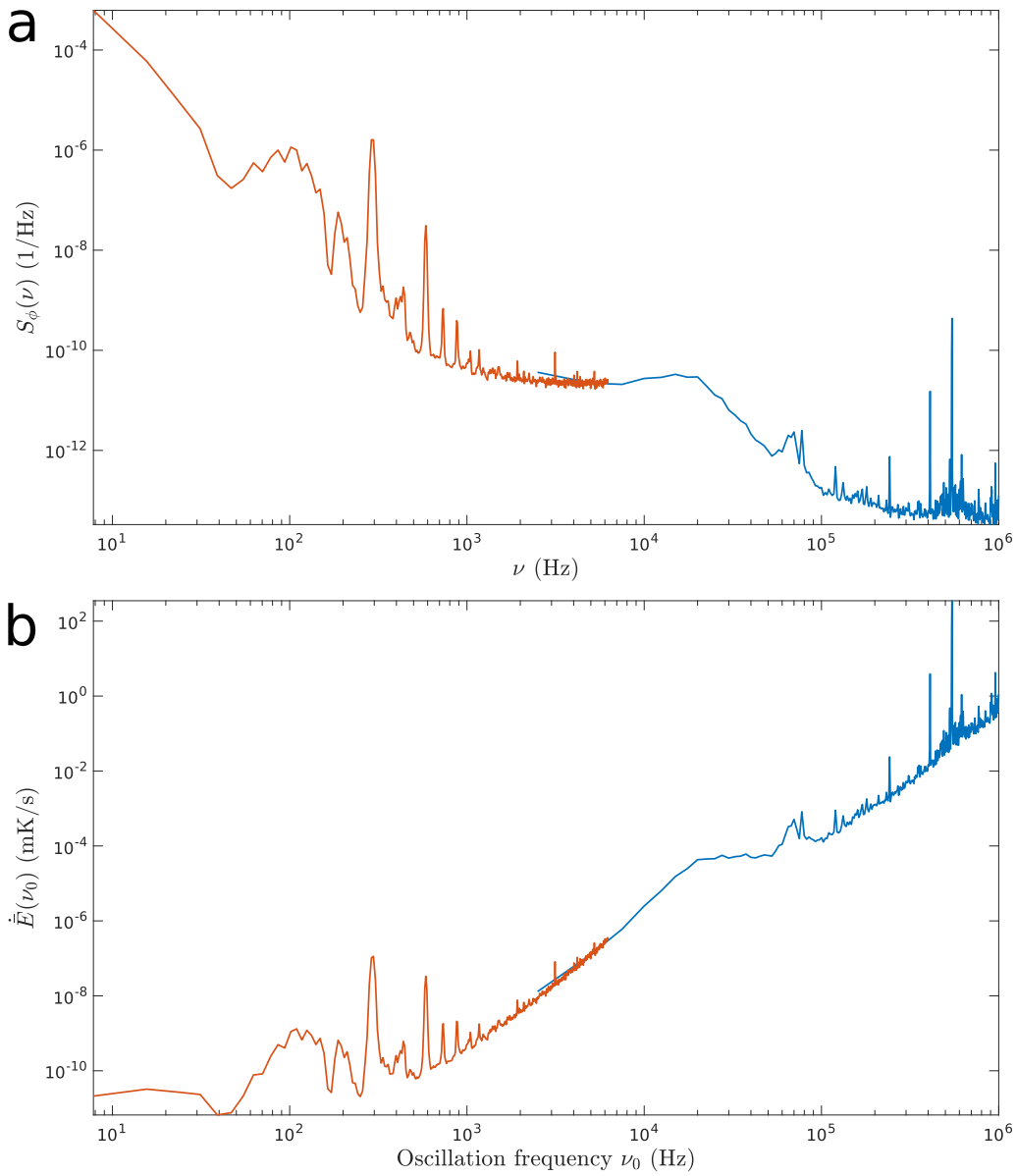

Figure 6.15: Electronic phase noise. In (a) the relative phase noise $S_\phi(\nu)$ in the electronic signal is shown. The different traces correspond to the use of different spans and bandwidths in the spectrum analyzer. Every trace is normalized accordingly to estimate the relative phase noise. In (b) the corresponding heating rate due to the position fluctuation caused by the phase noise is shown using Eq(6.13) and Eq(6.14). Only the peak at ν_0 = 545kHz represents a significant problem.

change its thermodynamic properties to adapt to the new trap, analogous to a gas compressed in a box. If the atoms remain in equilibrium during this adiabatic change, its temperature will change too. This is relevant because over the transport distance the trap suffers significant modifications.

Radially, the potential length scale is given by the beam waist, while axially the wavelength dominates the behavior. The thermal properties of the trapped atomic gas were described in Section 3.3. In equilibrium, the thermal length scale along each direction, L_{th}, describes the spatial density distribution. Each pancake can be consider as an identical and independent trap given that the atoms occupy an extent much smaller than the beam Rayleigh length z_R and the atoms are sufficiently localized near the bottom of the trap. Therefore, the effective volume of each of these separate traps is

$$V_{eff} = (L_{th}^{\rho})^2 L_{th}^{z} \propto (\nu_\rho^2 \nu_z)^{-1/2}, \tag{6.15}$$

because $L_{th} \propto \nu^{-1/2}$. For the scaling described before in Eq(3.13) and Eq(3.15) where $\nu_z \propto \sqrt{U_0}$ and $\nu_\rho \propto \sqrt{U_0/w(z)^2}$ with U_0 the trap depth, the effective volume depends on the power P and the waist $w(z)$ of the beams, such that

$$V_{eff} \propto \frac{(w(z))^{5/2}}{P^{3/4}}. \tag{6.16}$$

At constant power P, for a $z_R = 1.11$cm Rayleigh length after moving 2.5cm towards the focus, the effective volume reduces by more than 9 times. For smaller focus beams, this effect is bigger.

In the adiabatic process, the phase space density is kept constant.Therefore, the ratio ν/T is constant during the process. The modifications are adiabatic if the change in the oscillation frequency in one cycle is much less than the oscillation frequency, that is $\dot{\nu}/\nu^2 \ll 1$. Under normal transport conditions, this is satisfied.

If the potential is assumed to be separable and the dynamic is conservative, following the Liouville's theorem, each direction is thermalized to its own temperature T_ρ and T_z radially and axially respectively. Therefore, during adiabatic compression

$$\nu_z/T_z \text{ is constant, and } \nu_\rho/T_\rho \text{ is constant.} \tag{6.17}$$

Under trap frequency changes the effective volume as a function of the temperature should change as

$$V_{eff} \propto (T_\rho^2 T_z)^{-1/2}. \tag{6.18}$$

In the example described before, a reduction in the effective volume comes along with an increment in the sample's temperature. If the two temperatures, T_ρ and T_z, where the same $\bar{T}$, once the atoms are at the focus they are more than 4 times hotter in a 6 times deeper trap. In the experiment, the measured temperature between the two directions after DRSC is usually different, but there exist mechanisms that tend to equilibrate them as elastic collisions.

To be specific, for any given two points along the lattice axis z_1 and z_2, the axial temperatures are related like

$$T_z(z_1) = T_z(z_2)\sqrt{\frac{P(z_1)w^2(z_2)}{P(z_2)w^2(z_1)}}, \tag{6.19}$$

where the power P can change, and the waist $w(z)$ changes as the atoms moves along the beams. For the radial direction,

$$T_\rho(z_1) = T_\rho(z_2)\sqrt{\frac{P(z_1)w^4(z_2)}{P(z_2)w^4(z_1)}}. \tag{6.20}$$

A comparison with numerical simulations confirm the simple thermodynamical model as the atoms move towards the focus. In this case, the simulation is done using a scalar Gaussian beam to generate each lattice beam and the device is not present. The initial cloud consisting of a few thousand atoms is trapped 1.0cm away from the focus and is thermalized along the three direction to $T = 30\mu$K. The optical frequency difference between the beams is $\Delta f = 1$MHz, such that the transport velocity is $v_{latt} = 0.43$m/s. The cloud moves and its momentum distribution spreading is used to extract the temperature along each direction. At the focus, the atoms are characterized by an axial temperature $T_z = 90\mu$K and radial $T_\rho = 210\mu$K as seen in Fig. 6.16(a), in agreement with the predictionss from Eq(6.19) and Eq(6.20). Meanwhile, the position spreading decreases along both directions, following the adiabatic criteria described before. Fig. 6.16(b)-(c) show the numerical simulation result and the model's prediction for the radial and axial direction respectively.

As part of the experimental efforts, the temperature has been measured at different positions between the science MOT and the chip. A set of observations seem to suggest that this effect is really relevant for the success of the transport. A common type of routine measurement to check if the system works as expected is the so-called torture test. The torture tests are based on a single back-and-forth transport, over a

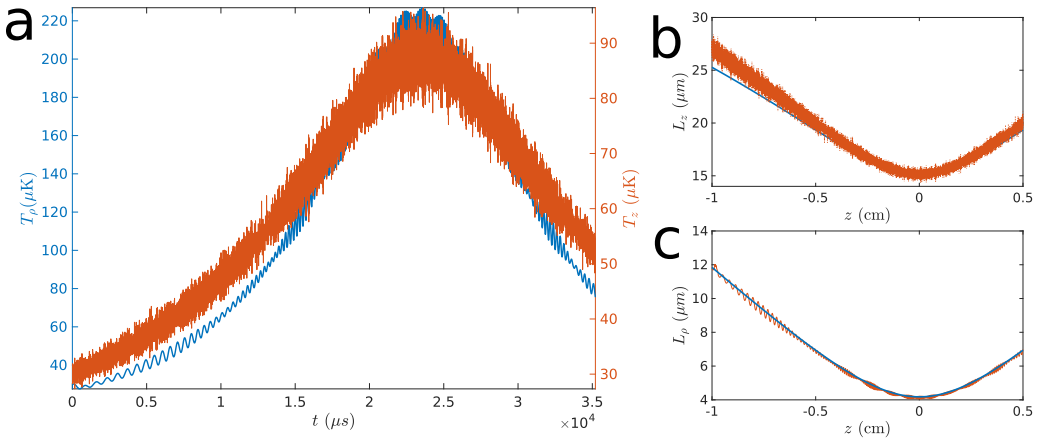

Figure 6.16: Simulating a long transport. In (a) the momentum distribution width is used to determine the temperature along each direction in agreement with the model. The red trace represents the axial direction, axis on the right side of the panel, while the blue trace represents the radial direction, axis on the left side of the panel. In (b) and (c) the position distribution width is plotted as the cloud moves for the radial and axial direction, respectively. Numerical simulations performed by Lucas Peng.

distance close to the 2.5cm separating the science MOT and the chip. The atoms are accelerated for 100μs at a constant acceleration a, and then they move at constant speed, v_{latt}, for a variable time T, with $T \gg 100\mu$s. An opposite acceleration to the initial one, $-a$, is applied for 200μs, followed by another constant speed interval with pf length T and value $-v_{latt}$. After that second interval of length T, the atoms are accelerated at a constant value a in order to stop them in 100μs at their initial position. In other words, it is a time symmetric back-and-forth trip as shown in Fig. 6.17(b). The temperature and atom number are measured once the trapped cloud comes back. If the power is kept constant during a $T = 35$ms test, less than 20% of the atoms come back and are significantly hotter. From the images taken, some atoms are really lost in the several acceleration stages, but during the constant speed trip atoms are also lost. Additionally, if the optical power in both beams is changed from an initial high power P_i to a final lower power P_f in the first trip and ramped up back to P_i in the second trip, the efficiency of the torture test can increase above 50% and the final temperature is almost as low as the initial temperature. Therefore, by keeping the trap as flat as possible, the transport is more efficient and keeps the atoms colder.

The efficiency of the round trip for different final power is shown in Fig. 6.17(a) and a detail on the transport sequence is shown in Fig. 6.17(b). When the optical power

in each beam is reduced to $P_f \approx 0.15 P_i$, about 55% of the initial atoms survive the 70ms round trip to the vicinity of the chip and back to the science MOT. For this optimal lattice, the projected lattice depth is kept relatively flat, changing by less than 20% as noted in the theoretical calculation in Fig. 6.17(c). As a comparison, if the power were kept constant the trap depth increases by a factor of 6. The projected equilibrium temperature $\bar{T}$ for the optimal case is shown in Fig. 6.17(d) and only increases by a factor less than two. It is indeed, similar to the temperature observed in the experiment. The axial and radial trap frequencies, ν_z and ν_ρ, are shown in Fig. 6.17(e) and (f) respectively. Axially the change is small, but radially it increases by a factor of 2.

When the power is kept constant during the transport, time of flight measurements are not reliable as the temperature is very high and the cloud expands quickly out of the 1.8mm wide window used to image the atoms. Another method was used to infer the temperature near the chip by performing spectroscopy on the AC-shifted density distribution of the atoms [198]. The idea is relatively simple: absorption images (and background images) of the sample of trapped atoms are taken in order to map the radial degrees of freedom. The imaging beam is locked to the Cs D1-line transition, such that the excited states are nor perturbed significantly by the trapping light. From the OD images it is possible to reconstruct the probability density $p(E)$ describing the trapped atoms. For an atom trapped in a harmonic potential the probability density in equilibrium is $p(E) \propto E^2 \mathrm{e}^{-E/k_B T}$. The result of this analysis is shown in Fig. 6.18, where the radial temperature is determined to be $T_{fit} = 300\mu$K, as the imaging is performed along the lattice axis. This method works well if the trap is very deep, in order to resolve the AC shifted atoms.

Resonant and parametric heating due to reflections in the moving lattice

The change in the trap as the atoms move might also enhance other heating mechanisms, therefore it is important to study numerically and experimentally their influence. To be specific, there could be an exchange of energy from the center of mass motion, dominated by the lattice chirp frequency Δf, to the oscillations in the trap site, dominated by the axial and radial trap frequencies. In different systems, losses were observed once the atoms move at certain speeds using the optical conveyor belt [194]. The explanation found for this phenomena [199] is going to be described here and is relevant to understand the transport near the device.

The example is relatively easy but it might have significant consequences. The

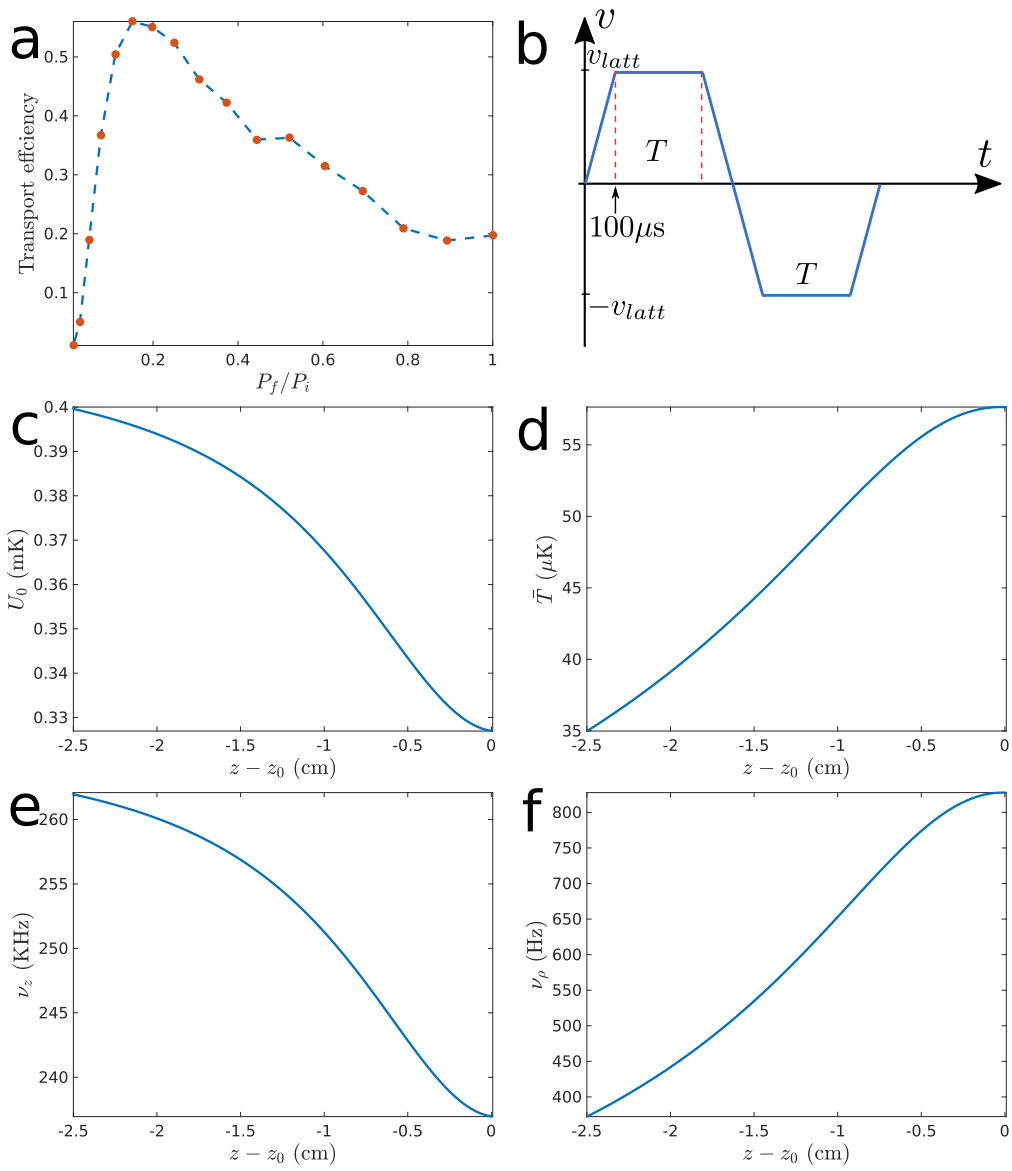

Figure 6.17: Torture test and lattice characteristics during optimized transport. In (a) the back-and-forth transport efficiency is measured for different final powers P_f. The motion is described in (b). The trap depth U_0, the mean temperature $\bar{T}$, and the axial and radial trap frequencies ν_z and ν_ρ for the optimized sequence with $P_f = 0.15P_i$ are shown in (c) to (f) respectively.

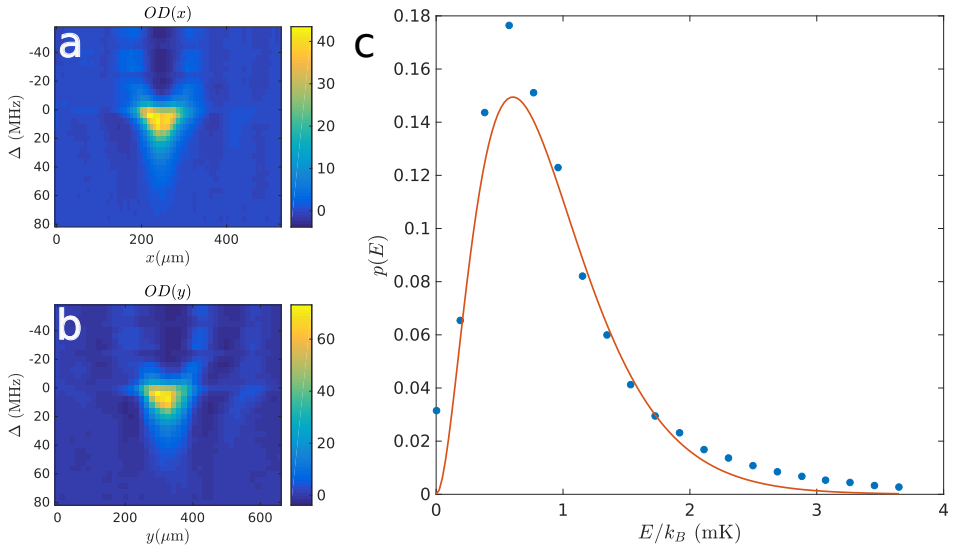

Figure 6.18: AC-shifts spectroscopy of the trap potential in the radial plane. The column optical depth along the (a) horizontal and (b) vertical direction is shown for different detunings for a sample of trapped atoms. The dark regions ($OD < 0$) correspond to a small leakage of the trap light. In (c) the reconstructed probability density $p(E)$ is shown. The fitted radial temperature is $T_{fit} = 303\mu$K.

idea is the following: apart from the two counter-propagating beams with a relative frequency shift Δf a third beam, a product of the reflection of one of the beams, is present as shown in Fig. 6.19. Two assumptions will be made. The first is that all the fields are plane waves, without variations in the radial direction. Furthermore, the amplitude of the two counter-propagating beams is the same, while the reflection coefficient changes the amplitude of the third reflected beam. Under this assumptions, the total electric field is the sum of these three fields

$$E(z,t) = \mathrm{Re}\left(\mathrm{e}^{(-i(kz+2\pi ft))} + \mathrm{e}^{(-i(-kz+2\pi(f+\Delta f)t))} + r\mathrm{e}^{(-i(-kz+2\pi ft))}\right), \tag{6.21}$$

with r the amplitude reflection coefficient. In the reference frame moving with a velocity $v = \Delta f\lambda/2$, the total electric field is the sum of the main standing wave and the weak third beam

$$E(z,t) \approx 2\cos(2\pi ft)\cos(kz) + r\cos(2\pi(f-\Delta f)t - kz). \tag{6.22}$$

For small reflections the potential is just

$$U(z,t) = U_0\left[\cos^2(kz)(1 + r\cos(2\pi\Delta ft)) - r\cos(kz)\sin(kz)\sin(2\pi\Delta ft)\right]. \tag{6.23}$$

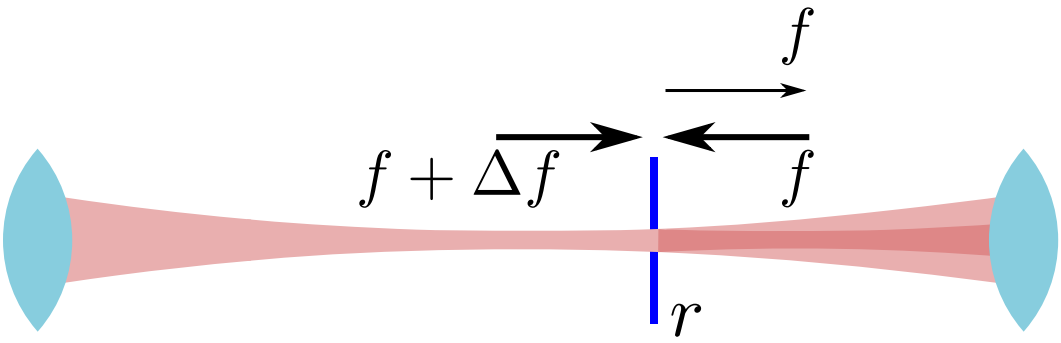

Figure 6.19: Partial reflection on the chip or any other surface can cause interference between the three beams that lead to different heating mechanisms.

The first term modulates the trap depth $U_0(1 + r\cos(2\pi\Delta f t))$ while the second generates a different kind of periodic driving force. The equation of motion for small oscillations ($kz \ll 1$) is

$$\ddot{z} = -\frac{1}{m}\frac{\partial U}{\partial z} = -\frac{2U_0k^2}{m}(1 + r\cos(2\pi\Delta f t))z - r\frac{U_0k}{m}\sin(2\pi\Delta f t). \tag{6.24}$$

Identifying the axial vibration frequency in these equations, $\omega_z = 2\pi\nu_z$, the equation of motion can be rewritten as

$$\ddot{z} = -\omega_z^2[1 + r\cos(2\pi\Delta f t)]z - r\frac{\omega_z^2}{2k}\sin(2\pi\Delta f t). \tag{6.25}$$

Each term can cause heating as it is forcing the atoms. A simple analysis considers each term resonating with the natural motion of the atom in the lattice in separate steps. For the resonant term $\omega_z = 2\pi\Delta f$ and small reflections, the equation of motion is

$$\ddot{z} = -\omega_z^2 z - r\frac{\omega_z^2}{2k}\sin(\omega_z t). \tag{6.26}$$

For a particle initially at rest at the trap minimum, the solution has a normal homogeneous oscillation part and another growing amplitude part that causes heating. That latter is

$$z(t) = \frac{\omega_z r}{4k}t\cos(\omega_z t). \tag{6.27}$$

As the amplitude of the oscillation grows linearly in time, the energy averaged over a cycle depends on the amplitude squares, and therefore it grows quadratically in time. The characteristic time T_{res} that it takes an atom to heat from the bottom to the top of the trap is

$$T_{res} = \frac{4}{r\omega_z}, \tag{6.28}$$

which could be about ten oscillation cycles.

The other term in Eq.(6.25) gives rise to a parametric heating effect [200]. At exact resonance $2\omega_z = 2\pi\Delta f$ the equation of motion is

$$\ddot{z} = -\omega_z^2 z - r\omega_z^2 \cos(2\omega_z t)z. \tag{6.29}$$

Over once cycle, the constant frequency harmonic force, $F_{har} = -m\omega_z^2 z$, does not increase the energy of the atom, assuming that the motion is unperturbed $z(t) = A\cos(\omega_z t)$. The harmonic time dependent force, $F_{dep} = -mr\omega_z^2 \cos(2\omega_z t)z$, is suppressed by the small reflection parameter r but its effect is to slowly increases the oscillation amplitude A. Therefore, the only non-zero work done on the particle is result of the explicit time dependent force, such that the energy increases at a rate

$$\dot{\bar{E}} =< F_{dep}\dot{z} >= \frac{r\omega_z}{2}E. \tag{6.30}$$

Therefore, the characteristic heating time is

$$T_{para} = \frac{2}{r\omega_z}. \tag{6.31}$$

Both parametric and resonant effects have similar time scales and are characterized by very selective rules for the lattice chirp frequency and oscillation frequency. That might limit the speed at which the atoms might move and how they scan different trap frequencies in the conveyor belt, in order to reduce the time span this "resonant" condition is encountered, in case it is. Besides, the reflection from the device can be significant as seen in Chapter 5, compromising the transport near the device. Numerical simulations show some evidence of this phenomena, although the reach of these specific effects is still under investigation.

6.3 Experimental results

After analyzing in detail the trapping and loading of the atoms in the dipole trap and its properties during the conveyor belt transport, it is time to describe the observations made with the nanostructure. The principal objective was to find a fringe sensitive signal as described in Chapter 5. This characteristic is intended in order to perform delicate triggered actions on the atoms, understand the atom localization near the device and eventually load an array of traps with high filling fraction. It also helps to identify the contribution of the atoms that go through the center of the APCW nanobeams and separate them from the many atoms that might be moving near the external surfaces of the nanobeams or crash into the nanobeams'

surface. Just recently, hints of a fringe sensitive signal have been observed. This is still under investigation, but there is strong evidence that the localized atoms arrive to the device and are affected by the presence of guided modes. New efforts by using a blue optical lattice will be described at the end of the section.

Measurement settings

In most cases the measurements are carried out by sending a weak probe near the Cs D1-line transition $6S_{1/2}\ F = 3 \rightarrow 6P_{1/2}\ F = 4$ because it has the largest relative hyperfine transition strength factor $S_{FF'} = 3/4$ [99]. The probe goes through a couple of VBG that spectrally separate and combine different fields in the same optical path. The probe and eventually guided mode trap beams are delivered to the device with the same optical fiber. Before the VBG setup, each beam has a set of a quarter and half waveplates that helps to align the polarization of the coupled light. In order to do so, the scattering from the tether closer to the coupler is employed. The waveguide and tether form a four-way dielectric right angle cross that scatters light with a very strong polarization dependence. If the polarization is parallel to the tether the scattering is very big. On the other hand, if light is polarized perpendicularly to the tether, the scattering is strongly suppressed. A camera monitors the tether scattering while the waveplates are used to minimize the scattering. This case excites the propagation of the TM-like mode. To excite the TE-like, the polarization is rotated by 90° using the waveplates. Usually, after setting up the fibers and polarization, and unless the fibers are shaken significantly, the polarization will remain aligned during the whole measurement period. This procedure is also used to probe the optical spectrum of the device by using a Velocity laser near the Cs D1- and D2-line resonances (New Focus TLB-6700). Characterization scans are performed every time a probe measurement is taken in order to keep track of spectral shifts and cavity features that modify the optical spectrum.

To align the lattice to the device the translational stages that hold the lenses that focus the optical lattice beams are used to center the scattering on the device. Previously, each beam is retro-reflected on the chip surface to have near normal incidence. To fine tune the alignment of the lattice beams, the scattering of the lattice beams onto the device is monitored. Part of the lattice light is scattered to the guided modes, usually a couple of nW. The scattering is not symmetric, meaning that even for very similar intensities for each beam at the APCW, the amount of light collected from each beam is not the same. The scattering of light is something that ideally should

not happen, but probably due to surface imperfections, cleanliness and not-normal incidence,, this effect is noticeable. This light is efficiently picked up in the VBG setup by adding a grating resonant with the lattice wavelength. Usually one of the two lattice beams is aligned to the device with the procedure just described, while the second beam is aligned by optimizing the back coupling in the optical fiber from which the first beam was launched.

In every experiment, the weak probe is sent to the device and its back reflection filtered by the VBG and monitored with a SPCM. The transmission of the weak probe is also monitored after being spectrally filtered by another VBG setup and detected in one or two SPCMs. As described before, the SPCM time traces are digitalized and recorded in a fast photon counting card. In most cases, there is not polarization filter in the path from the device output to the detectors where the probe reflection or transmission are measured.

Stop-and-go

After subsequent optimization, atoms are transported to the device by creating a $\Delta f = 1.6$MHz optical beat note between the lattice beams. After transporting the atoms for $T_1 = 35.2$ms, the atoms stop 1mm away from the device. Thereafter the lattice stops for $T_2 = 10$ms before the final transport stage at a speed v. The stop-and-go procedure intends to get rid of atoms that might have heated up and are not really trapped. In most cases, those are a considerable fraction of the total, around 20% in most cases. The presumed untrapped atoms usually continue flying at the original speed and can be detected by the guided mode probe. A common tool to study the signal is a time-detuning plot. The normalized atomic reflection (R/R_0) and transmission (T/T_0) is recorded, and it is plotted in a two dimensional plot where the horizontal axis is the time axis, with $t = 0$ some instant in the T_1 long interval, and the vertical axis is the detuning from the Cs D1-line transition in free-space. Fig. 6.20 shows the time-frequency signals for optical conveyor belts with the same optical power but moving at different velocities after the T_2 waiting period. In all cases the probe is weak and TE-like polarized.

Contribution of atoms around the device

Contrary to the case of a few trapped atoms in the reflection trap described in Chapter 5 and used in the Lab 11 experiment, the atoms in the lattice are not localized respect to the waveguide for a significant time. Only a small fraction of the trapped atoms in each pancake will effectively interact with the device. Even though the probe is

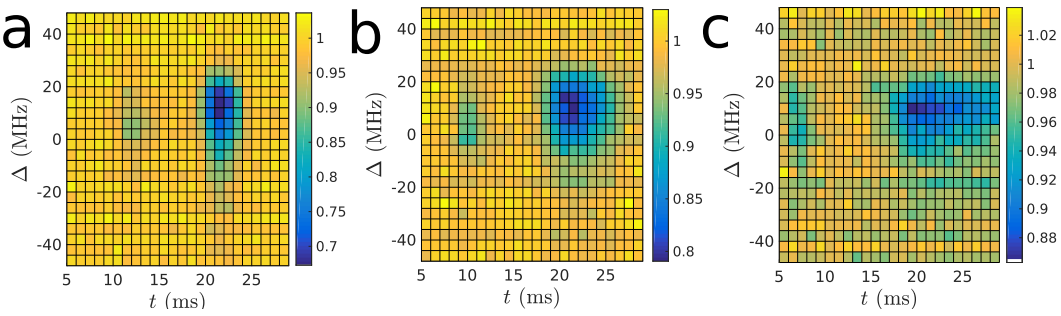

Figure 6.20: Stop-and-go sequence and probe normalized transmission through the APCW for different lattice speeds. Each time-detuning plot shows the normalized transmission $T(\Delta, t)/T_0$. Lattice speed determined by the frequency detuning (a) Δf = 800KHz, (b) Δf = 400KHz and (c) Δf = 200KHz.

evanescent with an exponential decay as shown in Chapter 5, the atoms are more or less uniformly distributed transversally along the central part of the pancakes as shown in images and numerical simulations. This is an approximation, as the near field of the lattice deviates appreciably from their free space form, as shown in Fig. 5.14 for example. The optical lattice potential deforms as the lattice anti-nodes approach the dielectric and the atoms adiabatically follows this deformation. In a very coarse approximation, the product $N \times \Gamma_{1D}$ determines the strength of the interaction, therefore that product will also decay roughly exponentially in space. That means that only atoms that are within $\sim$ 200nm to the device will contribute to the signal.

The complicated light pattern of the lattice around the device shifts the energy levels of the different atoms in a position dependent way. In principle, this manifests as an inhomogeneous broadening effect that will be reflected in broader line shapes once spectroscopic measurements are taken. In numerical simulations this is manifest too. After a million trajectories are simulated, the probe transmission for a given atomic sample can be computed. A transfer matrix model can be used by picking a representative sample of atoms with position dependent coupling $\Gamma_{1D}(\mathbf{r}(t))$ and light shifts $\delta_{LS}(\mathbf{r}(t))$ and monitoring in time the transmission through the system [39, 40]. These simulations can be quite rich, as several experimental parameters can be changed and their effects can be mapped in the normalized probe transmission. This analysis was performed by Lucas Peng.

As described by Asenjo-Garcia et al. [30] the characteristics of the transmission depends not only on the optical properties of the device and the light-matter coupling of an individual atom, but also on the relative position between the atoms. In

the experiment performed here, as the atoms are not trapped their coupling fluctuate and analyses based on [30, 29] are more complicated to perform. An easier approximation is found by using the optical bistability equations [201, 202] that describe the semiclassical structure of an atom-cavity system, that in the APCW of Lab 11 resembles the ones found in [30]. The electric field transmission for such an atom-cavity system can be written as

$$t(\phi, \delta, C_0) = \left(\left(1 + \frac{2C_0}{1+\delta^2}\right) + i\left(\phi + \frac{2C_0\delta}{1+\delta^2}\right)\right)^{-1}, \tag{6.32}$$

with $\delta = \frac{\Delta - \Delta_0}{\Gamma}$ the normalized detuning from the light shifted resonance Δ_0, C_0 the cooperative parameter and ϕ a parameter that describes the transmission of the empty cavity $t_0 = 1/(1 + i\phi)$ and hence carries information about the cavity characteristics. The effect of the atoms on the cavity is to shift the output field's phase and its amplitude with respect to its empty cavity value. Fig. 6.21(a) shows the fitting for the spectrum showed in Fig. 6.20(a) for the data integrated in the interval [21, 22]ms.

The atom number loaded into the lattice N_{latt}, is changed by modifying the push beam pulse width and is calibrated using absorption images. For the standard 450μs pulse width, $N_{latt} = 2.6 \times 10^6$ atoms are loaded. Transmission spectra is shown in Fig. 6.21(b) for different values of N_{latt}. The cooperativity parameter for these spectra is shown in Fig. 6.21(c), a linear fit describes well the relationship between C_0 and N_{latt} in this parameter regime.

Differences between TE-like and TM-like probe modes should be reflected in the probe transmission due to the different spatial intensity profile and the different factors that enter into the signal enhancement. For example, the TM-like mode might be more sensitive than the TE-like mode to the class of atoms that crash or are close to the beam top and bottom surfaces. Furthermore, the TM-like mode lacks the high spatial contrast from the Bloch mode function because it is far from the small bandgap, and hence it falls into the so-called waveguide regime described in Chapter 4. As described in [30, 203], for random filling the atoms might be consider as a "noninteracting" system where each atom might decay into the specific guided mode and others mode with rates Γ_{1D} and Γ', respectively. A modified version of the Beer-Lambert law for the normalized power transmission can be recovered in this regime

$$\frac{T(\delta)}{T_0(\delta)} = \exp\left[-N \ln\left(\frac{\delta^2 + (\Gamma' + \Gamma_{1D})^2/4}{\delta^2 + (\Gamma')^2/4}\right)\right]. \tag{6.33}$$

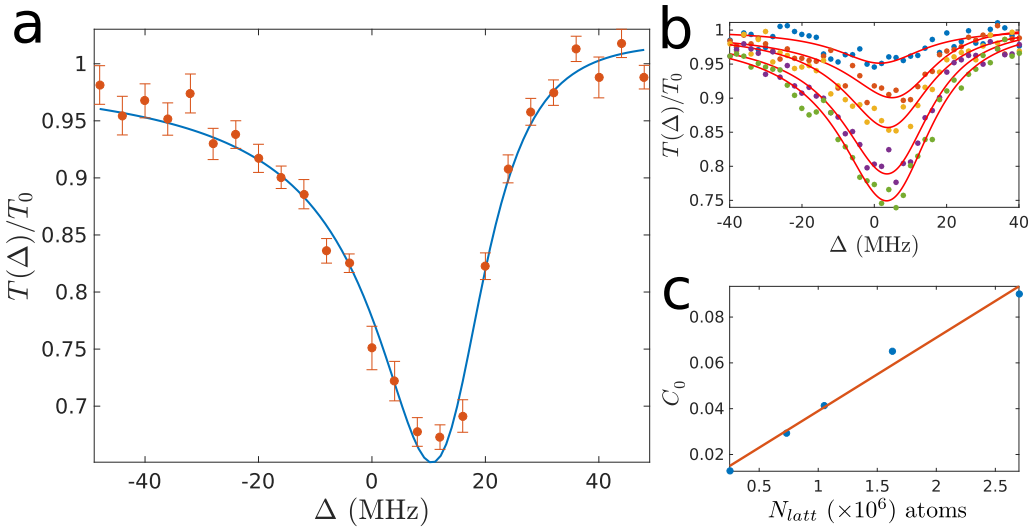

Figure 6.21: Optical bistability equation fitting. The fitting parameters are $(\phi, \Delta_0, C_0, \Gamma)$. In (a) the data shown in Fig. 6.20(a) is fitted for the [21,22]ms interval. The fitting values are $(\phi = -0.4, \Delta_0 = 12\text{MHz}, C_0 = 0.13, \Gamma = 9.6\text{MHz})$. In (b) the atom number loaded into the lattice is changed and the spectra are fitted for the same time interval as in (a). (c) The dependence of the cooperativity C_0 on the atom number N_{latt} loaded in the lattice is plotted, for the plots show in (b). The horizontal axis in (c) is calibrated using absorption imaging.

In the case where the coupling to the guided mode is small compared to the coupling to free space and other channels, $\Gamma_{1D}/\Gamma' \ll 1$, it is possible to recover the usual form of the Beer-Lambert law

$$\frac{T(\delta)}{T_0(\delta)} \approx \exp\left[-\frac{OD}{1+(2\delta/\Gamma')^2}\right], \tag{6.34}$$

where the optical depth is $OD = 2N\Gamma_{1D}/\Gamma'$. Fig. 6.22 shows a TE-like and TM-like probe transmission spectrum under the same delivery conditions and the associated fits from in Eq(6.34). The measured linewidths are $\Gamma'_{\text{TE}} = 2\pi \times 28\text{MHz}$ and $\Gamma'_{\text{TM}} = 2\pi \times 21\text{MHz}$, and are heavily influenced by the AC-shifts inhomogeneous broadening. The optical depths are $OD_{\text{TE}} = 0.38$ and $OD_{\text{TM}} = 0.33$. From these measurements the fitted $N\Gamma_{1D}$ is $(N\Gamma_{1D})_{\text{TE}} = 2\pi \times 5.2\text{MHz}$ and $(N\Gamma_{1D})_{\text{TM}} = 2\pi \times 3.5\text{MHz}$. The inset shown in Fig. 6.22 shows the optical spectrum for the TE-like mode near the Cs D1-line, indicated by the black vertical line.

Certainly, this model does not capture the full spatial details that determine the spectrum characteristics. However, it helps as a tool in the laboratory to monitor and optimize the experiment. A detailed time analysis of the acquired data might

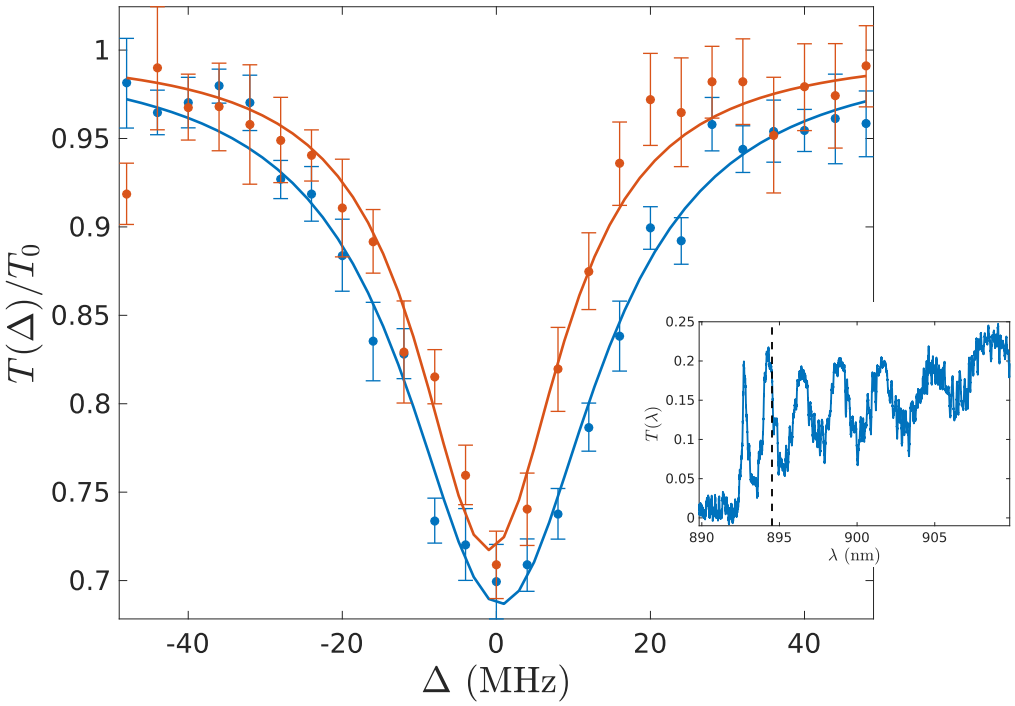

Figure 6.22: Noninteracting system - OD fitting. The normalized probe transmission is measured for the same transport conditions. The D1 TE-like probe (blue trace) is near a cavity resonance, hence the near symmetric profile. The TM-like probe (red trace) is also shown. The inset shows the optical spectrum of the device for the TE-like mode near the Cs D1-line transition (indicated by the black vertical line).

be the best way to analyze the atoms delivered by the lattice.

Guided mode potentials

The atoms trapped in the optical lattice experience light shifts that modify its spectrum too. Furthermore, any guided mode will generate similar shifts, with their intensity pattern imprinted on them. For the guided modes used to create the atomic traps that we hope to realize, a few effects need to be taken into account. Due to the limited power capabilities of the APCW devices under vacuum, the guided mode traps are usually detuned by less than 1nm, with associated high scattering rates (e.g. relative to those required for magic wavelength traps [25]). Moreover, the spatial profile of the guided mode translates into a very complex structure for the light shifts the atoms might suffer[9]. For example, a blue detuned TM-like guided mode will create a repulsive barrier on the top and bottom surfaces, while a red

[9]Light-shifts due to surface potentials can also be significantly close to the surfaces < 50nm.

detuned TE-like mode will create a saddle-point potential between the beams that will attract atoms to crash onto their inner surfaces.

The intensity of the guided mode depends also on other optical properties of the photonic crystal waveguide. The slow light effect, group index $n_g > 2$, and the Bloch mode contrast can alter the intensity of the guided modes, because for the same total optical power, the intensities can be very different depending on the closeness to the band edge as explained in Chapter 4. Therefore, it is really hard to calibrate the potentials created by guided mode fields and balance them to create traps. In order to do so, the atomic signal in presence of guided mode potentials is compared to numerical simulations where different effects can be taken into account. Numerical simulations are extremely relevant in this context as the AC-shift spatial pattern and its dependence on a set of parameters is complex.

The effect of the guided mode traps need to be balanced against the energy of the atoms transported by the optical conveyor belt. The atoms moving with the lattice can have kinetic energies on the order of a few mK. For example, for atoms moving in a $\Delta f = 800$kHz conveyor belt, the kinetic contribution is $K_{latt} = mv^2/2 = k_B \times 0.93$mK. Repulsive potential barriers created by the guided modes can reduce the atoms' kinetic energy and also exert an appreciable force, guiding atoms to the space in the gap between the beams or completely repelling them from the structure surroundings depending on its magnitude. If the barrier is too small ($\ll K_{latt}$), it will have a negligible effect and will not appreciably deflect atoms. If, on the other hand, it is too high ($\gg K_{latt}$) it will shield the device from the atoms. If the height is comparable to the kinetic energy K_{latt}, the spatial dependence of the guided mode can enhance the contribution of some atoms in regions where the barrier is not that high, and reduce the contribution of atoms in regions where the barrier has strength to deflect atoms away from the device. This specific calibration is challenging as the distribution of power in the device is not known in such a detailed way every time a signal is acquired. Fig. 6.23 describes this situation for a blue detuned TM-like guided mode. In (a), (b), and (c) the total potential, lattice, and guided mode is plotted for different magnitudes of the guided mode potential as indicated in the figure caption.

The numerical simulations allows to distinguish different atomic trajectories. It is possible to study only the atoms that will go through the center of the beams or the ones that crash into the top and bottom surfaces. As the guided mode potential increases, the contribution from each class changes. Fig. 6.23(d) indicates the

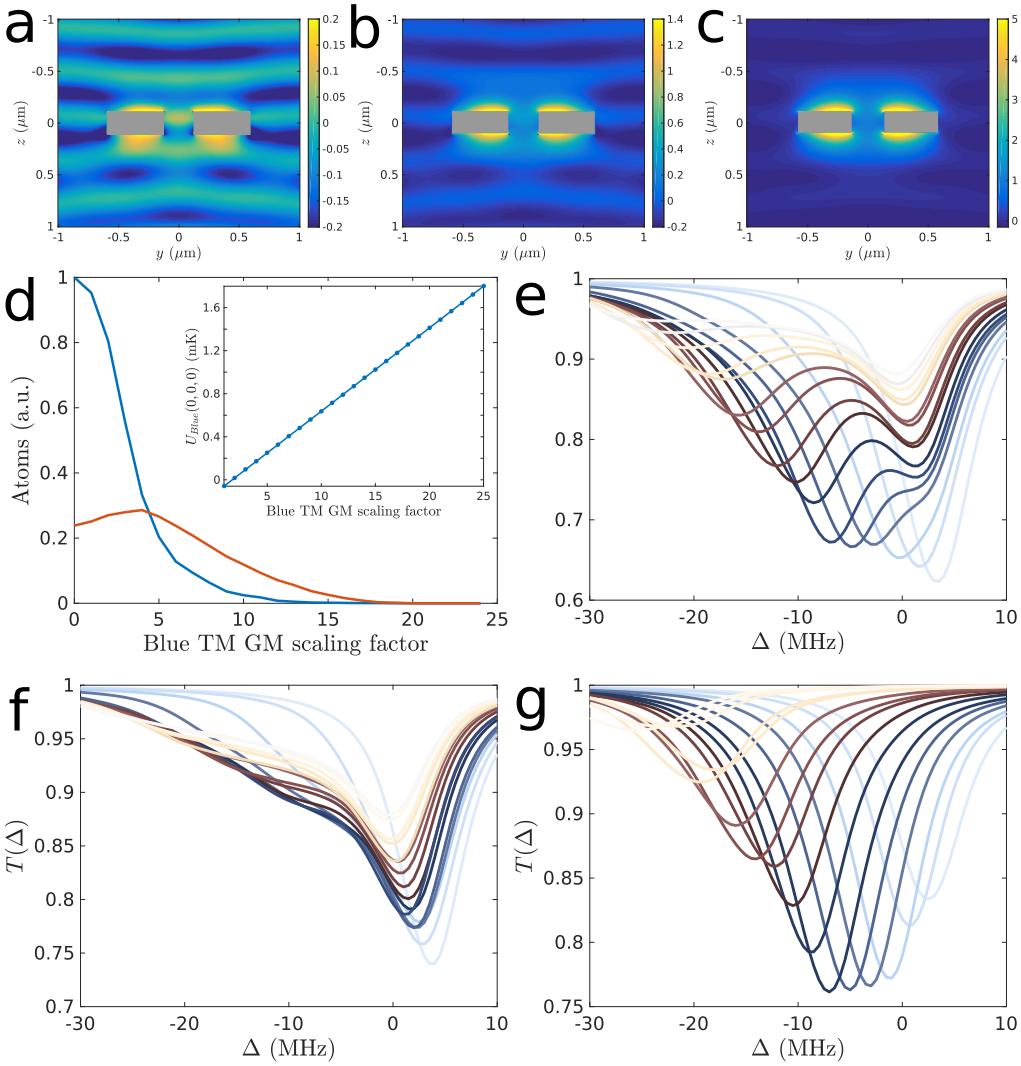

Figure 6.23: Numerical simulations for the lattice potential and a blue detuned TM-like guided mode. For (a), (b) and (c) the total potential (lattice plus guided mode) in mK is shown. The lattice is 130μK deep (ν_z = 150KHz), comparable to the lattice at the time of the measurement. The guided mode potential is indexed from its value at center of gap between the beams: (a) $U_{blue}(0,0,0)$ = 80μK represents the index 2, (b) $U_{blue}(0,0,0)$ = 320μK represents the index 5 and (c) $U_{blue}(0,0,0)$ = 1.1mK represents the index 15. Given the structure of the intensity for the TM-like mode, it is much stronger at the beams' top and bottom surfaces. The relative contribution for each class of atoms, for the different guided mode powers, is shown in (d). The inset represent the calibration between the index and the potential at $U_{blue}(0,0,0)$. The normalized transmission spectrum for a TE-like probe is shown for (e) all the atoms, (f) atoms that crash and (g) atoms that go through the gap. Indexes 1 to 16 are shown and colored in light blue, dark blue, dark brown, and then light brown in that order. Numerical simulations performed by Lucas Peng.

number of atoms that crash into the beams' top surface (blue) and the atoms that go through the gap between the beams (red). The guided mode potential is indicated as an index, and its calibration is shown in the inset in Fig. 6.23(d), where each index corresponds to a value of the potential at the center of the beams ($U(0,0,0)$).

The time average transmission spectrum can be calculated using transfer matrices for a representative sample of atoms, taking into account the spatial varying AC-shifts $\delta_{LS}(\mathbf{r}(t))$ and coupling $\Gamma_{1D}(\mathbf{r}(t))$ resulting from the trajectory simulations. These results are shown in Fig. 6.23(e), (f) and (g). In (e) the transmission spectrum for all the atoms is computed for different guided mode potentials. As the potential increases, as shown in the inset of (d), the color of the lineshape goes from light blue, to dark blue, to dark brown and then light brown, in that order. As the guided mode potential increases, the lineshapes move to the lower frequencies due to the AC-shift created by the blue detuned light. For the sample containing all the atoms, without distinguishing among classes, the lineshapes deform to exhibit two peaks. The origin of these peaks is clarified in Fig. 6.23(f) and (g). When only the atoms that crash are considered, Fig. 6.23(f), a big central peak near 0 detuning stays in that place and decreases its size. A wider tail appear in the negative detuning area, creating a very asymmetric lineshape. In case only the atoms that go through the gap between the beams are taken into account, as seen in Fig. 6.23(g), the lineshape is mostly symmetric, moves uniformly to the negative frequencies and increases its depth followed by a reduction, with a similar trend as the atom number contribution for atoms in the gap in Fig. 6.23(d). Therefore, a signature of the atoms that go through the gap can be obtained by mapping these lineshapes.

The same measurements described by the simulations were performed in the laboratory, although the calibration between input power and potential is not known precisely. The optical power of the two counter-propagating TM-like blue detuned beams that create the guided mode potential[10] is changed and the normalized probe transmission spectrum is acquired. Fig. 6.24(a) and (b) show the numerical simulations and the experimental measurements for the normalized probe transmission for different powers, respectively. Notice that the feature at 60μW and around -20MHz for the experimental data (b) follows the expected behavior for indexes around 5. Therefore, 60μW have a similar effect as the potential for index 5 $U_{blue}(0,0,0) = 320\mu$K. Further analysis is being performed in recent measurements.

[10] A counter-propagating scheme is used in order to suppress elliptical components in the polarization.

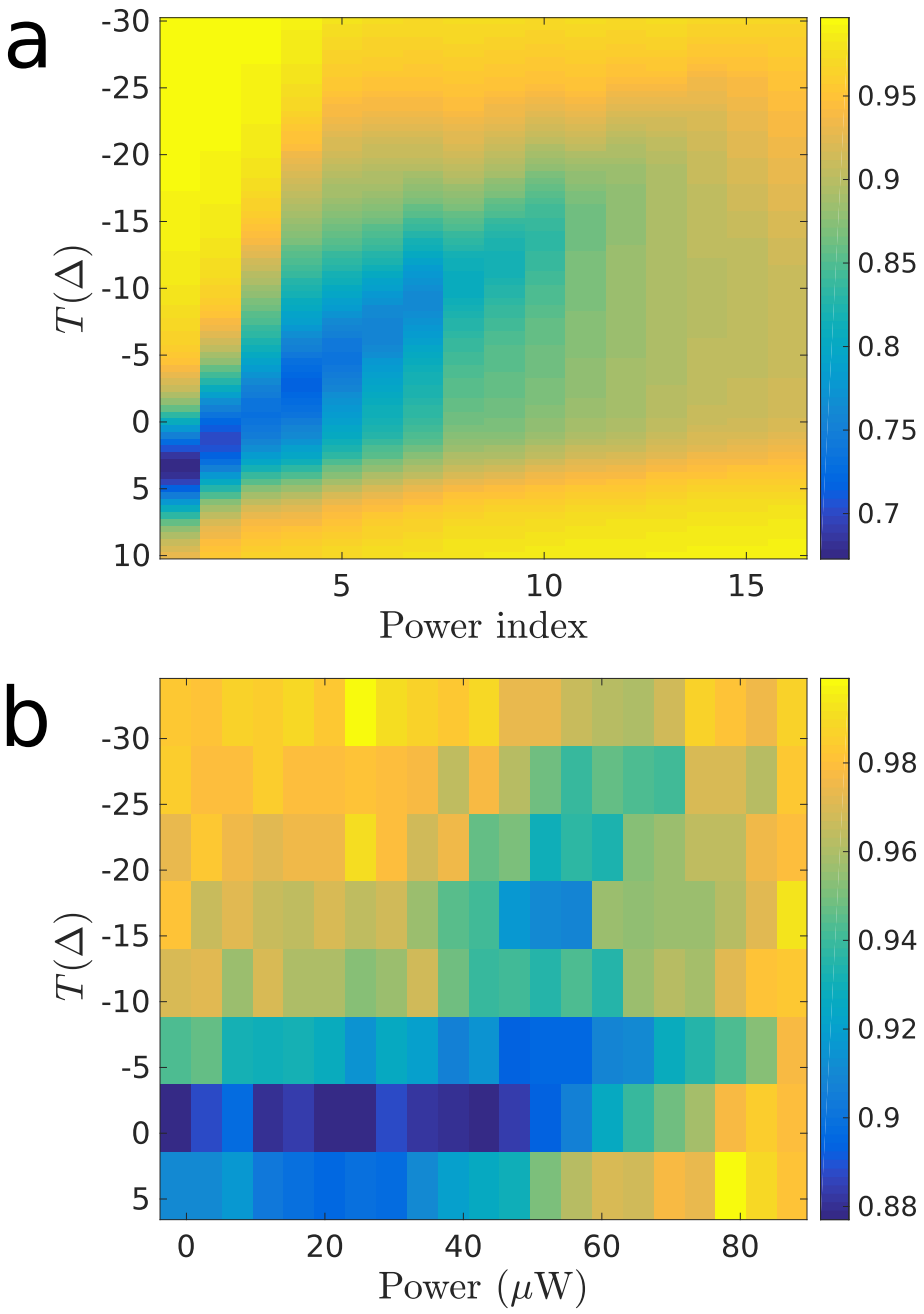

Figure 6.24: Numerical simulation and experimental lineshapes for different blue TM-like guided mode powers. In (a) the numerical simulations rearrange the lineshapes shown in Fig. 6.23(d) for all the atoms, indexed according to the criteria shown in Fig. 6.23(d). The experimental result is shown in (b). The features appearing in the region near -20MHz are similar to the features for indexes around 5. Therefore, 60μW have a similar effect as the potential for index 5 $U_{blue}(0,0,0)$ = 320μK. Lattice moves at Δf = 800KHz.

Saturation and optical pumping

In order to address atoms that are at a specific position the fact that the atoms can saturate and have two different hyperfine ground states can be used. For example, the two atomic ground states can be addressed independently by using different lasers. During the loading and transport, the atoms are continuously pumped to $6S_{1/2}F = 3$ via a near resonant $F = 4 \rightarrow F = 4$ beam. Otherwise, the lattice beams pump the atoms into a depolarized mixture of $F = 3$ and $F = 4$ in about 3ms for the intensity and detunings usually employed, Section 6.2, and apart from this source, there is no other light process that might pump the beams to $F = 4$. Therefore, the atoms are in $F = 3$ once they arrive to the device such that if the atoms are probed in the $F = 4$ state, there will be no absorption signal.

A few scattering events in an open transition are needed to pump the atoms to one of the two ground states[11]. As the scattering rate is strongly dependent on the spatial profile of the optical field through the saturation intensity $s(\mathbf{r})$, the guided mode can be used as a tool to make atoms in a certain region bright respect to the probe. This process might take some time such that convoluted with the motion of the atoms in the lattice cannot completely resolve their position with respect to the APCW. In case a few photons are needed to be scattered, it is safe to say that in at least $\sim$ 300ns the sample can be optically pumped to a given ground state. For a $\Delta f = 800$KHz conveyor belt, in 300ns the atoms move around $\delta z \approx \lambda/8 \approx 100$nm which could be relevant if the atoms are near the nanobeams. Recently, Raman transition schemes have been considered to pump atoms and probably will be applied in the near future.

In the laboratory, two different frequencies can be used to perform the pump and probe experiment. The atoms are pumped to the $F = 4$ ground state using a TE-like or TM-like guided mode near resonant with the Cs D1-line transition $6S_{1/2}\ F = 3 \rightarrow 6P_{1/2}\ F = 4'$ and with power P_{OP} while they are probed by a weak TE-like guided mode resonant with the $6S_{1/2}\ F = 4 \rightarrow 6P_{3/2}\ F = 5'$ transition. The TE-like probe is well localized in space and mostly sees atoms that might be very close to the device center. The guided mode optical pumping power P_{OP} is changed and the normalized probe transmission signal is monitored. The lattice is moved at $\Delta f = 800$kHz and its settings are the same in previous sections. As the power P_{OP} increases, the atoms are pumped to the $F = 4$ ground state and can therefore interact much more strongly with the resonant probe mode. Fig. 6.25(a) shows the signal strength as the optical pumping power is modified.

[11] Selections rules might apply

In the limit where the coupling to a specific mode of the device is small compared to the coupling to other channels $N\Gamma_{1D}/\Gamma' \ll 1$, the saturation parameter $s(\mathbf{r})$ is expected to scale as

$$s(\mathbf{r}) \approx n_g I(\mathbf{r})/I_{sat}, \tag{6.35}$$

where the intensity is

$$I(\mathbf{r}) = P/A_{eff}(\mathbf{r}). \tag{6.36}$$

$A_{eff}(\mathbf{r})$ is the effective mode area as defined in Chapter 2 and the free-space saturation intensity $I_{sat} = 2.7\text{mW/cm}^2$ for the D2-line and $I_{sat} = 2.5\text{mW/cm}^2$ for D1-line[12] [99]. This is an expected result as the atoms saturate easier if the electric field is more confined or the group velocity is smaller. Therefore, given a measured saturation optical power from the data shown in Fig. 6.25(a), the intensity and effective mode area $A_{eff}(\mathbf{r})$ can be mapped out.

As the optical pumping measurements just described are performed, the results are shown in Fig. 6.25(a) for a large span on the optical pumping power P_{OP}. The power associated with the $1/e$ transmission dip maximum happens for $P^*_{OP} = 15\text{pW}$ for both TE-like and TM-like repumping. For $n_g = 2$, that is absent group velocity enhancement, the area associated with saturation, $s = 1$, is $A_{eff}(\mathbf{r}) = 1.2\mu\text{m}^2$. From Eq(2.47), this means that $\Gamma_{1D}/\Gamma_0 = 0.3$. Both TE-like and TM-like repumping have the same strength at around 60nm from the APCW top and bottom surfaces as seen in Fig. 6.25(c) and (d) respectively. However, the fact that the two curves shown in Fig. 6.25(a) are so similar could also indicate that atoms are pumped once they are really far from the device as they might spend enough time there. Future measurements combined with the fringe sensitive data will allow a better understanding of these processes.

The absorbed power P_{abs} carries information about the saturation power. In free-space an atom only can absorb as much as it scatters, that is $P_{sc} = \frac{\hbar\omega_0\Gamma_0}{2} = 3.8\text{pW}$. Therefore, by measuring the absorbed power under saturation, it is possible to determine the atom number in free space. That is similar to the absorption imaging technique. In a nanophotonic environment, this might change. First of all, the saturation power might depend in a nontrivial way on the atom number as collective changes on the spontaneous rate exist. Second, the intensity has a clear position dependence that as usual makes the problem more complicated. Without a better understanding of the position of the atoms sampled, these measurements might not inform the atoms coupling and number.

[12] These values might change with polarization for example.

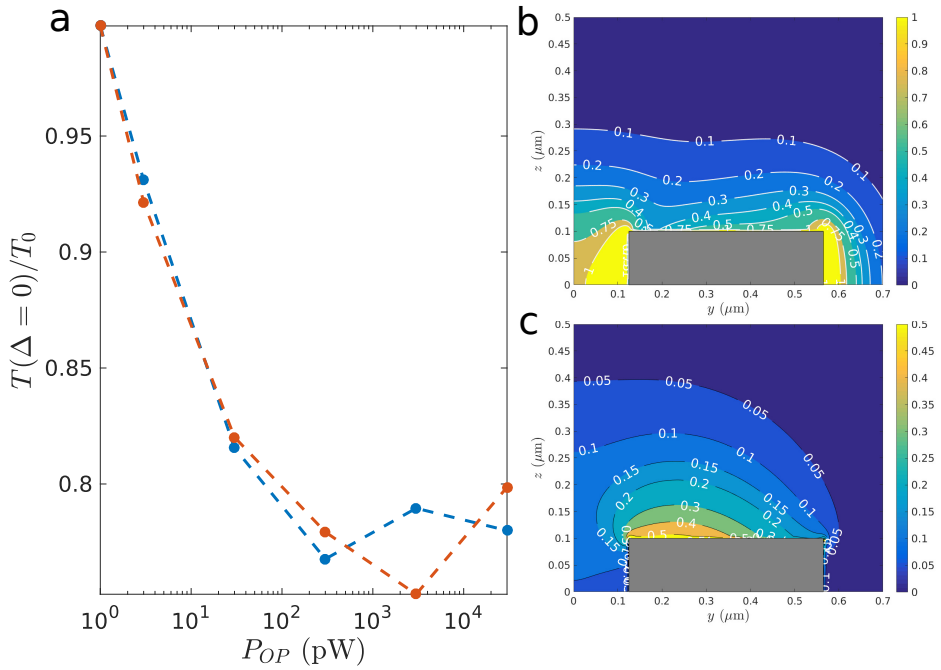

Figure 6.25: Guided mode optical pumping and probe saturation. In (a) the normalized transmission dip vs the repumper guided mode power is shown. The blue trace corresponds to a TE-like repumping beam and the red trace is for the TM-like mode. (b) A $y-z$ plane cut for the TE-like $\Gamma_{1D}(\mathbf{r})/\Gamma_0$ is shown. (c) A $y-z$ plane cut for the TM-like $\Gamma_{1D}(\mathbf{r})/\Gamma_0$ is shown. For (b) and (c), no velocity group enhancement is taken ($n_g = 2$) in Eq(2.47).

Even though the arguments are just back of the envelope estimations, the only reason they are presented is to make the point that only a few atoms are effectively probed and are weakly coupled, but close to the device. With new time dependent techniques, the saturation of atoms with different locations could be probed.

Device shifting

An important problem found during the experiment has been the shifts observed in the optical spectrum. In the miniMOT era, the observed shift was small and not really significant. In general, the shift moves the optical features towards lower frequencies. After having set up the one dimensional lattice transport, the form and speed at which thee shifts happened have changed. In Andrew McClung's thesis a more detailed description of this process can be found [144].

From the observed shift in the optical properties of the two bands correlated to running the experiment and from the SEM images taken after a chip has been used

for a couple of months, it is clear that there is material depositing on the APCW's surface. Furthermore, the modeling performed by Andrew suggests that material deposit in localized parts of the crystal and the band structure changes locally.

This limits the lifetime of the devices to a few weeks. Usually the device needs some time to activate and then the shift happens faster. In the last chip transfer, 8 devices were coupled. In the near future, free space coupling might allow us to fabricate more devices per chip.

6.4 Pursuing a fringe sensitive signal

A large part of the current and past efforts in the laboratory have focused on finding a *fringe sensitive signal*, that is, a probe transmission signal that is modulated in time with the same periodicity of the transport lattice passing through the APCW. The transport simulations show that for sufficiently localized atoms in the lattice, their arrival to the device produce a time varying signal that has details on the the probe structure and the atomic density distribution as described in Chapter 5, particularly it can be seen in Fig. 5.15. In order to pursue this search different analysis methods had been used, different experimental techniques tried and a lot of measurements performed. Very recently, there is strong evidence that this signal has been observed. Comparison with simulations under different conditions are being done and, so far, the two have a qualitative correspondence at least.

For a red detuned lattice polarized perpendicular to the device longitudinal axis x, the near field and the numerical simulations suggest that a big fraction of atoms crash into the device's top surface and some atoms might go through the space in between the nanobeams[13]. These two events happen at similar times. Therefore the relative contrast in the transmission signal can be reduced. For a blue detuned lattice instead, the two cases are separated in time in a more sensitive way and the expected contrast might be bigger. However, the atoms that crash on the beams might last shorter, such that even in the red detuned case the two populations can be partially distinguished in time. The use of guided modes as described in Section 6.3 can enhance the distinction between the different populations.

A relevant tool to characterize a possible fringe sensitive signal is the frequency filtered pick up lattice light that couples to the device. The light, about 5nW, is usually measured in a fast, high gain APD (Hamamatsu C10508-01) and the analog

[13] Over 100000 trajectories simulated in a lattice with ν_z = 150kHz moving at Δf = 800kHz, for no guided mode potentials, about 1.5% of the atoms crash into the surface, while 0.5% go through the gap between the beams.

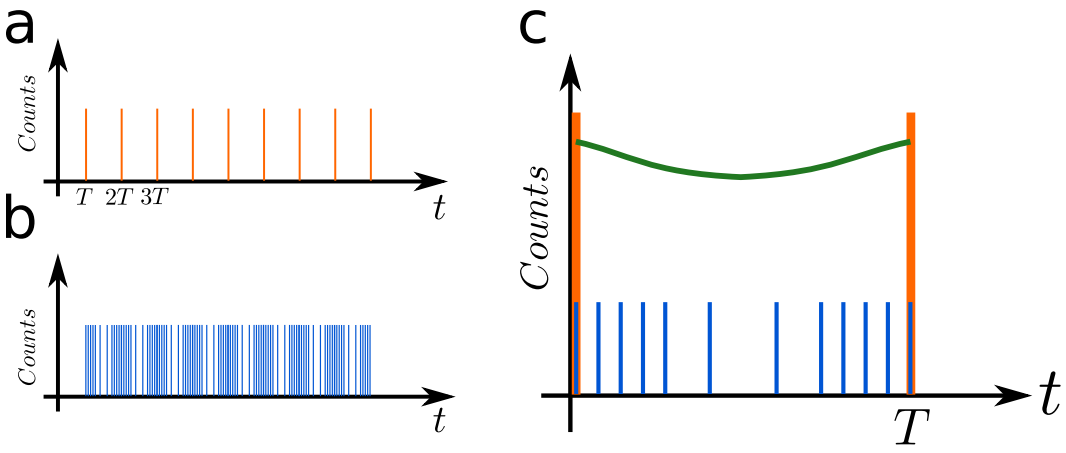

Figure 6.26: Boxcar analysis to detect a fringe sensitive signal. (a) The zero-crossing signal (orange), with periodicity T, is recorded in a channel of the photon counting card. (b) The transmitted probe counts (blue) are recorded in another channel. (c) By performing the boxcar analysis and folding the probe counts in the span of the zero-crossing period T, taking as $t = 0$ the zero-crossing time, the accumulated probe counts are used to compute the probe transmission (green curve). A fringe sensitive signal is present as it has the same modulation as the optical lattice. In the figure, noise was not added for the sake of simplicity.

output signal is used for multiple purposes. A zero-crossing detector circuit based on the fast precision comparator AD790JN digitize the lattice light oscillations. The logical output is sent to a channel in the photon counting card and its time trace is recorded together with the probe detected photons in the SPCMs. Recently, the analog signal from the fringe has been recorded on a fast oscilloscope (FPGA module).

Under normal conditions, the observed jitter on the logical output is below 10% the mean period. Apart from the electronic noise in the signal that drives the AOMs, motion of the device or the optical elements can contribute to the jitter observed in the zero-crossing signals. The pick-up light partially is sensitive to them. In recent experiments, partial reduction of the jitter has been observed by using different recording techniques and changing the amplification settings of the optical signal. The role of this jitter on the character of the expected signal is still being investigated.

Different techniques can help to detect the fringe sensitive signal and some of them will be described here. The most standard method is based on the boxcar average analysis [204] shown in Fig. 6.26. Here the input signal is integrated after certain waiting time, the trigger delay, over a specific period of time, the gate width, and then averaged or accumulated over multiple samples. To be concrete, the logic

output from the zero-crossing detector, or any other reference with respect to the fringe, is used as a trigger as seen in Fig 6.26(a). In between each trigger, the time is distributed over N_{bc} equally τ_{bc} long time bins and the probe photon counts c_i for each bin, for $i = 1, 2, ..., N_{bc}$, are recorded as in Fig. 6.26(b). This can be done in software post-analysis because the photon counting card record the time trace of each event. After doing that for several fringe cycles, the counts are averaged and the transmission signal for each time bin, with respect to the trigger, is computed as seen in Fig. 6.26(c). In general, the boxcar average improves the signal to noise ratio of n samples compared to one sample by $\sqrt{n}$.

It is expected, as observed in the numerical simulations, that the fringe sensitive probe transmission signal should be reflected in the periodicity over the N_{bc} bins. Fig. 6.27 shows the result of the boxcar analysis for the same transport sequence, red lattice moving at $\Delta f = 800$KHz, with a (a) TE-like probe and (b) TM-like probe. The sought signal is visible in both cases. The time reference, $t = 0$, is taken from the zero-crossing detector, and in the post-analysis the counts are accumulated using the boxcar technique and the compared with the same no-modulated signal taken 10ms later when no atoms are present. The signal seems to reflect some of the expected features, as for example differences between TE-like and TM-like probes can reflect the population sampled by each probe as described in Section 6.3. The TM-like samples the atoms that crash into the beams' surfaces better than the TE-like probe, that on the other hand probes the atoms that go through the beams. Those populations might be seen with different contrast in a fringe and with different timings respect to the zero-crossing. Further analysis are still pending, as for example the right interpretation of the lattice scattered light into the device is not know yet.

When guided modes are added, the spatial dependent forces exerted on the atoms can change the timing and strength of the signal. For a blue detuned TM-like guided mode with power P_{blue} and a lattice moving at $\Delta f = 800$kHz, the boxcar analysis is done for different values of P_{blue}. The normalized probe transmission plots are shown in Fig. 6.28 for a TE-like probe. In (a) the blue detuned guided mode is not present $P_{blue} = 0$, the signal is stronger near the central time, $t \sim 600$ns, and shows a very dispersive lineshape due to the position of the Cs D1-line resonance respect to the resonances near the band-edge. The red lines indicate the $\Delta = 0$MHz and $\Delta = -20$MHz values. From (b) to (d) the guided mode power increases. The central dip moves closer to $t = 0$ while it acquires a diagonal structure in the time-detuning

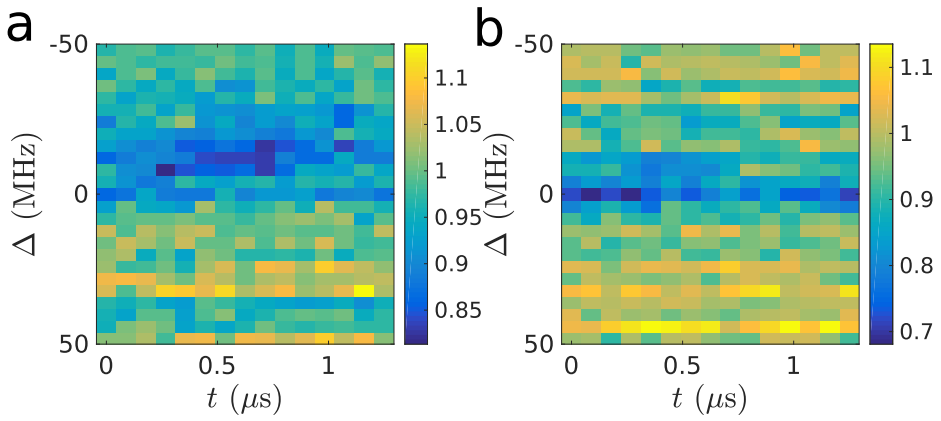

Figure 6.27: Fringe sensitive signals. The probe transmission is recorded for 2.5ms, the time it that takes for the atomic cloud to move through the device. The boxcar analysis is performed with respect to the zero-crossing signal. In (a) the probe is TE-like while in (b) it is TM-like. The analysis was performed binning the time in 15 phases with respect to the zero-crossings triggers.

plane. Both this motion and the stretching are observed in numerical simulations too. The hypothesis is that it corresponds to an enhancement in the population that goes through the gap center while different populations see different AC-shifts that explain the stretching along the detuning axis. Further analysis are still pending in order to obtain a ore accurate comparison between the two.

A normal Fourier transform on the probe photon count events can also show the periodicity of the signal. However, under normal experimental conditions the best signals are acquire when the probe count rate is around 1 mega-count/s (MC/s), so usually only about one count per cycle can be detected. Due to the photon shot noise, the fluctuation on the counts in each cycle is significant and the hope to find a representative peak in the counts power spectrum at the lattice frequency vanishes. A better way to implement a this kind of analysis is to use a lock-in amplifier.

The lock-in method can be thought as technique to amplify a signal in a fringe sensitive way. The idea behind the lock-in technique is relatively straightforward. In the analog version, a time varying signal $F(t)$ is multiplied by a known function $g(t)$ and then integrated over one period, such that $L(T,\delta) = (1/T)\int_T dt F(t)g(t)$, where δ is a relative phase that can be changed in the reference function $g(t)$. This is not more than a way to cross correlate the signal with a known reference signal. In the particular case where $g(t) = \cos(2\pi f_0 t + \delta)$ and if T is long compared to the periodicity of $g(t)$, then $L(T,\theta) = (F_0/2)\cos(\theta)$ where F_0 is the amplitude of the signal $f(t)$ at the frequency f_0 and θ is the relative phase between the

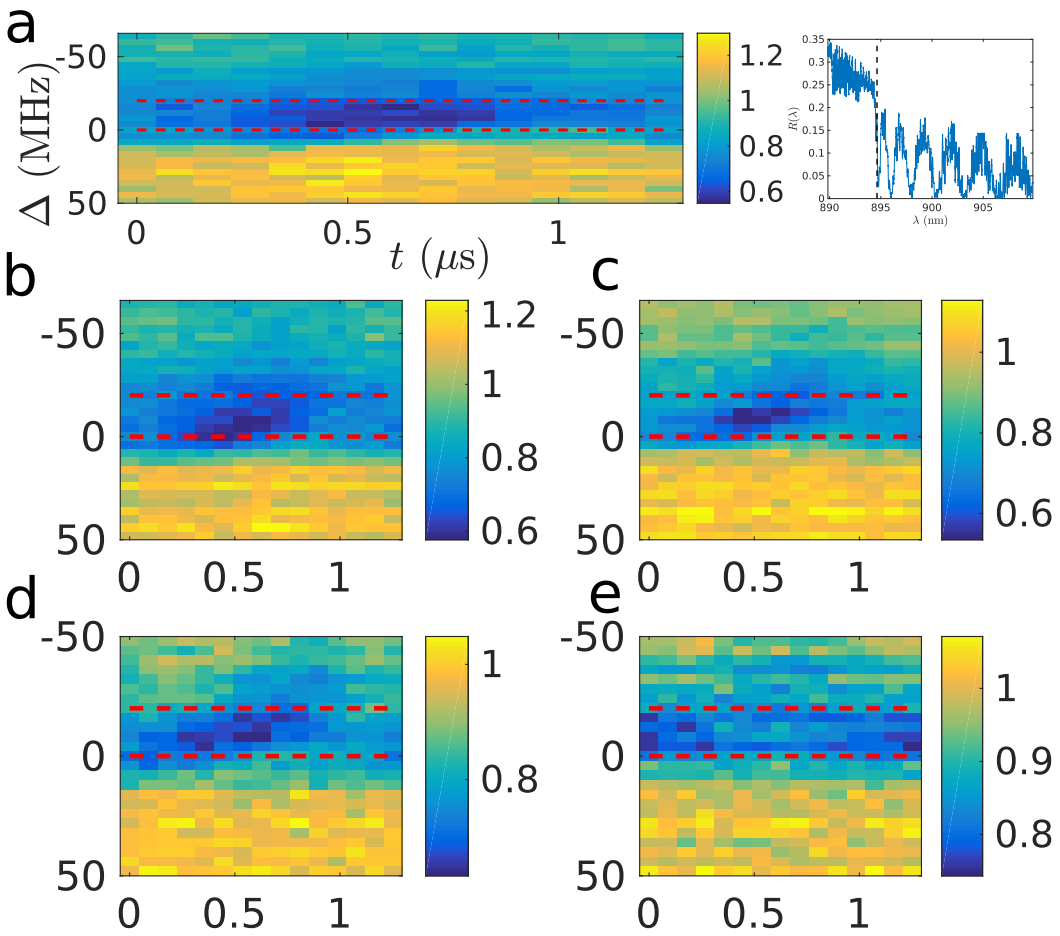

Figure 6.28: Fringe sensitive signals with a blue detuned TM-like guided mode. The probe transmission is recorded for 2.5ms, the time it that takes for the atomic cloud to move through the device. The boxcar analysis is performed with respect to the zero-crossing signal. The probe is TE-like in every plot. Axis units are only in (a), but are identical in every plot. The device reflection spectrum is shown, the dispersive lineshapes are consequence of the cavity resonance. The $\Delta = 0$MHz and $\Delta = -20$MHz lines are shown as a reference in every plot. In (a) no guided potential is present. For the rest of the sequences, the power on the blue detuned beam is (b) $P_{blue} = 33\mu$W,(c) $P_{blue} = 65\mu$W, (c) $P_{blue} = 88\mu$W, and (d) $P_{blue} = 110\mu$W.

two signals, hence a function of δ. The lock-in techniques can have significant advantages to reduce sources of frequency dependent noise. For example, if the noise is broadband, the lock-in is able to extract small modulated signals even if a sufficiently small bandwidth can be achieved. In summary, even when the noise is bigger than the signal and are indistinguishable in the time domain, if the signal has a definite frequency band and there is no large noise peak within that band, noise and signal can be separated sufficiently in the frequency domain.

The probe counts are a positive defined function, modulated at the frequency of the conveyor belt Δf. They can be hence represented by a function like $f(t) = F_0 + F_1 \cos(2\pi\Delta f t)$. Therefore, the frequency component is the same as the lattice relative frequency. Currently, analysis are being performed in conjunction with the boxcar analysis to compare and obtain evidence of a fringe sensitive signal without using the fringe as a resource.

Finally, a remark about the characteristics of the observed lattice pick-up light in the device, that we have been calling the fringe. Presumably, it is the result of the scattering of the lattice light by imperfections, roughness or dirt on the device surface all along the APCW. Numerical simulations allow us to evaluate the lattice intensity at the surface as it passes through the APCW. Together with the trajectory calculations and the calibrations of delays in the setup, the instance in each "period" where the atoms might arrive to the structure can be determined. For the plots shown in Fig. 6.28, the atoms pass through the gap between the beams at $t = 900$ns. This is still under investigation, as differences when adding guided modes can be present.

Chapter 7

TWO-DIMENSIONAL SLAB PHOTONIC CRYSTALS

This chapter will describe part of the research done a couple of years ago. Most of the theoretical contributions have been part of the work of Chen-Lung Hung, postdoctoral scholar in our group, and Alejandro Gonzalez-Tudela, postdoctoral scholar in the Theory Division at MPQ in Munich, Germany. Chen-Lung and Alejandro investigated several interesting phenomena that happen in two-dimensional photonic crystal slabs. For example, trapping deep in the subwavelength domain, where tunneling coupling grows significantly, spin-spin physics mediated by photons, and engineering long-range tunable spin interactions for trapped atoms in photonic crystal slabs [31, 33].

The focus of this chapter is on how to design a first stage two-dimensional structure, where the band structure and the structure dimensions requirements are not so challenging as in the previous articles, but still allow us to learn how to deliver and trap atoms in two dimensional structures. Both Su-Peng Yu and I have been working on this for a while. His work focus on the design and fabrication of more complex 2D structures [143].

7.1 What is new in two dimensions?

The core physics of atoms coupled to photonic crystals was described previously in Chapter 2. As a fundamental objective, the experiment aims to achieve strong atom-light coupling, and enhance collective phenomena by using guided mode photons. The knobs that can help to engineer the light-matter coupling are several. For example, the band structure $\omega(k)$ and its curvature are relevant to determine the local density of states. The strength of the electric field enhance the light-matter coupling, hence it is desirable to trap atoms in positions with high intensity. A third factor that is relevant is the dimensionality.

This is evident as soon the density of states comes along in the derivation of the coupling of the emitters to the electric field guided modes of the structure. The local density of states, $\rho(\omega)$ is, as defined in Chapter 2,

$$\rho(\omega) = \frac{1}{V}\sum_{\mathbf{k}} \delta(\omega - \omega(\mathbf{k})) = \int \frac{d^d\mathbf{k}}{(2\pi)^d}\delta(\omega - \omega(\mathbf{k})). \tag{7.1}$$

The dimensionality d is relevant then.

For the relevant "van-Hove"-like dispersion relations of the form $\omega_{vH}(\mathbf{k}) = \omega_0(1 + \alpha(\mathbf{k} - \mathbf{k}_0)^s)^{1/s}$ it is possible to express the density of states analytically. This band structure model is just taken as an example, as both this or a quadratic band structure model describe well the behavior near the band edge ($\mathbf{k} = \mathbf{k}_0$) for the structure we have been working with. For the one-dimensional case and the most common case $s = 2$,

$$\rho_{vH}^{1\mathrm{D}}(\omega) = \frac{1}{2\pi} \frac{\omega}{\sqrt{\alpha(\omega_0^2 - \omega^2)}}, \tag{7.2}$$

but for two-dimensional systems it is

$$\rho_{vH}^{2\mathrm{D}}(\omega) = \frac{1}{2\pi\alpha} \frac{\omega}{\omega_0}. \tag{7.3}$$

For a parabolic or quadratic dispersion relation the results is a bit more striking, as for two-dimensional systems the density of space can be even constant. Even in this general situations the discrepancies between the different spatial dimensionalities are reflected in the divergence of the density of states near the band edge. The one-dimensional case shows a square root singularity, while the two-dimensional case is flat or linear close to the band edge.

Another relevant dispersion relation is the Dirac or linear dispersion relation $\omega_D(\mathbf{k}) = \omega_D + \alpha(\mathbf{k} - \mathbf{k}_0)$. Near the special point $\mathbf{k}_0$, where the energy dispersion is not gapped. This relation can be relevant on certain structures and several interesting works have been carried out with this situation. An interesting point is that the density of states for any dimension $d \geq 2$ will vanish near the band edge following the relation

$$\rho_D^{d\geq 2}(\omega) \propto (\omega - \omega_D)^d, \tag{7.4}$$

while it is flat for the unidimensional case $\rho_D^1 = \frac{1}{2\pi\alpha}$. Particularly, for a 2D structure at the critical point $\mathbf{k}_0$, Xie et al. [205] determined that the interaction can be purely coherent as the dissipation $\Gamma_{2\mathrm{D}}^{ij} = 0$ and the interaction is purely due to a Coulomb like spin-exchange term $J_{2\mathrm{D}}^{ij}(\mathbf{r}_{ij}) = -J_0/r_{ij}$, in terms of the ideas developed in Chapter 2 extended to two-dimensional cases [31]. This leads to photon trapping if a defect, maybe an atom, is present in the lattice, even without a band gap as reported using numerical simulations in [205].

Two-dimensional structures are more complicated than the one-dimensional ones. The reduced Brillouin zone now expands in two dimensions and the high symmetry

points are more abundant. The easier case is a square lattice. For instance, a square array of holes in a dielectric slab with spacing a in the x and y directions. The reciprocal lattice is also a square lattice with lattice constant $2\pi/a$ [84]. If a bandgap for some polarization were present, or a full bandgap, the frequency at one of the two high symmetry points, will determine the span of the bandgap. In this case, the two frequencies at the two high symmetry points will define different detunings for the same atomic transition, associated with different values of the decay length of the localized modes inside the bandgap. Following the procedures discussed in Douglas et al. [28] and in González-Tudela et al. [31], it is expected that the bounded photonic cloud can reflect the directional features associated with the 2D band structure. The asymmetry of this cloud could be used, for example, in photon routing experiments if interactions between photons are considered as in the one dimensional case discussed in Douglas, Caneva, and Chang [38].

New regimes in the Hubbard model can be explored by using the photonic crystal slabs to localize atoms at closer distances. If structural details are made smaller and smaller, and the patterned dielectric slab ca be used only as a way to trap atoms within these subwavelegth scales, then tunneling coefficient between adjacent sites can increase significantly [31]. If external illuminations fields are used as in the APCW case, the requirements to achieve enough contrast in the intensity pattern to provide stable trapping, are harder as the dielectric features are smaller [31, 25]. Usually, higher powers and smaller detunings are required, with the consequent changes in the eating mechanisms. Vacuum forces can help to provide confinement in these cases if the structure is designed and fabricated with the right features [31].

For different structures, where a careful design of the guided modes is taken into account by, for example, aligning the band edges with relevant atomic transitions of special trapping frequencies, the trapping can be provided with the help of different combinations of symmetries and bands as in the APCW [31]. Not only strong coupling can be also implemented near band edges, but if there is a photonic bandgap and the atom is inside a hole for example, the spontaneous emission to free space and other channels, Γ', can be reduced as the emission in that plane is suppressed. Therefore, relative enhancement in the factor Γ_{2D}/Γ' can be achieved from two effects in slab structures. It is also possible to observe this same effect for dipoles placed in some quasi-1D systems but that inherit that property from a linear defect in a 2D slab structure, for example in slotted waveguides designed and fabricated by Su-Peng Yu.

Challenges in creating a two dimensional photonic crystal slab are several. The fabrication is still complex, as more area is present, it is more probable defects and localized modes. Coupling light into the structures is complex. The light dispersion in 2D slabs is different than in 1D and, as a consequence, one can imagine that light spreads across the slab. Therefore there is a necessity to couple light from several directions. From the point of view of the light-atom coupling, the richer band structure could induce a more complex structure in terms of resonances and coupling to other modes.

Two-dimensional free space systems are also very interesting. Atoms trapped in two dimensional lattices are more common now in degenerate quantum gases experiments, but even far from this regime, collective phenomena associated with the geometry and filling fraction can reveal interesting properties about the scattering of light by atomic arrays. This results is well known in the nanophotonic community, where for a two-dimensional array of particles, or holes, big reflection factors can be found near wavelengths comparable to the lattice periodicity [206]. For atomic arrays, recent work by Shahmoon et al. [207] have shown that cooperative effects in the light scattering properties are present. Both phenomena are associated with resonances between the incident field and the scattered field, described by the corresponding Green's function. This is also an interesting prospective for the work carried out here and in the optical tweezers community. Recently, novel work by Perczel et al. [208] have shown that atomic quantum optical system in two dimensional arrays can display interesting topological properties. In the system that the authors of the article considered, a honeycomb array of atoms displays a broken time-reversal symmetry regime due to the presence of magnetic fields and Zeeman structure of the atoms. The result is the creation of topological protected optical modes that are robust not only against imperfections, but also with respect to scattering into free-space or other modes.

7.2 Designing a two-dimensional structure

The design of a nanostructure that can fit into the science vacuum chamber and be suitable to do reasonable experiments is a multi step process. Not only the nominal photonic crystal section needs to be designed according to the purpose of the experiment, but also all the other mechanical and optical subcomponents need for the integration into the atomic experiment. In this section, a partial description of a structure where light can be couple in and out the nominal section with high efficiency along one direction will be presented. This resembles a first step towards

studying a similar problem as in the APCW system. After a preliminary structure was designed, Su-Peng Yu was able to fabricate a couple of structures where the reflection and transmission were characterized. Therefore, part of the work in this section overlaps and complements with the one appearing in Su-Peng Yu's thesis.

Nominal photonic crystal

The nominal section of the photonic crystal can be designed for different purposes. In the specific case of this application, in order to reduce the complexity of the problem in a first stage, a square lattice of holes in a slab is considered. As shown in Fig. 7.1(a), a Si_3N_4 slab with thickness $t = 200$nm has been extruded with holes with radius R and in a square lattice array with lattice constant a, oriented along the x and y direction. The symmetry of the guided modes can be classified with respect to the symmetry along the $z = 0$ plane, such that the TE-like guided modes are polarized mostly parallel to the $z = 0$ plane, while the TM-like modes are polarized mostly perpendicular to the $z = 0$ plane. The band structure is determined by the triad of high symmetry points with coordinates in the reciprocal space (k_x, k_y): $\Gamma = (0, 0)$, $X = \frac{\pi}{a}(1, 0)$ and $M = \frac{\pi}{\sqrt{2}a}(1, 1)$ as seen in Fig. 7.1(b). There is also the Y-point with coordinates $Y = \frac{\pi}{a}(0, 1)$. The band structure is usually presented along the $\Gamma - X - M - \Gamma$ closed circuit and the light line is defined by $\omega_{LL} = c|\mathbf{k}|$ along that path.

There exist several a and R values where the frequency at the X-point or the M-point can be placed close to the Cs D1-line or D2-line transition. For example, Fig. 7.1(c)-(d) shows the lowest two bands for the TE-like and TM-like modes, respectively, for a structure with $a = 290$nm and $R = 103$nm. In general, the frequency at the M-point in the dielectric band is higher than the lowest frequency in the air band, therefore there is not a bandgap present.

The mode profiles can be calculated numerically as in the APCW case, by properly changing the boundary conditions to reflect the 2D periodicity. For the TE-like modes near the high symmetry points, the guided mode field amplitude $|\mathbf{E}(\mathbf{r})|$ for different plane cuts are shown in Fig. 7.2. The first row corresponds to the dielectric function $\epsilon(\mathbf{r})$ for different planes. The first plane (first column) is the $z = 0$ plane, the second plane (second column) is the $y = 0$ plane, and the third one (third column) is the $x = 0$ plane. For each plane, the corresponding field amplitudes for the TE-like mode for different bands and at different high symmetry points are plotted in the different rows in Fig. 7.2 as explained in the caption.

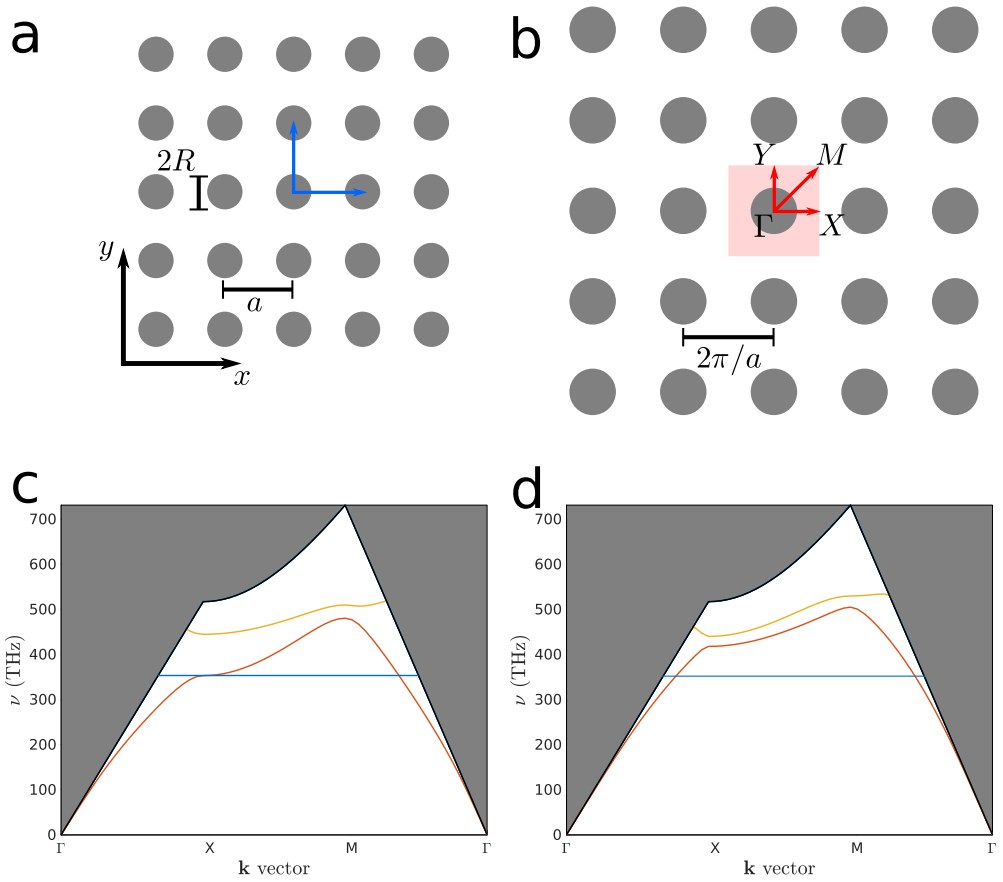

Figure 7.1: Photonic crystal slab with square lattice of holes. (a) In real space, the holes with radius R are arranged in a square array in the $x-y$ plane with lattice constant a. The reciprocal lattice is shown in (b), with the Brillouin zone (red region) and the high symmetry points indicated. For the values $(a, R) = (290, 103)$nm the (c) TE-like modes and (d) TM-like modes projected band structure are shown. The gray region indicates the light cone and the blue line indicates the Cs D2-line frequency.

The air and dielectric bands show higher intensity in the regions where vacuum or dielectric are present, respectively. The combination of the relevant symmetries and the propagation direction create the observed patterns. For example, for the dielectric band TE-like mode near the X-point (second column) the propagation vector is along the x-direction and as the field is polarized in the $z = 0$ plane, the high intensity regions are along the y-direction. Similar features happen for the different propagation directions and bands. Interestingly, for the air band the TE-like field near the X-point has a strong amplitude in the hole, while near the M-point it has an intensity minimum in the middle, suitable for probing and trapping. The TM-like modes exhibit the expected behavior, and the field is strong on the top and bottom of the slab, leaving a series of interesting minimums near the center of the

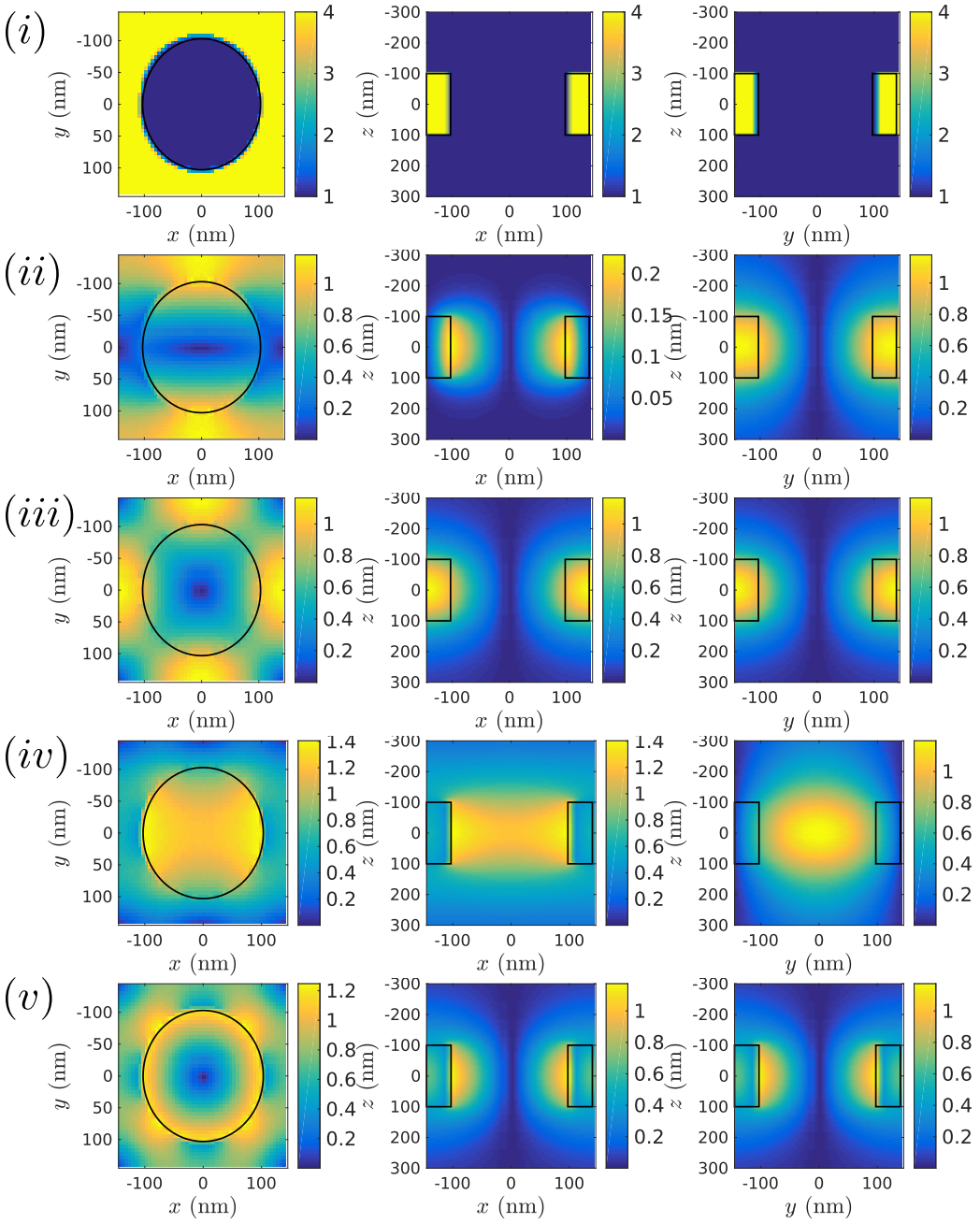

Figure 7.2: Electric field amplitude for TE-like guided modes. Each row correspond to a different band and high symmetry point, while each column represents the same plane $z = 0$, $y = 0$and $x = 0$, respectively. Rows: (i) dielectric function $\epsilon(\mathbf{r})$, (ii) X-point, dielectric band, (iii) M-point, dielectric band, (iv) X-point, air band, and (v) M-point, air band. The unit cell has $(a, R) = (290, 103)$nm.

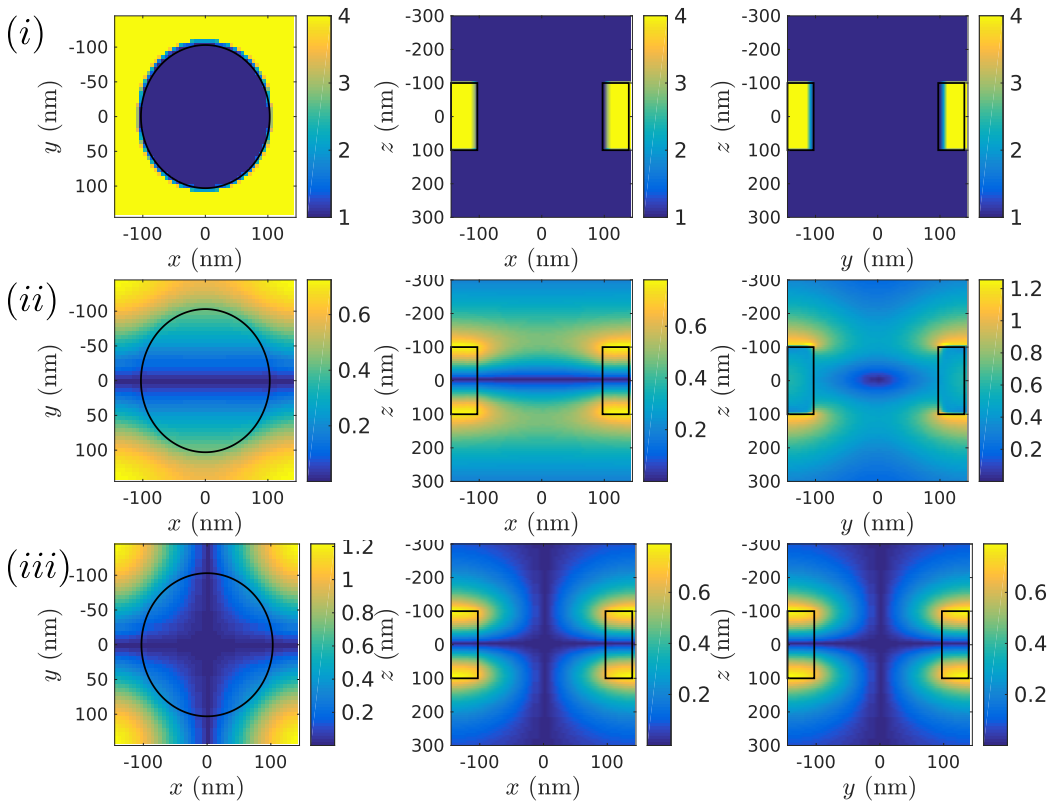

Figure 7.3: Electric field amplitude for TM-like guided modes. Each row correspond to a different band and high symmetry point, while each column represents the same plane $z = 0$, $y = 0$ and $x = 0$, respectively. Rows: (i) dielectric function $\epsilon(\mathbf{r})$, (ii) X-point, dielectric band, and (iii) M-point, dielectric band. The unit cell has $(a, R) = (290, 103)$nm.

holes. The main characteristics for the high symmetry points in the air band are shown in Fig. 7.3, where the plots follow the same logic as before. Note the very high intensity contrast that can be found for several TE-like and TM-like guided mode amplitude profiles.

In order to understand the light-matter coupling in these two dimensional structures, the electric field generated by a dipole near the structure was simulated using FDTD simulations as described in Chapter 2. These simulations allow to characterize the different spectral features of the Green's functions. The dipole source is placed 100nm above of the structure surface at different relative positions with respect to the array of holes. As the computation can be quite intensive, due to the spatial extent of the device and the dipole emission pattern, the first round of simulations were done with a small 15×15 array. In Fig. 7.4 the position of the dipole relative to the dielectric function is shown in the top-right insets on each plot. Each row shows

the enhancement of the total spontaneous emission rate compared to free-space, expressed by the ratio $\mathrm{Im}\left(\bar{\mathbf{G}}_{ii}(\nu)\right)/\mathrm{Im}\left(\bar{\mathbf{G}}^{0}_{ii}(\nu)\right)$. Most of the features are associated with the band structure of the photonic crystal and others are associated with the behavior of an atom near a uniform dielectric slab. For comparison, the uniform slab enhancement is shown in Fig. 7.5(a).

The first row, Fig. 7.4(a), places the dipole source at $z = 200$nm, in the center of the system, equidistant from the nearest 4 holes. There, the Green's function components in the x and y direction are identical ($\bar{\mathbf{G}}_{xx} = \bar{\mathbf{G}}_{yy}$) due to the positioning and lattice symmetry. The xx component is almost flat, following the xx slab-like variations. The peak at $\sim$ 350THz is associated with the TE-like dielectric band modes near the X- and Y-points that have some intensity at the dipole's position, as seen in the second row of Fig. 7.2. The zz component has a different structure, also following the broad features of the zz slab-like component. The peak at $\sim$ 410THz is associated with the TM-like dielectric band mode at the X- and Y-points. The small peaks between 450THz and 500THz could be associated with resonances with the dielectric TM-like modes near the M-point. Both features are consistent with the dipole position and the field intensity pattern for the different modes.

The second row, Fig. 7.4(b), corresponds to the case where the dipole is at $z =$ 200nm but equidistant only to two centers aligned in the y-direction. At this position, the dipole sees the lattice in a different way in the $x - y$ directions, such that the three diagonal terms will be different between each other. The yy have a series of oscillations at lower frequencies that end up in the big resonance around 350THz. Given the dipole orientation and the relative position, this peak is consequence of the resonance due to the dielectric TE-like mode near the X-point. The Y-point contribution is significantly suppressed as the intensity there is small. Over that same range, the emission of a dipole aligned along the x direction is not enhanced. That is because the dielectric TE-like mode near the Y-point, polarized along the x-direction, has a smaller intensity at the dipole's position. The dielectric M-point contributes, but its polarization is mostly along the diagonal direction. In the band between 450THz to 500THz there are multiple resonances and features the lowest level seems to be well above 1. These can be associated with resonances with the TE-like air band modes; even though it has a smaller intensity there, it has a flatter band, and hence smaller group velocity. For the zz components the same dielectric TM-like X-point feature appears near 400THz. The feature around 450THz is probably associated with dielectric TM-like mode at the M-point.

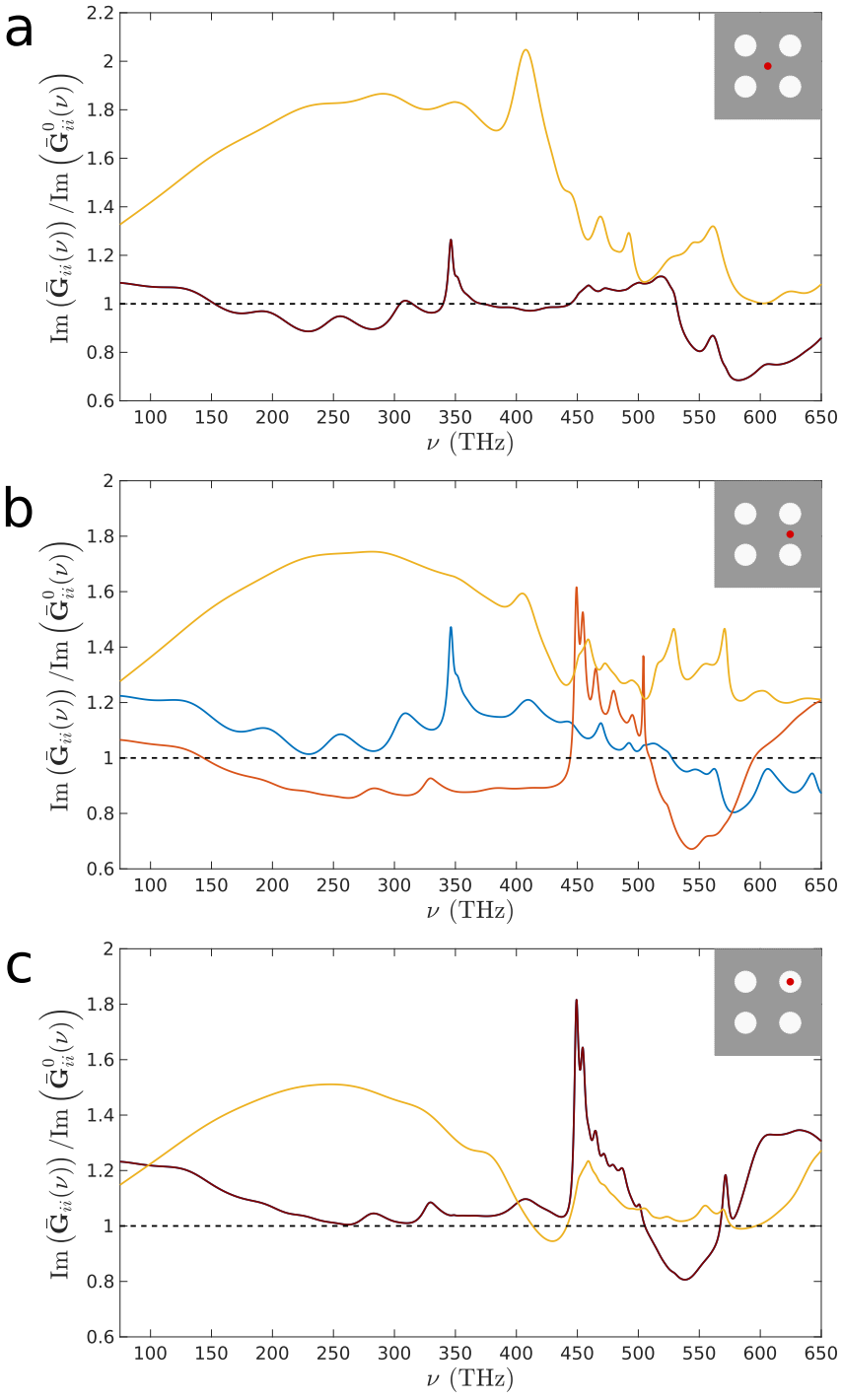

Figure 7.4: Spontaneous emission rate enhancement for a single dipole near a small 15×15 array. In each case the dipole is at $z = 200$nm, that is 100nm from the dielectric surface. Yellow traces corresponds to the zz components, red traces are xx, yy is represented with blue traces, and, whenever the symmetry makes $xx = yy$, their trace is dark red. The unit cell has $(a, R) = (290, 103)$nm.

The third row, Fig. 7.4(c), shows the case of a dipole on top of a hole at $z = 200$nm. Due to dipole's position and the lattice symmetry, the x and y contribution are equal. For the xx and yy components, a strong peak near 450THz appears. As the atom is now above the holes, the suspect is the TE-like air band. The zz component follows the usual broad feature peaked at 250THz, but it also shows a small peak near 470THz probably associated with the TM-like air band mode, as it has a significant intensity there.

A few more FDTD simulations are shown in Fig. 7.5. The 200nm thick nitride slab Green's function contribution is calculated at 100nm from the dielectric surface and shown in Fig. 7.5(a). In order to resolve better the spectral feature in Fig. 7.4, for the second cases studied there a bigger array with 50×50 sites is simulated and shown in Fig. 7.5(b). The resonant features are narrower and taller, and also shows further structures associated with the finite size simulation volume. The narrow peak is associated with the dielectric TE-like X- and Y-points as before. A series of smaller peaks for higher frequencies are now resolved. If the dipole is positioned 200nm from the surface, most of the photonic crystal substructure vanishes, and the strong modulations due to the slab-like characteristics dominate. That can be seen in Fig. 7.5(c) for a small 15×15 array.

Trapping in this photonic crystal slab can be also performed by using high contrast guided modes as described in González-Tudela et al. [31]. A different possibility is to use a external illumination techniques, also explored in [31]. In particular, a moving standing wave is suitable to transport atoms near the device. Further investigation is being performed to take into account the different effects discussed in the APCW case.

Coupling in and out along one direction

A simple experiment that can be performed with atoms trapped near the two dimensional slab is to study one dimensional transport properties. In that case, atoms arranged near the patterned slab can be interrogated with a beam propagating in a specific direction, and then, that light can be efficiently collected at the other side of the device. There are more interesting things to do, but for the sake of keeping the discussion simple, this is the case that will be considered here.

For instance, suppose that the fundamental mode of a rectangular cross section waveguide propagates along its axis, the x-direction. The waveguide ends in much a wider rectangular cross section waveguide with the same thickness that extends

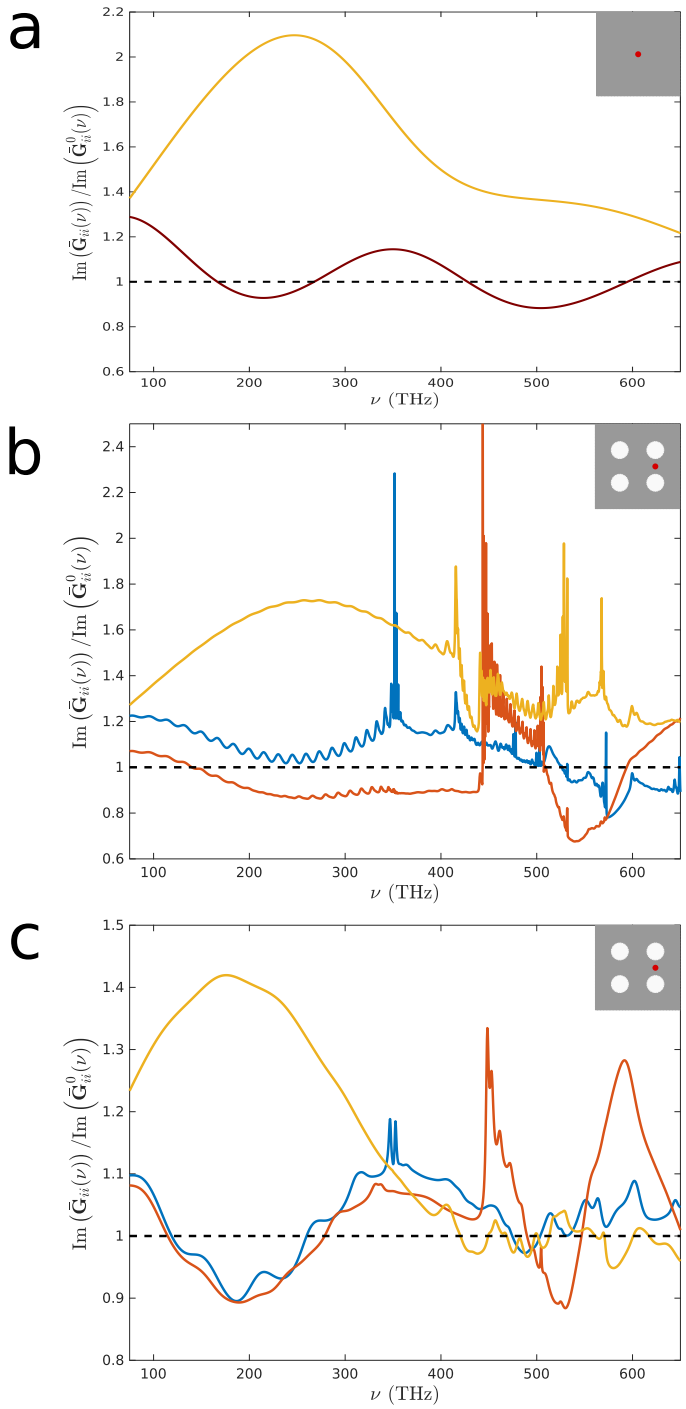

Figure 7.5: Spontaneous emission rate enhancement for a single dipole near different dielectric structures. In (a) a uniform dielectric slab contribution is shown for the used thickness and refractive index. In (b) a bigger array of 50×50 was used to resolve better the features. Finally, in (c) the dipole is placed at $z = 300$nm and the array is just 15×15. The color code is the same as in Fig. 7.4. The unit cell has $(a, R) = (290, 103)$nm.

along the x-direction as seen in Fig. 7.6(a). Intuitively, the incoming field spans transversally along the $y-z$-plane with associated momentum components in a region with span $\Delta\mathbf{k}_\perp$. When the field propagates in the slab-like section, the dispersion relation, $\omega(k_x, k_y) = v\sqrt{k_x^2 + k_y^2}$, imprints a different behavior for the momentum components of the incoming field. To be specific, the equi-frequency curves (EFC) are circles with center in the origin and the group velocity, $v_g(\mathbf{k}) = \nabla_\mathbf{k}\omega(\mathbf{k})$, is perpendicular to the EFCs. For a slab, the EFCs are shown in Fig. 7.6(b). Given the initial spreading of the incoming field and its frequency, the slab will spread the initial field over a broader transversal region as the different components will acquire very different group velocities.

If additional structure is added to the slab, for instance a periodic hole pattern as in Fig. 7.6(c), the dispersion relation and the EFCs will change. For example, Fig. 7.6(d) shows the dielectric TE-like EFCs for a square lattice photonic crystal slab with $(a, R) = (290, 103)$nm. As it can be seen, the EFC are flat for frequencies higher to 350THz near the M-point. The dashed black square in the figure is the region where the group velocity direction is almost uniform. Near the Γ-point, the dispersion relation is similar to the slab, but as the frequency approaches the frequency at the special high-symmetry points, the EFC deform and exhibit regions where it is flat over a significant space. For the TE-like dielectric band in square lattice structure, this only happens near the M-point as the X- and Y-points are saddle points for the dispersion relation $\omega(\mathbf{k})$. For the air band, not shown here, it might be possible to get flat EFCs near the X- and Y-points. The original idea behind this design, referred in the literature as self-collimation, is due to Witzens, Loncar, and Scherer [209].

A high input-output efficiency system can be designed by coupling a rectangular cross section waveguide to a photonic crystal slab with the dimensions described before and the M-point aligned along the propagation direction. In this system, the frequencies that can be self-collimated will propagate through the slab without significantly spreading over different transversal regions of the waveguide. The spreading is a consequence of the small curvature of the EFCs and the span of the initial input mode. For example, the narrower the input waveguides, the more the field spreads transversally in the patterned slab as it occupies a bigger range in the (k_x, k_y) plane. The reflection and transmission simulations usually take a long time, so in this case there was not a systematic characterization of the parameter space.

The optimized self-collimation band structure for $(a_{sc}, R_{sc}) = (330, 103)$nm has the

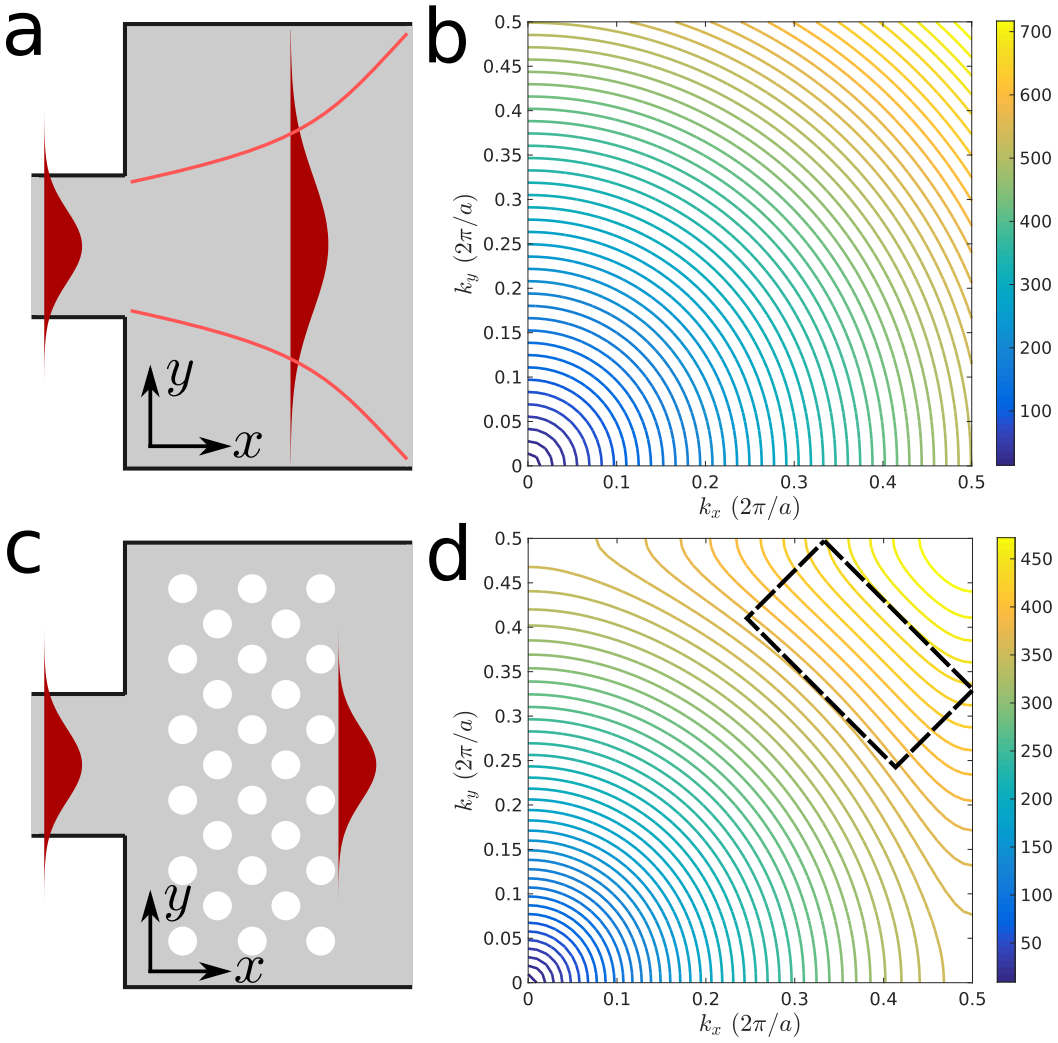

Figure 7.6: Self-collimation in photonic crystal slabs. In (a) and (c) the propagation of light from a narrow to a wider waveguide is depicted for cases with and without holes in the slab. The EFCs are plotted for (b) a uniform slab and (d) a $(a, R) = (290, 103)nm$ unit cell. The black square indicates the region in **k**-space where the group velocity (perpendicular to the EFCs) has uniform direction and can be used in the self collimation section.

Cs D2-line a few tens of THz below the M-point frequency, such that its EFC is as flat as possible for that frequency. On the other hand, the nominal section has its M-point aligned with the Cs D2-line with $(a_{nom}, R_{nom}) = (360, 103)$nm. The two sections can be connected by an impedance matching section where the lattice constant a and hole radius R are changed progressively from (a_{sc}, R_{sc}) to (a_{nom}, R_{nom}). In the nominal section the self collimation is not so effective, but if its length is short enough to not show significant transversal spreading it is still an acceptable solution. After the nominal section, another impedance matching stage followed by a self-collimation section ends in a wide waveguide.

The last step in the coupling is what we called an anti-reflective (AR) coating. Its purpose is to suppress the reflection from the multiple interfaces of the system. The method is based on work by Lee et al. [210]. To be specific, after the input waveguide an additional single row of holes, at a distance d_{ar} from the first row of holes in the self collimation section, is added. The holes of the AR coating feature are separated between them by $\sqrt{2}a_{sc}$ and have a radius R_{ar}. The setup can be seen in Fig. 7.7(b).

In a simple model where a light beam normally incident from a first homogeneous medium n_1 onto the second thin slab n_2 placed before the second semi-infinite section n_3 as in Fig. 7.7(a), the total amplitude reflection coefficient r is

$$r = \frac{r_{12} + r_{23}\mathrm{e}^{i2\phi}}{1 + r_{12}r_{23}\mathrm{e}^{i2\phi}}, \tag{7.5}$$

where r_{ij} is the reflection coefficient at the $n_i - n_j$ interface [51] and ϕ is the accumulated phase change across the slab n_2 region. The reflection coefficient can be made zero in case $r_{12} = -r_{23}\mathrm{e}^{i2\phi}$. Therefore, by changing the properties of the slab section n_2, the amplitude and phase of the coefficients can be adjusted in order to suppress the reflection r. In the present case, a systematic study was performed to optimize the values of d_{ar} and R_{ar} that minimizes the reflection, resulting in $(d_{ar}, R_{ar}) = (190, 80)$nm.

The full structure model has then 5 fundamental components as seen in Fig. 7.7(c). The first component is the input waveguide. This waveguide can be wired to the rest of the chip's infrastructure, as done in the APCW. The light enters the slab region and the first thing it encounters is the AR-coating row of holes (orange circles in Fig. 7.7(c)) with radius R_{ar}, spacing $\sqrt{2}a_{sc}$ and at a distance d_{ar} from the first row of holes in the self-collimation section. Then, the self-collimation section (green circles in Fig. 7.7(c)), consisting of a M-point oriented square array with (a_{sc}, R_{sc}),

transitions, through an impedance matching section (not shown), to the nominal section. The nominal section (blue circles in Fig. 7.7(c)) has (a_{nom}, R_{nom}), such that its M-point dielectric TE-like frequency is aligned with Cs D2-line.

The final reflection and transmission simulations for the full designed structure are shown in Fig. 7.7(d) and (e). The reflected and transmitted power is projected into the input-output waveguide modes for cases with (d) and without (e) the single row of AR coating near the two waveguides. Transmission regions higher than 80% are found for this system and the resonances are extinguished in the relevant frequency range near the Cs D2 transition (black vertical lines).

For that device simulated in Fig. 7.7(d), the field intensity $|\mathbf{E}(\mathbf{r})|^2$ for the $z = 0$ plane is plotted in Fig. 7.8. The different sections can be seen along the collimation of the input waveguide mode.

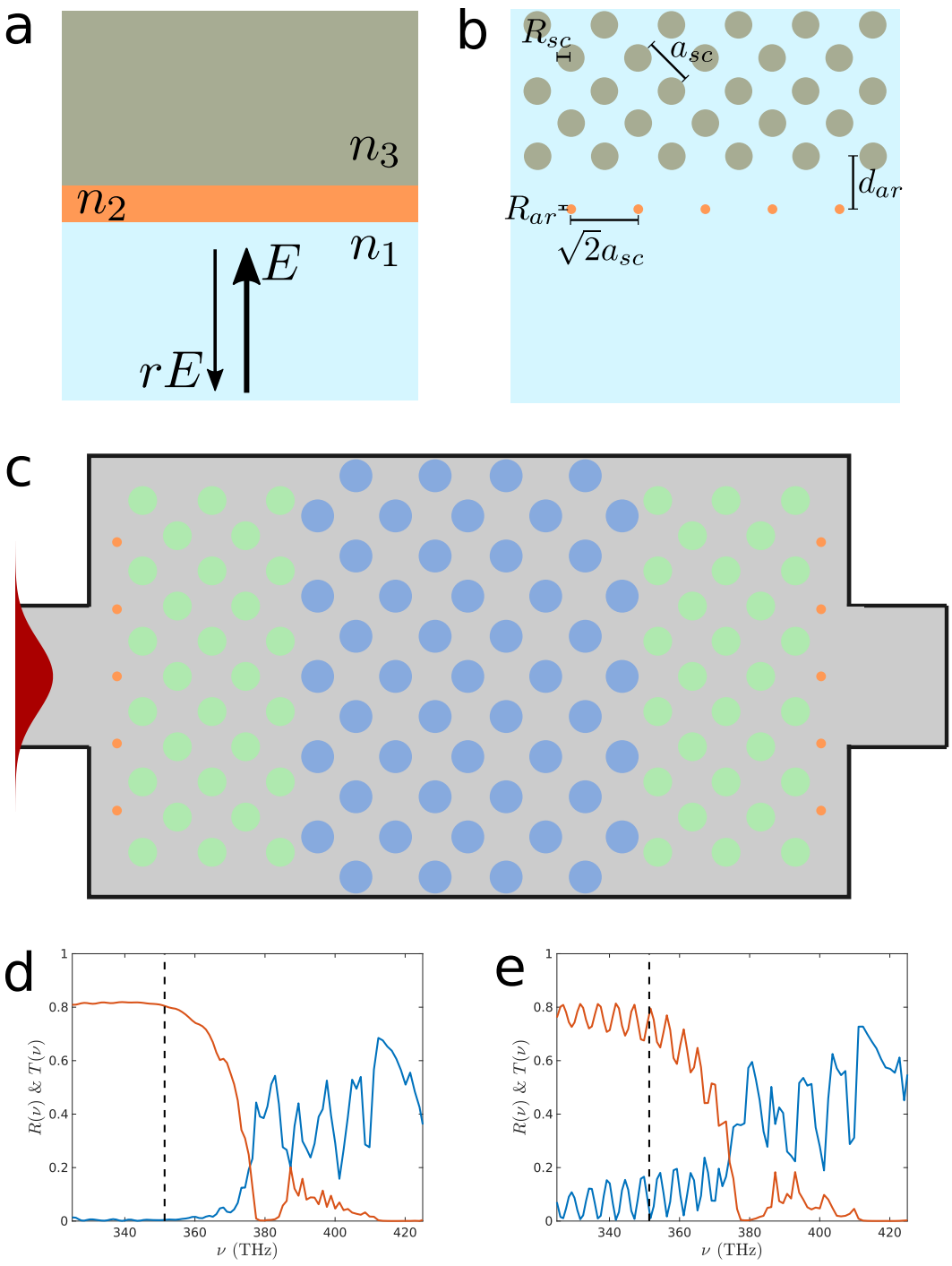

Figure 7.7: AR-coating and full device description. The AR-coating can be understood in a simple slab model as in (a) and the photonic crystal implementation is shown in (b). The full structure sketched in (c) (orange-AR-coating, green-self-collimation, blue-nominal) can be simulated using FDTD techniques. The transmission and reflection simulations (d) with and (e) without the AR-coating row are plotted. The black vertical line is the Cs D2-line frequency.

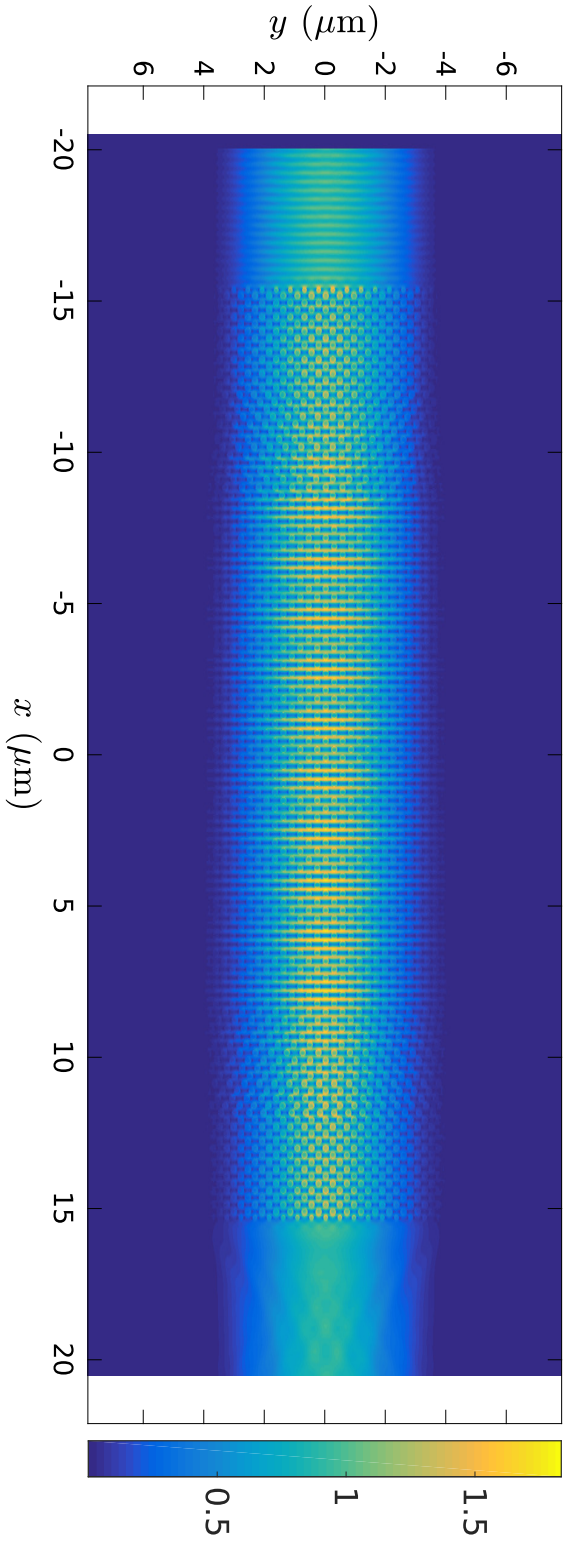

Figure 7.8: Field intensity $|\mathbf{E}(\mathbf{r})|^2$ for the full device at the plane $z = 0$.

Chapter 8

CONCLUSION AND OUTLOOK

This final chapter summarizes the key results presented in this thesis. Additionally, forthcoming changes in the experiment are discussed in the outlook.

8.1 Conclusion

Photonic crystal systems represent a new challenge for quantum optics and atomic physics. Starting from the design, accomplishing the nano-fabrication procedures, followed by the understanding of light-matter interaction in nanophotonic environments and ending with realization of an atomic physics experiment. A new field that combines all these characteristics is drawing more attention from researchers, and it is expected that further developments will happen in the future using some of the techniques already developed. This thesis tries to introduce some of these issues and related results obtained recently using the APCW device developed in the group.

Several aspects regarding the device design and trap designs, using guided modes and external illumination, can be found in Chapter 4 and Chapter 5. Two external illumination trap schemes are proposed. One of them relies on the high reflectivity of the APCW when light is polarized along its axis. The other method relies on the lower reflectivity when the light is polarized transversally. In latter case, atoms are loaded into a standing wave trap far from the device and are transported with good control into the device's vicinity, a process analyzed in detail in Chapter 6.

The experiment design and its characterization is shown in Chapter 6. Finally, recent results show the observation of a periodic modulation of a weak probe transmission when atoms are moved periodically trough the device using an external trapping optical lattice. This is the first step to gain higher control over the motion of the atoms, and eventually succeed in loading many guided mode traps with single atoms, thereby achieving a high filling factor.

In the last section, the design of a simple 2D structure is described in Chapter 7. Numerical simulations showing the coupling of single dipoles to the guided modes of the structure are shown. Moreover, a dispersion engineer section along the 2D slab provides efficient input-output coupling along one direction. Similar results

can be extended to other lattices geometry.

8.2 Outlook

As experimental progress is made on two main fronts, device design and atom trapping near nanostructures, new possibilities will open. A new experimental setup that integrates larger optical access, efficient free-space coupling, and atom trapping and cooling capabilities is needed to make the fabrication-experiment circuit being faster and more efficient. Several members of the Quantum Optics group in collaboration with Cindy Regal's group at JILA have been working on the new platform.

New designs where not only the light-matter coupling with an specific guided mode is enhanced, but also the spontaneous emission into other modes and free-space is conveniently suppressed, will pave the way to observe cleaner signatures of long-range interaction, and maybe some of the photon mapping protocols developed for other systems can be observed.

Trapping is still one of the most challenging aspects of this experiment. A better understanding of the loading limitations and the near field pattern is needed to trap more atoms in the side illumination and standing wave traps. Numerical tools are essential to understand how the traps near the dielectric work, and the encouraging results for detecting fringe sensitive signals need to be used together with them to calibrate the experimental parameters and achieve trapping.

An additional possibility is to improve the optical pumping scheme to be faster and more spatially selective, such that the single photon loading schemes can be tested. For example, by using Raman lasers, a good control on the coherent exchange of population between two Cs ground states can be achieved in terms of parameters like their intensity and detuning. Therefore, the optical pumping experiment will benefit significantly by using a pair of lasers that excite guided modes with high contrast in its intensity pattern.

A better RF signal source can be used to allow a faster and lower noise phase modulation control. A good example is described in [211, 212]. In principle, together with modern FPGA technology, this will allow real time, phase preserving changes in the optical potential created by the standing wave. For instance, it can be used to lock the standing wave to the device, as its motion can change near field diffraction pattern, or to trigger guided mode potentials or resonant light processes that can enhance trapping.

Finally, numerical simulations suggest that deep blue detuned lattices can enhance the transport quality near the APCW in two ways. First, the trap potential minimum does not split into two minimum as the lattice approaches the device, because the potential minimum, this time, is the intensity nodal planes of the standing wave that are not pulled by the dielectric nanobeams. That results in a small "droplet" moving smoothly through the nanobeams. Furthermore, numerical simulations have shown that for deep potentials ($U_0 \geq K_{latt}$), the class of atoms that still crash into the beams' surfaces are significantly separated in time with respect to the atoms that go through the device center. In Lab 2, a hybrid blue detuned lattice and red detuned single beam have already been successfully loaded and used to transport atoms near the device. The red beam serves the purpose of providing transversal confinement, as the blue detuned standing wave does not provide confinement parallel to its nodal planes. We expect that by improving the loading of this lattice and making it deeper, better time resolved measurements and actions can be performed.

BIBLIOGRAPHY

[1] J Ignacio Cirac and H Jeff Kimble. "Quantum optics, what next?" In: *Nature Photonics* 11.1 (2017), pp. 18–20.

[2] H Jeff Kimble. "The quantum internet". In: *Nature* 453.7198 (2008), pp. 1023–1030.

[3] Michel H Devoret and Robert J Schoelkopf. "Superconducting circuits for quantum information: an outlook". In: *Science* 339.6124 (2013), pp. 1169–1174.

[4] MD Reed et al. "Realization of three-qubit quantum error correction with superconducting circuits". In: *Nature* 482.7385 (2012), pp. 382–385.

[5] Rami Barends et al. "Superconducting quantum circuits at the surface code threshold for fault tolerance". In: *Nature* 508.7497 (2014), pp. 500–503.

[6] Emre Togan et al. "Quantum entanglement between an optical photon and a solid-state spin qubit". In: *Nature* 466.7307 (2010), pp. 730–734.

[7] A. Imamoglu et al. "Quantum Information Processing Using Quantum Dot Spins and Cavity QED". In: *Phys. Rev. Lett.* 83 (20 Nov. 1999), pp. 4204–4207.

[8] P. Michler et al. "A Quantum Dot Single-Photon Turnstile Device". In: *Science* 290.5500 (2000), pp. 2282–2285.

[9] A. Sipahigil et al. "An integrated diamond nanophotonics platform for quantum-optical networks". In: *Science* 354.6314 (2016), pp. 847–850.

[10] P. C. Maurer et al. "Room-Temperature Quantum Bit Memory Exceeding One Second". In: *Science* 336.6086 (2012), pp. 1283–1286.

[11] Igor Aharonovich, Andrew D Greentree, and Steven Prawer. "Diamond photonics". In: *Nature Photonics* 5.7 (2011), pp. 397–405.

[12] Serge Haroche and Daniel Kleppner. "Cavity quantum electrodynamics". In: *Physics Today* 42.1 (1989), pp. 24–30.

[13] Immanuel Bloch, Jean Dalibard, and Wilhelm Zwerger. "Many-body physics with ultracold gases". In: *Rev. Mod. Phys.* 80 (3 July 2008), pp. 885–964.

[14] Michael J Hartmann, Fernando GSL Brandao, and Martin B Plenio. "Quantum many-body phenomena in coupled cavity arrays". In: *Laser & Photonics Reviews* 2.6 (2008), pp. 527–556.

[15] Onur Hosten et al. "Measurement noise 100 times lower than the quantum-projection limit using entangled atoms". In: *Nature* (2016).

[16] Kevin C. Cox et al. "Deterministic Squeezed States with Collective Measurements and Feedback". In: *Phys. Rev. Lett.* 116 (9 Mar. 2016), p. 093602.

[17] Kerry J Vahala. "Optical microcavities". In: *Nature* 424.6950 (2003), pp. 839–846.

[18] Takao Aoki et al. "Observation of strong coupling between one atom and a monolithic microresonator". In: *Nature* 443.7112 (2006), pp. 671–674.

[19] JD Thompson et al. "Coupling a Single Trapped Atom to a Nanoscale Optical Cavity". In: *Science* 340.6137 (2013), pp. 1202–1205.

[20] Darrick E Chang et al. "A single-photon transistor using nanoscale surface plasmons". In: *Nature Physics* 3.11 (2007), pp. 807–812.

[21] Darrick E Chang et al. "Cavity QED with atomic mirrors". In: *New Journal of Physics* 14.6 (2012), p. 063003.

[22] J. T. Shen and Shanhui Fan. "Coherent photon transport from spontaneous emission in one-dimensional waveguides". In: *Opt. Lett.* 30.15 (Aug. 2005), pp. 2001–2003.

[23] E. Vetsch et al. "Optical Interface Created by Laser-Cooled Atoms Trapped in the Evanescent Field Surrounding an Optical Nanofiber". In: *Phys. Rev. Lett.* 104 (20 May 2010), p. 203603.

[24] Fam Le Kien et al. "Spontaneous emission of a cesium atom near a nanofiber: Efficient coupling of light to guided modes". In: *Phys. Rev. A* 72 (3 Sept. 2005), p. 032509.

[25] C-L Hung et al. "Trapped atoms in one-dimensional photonic crystals". In: *New Journal of Physics* 15.8 (2013), p. 083026.

[26] S-P Yu et al. "Nanowire photonic crystal waveguides for single-atom trapping and strong light-matter interactions". In: *Applied Physics Letters* 104.11 (2014), p. 111103.

[27] Sajeev John. "Strong localization of photons in certain disordered dielectric superlattices". In: *Physical review letters* 58.23 (1987), p. 2486.

[28] James S Douglas et al. "Quantum many-body models with cold atoms coupled to photonic crystals". In: *Nature Photonics* 9.5 (2015), pp. 326–331.

[29] JD Hood et al. "Atom–atom interactions around the band edge of a photonic crystal waveguide". In: *Proceedings of the National Academy of Sciences of the United States of America* 113.38 (2016), pp. 10507–10512.

[30] A. Asenjo-Garcia et al. "Atom-light interactions in quasi-one-dimensional nanostructures: A Green's-function perspective". In: *Phys. Rev. A* 95 (3 Mar. 2017), p. 033818.

[31] Alejandro González-Tudela et al. "Subwavelength vacuum lattices and atom–atom interactions in two-dimensional photonic crystals". In: *Nature Photonics* 9.5 (2015), pp. 320–325.

[32] A Asenjo-Garcia et al. “Exponential improvement in photon storage fidelities using subradiance and" selective radiance" in atomic arrays”. In: *arXiv preprint arXiv:1703.03382* (2017).

[33] C.-L. Hung et al. “Quantum spin dynamics with pairwise-tunable, long-range interactions”. In: *Proceedings of the National Academy of Sciences* 113.34 (2016), E4946–E4955.

[34] DE Chang et al. “Trapping atoms using nanoscale quantum vacuum forces”. In: *Nature communications* 5 (2014).

[35] Marco T Manzoni, Ludwig Mathey, and Darrick E Chang. “Designing exotic many-body states of atomic spin and motion in photonic crystals”. In: *Nature Communications* 8 (2017).

[36] D. E. Chang, J. I. Cirac, and H. J. Kimble. “Self-Organization of Atoms along a Nanophotonic Waveguide”. In: *Phys. Rev. Lett.* 110 (11 Mar. 2013), p. 113606.

[37] Darrick E Chang, Vladan Vuletić, and Mikhail D Lukin. “Quantum nonlinear optics [mdash] photon by photon”. In: *Nature Photonics* 8.9 (2014), pp. 685–694.

[38] James S. Douglas, Tommaso Caneva, and Darrick E. Chang. “Photon Molecules in Atomic Gases Trapped Near Photonic Crystal Waveguides”. In: *Phys. Rev. X* 6 (3 Aug. 2016), p. 031017.

[39] A Goban et al. “Atom–light interactions in photonic crystals”. In: *Nature communications* 5 (2014).

[40] A. Goban et al. “Superradiance for Atoms Trapped along a Photonic Crystal Waveguide”. In: *Phys. Rev. Lett.* 115 (6 Aug. 2015), p. 063601.

[41] Eric Betzig. “Nobel Lecture: Single molecules, cells, and super-resolution optics”. In: *Rev. Mod. Phys.* 87 (4 Oct. 2015), pp. 1153–1168.

[42] Stefan W. Hell. “Nobel Lecture: Nanoscopy with freely propagating light”. In: *Rev. Mod. Phys.* 87 (4 Oct. 2015), pp. 1169–1181.

[43] W. E. (William E.) Moerner. “Nobel Lecture: Single-molecule spectroscopy, imaging, and photocontrol: Foundations for super-resolution microscopy”. In: *Rev. Mod. Phys.* 87 (4 Oct. 2015), pp. 1183–1212.

[44] Peter L Wizinowich et al. “The WM Keck Observatory laser guide star adaptive optics system: overview”. In: *Publications of the Astronomical Society of the Pacific* 118.840 (2006), p. 297.

[45] Victor Weisskopf and Eugene Wigner. “Berechnung der natürlichen linienbreite auf grund der diracschen lichttheorie”. In: *Zeitschrift für Physik* 63.1-2 (1930), pp. 54–73.

[46] E. M. Purcell. “Spontaneous Emission Probabilities at Radio Frequencies”. In: *Phys. Rev.* 69 (11-12 June 1946), pp. 674–674.

[47] Peter Lodahl, Sahand Mahmoodian, and Søren Stobbe. "Interfacing single photons and single quantum dots with photonic nanostructures". In: *Rev. Mod. Phys.* 87 (2 May 2015), pp. 347–400.

[48] C. Cohen-Tannoudji, J. Dupont-Roc, and G. Grynberg. *Photons and Atoms: Introduction to Quantum Electrodynamics*. Wiley, 1997.

[49] M.O. Scully and M.S. Zubairy. *Quantum Optics*. Cambridge University Press, 1997.

[50] L. Mandel and E. Wolf. *Optical Coherence and Quantum Optics*. Cambridge University Press, 1995.

[51] John David Jackson. *Classical electrodynamics*. New York, NY: Wiley, 1999.

[52] L. Novotny and B. Hecht. *Principles of Nano-Optics*. Cambridge University Press, 2012.

[53] H. J. Kimble and L. Mandel. "Problem of Resonance Fluorescence and the Inadequacy of Spontaneous Emission as a Test of Quantum Electrodynamics". In: *Phys. Rev. Lett.* 34 (24 June 1975), pp. 1485–1488.

[54] V. S. C. Manga Rao and S. Hughes. "Single Quantum Dot Spontaneous Emission in a Finite-Size Photonic Crystal Waveguide: Proposal for an Efficient "On Chip" Single Photon Gun". In: *Phys. Rev. Lett.* 99 (19 Nov. 2007), p. 193901.

[55] H.P. Breuer and F. Petruccione. *The Theory of Open Quantum Systems*. OUP Oxford, 2007.

[56] T Gruner and D-G Welsch. "Green-function approach to the radiation-field quantization for homogeneous and inhomogeneous Kramers-Kronig dielectrics". In: *Physical Review A* 53.3 (1996), p. 1818.

[57] Ho Trung Dung, Ludwig Knöll, and Dirk-Gunnar Welsch. "Resonant dipole-dipole interaction in the presence of dispersing and absorbing surroundings". In: *Physical Review A* 66.6 (2002), p. 063810.

[58] Stefan Yoshi Buhmann and Dirk-Gunnar Welsch. "Dispersion forces in macroscopic quantum electrodynamics". In: *Progress in quantum electronics* 31.2 (2007), pp. 51–130.

[59] Stefan Yoshi Buhmann. *Dispersion forces I: Macroscopic quantum electrodynamics and ground-state Casimir, Casimir–Polder and van der Waals Forces*. Springer Berlin Heidelberg, 2013.

[60] S. Buhmann. *Dispersion Forces II: Many-Body Effects, Excited Atoms, Finite Temperature and Quantum Friction*. Springer Berlin Heidelberg, 2013.

[61] G. S. Agarwal. "Quantum electrodynamics in the presence of dielectrics and conductors. IV. General theory for spontaneous emission in finite geometries". In: *Phys. Rev. A* 12 (4 Oct. 1975), pp. 1475–1497.

[62] JA Mlynek et al. “Observation of Dicke superradiance for two artificial atoms in a cavity with high decay rate”. In: *Nature communications* 5 (2014).

[63] Kevin Lalumière et al. “Input-output theory for waveguide QED with an ensemble of inhomogeneous atoms”. In: *Phys. Rev. A* 88 (4 Oct. 2013), p. 043806.

[64] AV Akimov et al. “Generation of single optical plasmons in metallic nanowires coupled to quantum dots”. In: *Nature* 450.7168 (2007), pp. 402–406.

[65] Julien Claudon et al. “A highly efficient single-photon source based on a quantum dot in a photonic nanowire”. In: *Nature Photonics* 4.3 (2010), pp. 174–177.

[66] Fam Le Kien et al. “Nanofiber-mediated radiative transfer between two distant atoms”. In: *Phys. Rev. A* 72 (6 Dec. 2005), p. 063815.

[67] VV Klimov and Martial Ducloy. “Spontaneous emission rate of an excited atom placed near a nanofiber”. In: *Physical Review A* 69.1 (2004), p. 013812.

[68] A Goban et al. “Demonstration of a state-insensitive, compensated nanofiber trap”. In: *Physical Review Letters* 109.3 (2012), p. 033603.

[69] Neil V. Corzo et al. “Large Bragg Reflection from One-Dimensional Chains of Trapped Atoms Near a Nanoscale Waveguide”. In: *Phys. Rev. Lett.* 117 (13 Sept. 2016), p. 133603.

[70] H. L. Sørensen et al. “Coherent Backscattering of Light Off One-Dimensional Atomic Strings”. In: *Phys. Rev. Lett.* 117 (13 Sept. 2016), p. 133604.

[71] A Gonzalez-Tudela et al. “Entanglement of two qubits mediated by one-dimensional plasmonic waveguides”. In: *Physical review letters* 106.2 (2011), p. 020501.

[72] Diego Martin-Cano et al. “Dissipation-driven generation of two-qubit entanglement mediated by plasmonic waveguides”. In: *Physical Review B* 84.23 (2011), p. 235306.

[73] Alejandro González-Tudela et al. “Deterministic generation of arbitrary photonic states assisted by dissipation”. In: *Physical review letters* 115.16 (2015), p. 163603.

[74] Vanessa Paulisch, HJ Kimble, and Alejandro González-Tudela. “Universal quantum computation in waveguide QED using decoherence free subspaces”. In: *New Journal of Physics* 18.4 (2016), p. 043041.

[75] Ephraim Shahmoon and Gershon Kurizki. “Nonradiative interaction and entanglement between distant atoms”. In: *Physical Review A* 87.3 (2013), p. 033831.

[76] Jan Petersen, Jürgen Volz, and Arno Rauschenbeutel. “Chiral nanophotonic waveguide interface based on spin-orbit interaction of light”. In: *Science* 346.6205 (2014), pp. 67–71.

[77] Jun Ye, DW Vernooy, and HJ Kimble. “Trapping of single atoms in cavity QED”. In: *Physical Review Letters* 83.24 (1999), p. 4987.

[78] Edwin T Jaynes and Frederick W Cummings. “Comparison of quantum and semiclassical radiation theories with application to the beam maser”. In: *Proceedings of the IEEE* 51.1 (1963), pp. 89–109.

[79] T. Hümmer et al. “Weak and strong coupling regimes in plasmonic QED”. In: *Phys. Rev. B* 87 (11 Mar. 2013), p. 115419.

[80] J.D. Joannopoulos et al. *Photonic Crystals: Molding the Flow of Light (Second Edition)*. Princeton University Press, 2011.

[81] John D Joannopoulos, Pierre R Villeneuve, and Shanhui Fan. “Photonic crystals: putting a new twist on light”. In: *Nature* 386.6621 (1997), p. 143.

[82] Eli Yablonovitch. “Inhibited spontaneous emission in solid-state physics and electronics”. In: *Physical review letters* 58.20 (1987), p. 2059.

[83] Sajeev John and Jian Wang. “Quantum electrodynamics near a photonic band gap: Photon bound states and dressed atoms”. In: *Physical review letters* 64.20 (1990), p. 2418.

[84] N.W. Ashcroft and N.D. Mermin. *Solid State Physics*. Holt, Rinehart and Winston, 1976.

[85] Daniel Kleppner. “Inhibited Spontaneous Emission”. In: *Phys. Rev. Lett.* 47 (4 July 1981), pp. 233–236.

[86] Peijun Yao, VSC Manga Rao, and Stephen Hughes. “On-chip single photon sources using planar photonic crystals and single quantum dots”. In: *Laser & Photonics Reviews* 4.4 (2010), pp. 499–516.

[87] Matt Eichenfield et al. “Optomechanical crystals”. In: *Nature* 462.7269 (2009), pp. 78–82.

[88] A Yu Petrov and M Eich. “Zero dispersion at small group velocities in photonic crystal waveguides”. In: *Applied physics letters* 85.21 (2004), pp. 4866–4868.

[89] S. Hughes et al. “Extrinsic Optical Scattering Loss in Photonic Crystal Waveguides: Role of Fabrication Disorder and Photon Group Velocity”. In: *Phys. Rev. Lett.* 94 (3 Jan. 2005), p. 033903.

[90] Stephan Smolka et al. “Probing the statistical properties of Anderson localization with quantum emitters”. In: *New Journal of Physics* 13.6 (2011), p. 063044.

[91] V. S. C. Manga Rao and S. Hughes. “Single quantum-dot Purcell factor and β factor in a photonic crystal waveguide”. In: *Phys. Rev. B* 75 (20 May 2007), p. 205437.

[92] G. Lecamp, P. Lalanne, and J. P. Hugonin. "Very Large Spontaneous-Emission β Factors in Photonic-Crystal Waveguides". In: *Phys. Rev. Lett.* 99 (2 July 2007), p. 023902.

[93] Kane Yee. "Numerical solution of initial boundary value problems involving Maxwell's equations in isotropic media". In: *IEEE Transactions on antennas and propagation* 14.3 (1966), pp. 302–307.

[94] "Lumerical Solutions, Inc. http://www.lumerical.com/tcad-products/fdtd/". In: ().

[95] Ardavan F. Oskooi et al. "MEEP: A flexible free-software package for electromagnetic simulations by the FDTD method". In: *Computer Physics Communications* 181 (Jan. 2010), pp. 687–702.

[96] Cole Percy Van Vlack. "Dyadic Green Functions and their applications in Classical and Quantum Nanophotonics". PhD thesis. Queen's University, 2012.

[97] H.J. Metcalf and P. van der Straten. *Laser Cooling and Trapping*. Graduate Texts in Contemporary Physics. Springer New York, 2012.

[98] J Ignacio Cirac and Peter Zoller. "Goals and opportunities in quantum simulation". In: *Nature Physics* 8.4 (2012), pp. 264–266.

[99] Daniel A Steck. "Cesium D line data". In: *Los Alamos - Theoretical Division* (1998).

[100] Paul D. Lett et al. "Observation of Atoms Laser Cooled below the Doppler Limit". In: *Phys. Rev. Lett.* 61 (2 July 1988), pp. 169–172.

[101] Jean Dalibard and Claude Cohen-Tannoudji. "Laser cooling below the Doppler limit by polarization gradients: simple theoretical models". In: *JOSA B* 6.11 (1989), pp. 2023–2045.

[102] P Jeffery Ungar et al. "Optical molasses and multilevel atoms: theory". In: *JOSA B* 6.11 (1989), pp. 2058–2071.

[103] E. L. Raab et al. "Trapping of Neutral Sodium Atoms with Radiation Pressure". In: *Phys. Rev. Lett.* 59 (23 Dec. 1987), pp. 2631–2634.

[104] C. G. Townsend et al. "Phase-space density in the magneto-optical trap". In: *Phys. Rev. A* 52 (2 Aug. 1995), pp. 1423–1440.

[105] Steven Chu et al. "Experimental Observation of Optically Trapped Atoms". In: *Phys. Rev. Lett.* 57 (3 July 1986), pp. 314–317.

[106] Rudolf Grimm, Matthias Weidemüller, and Yurii B Ovchinnikov. "Optical dipole traps for neutral atoms". In: *Advances in atomic, molecular, and optical physics* 42 (2000), pp. 95–170.

[107] Andrew D. Ludlow et al. "Optical atomic clocks". In: *Rev. Mod. Phys.* 87 (2 June 2015), pp. 637–701.

[108] A. M. Kaufman et al. “Two-particle quantum interference in tunnel-coupled optical tweezers”. In: *Science* 345.6194 (2014), pp. 306–309.

[109] Brian J. Lester et al. “Rapid Production of Uniformly Filled Arrays of Neutral Atoms”. In: *Phys. Rev. Lett.* 115 (7 Aug. 2015), p. 073003.

[110] Manuel Endres et al. “Atom-by-atom assembly of defect-free one-dimensional cold atom arrays”. In: *Science* (2016), aah3752.

[111] Daniel Barredo et al. “An atom-by-atom assembler of defect-free arbitrary two-dimensional atomic arrays”. In: *Science* 354.6315 (2016), pp. 1021–1023.

[112] B.H. Bransden and C.J. Joachain. *Physics of Atoms and Molecules*. Pearson Education. Prentice Hall, 2003.

[113] “Quantum control and measurement of atomic spins in polarization spectroscopy”. In: *Optics Communications* 283.5 (2010). Quo vadis Quantum Optics?, pp. 681–694.

[114] Bindiya Arora, M. S. Safronova, and Charles W. Clark. “Magic wavelengths for the $np-ns$ transitions in alkali-metal atoms”. In: *Phys. Rev. A* 76 (5 Nov. 2007), p. 052509.

[115] P. Rosenbusch et al. “ac Stark shift of the Cs microwave atomic clock transitions”. In: *Phys. Rev. A* 79 (1 Jan. 2009), p. 013404.

[116] Fam Le Kien, Philipp Schneeweiss, and Arno Rauschenbeutel. “Dynamical polarizability of atoms in arbitrary light fields: general theory and application to cesium”. In: *The European Physical Journal D* 67.5 (2013), p. 92.

[117] Ivan H. Deutsch and Poul S. Jessen. “Quantum-state control in optical lattices”. In: *Phys. Rev. A* 57 (3 Mar. 1998), pp. 1972–1986.

[118] D Ding et al. “Corrections to our results for optical nanofiber traps in Cesium”. In: *arXiv preprint arXiv:1212.4941* (2012).

[119] Amnon Yariv. *Quantum electronics*. Wiley, 1989.

[120] S. Blatt et al. “Rabi spectroscopy and excitation inhomogeneity in a one-dimensional optical lattice clock”. In: *Phys. Rev. A* 80 (5 Nov. 2009), p. 052703.

[121] Michael J Martin. “Quantum metrology and many-body physics: pushing the frontier of the optical lattice clock”. PhD thesis. University of Colorado - JILA, 2013.

[122] S. J. M. Kuppens et al. “Loading an optical dipole trap”. In: *Phys. Rev. A* 62 (1 June 2000), p. 013406.

[123] S. Bali et al. “Quantum-diffractive background gas collisions in atom-trap heating and loss”. In: *Phys. Rev. A* 60 (1 July 1999), R29–R32.

[124] TA Savard, KM O'hara, and JE Thomas. "Laser-noise-induced heating in far-off resonance optical traps". In: *Physical Review A* 56.2 (1997), R1095.

[125] ME Gehm et al. "Dynamics of noise-induced heating in atom traps". In: *Physical Review A* 58.5 (1998), p. 3914.

[126] John Weiner et al. "Experiments and theory in cold and ultracold collisions". In: *Rev. Mod. Phys.* 71 (1 Jan. 1999), pp. 1–85.

[127] J. Weiner. *Cold and Ultracold Collisions in Quantum Microscopic and Mesoscopic Systems*. Cambridge University Press, 2003.

[128] Benjamin L Lev. "Magnetic microtraps for cavity QED, Bose-Einstein condensates, and atom optics". PhD thesis. California Institute of Technology, 2005.

[129] Angharad Mair Thomas. "Ultra-cold collisions and evaporative cooling of caesium in a magnetic trap". PhD thesis. University of Oxford, 2004.

[130] Jie Ma et al. "High sensitive photoassociation spectroscopy of the Cs molecular and 1 g long-range states below the 6S 1/2+ 6P 3/2 limit". In: *Journal of Molecular Spectroscopy* 255.2 (2009), pp. 106–110.

[131] D. Sesko et al. "Collisional losses from a light-force atom trap". In: *Phys. Rev. Lett.* 63 (9 Aug. 1989), pp. 961–964.

[132] Stephan Dürr, Kurt W. Miller, and Carl E. Wieman. "Improved loading of an optical dipole trap by suppression of radiative escape". In: *Phys. Rev. A* 63 (1 Dec. 2000), p. 011401.

[133] Alan Gallagher and David E. Pritchard. "Exoergic collisions of cold Na^*-Na". In: *Phys. Rev. Lett.* 63 (9 Aug. 1989), pp. 957–960.

[134] Marcel Mudrich et al. "Hyperfine-changing collisions in an optically trapped gas of ultracold cesium and lithium". In: *Phys. Rev. A* 70 (6 Dec. 2004), p. 062712.

[135] Tino Weber et al. "Bose-Einstein Condensation of Cesium". In: *Science* 299.5604 (2003), pp. 232–235.

[136] C. R. Monroe et al. "Measurement of Cs-Cs elastic scattering at T=30 μK". In: *Phys. Rev. Lett.* 70 (4 Jan. 1993), pp. 414–417.

[137] Paul J. Leo, Carl J. Williams, and Paul S. Julienne. "Collision Properties of Ultracold ^{133}Cs Atoms". In: *Phys. Rev. Lett.* 85 (13 Sept. 2000), pp. 2721–2724.

[138] Vladan Vuletić et al. "Degenerate Raman Sideband Cooling of Trapped Cesium Atoms at Very High Atomic Densities". In: *Phys. Rev. Lett.* 81 (26 Dec. 1998), pp. 5768–5771.

[139] Andrew J. Kerman et al. "Beyond Optical Molasses: 3D Raman Sideband Cooling of Atomic Cesium to High Phase-Space Density". In: *Phys. Rev. Lett.* 84 (3 Jan. 2000), pp. 439–442.

[140] S. E. Hamann et al. “Resolved-Sideband Raman Cooling to the Ground State of an Optical Lattice”. In: *Phys. Rev. Lett.* 80 (19 May 1998), pp. 4149–4152.

[141] Nicolas Schlosser et al. “Sub-poissonian loading of single atoms in a microscopic dipole trap”. In: *Nature* 411.6841 (2001), pp. 1024–1027.

[142] N. Schlosser, G. Reymond, and P. Grangier. “Collisional Blockade in Microscopic Optical Dipole Traps”. In: *Phys. Rev. Lett.* 89 (2 June 2002), p. 023005.

[143] Su-Peng Yu. “Nano-Photonic Platform for Atom-Light Interaction”. PhD thesis. California Institute of Technology, 2017.

[144] Andrew C MClung. “Nano-fabricated Photonic Crystal Waveguides for Atomic Physics”. PhD thesis. California Institute of Technology, 2017.

[145] DM Harber et al. “Thermally induced losses in ultra-cold atoms magnetically trapped near room-temperature surfaces”. In: *Journal of low temperature physics* 133.3-4 (2003), pp. 229–238.

[146] D. Rychtarik et al. “Two-Dimensional Bose-Einstein Condensate in an Optical Surface Trap”. In: *Phys. Rev. Lett.* 92 (17 Apr. 2004), p. 173003.

[147] Birgit Brandstätter et al. “Integrated fiber-mirror ion trap for strong ion-cavity coupling”. In: *Review of Scientific Instruments* 84.12 (2013), p. 123104.

[148] G. Sagué et al. “Cold-Atom Physics Using Ultrathin Optical Fibers: Light-Induced Dipole Forces and Surface Interactions”. In: *Phys. Rev. Lett.* 99 (16 Oct. 2007), p. 163602.

[149] K. P. Nayak et al. “Optical nanofiber as an efficient tool for manipulating and probing atomic fluorescence”. In: *Opt. Express* 15.9 (Apr. 2007), pp. 5431–5438.

[150] D Reitz et al. “Coherence properties of nanofiber-trapped cesium atoms”. In: *Physical review letters* 110.24 (2013), p. 243603.

[151] Clément Sayrin et al. “Nanophotonic Optical Isolator Controlled by the Internal State of Cold Atoms”. In: *Physical Review X* 5.4 (2015), p. 041036.

[152] Alejandro W Rodriguez, Federico Capasso, and Steven G Johnson. “The Casimir effect in microstructured geometries”. In: *Nature photonics* 5.4 (2011), pp. 211–221.

[153] Justin D. Cohen, Seán M. Meenehan, and Oskar Painter. “Optical coupling to nanoscale optomechanical cavities for near quantum-limited motion transduction”. In: *Opt. Express* 21.9 (May 2013), pp. 11227–11236.

[154] Paul E Barclay et al. “Integration of fiber-coupled high-Q Si N x microdisks with atom chips”. In: *Applied physics letters* 89.13 (2006), p. 131108.

[155] D. J. Wilson et al. “Cavity Optomechanics with Stoichiometric SiN Films”. In: *Phys. Rev. Lett.* 103 (20 Nov. 2009), p. 207204.

[156] A M Jayich et al. “Dispersive optomechanics: a membrane inside a cavity”. In: *New Journal of Physics* 10.9 (2008), p. 095008.

[157] P Temple-Boyer et al. “Residual stress in low pressure chemical vapor deposition SiN x films deposited from silane and ammonia”. In: *Journal of Vacuum Science & Technology A: Vacuum, Surfaces, and Films* 16.4 (1998), pp. 2003–2007.

[158] Paul Edward Barclay. “Fiber-coupled nanophotonic devices for nonlinear optics and cavity QED”. PhD thesis. California Institute of Technology, 2007.

[159] Eric R.I. Abraham and Eric A. Cornell. “Teflon feedthrough for coupling optical fibers into ultrahigh vacuum systems”. In: *Appl. Opt.* 37.10 (Apr. 1998), pp. 1762–1763.

[160] N. Le Thomas et al. “Light transport regimes in slow light photonic crystal waveguides”. In: *Phys. Rev. B* 80 (12 Sept. 2009), p. 125332.

[161] Stefan Yoshi Buhmann et al. “Casimir-Polder forces: A nonperturbative approach”. In: *Phys. Rev. A* 70 (5 Nov. 2004), p. 052117.

[162] T. Søndergaard and B. Tromborg. “General theory for spontaneous emission in active dielectric microstructures: Example of a fiber amplifier”. In: *Phys. Rev. A* 64 (3 Aug. 2001), p. 033812.

[163] R. J. Thompson, G. Rempe, and H. J. Kimble. “Observation of normal-mode splitting for an atom in an optical cavity”. In: *Phys. Rev. Lett.* 68 (8 Feb. 1992), pp. 1132–1135.

[164] J. McKeever et al. “State-Insensitive Cooling and Trapping of Single Atoms in an Optical Cavity”. In: *Phys. Rev. Lett.* 90 (13 Apr. 2003), p. 133602.

[165] H. Mabuchi et al. “Real-time detection of individual atoms falling through a high-finesse optical cavity”. In: *Opt. Lett.* 21.17 (Sept. 1996), pp. 1393–1395.

[166] Serge Haroche and Jean-Michel Raimond. *Exploring the quantum: atoms, cavities, and photons*. Oxford university press, 2006.

[167] J. M. Raimond, M. Brune, and S. Haroche. “Manipulating quantum entanglement with atoms and photons in a cavity”. In: *Rev. Mod. Phys.* 73 (3 Aug. 2001), pp. 565–582.

[168] Tian Zhong et al. “Nanophotonic coherent light-matter interfaces based on rare-earth-doped crystals”. In: *Nature communications* 6 (2015).

[169] B. J. M. Hausmann et al. “Coupling of NV Centers to Photonic Crystal Nanobeams in Diamond”. In: *Nano Letters* 13.12 (2013), pp. 5791–5796.

[170] BJ Bloom et al. “An optical lattice clock with accuracy and stability at the 10-18 level”. In: *Nature* 506.7486 (2014), pp. 71–75.

[171] Jacob F Sherson et al. “Single-atom-resolved fluorescence imaging of an atomic Mott insulator”. In: *Nature* 467.7311 (2010), pp. 68–72.

[172] Waseem S Bakr et al. “A quantum gas microscope for detecting single atoms in a Hubbard-regime optical lattice”. In: *Nature* 462.7269 (2009), pp. 74–77.

[173] T Grünzweig et al. “Near-deterministic preparation of a single atom in an optical microtrap”. In: *Nature Physics* 6.12 (2010), pp. 951–954.

[174] H.C. van de Hulst. *Light Scattering by Small Particles*. Dover Books on Physics Series. Dover Publications, 1957.

[175] Daniel S. Benincasa et al. “Spatial distribution of the internal and near-field intensities of large cylindrical and spherical scatterers”. In: *Appl. Opt.* 26.7 (Apr. 1987), pp. 1348–1356.

[176] Fam Le Kien and K. Hakuta. “Microtraps for atoms outside a fiber illuminated perpendicular to its axis: Numerical results”. In: *Phys. Rev. A* 80 (1 July 2009), p. 013415.

[177] Daniel James Alton. “Interacting single atoms with nanophotonics for chip-integrated quantum networks”. PhD thesis. California Institute of Technology, 2013.

[178] Alejandro W. Rodriguez et al. “Casimir forces in the time domain: Theory”. In: *Phys. Rev. A* 80 (1 July 2009), p. 012115.

[179] DJ Alton et al. “Strong interactions of single atoms and photons near a dielectric boundary”. In: *Nature Physics* 7.2 (2011), pp. 159–165.

[180] P.K. Ghosh. *Ion Traps*. International series of monographs on physics. Clarendon Press, 1995.

[181] Dong Sheng, Jiehang Zhang, and Luis A Orozco. “Sensitivity test of a blue-detuned dipole trap designed for parity non-conservation measurements in Fr”. In: *Review of Scientific Instruments* 83.4 (2012), p. 043106.

[182] T. Kishimoto et al. “Electrodynamic Trapping of Spinless Neutral Atoms with an Atom Chip”. In: *Phys. Rev. Lett.* 96 (12 Mar. 2006), p. 123001.

[183] M. Mansuripur. “Distribution of light at and near the focus of high-numerical-aperture objectives”. In: *J. Opt. Soc. Am. A* 3.12 (Dec. 1986), pp. 2086–2093.

[184] AN Grigorenko et al. “Nanometric optical tweezers based on nanostructured substrates”. In: *Nature Photonics* 2.6 (2008), pp. 365–370.

[185] S Travis Bannerman et al. “Single-photon cooling at the limit of trap dynamics: Maxwell’s demon near maximum efficiency”. In: *New Journal of Physics* 11.6 (2009), p. 063044.

[186] Gabriel Noam Price et al. “Single-photon atomic cooling”. In: *Laser physics* 17.7 (2007), pp. 965–968.

[187] R. Taïeb et al. “Cooling and localization of atoms in laser-induced potential wells”. In: *Phys. Rev. A* 49 (6 June 1994), pp. 4876–4887.

[188] Kurt W. Miller, Stephan Dürr, and Carl E. Wieman. “rf-induced Sisyphus cooling in an optical dipole trap”. In: *Phys. Rev. A* 66 (2 Aug. 2002), p. 023406.

[189] Thibault Peyronel. “Quantum nonlinear optics using cold atomic ensembles”. PhD thesis. Massachusetts Institute of Technology, 2013.

[190] Ralf Ritter et al. “Coupling thermal atomic vapor to an integrated ring resonator”. In: *New Journal of Physics* 18.10 (2016), p. 103031.

[191] W Wohlleben et al. “An atom faucet”. In: *The European Physical Journal D-Atomic, Molecular, Optical and Plasma Physics* 15.2 (2001), pp. 237–244.

[192] W Ketterle, DS Durfee, and DM Stamper-Kurn. “Making, probing and understanding Bose-Einstein condensates”. In: *arXiv preprint cond-mat/9904034* 5 (1999).

[193] R.W. Boyd. *Nonlinear Optics*. Nonlinear Optics Series. Elsevier Science, 2008.

[194] D. Schrader et al. “An optical conveyor belt for single neutral atoms”. In: *Appl. Phys. B* 73 (2001), p. 819.

[195] Stefan Kuhr et al. “Deterministic delivery of a single atom”. In: *Science* 293.5528 (2001), pp. 278–280.

[196] D. Frese et al. “Single Atoms in an Optical Dipole Trap: Towards a Deterministic Source of Cold Atoms”. In: *Phys. Rev. Lett.* 85 (18 Oct. 2000), pp. 3777–3780.

[197] J. Dalibard and C. Cohen-Tannoudji. “Dressed-atom approach to atomic motion in laser light: the dipole force revisited”. In: *J. Opt. Soc. Am. B* 2.11 (Nov. 1985), pp. 1707–1720.

[198] J. P. Brantut et al. “Light-shift tomography in an optical-dipole trap for neutral atoms”. In: *Phys. Rev. A* 78 (3 Sept. 2008), p. 031401.

[199] Wolfgang Alt et al. “Single atoms in a standing-wave dipole trap”. In: *Phys. Rev. A* 67 (3 Mar. 2003), p. 033403.

[200] L.D. Landau and E.M. Lifshitz. *Mechanics*. v. 1. Elsevier Science, 1982.

[201] R. J. Thompson et al. “Nonlinear spectroscopy in the strong-coupling regime of cavity QED”. In: *Phys. Rev. A* 57 (4 Apr. 1998), pp. 3084–3104.

[202] H. Carmichael. *An Open Systems Approach to Quantum Optics: Lectures Presented at the Université Libre de Bruxelles, October 28 to November 4, 1991*. An Open Systems Approach to Quantum Optics: Lectures Presented at the Université Libre de Bruxelles, October 28 to November 4, 1991 v. 18. Springer Berlin Heidelberg, 1993.

[203] J. T. Shen and Shanhui Fan. “Coherent photon transport from spontaneous emission in one-dimensional waveguides”. In: *Opt. Lett.* 30.15 (Aug. 2005), pp. 2001–2003.

[204] J.L. Lawson and G.E. Uhlenbeck. *Threshold Signals*. Dover books on engeineering and engineering physics. Dover, 1964.

[205] Kang Xie et al. “Trapped photons at a Dirac point: a new horizon for photonic crystals”. In: *Laser & Photonics Reviews* 8.4 (2014), pp. 583–589.

[206] F. J. García de Abajo. “Colloquium: Light scattering by particle and hole arrays”. In: *Rev. Mod. Phys.* 79 (4 Oct. 2007), pp. 1267–1290.

[207] Ephraim Shahmoon et al. “Cooperative Resonances in Light Scattering from Two-Dimensional Atomic Arrays”. In: *Phys. Rev. Lett.* 118 (11 Mar. 2017), p. 113601.

[208] Janos Perczel et al. “Topological Quantum Optics in Two-Dimensional Atomic Arrays”. In: *arXiv preprint arXiv:1703.04849* (2017).

[209] J. Witzens, M. Loncar, and A. Scherer. “Self-collimation in planar photonic crystals”. In: *IEEE Journal of Selected Topics in Quantum Electronics* 8.6 (Nov. 2002), pp. 1246–1257.

[210] Sun-Goo Lee et al. “Reflection minimization at two-dimensional photonic crystal interfaces”. In: *Opt. Express* 16.6 (Mar. 2008), pp. 4270–4277.

[211] Carsten Robens et al. “Fast, high-precision optical polarization synthesizer for ultracold-atom experiments”. In: *arXiv preprint arXiv:1611.07952* (2016).

[212] Carsten Robens et al. “Low-Entropy States of Neutral Atoms in Polarization-Synthesized Optical Lattices”. In: *Phys. Rev. Lett.* 118 (6 Feb. 2017), p. 065302.